

Christoph Slaby

Gyro-kinetic simulations of tokamaks and stellarators including collisions

**IPP 2019-12
Juni 2019**

Gyro-kinetic simulations of tokamaks and stellarators including collisions

Inauguraldissertation

zur

Erlangung des akademischen Grades eines
Doktors der Naturwissenschaften (Dr. rer. nat.)

der

Mathematisch-Naturwissenschaftlichen Fakultät

der

Universität Greifswald

vorgelegt von

Christoph Slaby

Greifswald, den 19. Dezember 2018

Dekan: Prof. Dr. Werner Weitschies

1. Gutachter: Prof. Dr. Per Helander

2. Gutachter: Prof. Dr. Laurent Villard

Datum der Promotion: 15. April 2019

Contents

Aims and structure of this thesis	1
1 Introduction and fundamentals	3
1.1 Introduction to nuclear fusion	3
1.2 The tokamak and the stellarator	5
1.3 Shear Alfvén waves and gap modes	6
1.4 Gyro-kinetic theory	9
1.5 Collisions	11
2 Summary of results	15
2.1 Initial benchmark of the implementation of collisions (A.1)	15
2.2 Collisions influence non-linear saturation levels (A.2)	16
2.3 Investigating a realistic Wendelstein 7-X case (A.3 and A.4)	19
2.4 Collisions and non-linear frequency chirping (A.5)	22
2.5 A simplified model for mode drive and damping (A.6)	23
2.6 Flux-surface variations of the electrostatic potential (A.7)	25
3 Summary and outlook	27
4 Bibliography	31
A Thesis articles	39
Article A.1: Combining electromagnetic gyro-kinetic particle-in-cell simulations with collisions	41
Article A.2: Effects of collisions on the saturation dynamics of TAEs in tokamaks and stellarators	53
Article A.3: Numerical investigation of fast-ion-driven modes in Wendelstein 7-X (non-referred)	71
Article A.4: Parametric study of fast-ion-driven modes in Wendelstein 7-X	77
Article A.5: On non-linear frequency chirping in connection with collisions	89
Article A.6: Numerical investigation of non-perturbative kinetic effects of energetic particles on toroidicity-induced Alfvén eigenmodes in tokamaks and stellarators	121
Article A.7: On-surface potential and radial electric field variations in electron root stellarator plasmas	139

B Additional unpublished material	155
B.1 An analytical dispersion relation including Krook collisions	155
B.2 The different formulations of gyro-kinetic theory	157
B.2.1 The v_{\parallel} -formulation	157
B.2.2 The p_{\parallel} -formulation	158
B.2.3 The mixed formulation	159
B.2.4 Comparison	160
B.3 Effect of collisions in velocity space (EUTERPE)	161
B.4 The conservation scheme	163
B.4.1 Benchmarking the conservation scheme	164
B.5 Implementation of the fast-ion collision operator	166
B.5.1 Testing the implementation	168
B.6 Evolving multiple modes in a single simulation	171
B.6.1 Case description	172
B.6.2 Damping rates	173
B.6.3 Multi-mode results	174
Nomenclature	177
Eigenständigkeitserklärung	183
Scientific contributions	185
Acknowledgement	187

Aims and structure of this thesis

This thesis, titled ‘Gyro-kinetic simulations of tokamaks and stellarators including collisions’, focusses on the modelling of resonant destabilization of Alfvén eigenmodes by fast ions in fusion plasmas. It especially addresses non-linear simulations of stellarator plasmas in which particle collisions are retained. This is in contrast to investigations done in the past (see e.g. Refs. [1, 2]), in which collisions were neglected. Here, it will be shown that collisions are required for a realistic description of Alfvén waves in plasmas relevant to nuclear fusion. In this sense, this thesis helps to enhance the level of realism in numerical simulations.

The work presented here was done in a period in which the stellarator Wendelstein 7-X (W7-X) had its first operation phases. The 2018 experimental campaign, for the first time, included neutral beam injection (NBI), which could trigger Alfvénic activity. Alfvén eigenmodes (AEs) present in the plasma can resonantly interact with the NBI ions (or alpha particles) and could lead to enhanced heat loads on the vessel wall. Such behaviour has been observed in the past in experiments with significant alpha-particle heating (e.g. in TFTR [3]), but also in smaller devices such as ASDEX Upgrade [4]. The TFTR example indicates the potentially destructive behaviour of fast-ion-driven AEs in fusion devices. Avoiding such a scenario is, of course, desirable in any machine.

For W7-X, there exist numerical predictions of the classical fast-ion losses to the first wall [5] which have been obtained using the ASCOT code [6, 7]. They are currently being validated using data gathered in the 2018 experimental campaign of W7-X. The question is in what way AE activity in the plasma, possibly influenced by collisions, changes the loss pattern. To answer this question, a coupling of ASCOT and EUTERPE is planned in the future. Before that, the non-linear dynamics and saturation of AEs in W7-X needs to be better understood. Since collisions play an important role in the formation of the fast-ion distribution function, it is only natural to also include them in EUTERPE simulations, especially since the saturation levels of the AEs are a function of collisionality (see article A.2).

At W7-X, experimental data (regarding the destabilization of AEs by fast ions) are produced now which means that the modelling tools need to be at a stage where simulations can readily be compared with experimental measurements. In part, this thesis contributed to code development and benchmarking activities in order to prepare the EUTERPE code for realistic cases. Articles A.3 and A.4 included in this thesis, in which realistic profiles and distribution functions were used to describe the plasma, can be viewed as a step in this direction.

For simplified cases, analytical theory regarding the interaction of Alfvén eigenmodes with fast ions while influenced by collisions is available. The well-established Berk-Breizman paradigm [8–12] is a prime example. However, the reduction of the complexity of the problem comes at a cost: The Berk-Breizman model is formulated in coordinates (e.g. a one-dimensional velocity space) that are not trivially related to tokamaks, let alone a stellarator. Furthermore, numerical simulations, building upon analytical theory by making use of invariants of the particle motion,

Aims and structure of this thesis

are often performed in tokamaks. An appropriate description of stellarators is more difficult. Here, we seek to understand if the effect of collisions on the mode non-linear dynamics in stellarators is comparable to tokamaks. Again, this is in particular important in order to assess Alfvén-eigenmode-induced transport of fast ions – an important issue for present-day devices and future reactors.

A future goal is that numerical simulations can guide the way towards a reduced transport model for fast ions in stellarators. Such models exist in the form of the so-called ‘Kick model’ [13,14] or the ‘resonance broadened quasi-linear (RBQ) model’ [15] for tokamaks, but are still lacking for stellarators.

The primary goals of this dissertation can be summarized as follows: It deals with the implementation of particle collisions into the EUTERPE code, the thorough benchmark of the implementation, and the application to realistic W7-X plasmas, where we confirm the importance of collisions in non-linear simulations.

The thesis is structured as follows: In Ch. 1 we give an introduction to the general topics covered. Ch. 2 summarizes the key findings of each paper and provides links to a number of appendices that contain additional unpublished material, also intended to bridge the gaps in between the individual papers. The thesis concludes with a summary and an outlook in Ch. 3. The published articles are included in App. A.

Chapter 1

Introduction and fundamentals

1.1 Introduction to nuclear fusion

There are several challenges that mankind will face in the course of the present century. One of the – still unanswered – questions is how we will satisfy our ever-rising need for more energy. This increasing demand for energy has two leading causes: Firstly, the population is growing worldwide. While in the year 2017, 7.6 billion people lived on the planet, the expected population is 9.8 billion for the year 2050 [16]. More people consume more energy. Secondly, the standard of living is increasing worldwide [17]. This also leads to more energy being consumed.

But the growing need for more energy is not a recent phenomenon. Since the start of the industrial revolution the global demand for energy has grown. In the past, we have mainly used fossil sources to convert to usable energy. This can be seen in Fig. 1.1 which shows the evolution of the primary energy being consumed globally and the means of its production.

There are two main considerations why we cannot continue like this: On the one hand, fossil sources will eventually be exhausted. Projections indicate that in approximately 40 (oil) to 130 (coal) years this could be the case [20]. Given the typical time it takes to progress from basic research to something usable and profitable on the free market, we need to start looking for alternative means of generating energy now. The second consideration is that we want [21] to combat global warming. Among other so-called greenhouse gasses carbon-dioxide, which is emitted into the atmosphere when fossil fuels are burned, is viewed to be responsible for global warming. Fig. 1.2 shows how the temperature has developed on the northern hemisphere for the past 4000 years. The last part, starting at approximately 1800 is widely considered to be man-made climate change. The data are taken from Refs. [22, 23] in which a one-dimensional energy-balance model (including orbital, solar and greenhouse-gas effects on the climate) is used to calculate the past temperatures from radioactive isotopes contained in air bubbles found in ice cores. More recent data [24] shows that by 2017 the global temperature had already increased by 0.9 K compared to the 1951-1980 average.

Nuclear fusion has the potential of providing a clean and virtually inexhaustible source of energy in the second half of the twenty-first century.

On the other hand, so-called renewable energies, such as solar energy and wind energy, can play an important role in bridging the time until nuclear fusion becomes available. They suffer from low energy densities at the production stage and are weather-dependent and thus difficult to integrate into a power grid and market structure where the consumer wants to decide when to consume energy.

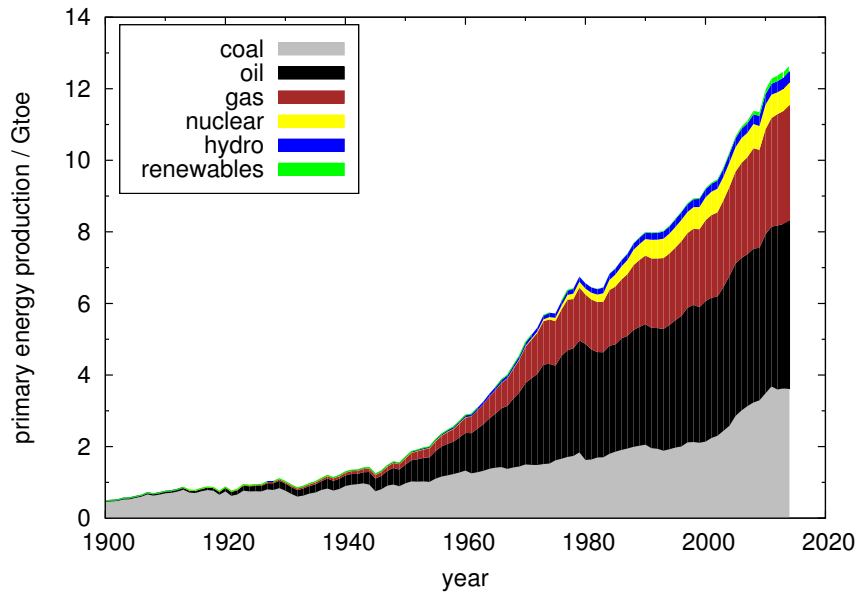


Figure 1.1: Increase of global primary energy consumption partitioned by means of production. Especially since 1950, energy consumption increases rapidly. Most of it comes from fossil sources. Data are taken from Refs. [18,19].

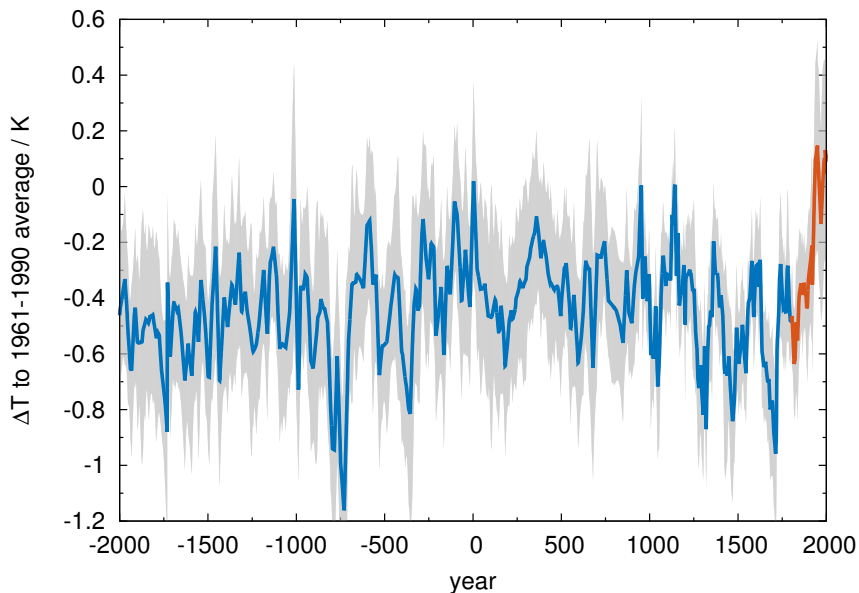


Figure 1.2: Development of the surface temperature on the northern hemisphere over the last 4000 years. Shown are the temperature differences compared with the 1961-1990 average. Since approximately 1800 (coloured red) the temperature increases rapidly. Data are taken from Refs. [22,23].

In nuclear fusion energy is gained by fusing light nuclei into heavier ones. Energy can be extracted from the binding energies of the fusing nuclei. The products of the fusion reaction are more stable than the initial nuclei, i.e. they are lighter. This mass difference Δm corresponds according to [25]

$$\Delta E = \Delta mc^2 \quad (1.1)$$

to a difference in binding energy ΔE which is released as kinetic energy of the reaction products. c denotes the speed of light in a vacuum.

The fusion reaction that is most easily realized [26] is fusing together deuterium and tritium, two hydrogen isotopes



Next to the neutron, which carries 4/5 of the total energy away from the plasma, the fusion reaction produces a very energetic (i.e. fast) helium nucleus or alpha particle, which is magnetically confined. Thus, if fusion is to be successful, a certain fraction of fast ions in the plasma cannot be avoided.

On the way to making nuclear fusion work, there still exist a number of unsolved problems. Towards the edge of the plasma, materials that can withstand the high heat and neutron fluxes have to be developed. In the plasma core, the mechanisms of turbulent heat and particle transport need to be understood. The EUTERPE code is a multi-purpose tool originally conceived to tackle the issue of plasma turbulence in stellarators. It was first designed in Lausanne [27] and came to Greifswald in 2001, where active development continues. In this thesis, it is used to address the topic of fast-ion-driven global electromagnetic modes. The problem is that fast ions, either generated by the fusion reactions or by auxiliary heating systems such as neutral beam injection (NBI) or ion-cyclotron-resonance heating (ICRH), can excite Alfvénic instabilities in the plasma. A brief introduction to this process and to the instabilities involved is given in Sec. 1.3. The interaction of fast ions with Alfvén waves non-linearly influences the orbits of the particles and typically leads to radial transport [4, 8, 14], i.e. profile flattening [28, 29]. If fast ions are lost from the plasma before they thermalize, the system loses energy. In severe cases, plasma-facing components may be damaged [3, 30]. This makes it paramount to control Alfvénic activity, especially with regard to a future fusion reactor.

It is important to note that in Wendelstein 7-X (W7-X), fast ions provided by the NBI system have the same normalized gyro-radius (normalized to the minor radius of the device) as alpha particles in ITER [31], the next-generation large tokamak currently being built in southern France. This makes W7-X a good candidate for studying the confinement of fast ions.

1.2 The tokamak and the stellarator

The challenge of nuclear fusion is to stably confine a plasma with ion temperatures in the range of several 10 keV. The two main approaches being pursued are magnetic-confinement and inertial-confinement fusion, with the latter being outside of the scope of this thesis. In the context of magnetic-confinement fusion, the high temperatures require, in particular, that the plasma be kept away from the wall of the device.

Magnetically confining a fusion plasma can be accomplished by means of a magnetic field in the topological shape of a torus. Necessary are furthermore nested surfaces of constant pressure – so-called flux surfaces [32] – and a twist in the magnetic field lines.

Currently, two leading concepts exist that are able of generating such a magnetic field. They are called the tokamak and the stellarator, respectively. The two devices are depicted side-by-side

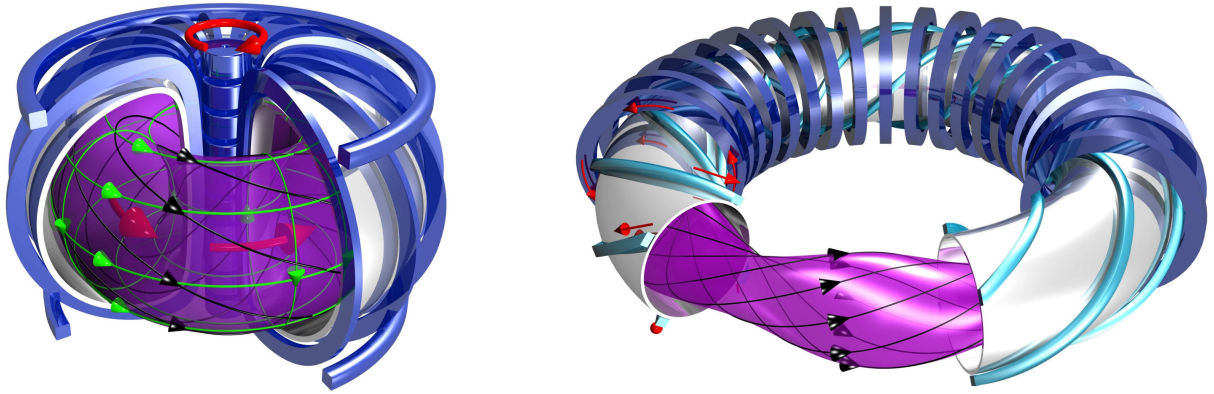


Figure 1.3: Schematic depiction of the two leading possibilities to magnetically confine a fusion plasma: A tokamak on the left-hand side and a classical stellarator on the right-hand side. While in the tokamak a central solenoid induces a plasma current to produce a poloidal magnetic field, only external currents are used in the stellarator. Both figures courtesy of IPP, Christian Brandt.

in Fig. 1.3. They differ in the way the twisted magnetic field is produced. The strength of the twist is measured by the rotational transform

$$\iota = \lim_{N_{\text{tor}} \rightarrow \infty} \frac{N_{\text{pol}}}{N_{\text{tor}}}, \quad (1.3)$$

which describes the number of N_{pol} poloidal turns a field line performs for N_{tor} toroidal turns [32] it takes. In tokamak research, the safety factor $q = 1/\iota$ is generally used.

In the tokamak (shown on the left-hand side of Fig. 1.3) so-called toroidal field coils produce the main toroidal magnetic field. The poloidal magnetic field is generated by changing the magnetic flux in a central solenoid, which induces a current in the plasma. This current creates an additional magnetic field in the poloidal direction. The superposition gives the desired twisted field. A major disadvantage is that the high plasma current can cause instabilities [33]. This can then trigger a disruption [34], a prompt loss of confinement, after which the plasma is unable to support the high current any longer. Furthermore, a tokamak operates intrinsically pulsed as, at some point, it becomes impossible to further change the magnetic flux in the central solenoid.

The stellarator, which is shown on the right-hand side of Fig. 1.3, does not have these disadvantages. Instead, it has a more complex coil set, i.e. additional helical coils in the case of a classical stellarator. The twisted magnetic field is produced purely by external currents, which gives a stellarator steady-state capability. An unavoidable feature of this approach is a magnetic field \mathbf{B} whose magnitude depends on the toroidal angle. Hence, compared to a tokamak, one continuous symmetry (leading to a conserved quantity [35]) is lost. This requires an intricate optimization of the magnetic field if the quality of the confinement in a stellarator is to be comparable to that of a tokamak [36].

Instead of planar toroidal field coils and helical coils, non-planar coils may be chosen. This approach has been pursued for the modular stellarators W7-AS and W7-X.

1.3 Shear Alfvén waves and gap modes

Most of the articles included in this thesis address the kinetic effect of fast particles on shear Alfvén waves. Shear Alfvén waves are transverse electromagnetic waves [37] that propagate in

astrophysical and fusion plasmas along the field lines of the confining magnetic field. Ref. [38] emphasizes the analogy of a shear Alfvén wave and a plucked string: The magnetic field lines provide the tension and the ion mass the inertia.

In cylindrical geometry, the dispersion relation of shear Alfvén waves is

$$\omega^2 = v_A^2 k_{\parallel}^2, \quad (1.4)$$

where $v_A = B/\sqrt{\mu_0 m_i n_i}$ is the local Alfvén velocity [37] and k_{\parallel} and ω are the parallel wave vector and the frequency of the mode, respectively. Further, m_i and n_i are the ion mass and density, and μ_0 denotes the vacuum permeability. This dispersion relation is the ideal-MHD limit of the more complex dispersion relation of kinetic Alfvén waves, which is derived in App. B.1 from kinetic theory. Waves that fulfil the dispersion relation Eq. (1.4) are called continuum modes. Typically, they are strongly damped.

In a toroidal fusion device, the strength of the magnetic field varies as $B \sim 1/R$ [33], where R measures the distance from the central symmetry axis. For a wave which propagates along a twisted magnetic field line, this gives rise to a periodic modulation of B and, as a consequence, of the refractive index. This effect is similar to electrons moving in the periodic potential of the atomic nuclei in condensed matter physics [39]. Both in solids as well as in fusion plasmas, the consequence are frequency (or energy) gaps in the otherwise continuous spectrum. A similar effect is known as the avoided crossing phenomenon in quantum mechanics [40].

As a consequence, the dispersion relation of shear Alfvén waves is more complex in a toroidal device compared with a slab or a cylinder. In a two-mode model [41], the dispersion relation (around the toroidicity-induced gap) can be expressed as

$$\left(k_{m,n}^2 - \frac{\omega^2}{v_A^2}\right) \left(k_{m+1,n}^2 - \frac{\omega^2}{v_A^2}\right) - \epsilon^2 \frac{\omega^4}{v_A^4} = 0. \quad (1.5)$$

The parameter ϵ is related to the toroidal geometry and is responsible for the formation of frequency gaps. In a large-aspect-ratio tokamak it can be expressed as $\epsilon = 2(\Delta' + a\sqrt{s}/R_0)$ [41]. The parallel wave vector with poloidal and toroidal mode numbers m and n is denoted by $k_{m,n} = (n + ml)/R_0$. Δ' is the radial derivative of the Shafranov shift, R_0 denotes the major radius of the toroidal device, and s is the normalized toroidal flux.

In a stellarator with N field periods, the equation for the continuum is slightly more complex [42]

$$\left(k_{m,n}^2 - \frac{\omega^2}{v_A^2}\right) \left(k_{m+\mu,n+\nu N}^2 - \frac{\omega^2}{v_A^2}\right) - \left(\epsilon^{(\mu,\nu)} \frac{\omega^2}{v_A^2} - \frac{\epsilon_g^{(\mu,\nu)}}{2} k_{m,n} k_{m+\mu,n+\nu N}\right)^2 = 0. \quad (1.6)$$

Here, $\epsilon^{(\mu,\nu)} = \epsilon_g^{(\mu,\nu)}/2 - 2\epsilon_B^{(\mu,\nu)}$, with $\epsilon_g^{(\mu,\nu)}$ and $\epsilon_B^{(\mu,\nu)}$ denoting the Fourier components of the g^{ss} metric tensor component and the magnetic field strength, respectively. The coupling of the two modes depends on μ and ν .

An example continuum (the parameters are those of the ITPA tokamak benchmark case [43,44]) is shown in Fig. 1.4. Clearly visible is the continuum (coloured lines) with the continuum gap around $\omega = 4.0 \cdot 10^5 \text{ s}^{-1}$. The corresponding cylindrical continuum (black dashed lines) is obtained by setting ϵ to zero. In fusion plasmas, global modes can exist in such frequency gaps. Because they only experience minimal interaction with the continuum modes, their damping is minimized.¹ This makes them ideal candidates for the excitation by fast ions. On the other

¹While continuum damping [41,45] is absent, other mechanisms such as Landau damping [46] or radiative damping [47] might still be present.

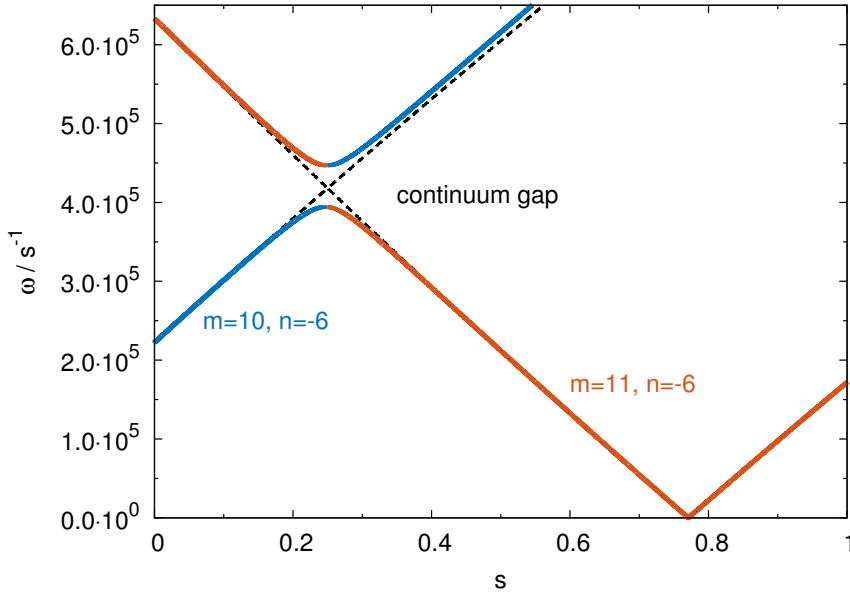


Figure 1.4: Shear Alfvén continuum of the ITPA tokamak benchmark case [43,44]. In toroidal geometry the continuum branches form a gap in the spectrum (coloured lines), while they cross in the cylindrical approximation (dashed black lines).

hand, if they were to experience an interaction with the continuum modes (for example close to the edge of the plasma where the Alfvén frequency quickly rises due to the density reducing to zero in realistic plasmas), the global modes would be damped via continuum damping [41, 45]. Gap modes will be the focus of this thesis. They have been observed experimentally in many tokamaks [48–52] and stellarators [53–55]. Recently, mode activity has been measured in W7-X in the frequency range expected for shear Alfvén waves [56].

Calculating the mode structure of these global modes can either be done using MHD, multi-fluid, or kinetic models. In order to describe the resonant interaction of fast ions with the mode a kinetic treatment of this particle species is required.

In fusion plasmas there exists a whole zoo of different Alfvén eigenmodes [38]. They can be beta-induced (BAEs), induced by toroidicity (TAEs), ellipticity (EAEs), or by an extremum in the Alfvén continuum (GAEs). In stellarators, also helicity-induced Alfvén eigenmodes (HAEs) are possible. With the exception of the GAE, all these gap modes arise from the breaking of the cylindrical symmetry. Since this symmetry can be broken in different ways, the modes vary in the way how the different poloidal (and toroidal) Fourier harmonics are coupled together. Fig. 1.5 shows the radial mode structures of two toroidicity-induced Alfvén eigenmodes (TAEs) found in the gap of the continuum shown in Fig. 1.4. These modes have been calculated using the STAE-K code [57].

Within ideal-MHD theory these global modes are neither driven nor damped (i.e. purely oscillating) as long as they do not interact with the continuum. Density or temperature gradients of a kinetic particle species, however, can be sources of an instability. Since the interaction of the particles with the mode is a resonance phenomenon, the particles need to have a very particular velocity. Among other possibilities (see articles A.4 and A.6 for a discussion), a typical resonance for TAEs in tokamaks is (see e.g. Ref. [38])

$$v_{\parallel}^{\text{res}} = \frac{v_A}{3} \quad (1.7)$$

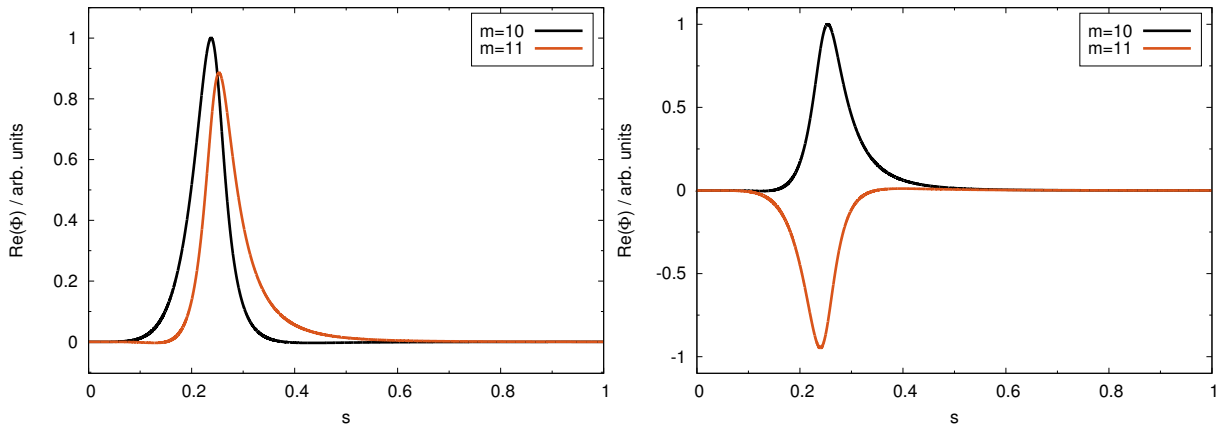


Figure 1.5: Even (left) and odd (right) TAE found in the TAE gap of the ITPA tokamak benchmark case [43,44] using the STAE-K code [57]. Such global modes are prime candidates to be resonantly destabilized by fast ions.

which, given the common Alfvén velocity in fusion plasmas, means that only particles faster than the bulk can fulfil the resonance condition.

This can be illustrated by considering a typical fusion plasma with $B = 2.5 \text{ T}$, $n = 2.0 \cdot 10^{19} \text{ m}^{-3}$, and $T = 2 \text{ keV}$ composed of hydrogen (parameters loosely based on first W7-X plasmas [58]). For such a plasma, the Alfvén speed is $v_A = 1.22 \cdot 10^7 \text{ m/s}$, which is about 28 times faster than the thermal speed of the background-plasma ions. This confirms that a fast-particle species is required to drive the modes unstable.²

1.4 Gyro-kinetic theory

This section aims to give a brief overview of gyro-kinetic theory, which is the underlying tool used for the majority of simulations presented in this thesis.

A plasma can be described on various levels of complexity. In practice, magneto-hydrodynamic (MHD) theory, multi-fluid approaches, and kinetic theory are used. The latter offers the most rigorous description of a fusion plasma and relies on a statistical treatment. Therefore, the plasma is described in terms of its particle distribution functions f_s , which for each particle species s is taken to fulfil the Boltzmann equation (see e.g. Ref. [59])

$$\frac{\partial f_s}{\partial t} + \dot{\mathbf{x}} \cdot \frac{\partial f_s}{\partial \mathbf{x}} + \frac{q_s}{m_s} (\mathbf{E} + \mathbf{v} \times \mathbf{B}) \cdot \frac{\partial f_s}{\partial \mathbf{v}} = \frac{\partial f_s}{\partial t} \Big|_{\text{coll}}. \quad (1.8)$$

Here, \mathbf{E} and \mathbf{B} are the electric and magnetic field and \mathbf{x} and \mathbf{v} denote the particle position and velocity, respectively. The phase-space has six dimensions which makes the problem seven-dimensional once the time t is included. The term on the right-hand side is the collision integral, which will be covered in Sec. 1.5. For now, it is ignored. In the absence of perturbed fields, the particles follow the characteristics of the kinetic equation [60] in a way that is shown in Fig. 1.6: On the fast time scale, they perform a gyrating motion around a magnetic field line. At much longer time scales they also drift away from the field line (not shown in the figure). In this thesis we study the interaction of fast particles with Alfvén eigenmodes. Important information to

²In principle, it is also possible for thermal electrons to excite AEs [38,56], but the excitation by fast ions is the more prevalent mechanism.

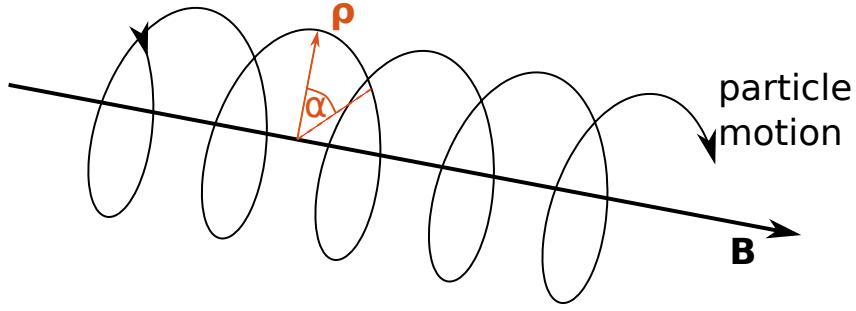


Figure 1.6: Schematic depiction of the unperturbed motion of a charged particle in the presence of a magnetic field. The particle performs a spiral motion (called gyration) around a magnetic field line. The radius of the spiral is given by $|\rho|$, with ρ being the Larmor or gyro-radius. The gyro-phase is denoted α .

describe the resonant wave-particle interaction are the parallel velocity of the fast ions as well as their drift. What is unimportant is the fast gyro-motion caused by the Lorentz force

$$F_{L,s} = q_s \mathbf{v} \times \mathbf{B} \quad (1.9)$$

around the field line. We can therefore reduce the dimensionality of the problem by transforming to phase-space coordinates in which the gyro-phase α is ignorable and the associated magnetic moment μ is constant [61]. A theory constructed that way is called guiding-centre or gyro-kinetic theory.³ A convenient analogy of this coordinate transformation is to think of the original particles as charged rings (quasi-particles) moving through phase-space.

The applicability of guiding-centre theory relies on a number of assumptions. Firstly, phenomena of interest (denoted by their frequency ω) must happen on a timescale much slower than the inverse ion-cyclotron frequency $\Omega_i = q_i B / m_i$, i.e.

$$\frac{\omega}{\Omega_i} = \mathcal{O}(\varepsilon_\omega) \ll 1. \quad (1.10)$$

Secondly, the gyro-radius ρ must be much smaller than the length scale on which the background magnetic field varies (denoted by L_B), i.e.

$$\frac{\rho}{L_B} = \mathcal{O}(\varepsilon_B) \ll 1. \quad (1.11)$$

This means that the plasma must be sufficiently magnetized. If those requirements are fulfilled, it is possible to find a coordinate transformation to guiding-centre coordinates, which effectively eliminates the fast time scale from the equations of motion. A modified magnetic moment, which is constant, can be found. But, as soon as time-varying electromagnetic fields (e.g. Alfvén waves with $\omega \ll \Omega_i$) are added to guiding-centre theory, the conservation of the magnetic moment is violated [62] (if $k_\perp \rho \sim 1$), which requires an additional transformation – the gyro-centre transformation – be carried out. This will restore the conservation of the magnetic moment in new coordinates as long as the fluctuations are small compared with the background fields

$$\frac{|\delta \mathbf{B}|}{|\mathbf{B}|} \sim |\delta \mathbf{E}| = \mathcal{O}(\varepsilon_\delta) \ll 1. \quad (1.12)$$

Thus, the derivation of gyro-kinetic equations is a two-step process [61]. For the description of Alfvén eigenmodes in the core of a magnetically confined fusion plasma, all of the above conditions

³If finite-Larmor-radius effects are ignored one speaks of drift-kinetic theory.

are fulfilled. Note however that gyro-kinetic theory is not restricted to magnetically confined fusion plasmas. Applications in an astrophysical setting are also possible if the conditions above are met [63].

Research on the derivation of non-linear gyro-kinetic equations has a long history. A good overview is given in Ref. [61]. While the initial approach [64] was an iterative derivation by expanding the distribution function and the fields in terms of the various small parameters defined above, it is also possible [61] to base the derivation on Lie-transform methods.

The transformation to new phase-space coordinates is accompanied by changes in the field equations for the electromagnetic potentials. There will be polarization and magnetization effects appearing, which come from the fact that we now treat charged rings rather than point particles.

Thus, while we lose the ability to describe some phenomena (such as for instance ion-cyclotron-resonance heating which obviously violates the conservation of the magnetic moment), we gain two important advantages: Firstly, as the gyro-phase becomes ignorable, the dimensionality of velocity space is reduced from three to two. Furthermore, μ is a parameter rather than a dynamical variable. This reduction of the dimensionality of the problem is particularly important for grid-based (Eulerian) codes, where it leads to a decrease of numerical cost. While a grid in the μ -direction is still necessary in order to calculate velocity-space moments, a coarse resolution can be chosen in practice. The second advantage is most important for particle-in-cell (PIC) codes. Since the fast gyro-motion has been eliminated, it needs no longer be resolved numerically. This permits a larger time step $\Delta t \gg \Omega_i^{-1}$ than would otherwise be possible, which again saves numerical resources.

There are several possible choices of variables to express gyro-kinetic theory. They give rise to the so-called v_{\parallel} -, p_{\parallel} -, and mixed formulations. A detailed description of their respective benefits and drawbacks will be given in App. B.2.

The equations presented in the remainder of the thesis are (unless stated otherwise) expressions for the gyro-centres of the particles.

1.5 Collisions

The main focus of this thesis is to include collisions in gyro-kinetic simulations of Alfvén eigenmodes (AEs). The goal is to arrive at a more realistic description of the plasma in general. This should facilitate a more rigorous comparison with experimental measurements, in particular for W7-X. Note that the 2018 experimental campaign of W7-X (from July to October) was the first operation phase that included NBI heating. (Later operation phases will also include ICRH.) Thus, fast ions that can potentially excite AEs, were present. This thesis shows that collisions are an important ingredient for the theoretical description and are required for any quantitative comparison to the experiment.

Very qualitatively, the impact of (pitch-angle) collisions is shown in Fig. 1.7 in a circular tokamak. While the red curve shows a collisionless orbit of a passing fast ion, the same particle is subject to pitch-angle scattering in a second simulation shown in blue. A high collision frequency has been chosen for illustrative purposes. It is clearly visible that the orbit changes dramatically: Without collisions, the projection of the particle orbit into a poloidal plane is a circle. This means that the particle is never reflected at local maxima of the magnetic field strength along its path, which makes it a so-called passing particle. Adding collisions, however, ‘reshuffles’ the velocity components of the particle. It now is reflected at certain values of B , indicated by the banana-shaped orbit of a trapped particle. Moreover, the particle crosses the passing-trapped

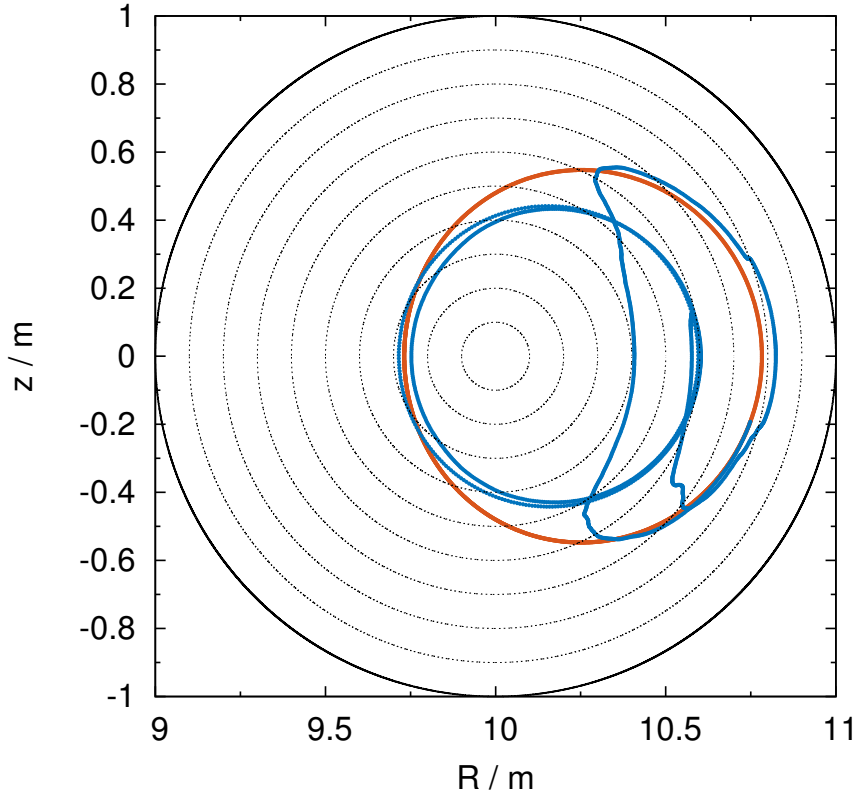


Figure 1.7: Schematic view on how (pitch-angle) collisions change the particle motion. Shown is the poloidal cross section of a large-aspect-ratio tokamak. The red circle shows the orbit of a passing particle in a collisionless simulation. When collisions are added (blue curve), the topology of the orbit changes. The particle crosses the passing-trapped boundary.

boundary (banana changes into a circle) during the simulation.

The interaction of AEs with particles is a resonance phenomenon in phase-space. Resonant ions need to be localized at the position of the AE in real space and fulfil a resonance condition in velocity space. Collisions directly influence the resonance condition by modifying the particle velocity. As shown in Fig. 1.7 they also change the position of the particle in real space (in combination with the magnetic equilibrium). The particle motion visualized in Fig. 1.7 is calculated in the absence of a mode. This is why the orbit closes poloidally for the red curve.

In this section, we briefly list all the collision operators that are used in the thesis. As mentioned for the pitch-angle scattering operator in article A.1, they are obtained by transforming the full Fokker-Planck operator to guiding-centre coordinates and neglecting energy and guiding-centre diffusion. Ref. [65] elaborates on this procedure. After the collision operator is transformed to guiding-centre coordinates, it describes diffusion of particles in real and in velocity space. The diffusion in real space scales with the square of the gyro-radius and can thus be neglected compared with the much larger orbit changes of the particle induced by changes of the velocity components during the collision. (The banana half-width is larger than the gyro-radius by approximately B/B_{pol} [33], where B_{pol} is the poloidal magnetic field.)

The general Fokker-Planck collision operator [66,67] for colliding species a and b is defined as

$$\mathcal{C}_{ab}(f_a, f_b) = \frac{\partial}{\partial v_k} \left[A_k^{ab} f_a + \frac{\partial}{\partial v_l} \left(D_{kl}^{ab} f_a \right) \right] \quad (1.13)$$

and describes drag (A_k^{ab}) and diffusion (D_{kl}^{ab}) of particles in velocity space. It simplifies considerably in the case of collisions with a Maxwellian background [66]

$$\mathcal{C}_{ab}(f_a, f_b^M) = \nu_D^{ab} \mathcal{L}(f_a) + \frac{1}{v^2} \frac{\partial}{\partial v} \left[v^3 \left(\frac{m_a}{m_a + m_b} \nu_s^{ab} f_a + \frac{1}{2} \nu_{\parallel}^{ab} v \frac{\partial f_a}{\partial v} \right) \right], \quad (1.14)$$

where m denotes the mass and ν_D , ν_s , and ν_{\parallel} are the pitch-angle scattering, slowing-down, and parallel velocity diffusion frequency, defined in Ref. [66]. The first term in the above equation denotes the pitch-angle ($\xi = v_{\parallel}/v$) scattering operator

$$\nu_D^{ab} \mathcal{L} = \frac{\nu_D^{ab}}{2} \frac{\partial}{\partial \xi} (1 - \xi^2) \frac{\partial}{\partial \xi}. \quad (1.15)$$

Its implementation into the electrostatic version of EUTERPE was first described in Ref. [67] and is briefly recapitulated in article A.1, where we benchmark it for electromagnetic applications. It is used in article A.2 to verify the theoretically predicted [8] scaling law of the non-linearly saturated amplitudes of AEs with respect to the collision frequency. Note that this operator has the property of keeping the total magnitude of the particle velocity constant, while ‘reshuffling’ the division into v_{\parallel} and v_{\perp} (or μ). Therefore, this operator does not conserve linear momentum. The implementation and benchmarking of a correction term is discussed in App. B.4.

Since the AEs are resonantly excited by fast ions, a fast-ion collision operator [66]

$$\mathcal{C}_{\text{fast}}(f_f) = \nu_D^{\text{fi}} \mathcal{L}(f_f) + \frac{1}{v^2} \frac{\partial}{\partial v} \left[v^3 \frac{m_f}{m_f + m_i} \nu_s^{\text{fi}} f_f \right] + \frac{1}{v^2} \frac{\partial}{\partial v} \left[v^3 \frac{m_f}{m_f + m_e} \nu_s^{\text{fe}} f_f \right] \quad (1.16)$$

$$\approx \nu_D^{\text{fi}} \mathcal{L}(f_f) + \frac{1}{v^2 \tau_s} \frac{\partial}{\partial v} [(v^3 + v_c^3) f_f] \quad (1.17)$$

has been implemented. It is used in articles A.3, A.4, and A.5. Throughout the thesis, the indices i, e, and f are used to label ions, electrons, and fast ions, respectively. The derivation and implementation of the fast-ion collision operator is discussed in article A.5. The correctness of the implementation is verified for the approximate version in App. B.5.

The final operator that will be used in this thesis is a Krook operator [68]

$$\mathcal{C}_{\text{Krook}}(f^{(1)}) = -\nu_{\text{Krook}} f^{(1)}, \quad (1.18)$$

which is used to bring back the distribution to its unperturbed value ($f^{(1)} = 0$) on a timescale $\sim \nu_{\text{Krook}}^{-1}$. (The perturbed part of the distribution function is labelled $f^{(1)}$.) Thus, as a ‘real’ collision operator, we can use the Krook operator to relax the distribution function towards a Maxwellian (other choices are also possible). The main benefit of this operator is its versatility as it can further be used to emulate a particle source. In that sense, the Krook operator is connected to the frequency chirping of AEs (which we hope to observe in the experiment) and will be discussed in article A.5. Note however that the Krook operators does not conserve particle number, linear momentum, and energy.

Chapter 2

Summary of results

2.1 Initial benchmark of the implementation of collisions (A.1)

Before any tokamak and stellarator cases (possibly with realistic plasma parameters) can be addressed, it is important to confirm that the numerical tools work reliably. Simulations for realistic W7-X cases will be performed in the later articles included in this thesis.

Hence, the topic of article A.1 is a thorough benchmark of the implementation of the pitch-angle scattering operator, as defined in Eq. (1.15), into the EUTERPE code. In this initial test case, we consider the damping rate of a kinetic Alfvén wave (KAW) in an unshered plasma slab. The simple geometry lends itself well to the comparison with the semi-analytical theory outlined below. We further test the compatibility of pitch-angle collisions with the electromagnetic version of EUTERPE. As is pointed out in the article, only electrostatic simulations had been combined with collisions previously [67]. Since this thesis focusses on the influence of collisions on fast-ion-driven AEs (which are electromagnetic perturbations) it has to be carefully checked whether the implementation of collisions also works for this case. Additionally, this is the first time that the mixed formalism of the equations of motion used in EUTERPE (pullback scheme [69, 70]) is combined with collisions. The pullback scheme is used for all fully gyro-kinetic simulations in EUTERPE. (See App. B.2 for more information on the different formulations of gyro-kinetic theory.) The long-term goal is to perform fully gyro-kinetic and non-linear simulations, including also collisions, for W7-X. Thus, article A.1 is a first step in this direction, testing the basic properties of the integration schemes.

Even the supposedly simple problem of a KAW in slab geometry becomes non-trivial once collisions are added. Since analytical theory is lacking, a semi-analytical approach (called the Legendre approach in the article) is constructed and compared to EUTERPE. This method employs a decomposition of the perturbed distribution function into Legendre polynomials, which are eigenfunctions of the pitch-angle scattering operator. In this way the problem becomes much simpler. We find that, even though collisions are treated very differently, both EUTERPE and the Legendre approach yield the same results for the frequency and damping rate of the KAW. This key result is shown in Fig. 2.1, which is a combination of Figs. 1 and 2 from article A.1. Thus, EUTERPE has been verified successfully and is ready to be applied to more difficult magnetic geometries, i.e. tokamaks and stellarators. This is done in the following articles. As far as physics is concerned, we find that collisions particularly influence the small scales, i.e. modes with a high $k_{\perp}\rho_s$. This is expected since Alfvén waves are undamped in the limit of ideal MHD, where $k_{\perp}\rho_s \rightarrow 0$.

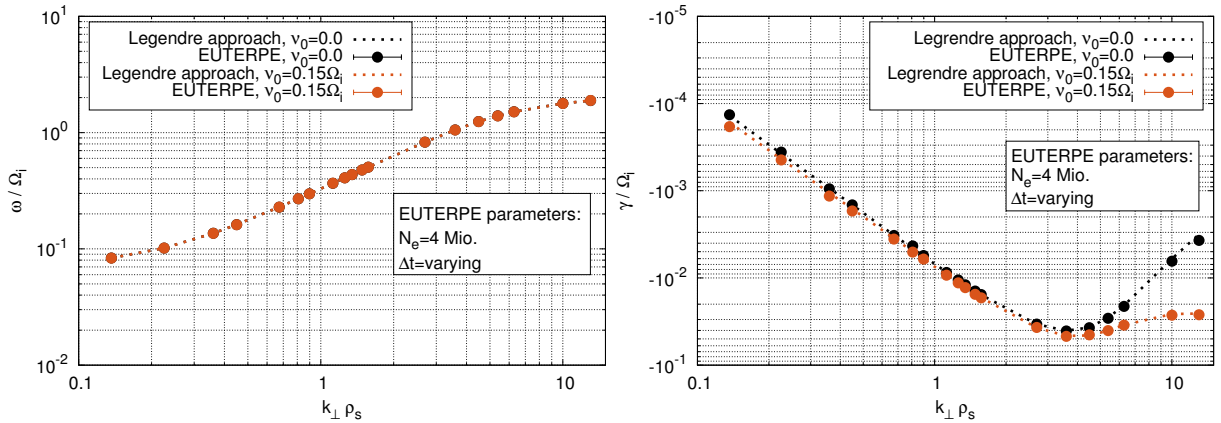


Figure 2.1: Frequency (left) and damping rate (right) of a KAW in slab geometry. Collisionless simulations are shown in black whereas red is used for the ones including a pitch-angle scattering operator. In any case, EUTERPE and the Legendre approach agree very well. Collisions do not affect the frequency, but lead to additional damping which is strongest for high- $k_{\perp} \rho_s$ modes.

The main point of article A.1 is to stress the good agreement between EUTERPE and the Legendre approach for the frequency and damping rate of the KAW. But, besides the main topic, further subjects have been investigated as well. We have performed convergence scans for the particle number and the time step. The goal is to become familiar with these parameters before more expensive simulations in a tokamak or stellarator are attempted. We confirm that choosing a small time step is more important than having many numerical marker particles in the simulation. The reason is that only a very slowly converging stochastic scheme is used for the collisional process (weak convergence of order one for the time step). This needs to be kept in mind for future simulations.

The Legendre approach is also used to calculate the direct influence of pitch-angle collisions on the perturbed distribution function in velocity space (see Fig. 4 on page 48). As expected, the inclusion of collisions leads to a more isotropic velocity space as they smooth the structures generated by Landau damping. The EUTERPE results, which show very good agreement, are presented in App. B.3 for comparison.

Finally, it needs to be pointed out that different formulations of gyro-kinetic theory are used in the paper. As mentioned before, EUTERPE uses the mixed formulation, which has considerable advantages for a PIC code. On the other hand, the p_{\parallel} - and, to a lesser extent, the v_{\parallel} -approaches are used for the Legendre approach. Since article A.1 only provides some detail about the different choices of variables to construct a gyro-kinetic theory, further explanation is provided in App. B.2, which may act as an extended introduction to article A.1. While there is some duplication of information, which cannot be avoided, App. B.2 also confirms that the v_{\parallel} -, p_{\parallel} -, and mixed formulation all yield the same results for the analytically solvable problem that only includes a Krook operator [68]. Thus, App. B.2 can also be understood as a benchmarking effort of the Legendre approach itself.

2.2 Collisions influence non-linear saturation levels (A.2)

Having confirmed the correct implementation of pitch-angle collisions into the electromagnetic version of EUTERPE in simple slab geometry (see article A.1), we now proceed to more realistic

tokamak and stellarator cases. Note that the way how collisions are treated is independent from the geometry.

Article A.2 deals with the resonant interaction of AEs with fast ions. We consider the fast ions to be the collisional species. In order to allow for a straightforward comparison with analytical theory [8], the collision frequency (considered as input parameter in this article) is varied over a wide range. We can treat it as an effective collision frequency including fast-ion self-collisions and collisions with the background plasma. The main topics of article A.2 are the effects that pitch-angle collisions have on the saturation dynamics of TAEs, both in tokamaks and in W7-X.

Recall that the non-linear phase of the mode evolution, in particular the saturated levels of the mode amplitude, determines the transport of the fast ions [4, 14]. Since fast ions need to be confined in the plasma until they have thermalized, increased transport due to AE activity is unfavourable. Analytical theory [8] predicts that the saturation level scales as $\nu^{2/3}$, where ν is the pitch-angle scattering frequency.

In order to extract scaling laws for the saturation amplitudes numerically, many simulations with various collision frequencies are performed. This would be prohibitively expensive if the fully gyro-kinetic version of EUTERPE were used. Instead we employ the reduced model implemented in CKA-EUTERPE [1]. In this model, the thermal species are described by reduced ideal-MHD equations and only the fast ions are treated gyro-kinetically, which saves computation time and allows for a larger time step. Furthermore, the model is perturbative as it uses the ideal-MHD code CKA [71] to compute the mode frequency and structure, which remains unchanged in the subsequent EUTERPE simulations. Instead of the field equations (Poisson's equation for the electrostatic potential and Ampère's law for the parallel vector potential), so-called amplitude equations are solved in CKA-EUTERPE. They determine the temporal evolution of the potentials with a fixed shape. This, again, saves computation time and makes the model more robust compared with fully gyro-kinetic approaches [72].

Note that collisions can often be neglected in linear simulations of AEs, since the mode frequency and growth rate typically do not depend on the presence of a collision operator. This is, for instance, visible on the left-hand side of Fig. 2.2, where it is shown that pitch-angle collisions barely change the linear phase. The same figure also shows that the non-linear phase, on the other hand, is sensitive to the value of the collision frequency. This figure is a combination of the middle panels of Figs. 2 and 3 shown in the article.

In article A.2, we first introduce the numerical tools and then investigate the saturation level of a TAE for variants of the ITPA benchmark case [43, 44]. In the simulations, both the so-called resonance-detuning and radial-decoupling regimes [73, 74] are covered. These are determined by different saturation mechanisms: While in the former the saturated amplitude is proportional to γ_L^2 , it only scales as γ_L in the latter. (γ_L is the linear growth rate of the mode.) We find that in the resonance-detuning regime, the analytically predicted $\nu^{2/3}$ scaling can be confirmed by CKA-EUTERPE for small-enough (i.e. smaller than a critical value) pitch-angle collision frequencies. The numerically extracted scaling law is shown as the red line on the right-hand side of Fig. 2.2. The validity range of the analytical theory is estimated and found to agree fairly well with our simulation results. Thus, the paper can, in part, be viewed as another benchmark against analytical theory, but now in a non-linear setting and in a more complicated magnetic geometry, which is more relevant to magnetic-confinement fusion.

In the radial-decoupling regime and for higher collision frequencies (outside the validity range of analytical theory) scaling laws other than the $\nu^{2/3}$ scaling are found numerically.

The pitch-angle scattering operator, introduced in Sec. 1.5 and benchmarked in article

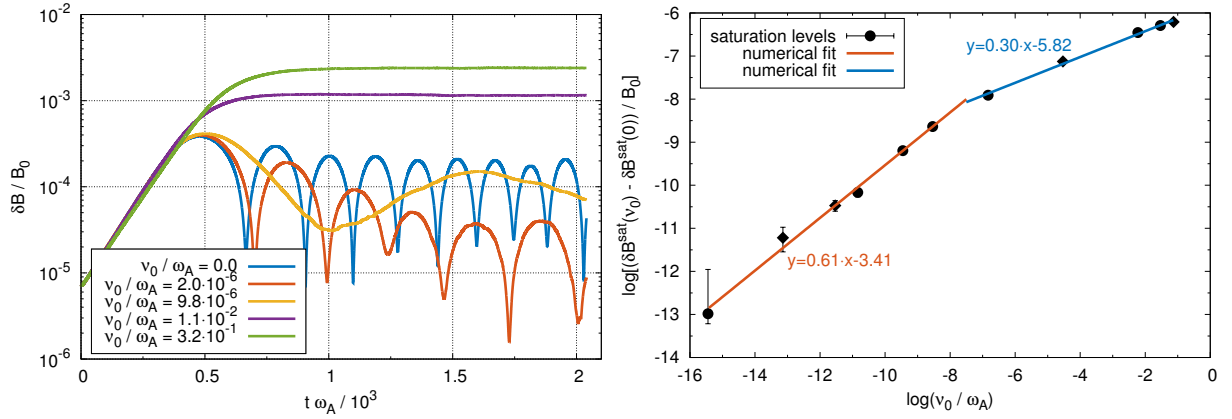


Figure 2.2: Time trace of the (poloidal) perturbed magnetic field of the mode for the standard ITPA benchmark case [43, 44] (left). Various collision frequencies are considered. Periodic or steady-state solutions are possible non-linearly. The right-hand side shows the dependence of the first maxima of δB after the linear phase on the collision frequency. The analytically predicted [8] scaling law is recovered for small-enough collision frequencies (red line).

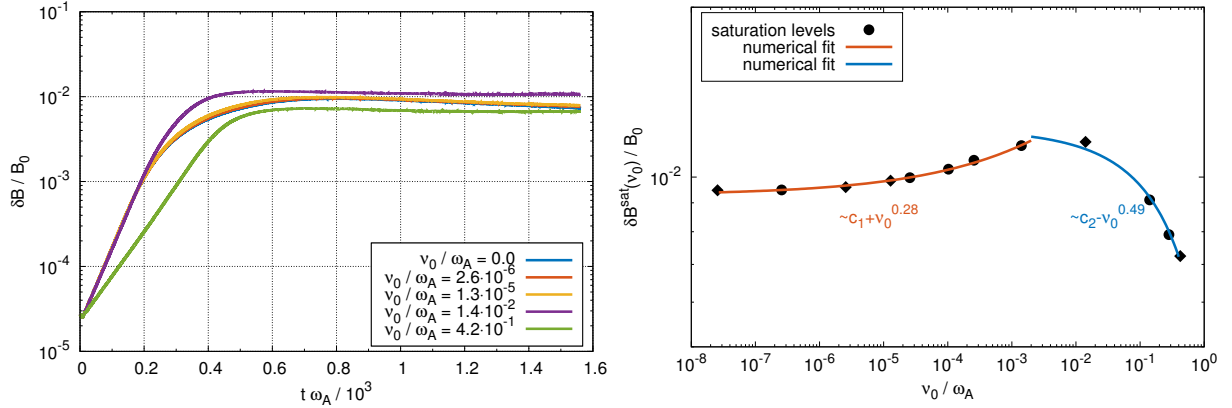


Figure 2.3: Same as Fig. 2.2, but for W7-X. Main differences compared with the tokamak are that the linear phase is more strongly influenced by collisions and that the saturation level (first maximum of δB after the linear phase) becomes a non-monotonic function of the collision frequency.

A.1, does not conserve linear momentum. We therefore use a correction scheme (called the conservation scheme in the article) which ensures the constancy of all moments of the collision operator that should be conserved analytically. It is found that neglecting the conservation of linear momentum leads to an overestimation of the effects of collisions. However, this only becomes important for very high collision frequencies. A description and benchmark of the conservation scheme are presented in App. B.4.

The final section of article A.2 is devoted to the stellarator W7-X. The main results are shown in Fig. 2.3, which appears as Fig. 10 in the article. It is found that W7-X behaves differently in terms of the scaling law than the tokamak: For very high collision frequencies the saturation level of the TAE is reduced by pitch-angle collisions and is thus a non-monotonic function of ν . A follow-up simulation in a quasi-axisymmetric stellarator could bridge the gap between the tokamak and W7-X investigated in article A.2. Such a simulation could help to isolate the cause for the changing scaling law.

Throughout the paper, the transport of fast ions is studied by investigating changes in the

2.3. Investigating a realistic Wendelstein 7-X case (A.3 and A.4)

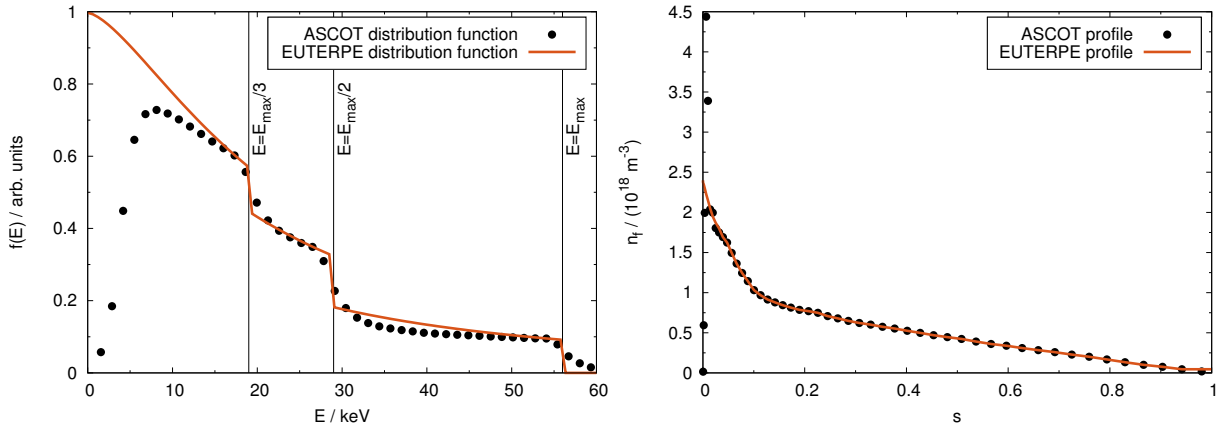


Figure 2.4: Realistic fast-ion distribution function (left) and density profile (right) used in articles A.3 and A.4. Both have been computed by the ASCOT code [6, 7] (black dots) and then fitted to the model implemented in EUTERPE (red lines).

fast-ion density profile. We confirm that transport takes place and that its strength is correlated with the saturated amplitude of the TAE. Further, if measurable flattening of the fast-ion density profile occurs, the range over which the profile flattens radially is roughly equal to the mode width. Hence, for the narrow mode studied in the tokamak the flattening is very local, whereas for the broad TAE in W7-X the profile is flattened over the entire minor radius.

2.3 Investigating a realistic Wendelstein 7-X case (A.3 and A.4)

Plasmas with realistic fast-ion parameters (most notably their density profile and distribution function in energy space) are the topic of articles A.3 and A.4. These investigations were carried out as part of the preparation of the CKA-EUTERPE model to be applied to realistic plasmas as expected for the 2018 experimental campaign (July to October 2018), also called operation phase (OP) 1.2b. We investigate a number of shear Alfvén eigenmodes that could potentially be driven unstable via the interaction with fast ions. Note that OP 1.2b is the first operation phase of W7-X to also include NBI heating, which supplies fast ions in order to heat the plasma. Later operation phases will also feature ion-cyclotron-resonance heating.

As in the previous article A.2, the perturbative model of CKA-EUTERPE [1], with a fixed MHD mode structure, is used for the non-linear numerical simulations. Due to the low fast-ion pressure (compared with the pressure of the background plasma), this is considered a good approximation. The simulations feature a realistic fast-ion distribution function and density profile as calculated (see Ref. [5]) by the ASCOT code [6, 7] for plasma parameters typical of the 2018 experimental campaign. Both are shown in Fig. 2.4, where the dots represent results from the ASCOT simulation and the red lines are the fits used in EUTERPE. Furthermore, the simulations include a dedicated fast-ion collision operator, which was introduced in Sec. 1.5. All together, this is the first time that CKA-EUTERPE simulations are performed at such a level of realism. While articles A.1 and A.2 mainly focussed on initial benchmarking and comparison to analytical theory, article A.3 is the first application to a realistic W7-X case.

We find that the Alfvén eigenmodes (GAEs [global], TAE [toroidicity-induced], and EAEs [ellipticity-induced]) investigated in article A.3 are weakly driven unstable by fast ions in the absence of a physical damping rate. The low growth rates are mainly due to the comparatively

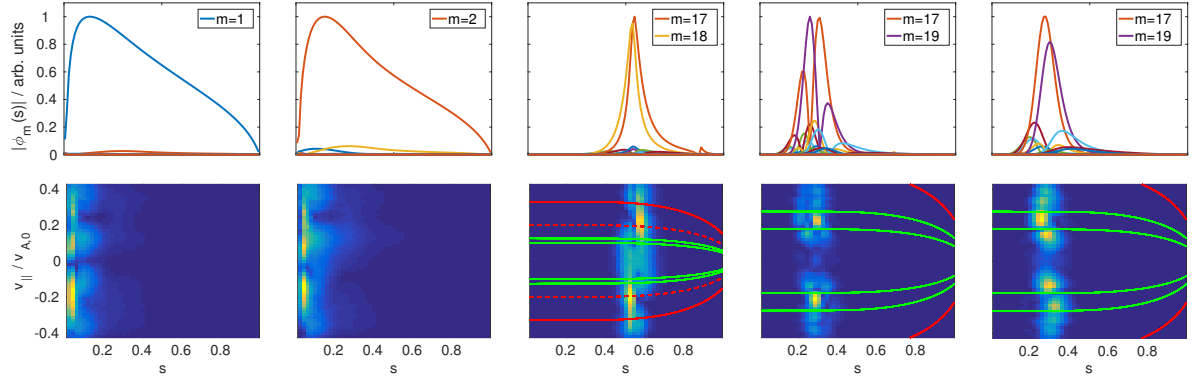


Figure 2.5: Radial mode structures (top row) and power transfer in arbitrary units in the s - $v_{||}$ -plane (bottom row). The modes are (from left to right): ($m = 1/n = -1$) GAE, ($m = 2/n = -2$) GAE, ($m = 17, 18/n = -16$) TAE, and two ($m = 17, 19/n = -16$) EAEs with even and odd parity, respectively. In case of the gap modes, the power transfer is radially localized at the same position as the mode. For the very extended GAEs, the power transfer coincides with the region of strongest gradient in the mode structure. Toroidal and helical resonances with the background magnetic field are shown in red and green, respectively.

low injection energy of the fast protons. In particular, their velocity is at most approximately half the Alfvén velocity, which limits the available resonances for the wave-particle energy exchange. All AEs saturate in the range of $\delta B/B_0 = 10^{-4} - 10^{-3}$. The non-linear simulations show that, thanks to these low saturation levels, the induced transport is also small.

Since the damping rate is an external parameter in the CKA-EUTERPE model, the code STAE-K (see article A.6) is used to estimate the radiative damping rates of the gap modes. We find that the damping exceeds the fast-ion drive for these modes. Unless there are other destabilizing mechanisms in the experiment (e.g. coming from the background plasma), it seems unlikely that the fast-ion drive would be sufficient to destabilize the AEs included in this investigation.

The numerical modelling of this realistic W7-X case is split over two separate publications, and article A.4 is a direct continuation of the previous article A.3. We reconsider exactly the same case with the aim of performing a more in-depth survey of possible actuators (ideally experimentally accessible) that control AE activity in W7-X.

Using article A.3 as a starting point, we first investigate the power transfer in phase space. The radial mode structures and the power transfer in the s - $v_{||}$ -plane are shown in Fig. 2.5, which is a combination of Figs. 1 and 2 from article A.4. Especially for global Alfvén eigenmodes (GAEs), which extend over the entire minor radius, it was previously not clear where the drive exactly comes from. In the article we show that the drive is localized to regions of large gradients in the radial mode structure. Subsequently, we ask the question – from the standpoint of trying to maximize the fast-ion drive – if hydrogen or helium plasmas should be preferred. Note that the NBI system of W7-X is designed in a way that for a hydrogen plasma with a density of $5.0 \cdot 10^{19} \text{ m}^{-3}$, at most $v_{||}/v_A \approx 0.43$ can be reached (corresponding to a maximal injection energy of 55 keV). In helium plasmas, on the other hand, the mass density is higher, which leads to a reduction of the Alfvén speed and should make it easier to excite AEs. In tokamaks this reasoning would be correct, but, as we point out in the paper, stellarators have a three-dimensional structure of the magnetic field which allows for additional helical resonances at lower values of $v_{||}/v_A$. This is the reason why helium plasmas are found to be more stable in W7-X.

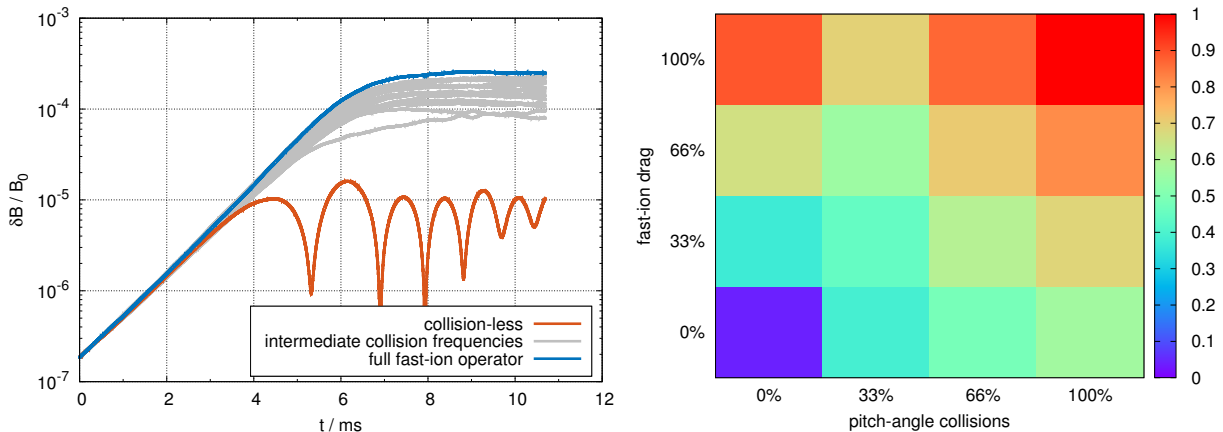


Figure 2.6: Time trace of the perturbed poloidal magnetic field of the TAE shown in Fig. 2.5 for various strengths of the fast-ion collision operator (left). The value of $\delta B/B_0$ at saturation (first maximum) is shown on the right-hand side. The saturation levels are normalized to the fully self-consistent case. The presence of a fast-ion collision operator increases the saturation level substantially with both pitch-angle scattering and drag contributing to the increase.

Next, we turn to the influence of collisions on the non-linear saturation levels of AEs. Recall that the AE-induced fast-ion transport depends on the saturated amplitudes [4, 14]. The fast-ion collision operator used in the simulations includes two basic effects: Pitch-angle scattering of the fast ions off the background-plasma ions and slowing-down (drag). In order to disentangle these two effects, we independently vary the pitch-angle scattering and slowing-down frequency for two of the modes found by CKA. For the TAE, the results are shown in Fig. 2.6, included in article A.4 as Fig. 5. Here, the fast-ion collision operator substantially increases the saturation level, with both pitch-angle collisions and drag contributing to the increase. Including a realistic collision operator in the simulation is required to accurately predict the non-linear saturation levels, which increase by more than a factor of ten. Furthermore, the GAE is found to behave differently compared with the TAE in the paper: The saturated amplitude depends less on the collision frequencies, and drag acts to decrease the saturation level. Since the collision frequencies are a strong function of density and temperature (and thus of the radial position in the plasma), collisions can act to favour a particular AE to be dominant in the experiment. This is a hypothesis that will be tested when the multi-mode version of CKA-EUTERPE (see App. B.6) is ready to be used.

Finally, the role of a radial electric field E_r on the linear and non-linear dynamics of the AEs is considered. A radial electric field is usually present in stellarators and ensures the overall ambipolarity of the plasma transport. For the present case, E_r is calculated from the parameters of the background plasma using the NTSS code [75]. We find that the inclusion of the radial electric field only very slightly changes the development of the mode amplitudes.

Note that throughout articles A.3 and A.4 each simulation was performed for each AE individually, as this was the state of the CKA-EUTERPE model at that time. More realistically, of course, the modes would interact with each other linearly as well as non-linearly. This would also affect their respective saturation levels. As mentioned in Ch. 3 a so-called multi-mode version of CKA-EUTERPE, able to handle the exchange of energy between multiple modes present in a single simulation, is currently being tested. App. B.6 reports on first results.

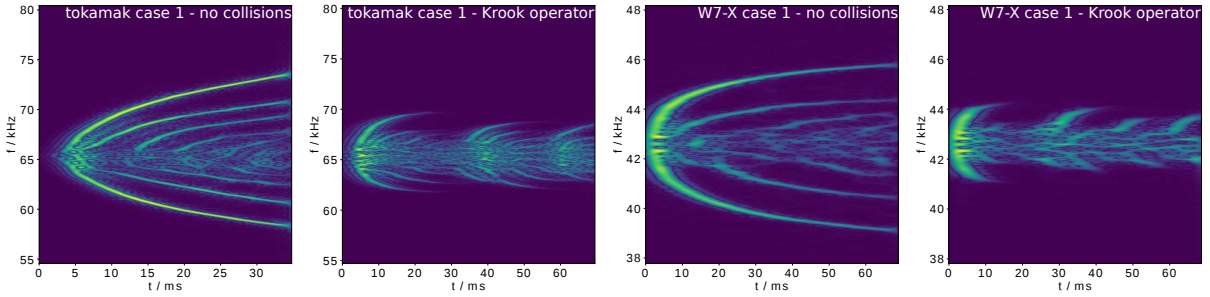


Figure 2.7: Frequency chirping for the ITPA tokamak [43, 44] (two figures on the left) and W7-X (two figures on the right). In both cases, periodic chirping events can be simulated using a Krook operator, which is used to emulate a fast-particle source.

2.4 Collisions and non-linear frequency chirping (A.5)

In article A.5, we investigate how collisions influence the long-term non-linear behaviour of AEs. Special emphasis is given to their frequency chirping. Throughout the paper a variety of collision operators are used: We study pitch-angle scattering and fast-ion drag. Both effects together are described by a dedicated fast-ion collision operator. Furthermore, a Krook operator [68] is used to emulate a particle source which leads to periodic chirping events. They are frequently observed in experiments [4, 76, 77] and in numerical simulations [78–81]. In article A.5, they are simulated for the first time in W7-X, in which a realistic slowing-down distribution function is used to describe the fast ions.

The numerical simulations are compared with the analytical Berk-Breizman model [8–12], which predicts a variety of possible non-linear scenarios depending on growth and damping rates and the collision frequencies. It is, however, a simplified one-dimensional model with the important difference that the drive comes from velocity-space gradients (bump-on-tail distribution function). In our case, the gradient of the fast-ion density profile is the source of the instability.

After describing the model (as in the previous articles, CKA-EUTERPE [1] is used) and deriving the fast-ion collision operator, we start with the familiar ITPA tokamak benchmark case [43, 44] and a W7-X high-mirror configuration in the absence of collisions. This gives us a baseline scenario in which the linear growth rate can be adjusted such that chirping is nicely visible. The first and the third panel of Fig. 2.7 shows the collisionless chirping for the ITPA case and W7-X, respectively. Regarding pitch-angle collisions for the ITPA tokamak case, we find that they lead to a more narrow chirping parabola and, despite increasing the first maximum of δB after the linear phase (as was thoroughly described in article A.2), they reduce the long-term average saturation level of the mode. The role of pitch-angle scattering in W7-X is found to be slightly different: Due to the much higher collision frequencies in W7-X (a consequence of the low injection energy of the NBI system), a steady state without any chirping develops non-linearly. Furthermore, self-consistently calculated collision frequencies lead to an increase of the long-term average saturation level. This could be of practical relevance for the machine since it could make detection of AEs easier. It could, however, also lead to enhanced transport.

Next, the role of fast-ion drag is investigated. The Berk-Breizman model predicts (as shown for example in Refs. [80, 81]) that only branches which are up-chirping in frequency should remain. Our simulations confirm this prediction both in the tokamak and in W7-X.

Lastly, we use a Krook operator to emulate a fast-particle source. This way, the Krook operator rebuilds the distribution function, which leads to periodic chirping events. This

2.5. A simplified model for mode drive and damping (A.6)

mechanism works for the tokamak case and for W7-X, as is shown in the second and fourth panel of Fig. 2.7, respectively. Within the Berk-Breizman paradigm pitch-angle scattering alone is sufficient to generate periodic chirping events [80]. The reason is that velocity-space gradients are the source of the instability in this model. In our case, however, the drive comes from the fast-ion density gradient in real space. Therefore, a particle source is needed to simulate the same effect.

To summarize, many features predicted by the Berk-Breizman paradigm are also visible in our simulations of much more complex systems. Exceptions include the different role of pitch-angle scattering and the Krook term regarding periodic chirping events. Furthermore, the Berk-Breizman paradigm is not applicable if a time-dependent damping rate γ_d is used. A time dependent damping rate was used in one simulation to show that frequency chirping can also be influenced by equilibrium changes,¹ which might change the ratio of γ_L and γ_d .

A future goal is to determine growth and damping rates of AEs observed in W7-X discharges, as well as collision frequencies, spectroscopically [79] by fitting the simulation results to the observed time traces of δB and comparing with the theoretically expected frequency change. This could prove difficult experimentally since a constant mode frequency is expected non-linearly (no chirping parabola) for W7-X due to the high pitch-angle scattering frequency. In any case, non-linear simulations are required to predict AE-induced fast-ion transport. In that sense, article A.5 represents one step towards a transport model for fast ions in W7-X. Lastly, the paper confirms that CKA-EUTERPE can routinely be used for long non-linear simulations due to a number of code improvements (discussed in Ch. 3) which make it run very stably.

2.5 A simplified model for mode drive and damping (A.6)

Article A.6 addresses a topic that I started working on for my M.Sc. thesis, but it also includes additional work done while being a Ph.D. student. This includes, in particular, an extension of the STAE-K code (described below) to also include the stellarator-specific helical Fourier components of the magnetic field. In the W7-X high-mirror configuration, the $B_{1,-1}$ Fourier component (helical) is larger in magnitude than the toroidal $B_{1,0}$ component. Thus, this paper is to be viewed as additional material that is somewhat separated from the other papers in this dissertation.

Article A.6 introduces a novel code called STAE-K. It is a shooting code able to compute frequencies and growth rates of TAE modes (and other gap modes) interacting with a kinetic fast-particle species. The code couples the background plasma (ideal-MHD description) and the fast ions (drift-kinetic theory) non-perturbatively. Simplifications are made regarding, for instance, the geometry and the fast-ion distribution function, which can only be a Maxwellian. Finite-Larmor-radius and finite-orbit-width effects are neglected. (Development of STAE-K is, however, on-going in order to relax some of the simplifications.) The final product is a code that is much faster than gyro-kinetic codes and still contains the most relevant physics. STAE-K is thus suited for parameter scans as the ones performed in article A.6.

After describing the physical model, its formulation as an eigenvalue problem and its subsequent numerical implementation, the article reports on benchmarking activities for a number of tokamak cases. As long as the initial approximations are satisfied (small fast-ion orbits and Larmor radii, i.e. sufficiently cold fast ions) the agreement with more advanced codes is good.

¹If the temperature and density of the background plasma change, damping of the mode due to radiative [47], background-plasma Landau [46], and possibly also continuum damping [41, 45] will vary.

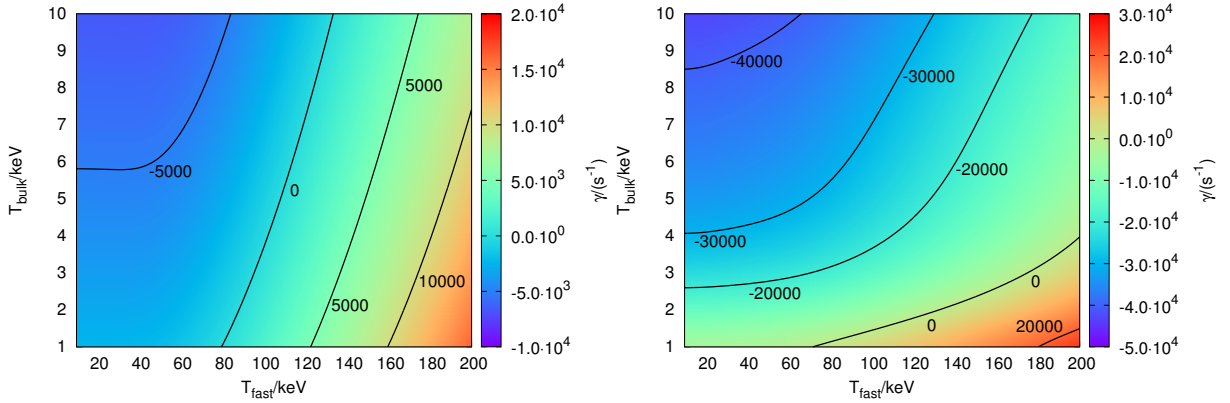


Figure 2.8: Stability diagrams for TAEs in the ITPA tokamak [43, 44] (left) and W7-X (right). The model includes the fast-ion drive as well as Landau damping of the background plasma and radiative damping. Lines of equal growth/damping rate are shown in black. W7-X is more stable than the tokamak because the existence of a helical Fourier component of the background magnetic field allows additional resonances in the temperature range of the background plasma. Since for the present case the background profiles are flat, these resonances act stabilizing.

We find that for a continuously increasing fast-ion temperature, a fast-ion-driven TAE can steadily be transformed into a kinetic Alfvén wave which resembles features of so-called energetic-particle modes (EPMs). Furthermore, STAE-K can compute the corresponding kinetically modified shear Alfvén continua, which aide in the interpretation of the other results. Article A.6 concludes with an application to Wendelstein 7-X.

A major advantage of STAE-K is that, next to the fast-particle drive, it can also compute the damping rate of the gap mode, which is generally a combination of Landau damping [46], radiative damping [47], and continuum damping [41, 45]. In the paper this advantage is utilized to calculate stability diagrams by varying the drive and the damping independently. Two example plots, showing the (in)stability of a fast-ion-driven TAE in the ITPA tokamak benchmark case [43, 44] and W7-X, are shown in Fig. 2.8 (see Fig. 10 in article A.6). Only thanks to the reduced physics model can the stability diagrams be computed in a reasonable amount of time. Looking at the right-hand side of Fig. 2.8, STAE-K predicts that this particular TAE is stable in W7-X, since the maximal injection energy of the NBI system is 55 keV for hydrogen. Note however that the results of this stability analysis need to be taken with care due to the reduced physics model employed by STAE-K, which includes the simplifications outlined above. Experimental data, which could help to test the region of validity of STAE-K, is still being evaluated.

Note that within the CKA-EUTERPE model (used in articles A.2, A.3, A.4, and A.5) the damping rate is an external parameter that somehow needs to be specified. This constitutes a perfect example where guidance from simplified models, such as STAE-K, is helpful to more advanced codes. That this approach has actively been pursued in article A.3 is the main reason why article A.6 is included in the dissertation.

Within the newly implemented multi-mode version of CKA-EUTERPE (see App. B.6 for details) the role of STAE-K becomes more important as we now require a damping rate for each mode in a combined simulation.

2.6 Flux-surface variations of the electrostatic potential (A.7)

The last article included in this thesis is different from the others, since it does not address fast-particle-driven Alfvén eigenmodes. Instead, electrostatic potential and radial electric field variations on a flux surface are the topic of this work. Still, collisions are an important aspect of article A.7. This aspect ties the present work to the other articles presented in this thesis. The radial electric field, which is needed in stellarators to ensure ambipolarity, is an important ingredient for neoclassical transport theory of high- Z impurities, whose resulting $\mathbf{E} \times \mathbf{B}$ -drift can reach a comparable magnitude as their magnetic drift.

Article A.7 reports on radial electric field asymmetries that have been observed in the TJ-II stellarator using Doppler reflectometry, most notably in electron-root plasmas. The neoclassical version of EUTERPE, including pitch-angle collisions and the momentum-conservation scheme presented in article A.2 (and benchmarked in App. B.4), is used for numerical simulations that are compared to the experiment.

Simulations are also performed for plasmas characteristic of the very first operation phase of W7-X (OP 1.1). Those plasmas were limited (instead of diverted) and only heated by electron-cyclotron-resonance heating (ECRH), which lead to electron-root conditions in the plasma centre. For such conditions, a W7-X high-mirror configuration is investigated. Note that this configuration is optimized to have the best fast-ion confinement and the least direct fast-ion losses to the wall [5]. It is thus the configuration that is preferably used for fast-ion studies as reported on in articles A.2, A.3, A.4, and A.5 of this thesis. On the other hand, this configuration, due to its larger effective ripple, is not optimized from the standpoint of neoclassical theory, which is the topic of article A.7.

The W7-X simulations are performed using both adiabatic and kinetic electrons. In most cases, the structure of the electrostatic potential variation on a flux surface, denoted by ϕ_1 , does not depend on whether adiabatic or kinetic electrons are used. This is an encouraging result for future simulations, since the approximation of adiabatic electrons reduces the numerical cost considerably. As in TJ-II, significant electrostatic potential variations on a flux surface are also found in W7-X, especially in the triangular plane and with kinetic electrons. The trend that such variations are larger in electron-root plasmas is seen in simulations and experiments alike.

It is found in TJ-II that $-\phi'_1$ can become comparable to the radial electric field $E_r = -\phi'_0$ (ϕ_0 denotes the electrostatic potential constant on the flux surface) in certain regions of the plasma. In the future, this will have to be taken into account in the equations of motion for the particles.

Chapter 3

Summary and outlook

In this thesis, we have addressed the problem of combining gyro-kinetic particle-in-cell simulations of fusion plasmas with collisions. Numerical simulations have been performed in tokamaks and stellarators – the two main approaches being pursued to magnetically confine a plasma. In general, gyro-kinetic simulations can be performed for a large number of instabilities, differing in frequency and spatial scales. Here, we have focussed on Alfvén eigenmodes, which are large-scale electromagnetic perturbations in the plasma. While stable within ideal-MHD theory, these modes can be resonantly excited by fast ions, which are generated in most fusion devices by the heating systems. The resonant interaction of fast ions with Alfvén eigenmodes can lead to enhanced fast-ion transport [4, 8, 14] and thus reduces plasma performance and can even damage the device [3, 30].

After carefully verifying our numerical tools, we showed through non-linear simulations that collisions play an important role as they determine the non-linear dynamics of the mode, including its saturation level. It is a well-known experimental observation [4] that the saturation level and the transport of fast ions out of the plasma are correlated. In the thesis, this correlation has been confirmed numerically in articles A.2 and A.3. Understanding and controlling Alfvén-eigenmode activity and the induced fast-ion transport will be crucial for a future fusion reactor.

Specifically, the correctness of the implementation of pitch-angle collisions is verified in slab geometry in article A.1. After this initial benchmark it was possible to apply the EUTERPE code to geometries and scenarios more relevant to nuclear fusion (see articles A.2, A.3, A.4, and A.5). In all these articles (i.e. for the majority of this thesis) the reduced model of CKA-EUTERPE [1] has been used. This is mainly due to the fact that non-linear parameter scans would be prohibitively expensive with a fully gyro-kinetic model. This is especially true for a stellarator like Wendelstein 7-X (W7-X).

In article A.2, we could verify the theoretically predicted [8] scaling of the TAE saturation level δB^{sat} with the pitch-angle collision frequency. This served as another benchmark, this time in the non-linear regime, of the correctness of the implementation. When applied to a W7-X high-mirror equilibrium, we find a non-monotonic behaviour of $\delta B^{\text{sat}}(\nu)$, which is not predicted by analytical theory. In the tokamak and W7-X alike, we observed a flattening of the fast-ion density profile induced by the presence of the mode.

We showed in articles A.3 and A.4 that the CKA-EUTERPE model, including a newly implemented fast-ion collision operator, can be applied to realistic W7-X cases. They feature a fast-ion distribution function in energy space and density profile taken from ASCOT [6, 7] simulations [5]. An approximation is however made by assuming the distribution function to

be isotropic in the pitch-angle variable. In the meantime a more comprehensive model, which still needs to be verified, has been implemented (see below). We studied the effects of fast-ion drag and pitch-angle collisions for a number of Alfvén eigenmodes in this W7-X high-mirror configuration. Different types of collisions are found to influence the saturation level differently, and they can be very important for specific modes. For instance, the saturation level of the TAE in article A.4 is increased tenfold in a simulation using the full fast-ion collision operator compared with the collisionless reference.

Very long non-linear simulations of Alfvén eigenmodes – simulating several 10 ms of mode development – have been performed in article A.5. These simulations confirm the high numerical stability of the CKA-EUTERPE model and its suitability for comparison to experimental measurements. In the non-linear phase the mode amplitude is large enough to significantly influence the particle trajectories and their distribution function. The resonant wave-particle interaction leads to holes (lack of particles) and clumps (surplus of particles) in phase space [10,82]. Both are found to slowly change in frequency giving rise to characteristic chirping parabolas. As shown in article A.5, critical parameters determining the shape of this parabola are the growth and damping rates as well as collision frequencies. A Krook operator is used in the simulation to emulate a particle source. This periodically rebuilds the distribution function as it fills in the holes and removes the clumps. The comparison to analytical Berk-Breizman theory [8–12] gives valuable information about the applicability of this simplified model to a real stellarator as W7-X.

Articles A.6 and A.7 are slightly away from the main topic of this thesis as outlined above. In article A.6 a novel numerical tool – the STAE-K code – is introduced. It models the resonant interaction of fast ions with Alfvén eigenmodes (AEs) non-perturbatively but starts from a drift-kinetic treatment of the fast ions and, among other approximations, neglects finite-orbit-width effects. Despite this simple model, it is one of very few codes that can estimate the damping rate of AEs in stellarators. Recognizing that the damping rate is a free parameter in the CKA-EUTERPE model, STAE-K can provide this information.

The final article, A.7, addresses a topic from neoclassical theory: It uses the neoclassical version of EUTERPE, including momentum-conserving pitch-angle collisions, to calculate variations of the electrostatic potential on a flux surface. This is particularly important for high- Z impurities since, for them, a strong $\mathbf{E} \times \mathbf{B}$ -drift (compared with their magnetic drift) may be the consequence. The simulations and the experiments agree on the observation that electrostatic potential variations on the flux surface are stronger in electron-root plasmas (positive radial electric field) than they are in ion-root plasmas (negative radial electric field).

In summary, various collision operators (pitch-angle collisions with and without momentum conservation and a fast-ion collision operator) have been implemented into the EUTERPE code. The implementation has been verified successfully. We could perform linear and non-linear gyrokinetic simulations of fast-ion-driven Alfvén eigenmodes in tokamaks and stellarators. Collisions are found to significantly influence the non-linear dynamics of the modes, which in turn affects the transport of fast ions. This is a topic of great importance for nuclear fusion as good fast-ion confinement is needed to achieve fusion in the first place and to avoid damaging the reactor. Article A.7 shows the application of EUTERPE to a problem from neoclassical theory.

It needs to be stressed that much work on the EUTERPE code itself was performed in the course of this thesis. This work, which ranges from the correction of minor bugs to rather substantial changes, has not been reported here, but is nevertheless vital for the success of the numerical simulations. Examples include improvements to the re-insertion scheme of lost particles to make the code more stable, a more rigorous coupling of the codes CKA and EUTERPE, and

an improvement of the slowing-down distribution function previously implemented in the code.

Many changes have also been made to EUTERPE in order to make the code ready for future tasks. These changes, which still need to be benchmarked and verified, include the following:

- We have implemented a new distribution function aimed at better describing the NBI injection geometry at W7-X. This distribution function also includes velocity-space anisotropies in the pitch-angle variable, which will be interesting to study, in particular in connection with collisions.
- Furthermore, progress has been made in implementing a multi-mode version of CKA-EUTERPE. This would be an improvement on the current work, which focusses on non-linear simulations of a single mode. More realistically, of course, multiple modes would exchange energy and influence each other especially in the non-linear phase. Due to the modes being localized at different radial positions, also the influence of collisions on the modes (collision frequencies depend on temperature and density profile) would be different. Such a model could be used to simulate the cascade-like transport of fast ions from the core all the way to the edge via the interaction with many modes. The thorough testing of this model is currently in progress. App. B.6 elaborates on the details of the multi-mode model. First results, indicating that the mode evolution can indeed change significantly, are also shown there.
- Lastly, efforts are made to extend the conservation scheme presented in article A.2 and App. B.4 to be applicable to inter-species collisions. A long-term goal would be to consistently model the slowing down of NBI-generated fast ions and the heating of the background plasma at the same time.

In addition to these goals, for which many of the necessary changes have already been made to the code, there exist a number of other long-term goals:

- We plan a coupling of the ASCOT [6, 7] and EUTERPE codes in order to specifically model AE-induced fast-ion losses (including heat loads) to the first wall. These simulations could be compared to measurements from fast-ion loss detectors.
- Furthermore, we aim to further develop the CKA-EUTERPE model into a fast-ion transport model for stellarators. Note that other transport models such as the ‘Kick model’ [13, 14] or the ‘resonance broadened quasi-linear (RBQ) model’ [15] are especially designed for tokamaks as they make use of the fact that the canonical toroidal angular momentum P_φ is conserved in the absence of a mode.

In the ‘Kick model’, as the name suggests, particles are assumed to experience sudden changes in energy and P_φ due to their resonant interaction with the mode. This diffusion in phase space will eventually lead to particle transport in real space [13]. Within this perturbative model, radial mode structures and frequencies are taken from NOVA-K [83] simulations. The ‘Kick probability’ in constants-of-motion space, $p(\Delta E, \Delta P_\varphi | E, P_\varphi, \mu, A_{\text{mode}})$, is extracted from ORBIT [84] simulations for a mode amplitude A_{mode} given by experimental measurements.

The RBQ model is a diffusive transport model which assumes, similarly to the ‘Kick model’, diffusion of particles along a $\omega P_\varphi + nE = \text{const.}$ path [15]. The model contains an equation linking the diffusion coefficient and mode amplitude, a time-evolution equation for the

latter, and an equation for the growth rate. Overall, this makes the model similar to the CKA-EUTERPE model addressed in this thesis.

An even simpler model is implemented into the TGLF code [85–87]. It assumes stiff fast-ion transport (based on experimental observations reported in e.g. Ref. [88]) near a critical gradient, for which the mode is exactly marginal. A diffusion coefficient, which is then used in a one-dimensional radial transport model for the fast-ion density, is defined to rapidly increase once the critical gradient is exceeded [87]. A steady state relaxed density profile can be computed by combining this transport model with a realistic source profile for the fast ions.

Chapter 4

Bibliography

- [1] T. B. Fehér. *Simulation of the interaction between Alfvén waves and fast particles*. Ph.D. thesis, Ernst-Moritz-Arndt-Universität Greifswald (2013).
- [2] M. D. J. Cole. *Global gyrokinetic and fluid hybrid simulations of tokamaks and stellarators*. Ph.D. thesis, Ernst-Moritz-Arndt-Universität Greifswald (2016).
- [3] D. S. Darrow, S. J. Zweben, S. Batha, R. V. Budny, C. E. Bush, Z. Chang, C. Z. Cheng, H. H. Duong, J. Fang, N. J. Fisch, *et al.* Alpha particle losses from Tokamak Fusion Test Reactor deuterium–tritium plasmas. *Physics of Plasmas*, **3** (5) 1875–1880 (1996).
- [4] M. García-Muñoz, N. Hicks, R. van Voornveld, I. G. J. Classen, R. Bilato, V. Bobkov, M. Bruedgam, H.-U. Fahrbach, V. Igochine, S. Jaemsae, *et al.* Convective and Diffusive Energetic Particle Losses Induced by Shear Alfvén Waves in the ASDEX Upgrade Tokamak. *Physical Review Letters*, **104** (18) 185002 (2010).
- [5] S. Äkäslompolo, M. Drevlak, Y. Turkin, S. Bozhenkov, T. Jesche, J. Kontula, T. Kurki-Suonio, R. C. Wolf, and the W7-X Team. Modelling of NBI ion wall loads in the W7-X stellarator. *Nuclear Fusion*, **58** (8) 082010 (2018).
- [6] J. A. Heikkinen and S. K. Sipilä. Power transfer and current generation of fast ions with large- k_{Θ} waves in tokamak plasmas. *Physics of Plasmas*, **2** (10) 3724–3733 (1995).
- [7] E. Hirvijoki, O. Asunta, T. Koskela, T. Kurki-Suonio, J. Miettunen, S. Sipilä, A. Snicker, and S. Äkäslompolo. ASCOT: Solving the kinetic equation of minority particle species in tokamak plasmas. *Computer Physics Communications*, **185** (4) 1310–1321 (2014).
- [8] H. L. Berk, B. N. Breizman, and Huanchun Ye. Scenarios for the Nonlinear Evolution of alpha-Particle-Induced Alfvén Wave Instability. *Physical Review Letters*, **68** (24) 3563–3566 (1992).
- [9] H. L. Berk, B. N. Breizman, and M. Pekker. Nonlinear Dynamics of a Driven Mode near Marginal Stability. *Physical Review Letters*, **76** (8) 1256–1259 (1996).
- [10] H. L. Berk, B. N. Breizman, and N. V. Petviashvili. Spontaneous hole–clump pair creation in weakly unstable plasmas. *Physics Letters A*, **234** (3) 213–218 (1997).
- [11] H. L. Berk, B. N. B. J. Candy, M. Pekker, and N. V. Petviashvili. Spontaneous hole–clump pair creation. *Physics of Plasmas*, **6** (8) 3102–3113 (1999).

- [12] M. Lesur. *The Berk-Breizman Model as a Paradigm for Energetic Particle-driven Alfvén Eigenmodes*. Ph.D. thesis, Ecole Doctorale de l’Ecole Polytechnique (2010).
- [13] M. Podestà, M. Gorelenkova, and R. B. White. A reduced fast ion transport model for the tokamak transport code TRANSP. *Plasma Physics and Controlled Fusion*, **56** (5) 055003 (2014).
- [14] M. Podestà, M. Gorelenkova, E. D. Fredrickson, N. N. Gorelenkov, and R. B. White. Effects of energetic particle phase space modifications by instabilities on integrated modeling. *Nuclear Fusion*, **56** (11) 112005 (2016).
- [15] N. N. Gorelenkov, V. N. Duarte, M. Podestà, and H. L. Berk. Resonance broadened quasi-linear (RBQ) model for fast ion distribution relaxation due to Alfvénic eigenmodes. *Nuclear Fusion*, **58** (8) 082016 (2018).
- [16] United Nations, Department of Economics and Social Affairs, Population Division. World Population Prospects: The 2017 Revision, Key Findings and Advance Tables. *ESA/P/WP/248*, 1 (2017).
- [17] R. A. Easterlin. The Worldwide Standard of Living Since 1800. *The Journal of Economic Perspectives*, **14** (1) 7–26 (2000).
- [18] B. Etemad and J. Luciani. *World Energy Production 1800-1985*. Librairie Droz (1991). via: www.tsp-data-portal.org (Link accessed 7 September 2018).
- [19] U.S. Energy Information Administration. International Energy Statistics. www.eia.doe.gov/cfapps/ipdbproject/. data accessed 5 August 2014, via: www.tsp-data-portal.org (Link accessed 7 September 2018).
- [20] F. F. Chen. *An Indispensable Truth; How Fusion Power Can Save the Planet*. Springer (2011).
- [21] United Nations Treaty Collection. Paris Agreement, Paris 12 December 2015. https://treaties.un.org/pages/ViewDetails.aspx?src=TREATY&mtdsg_no=XXVII-7-d&chapter=27&clang=_en. Registration: 4 November 2016, No. 54113 (Link accessed 26 July 2018).
- [22] T. Kobashi, K. Goto-Azuma, J. E. Box, C.-C. Gao, and T. Nakaegawa. Causes of Greenland temperature variability over the past 4000 yr: implications for northern hemispheric temperature changes. *Climate of the Past*, **9** (5) 2299–2317 (2013).
- [23] T. Kobashi, K. Goto-Azuma, J. E. Box, C.-C. Gao, and T. Nakaegawa. Data published alongside Ref. [22]. <https://www.ncdc.noaa.gov/paleo/study/15535>. (Link accessed 7 September 2018).
- [24] NASA’s Goddard Institute for Space Studies (GISS). <https://climate.nasa.gov/vital-signs/global-temperature/>. (Link accessed 4 December 2018).
- [25] A. Einstein. Ist die Trägheit eines Körpers von seinem Energieinhalt abhängig? *Annalen der Physik*, **323** (13) 639–641 (1905).

- [26] J. D. Lawson. Some Criteria for a Power Producing Thermonuclear Reactor. *Proceedings of the Physical Society. Section B*, **70** (1) 6–10 (1957).
- [27] G. Jost. *Simulations particulières d’ondes de dérive dans des configurations magnétiques 3D*. Ph.D. thesis, Ecole Doctorale de l’Ecole Polytechnique (2000).
- [28] M. K. Lilley and B. N. Breizman. Convective transport of fast particles in dissipative plasmas near an instability threshold. *Nuclear Fusion*, **52** (9) 094002 (2012).
- [29] Y. Todo, M. A. Van Zeeland, A. Bierwage, and W. W. Heidbrink. Multi-phase simulation of fast ion profile flattening due to Alfvén eigenmodes in a DIII-D experiment. *Nuclear Fusion*, **54** (10) 104012 (2014).
- [30] H. H. Duong, W. W. Heidbrink, E. J. Strait, T. W. Petrie, R. Lee, R. A. Moyer, and J. G. Watkins. Loss of energetic beam ions during TAE instabilities. *Nuclear Fusion*, **33** (5) 749–765 (1993).
- [31] R. Aymar, P. Barabaschi, and Y. Shimomura (for the ITER Team). The ITER design. *Plasma Physics and Controlled Fusion*, **44** (5) 519–565 (2002).
- [32] P. Helander. Theory of plasma confinement in non-axisymmetric magnetic fields. *Reports on Progress in Physics*, **77** (8) 087001 (2014).
- [33] J. Wesson. *Tokamaks*. Oxford University Press, Fourth edition (2011).
- [34] F. C. Schüller. Disruptions in tokamaks. *Plasma Physics and Controlled Fusion*, **37** (11A) A135–A162 (1995).
- [35] E. Noether. Invariante Variationsprobleme. *Nachrichten von der Gesellschaft der Wissenschaften zu Göttingen, Mathematisch-Physikalische Klasse*, **1918** 235–257 (1918).
- [36] G. Grieger, W. Lotz, P. Merkel, J. Nührenberg, J. Sapper, E. Strumberger, H. Wobig, the W7-X Team, R. Burhenn, V. Erckmann, *et al.* Physics optimization of stellarators. *Physics of Fluids B: Plasma Physics*, **4** (7) 2081–2091 (1992).
- [37] H. Alfvén. Existence of Electromagnetic-Hydrodynamic Waves. *Nature*, **150** (3805) 405–406 (1942).
- [38] W. W. Heidbrink. Basic physics of Alfvén instabilities driven by energetic particles in toroidally confined plasmas. *Physics of Plasmas*, **15** (5) 055501 (2008).
- [39] W. Demtröder. *Experimentalphysik 3; Atome, Moleküle und Festkörper*. Springer Lehrbuch (1996).
- [40] C. Zener. Non-Adiabatic Crossing of Energy Levels. *Proceedings of the Royal Society of London A: Mathematical, Physical and Engineering Sciences*, **137** (833) 696–702 (1932).
- [41] H. L. Berk, J. W. Van Dam, Z. Guo, and D. M. Lindberg. Continuum damping of low- n toroidicity-induced shear Alfvén eigenmodes. *Physics of Fluids B: Plasma Physics*, **4** (7) 1806–1835 (1992).

- [42] Ya. I. Kolesnichenko, V. V. Lutsenko, H. Wobig, Yu. V. Yakovenko, and O. P. Fesenyuk. Alfvén continuum and high-frequency eigenmodes in optimized stellarators. *Physics of Plasmas*, **8** (2) 491–509 (2001).
- [43] A. Könies, S. Briguglio, N. Gorelenkov, T. Fehér, M. Isaev, Ph. Lauber, A. Mishchenko, D. A. Spong, Y. Todo, W. A. Cooper, *et al.* Benchmark of gyrokinetic, kinetic MHD and gyrofluid codes for the linear calculation of fast particle driven TAE dynamics. ITR/P1-34. 24th IAEA Int. Conf. on Fusion Energy (San Diego, CA, USA) (2012). http://www-naweb.iaea.org/napc/physics/FEC/FEC2012/papers/437_ITRP134.pdf (Link accessed 27 October 2015).
- [44] A. Könies, S. Briguglio, N. Gorelenkov, T. Fehér, M. Isaev, Ph. Lauber, A. Mishchenko, D. A. Spong, Y. Todo, W. A. Cooper, *et al.* Benchmark of gyrokinetic, kinetic MHD and gyrofluid codes for the linear calculation of fast particle driven TAE dynamics. *Nuclear Fusion*, **58** (12) 126027 (2018).
- [45] A. Könies and R. Kleiber. A computational approach to continuum damping of Alfvén waves in two and three-dimensional geometry. *Physics of Plasmas*, **19** (12) 122111 (2012).
- [46] L. Landau. On the vibrations of the electronic plasma. *Journal of Physics*, **X** (1) 25–34 (1946).
- [47] G. Y. Fu, H. L. Berk, and A. Pletzer. Kinetic damping of toroidal Alfvén eigenmodes. *Physics of Plasmas*, **12** (8) 082505 (2005).
- [48] K. L. Wong, R. J. Fonck, S. F. Paul, D. R. Roberts, E. D. Fredrickson, R. Nazikian, H. K. Park, M. Bell, N. L. Bretz, R. Budny, *et al.* Excitation of toroidal Alfvén eigenmodes in TFTR. *Physical Review Letters*, **66** (14) 1874–1877 (1991).
- [49] Ph. Lauber, I. G. J. Classen, D. Curran, V. Igochine, B. Geiger, S. da Garça, M. García-Muñoz, M. Maraschek, P. McCarthy, and the ASDEX Upgrade Team. NBI-driven Alfvénic modes at ASDEX Upgrade. *Nuclear Fusion*, **52** (9) 094007 (2012).
- [50] S. E. Sharapov, B. Alper, Yu. F. Baranov, H. L. Berk, D. Borba, C. Boswell, B. N. Breizman, C. D. Challis, M. de Baar, E. De La Luna, *et al.* Alfvén cascades in JET discharges with NBI-heating. *Nuclear Fusion*, **46** (10) S868–S879 (2006).
- [51] M. A. Van Zeeland, M. E. Austin, T. N. Carlstrom, T. Deterly, D. K. Finkenthal, C. T. Holcomb, R. J. Jayakumar, G. J. Kramer, M. A. Makowski, G. R. McKee, *et al.* Internal Alfvén eigenmode observations on DIII-D. *Nuclear Fusion*, **46** (10) S880–S887 (2006).
- [52] K. Shinohara, Y. Kusama, M. Takechi, A. Morioka, M. Ishikawa, N. Oyama, K. Tobita, T. Ozeki, S. Takeji, S. Moriyama, *et al.* Alfvén eigenmodes driven by Alfvénic beam ions in JT-60U. *Nuclear Fusion*, **41** (5) 603–612 (2001).
- [53] A. Weller, M. Anton, J. Geiger, M. Hirsch, R. Jaenicke, A. Werner, W7-AS Team, C. Nührenberg, E. Sallander, and D. A. Spong. Survey of magnetohydrodynamic instabilities in the advanced stellarator Wendelstein 7-AS. *Physics of Plasmas*, **8** (3) 931–956 (2001).
- [54] K. Toi, S. Ohdachi, S. Yamamoto, N. Nakajima, S. Sakakibara, K. Watanabe, S. Inagaki, Y. Nagayama, Y. Narushima, H. Yamada, *et al.* MHD instabilities and their effects on

- plasma confinement in Large Helical Device plasmas. *Nuclear Fusion*, **44** (2) 217–225 (2004).
- [55] R. Jiménez-Gómez, A. Könies, E. Ascasíbar, F. Castejón, T. Estrada, L. G. Eliseev, A. V. Melnikov, J. A. Jiménez, D. G. Pretty, D. Jiménez-Rey, *et al.* Alfvén eigenmodes measured in the TJ-II stellarator. *Nuclear Fusion*, **51** (3) 033001 (2011).
- [56] T. Windisch, A. Krämer-Flecken, J. L. Velasco, A. Könies, C. Nührenberg, O. Grulke, T. Klinger, and the W7-X team. Poloidal correlation reflectometry at W7-X: radial electric field and coherent fluctuations. *Plasma Physics and Controlled Fusion*, **59** (10) 105002 (2017).
- [57] C. Slaby, A. Könies, and R. Kleiber. Numerical investigation of non-perturbative kinetic effects of energetic particles on toroidicity-induced Alfvén eigenmodes in tokamaks and stellarators. *Physics of Plasmas*, **23** (9) 092501 (2016).
- [58] A. Dinklage, C. D. Beidler, P. Helander, G. Fuchert, H. Maaßberg, K. Rahbarnia, T. Sunn Pedersen, Y. Turkin, R. C. Wolf, A. Alonso, *et al.* Magnetic configuration effects on the Wendelstein 7-X stellarator. *Nature Physics*, **14** 855–860 (2018).
- [59] W. Baumjohann and R. A. Treumann. *Basic Space Plasma Physics*. Imperial College Press (1997).
- [60] S. J. Allfrey and R. Hatzky. A revised δf algorithm for nonlinear PIC simulation. *Computer Physics Communications*, **154** (2) 98–104 (2003).
- [61] A. J. Brizard and T. S. Hahm. Foundations of nonlinear gyrokinetic theory. *Reviews of Modern Physics*, **79** (2) 421–468 (2007).
- [62] J. B. Taylor. Magnetic Moment Under Short-Wave Electrostatic Perturbations. *The Physics of Fluids*, **10** (6) 1357–1359 (1967).
- [63] G. G. Howes, S. C. Cowley, W. Dorland, G. W. Hammett, E. Quataert, and A. A. Schekochihin. Astrophysical Gyrokinetics: Basic Equations and Linear Theory. *The Astrophysical Journal*, **651** (1) 590–614 (2006).
- [64] E. A. Frieman and L. Chen. Nonlinear gyrokinetic equations for low-frequency electromagnetic waves in general plasma equilibria. *The Physics of Fluids*, **25** (3) 502–508 (1982).
- [65] E. Hirvijoki, A. Brizard, A. Snicker, and T. Kurki-Suonio. Monte Carlo implementation of a guiding-center Fokker-Planck kinetic equation. *Physics of Plasmas*, **20** (9) 092505 (2013).
- [66] P. Helander and D. J. Sigmar. *Collisional Transport in Magnetized Plasmas*. Cambridge University Press (2002).
- [67] K. Kauffmann. *Including Collisions in Gyrokinetic Tokamak and Stellarator Simulations*. Ph.D. thesis, Ernst-Moritz-Arndt-Universität Greifswald (2011).
- [68] P. L. Bhatnagar, E. P. Gross, and M. Krook. A Model for Collision Processes in Gases. I. Small Amplitude Processes in Charged and Neutral One-Component Systems. *Physical Review*, **94** (3) 511–525 (1954).

- [69] A. Mishchenko, A. Könies, R. Kleiber, and M. Cole. Pullback transformation in gyrokinetic electromagnetic simulations. *Physics of Plasmas*, **21** (9) 092110 (2014).
- [70] R. Kleiber, R. Hatzky, A. Könies, A. Mishchenko, and E. Sonnendrücker. An explicit large time step particle-in-cell scheme for nonlinear gyrokinetic simulations in the electromagnetic regime. *Physics of Plasmas*, **23** (3) 032501 (2016).
- [71] A. Könies. A code for the calculation of kinetic Alfvén waves in three-dimensional geometry. 10th IAEA TM on Energetic Particles in Magnetic Confinement Systems (Kloster Seon, Germany) (2007).
- [72] M. D. J. Cole, A. Mishchenko, A. Könies, R. Hatzky, and R. Kleiber. A hierarchy of electromagnetic gyrokinetic and fluid hybrid models for the simulation of global modes. *Plasma Physics and Controlled Fusion*, **57** (5) 054013 (2015).
- [73] S. Briguglio, X. Wang, F. Zonca, G. Vlad, G. Fogaccia, C. Di Troia, and V. Fusco. Analysis of the nonlinear behavior of shear-Alfvén modes in tokamaks based on Hamiltonian mapping techniques. *Physics of Plasmas*, **21** (11) 112301 (2014).
- [74] X. Wang, S. Briguglio, Ph. Lauber, V. Fusco, and F. Zonca. Structure of wave-particle resonances and Alfvén mode saturation. *Physics of Plasmas*, **23** (1) 012514 (2016).
- [75] Y. Turkin, C. D. Beidler, H. Maaßberg, S. Murakami, V. Tribaldos, and A. Wakasa. Neoclassical transport simulations for stellarators. *Physics of Plasmas*, **18** (2) 022505 (2011).
- [76] A. V. Melnikov, L. G. Eliseev, E. Ascasíbar, A. Cappa, F. Castejón, C. Hidalgo, T. Ido, J. A. Jiménez, A. S. Kozachek, L. I. Krupnik, *et al.* Transition from chirping to steady NBI-driven Alfvén modes caused by magnetic configuration variations in the TJ-II stellarator. *Nuclear Fusion*, **56** (7) 076001 (2016).
- [77] A. V. Melnikov, L. G. Eliseev, F. Castejón, C. Hidalgo, P. O. Khabanov, A. S. Kozachek, L. I. Krupnik, M. Liniers, S. E. Lysenko, J. L. de Pablos, *et al.* Study of NBI-driven chirping mode properties and radial location by the heavy ion beam probe in the TJ-II stellarator. *Nuclear Fusion*, **56** (11) 112019 (2016).
- [78] M. Lesur, Y. Idomura, and X. Garbet. Fully nonlinear features of the energetic beam-driven instability. *Physics of Plasmas*, **16** (9) 092305 (2009).
- [79] M. Lesur, Y. Idomura, K. Shinohara, X. Garbet, and the JT-60 Team. Spectroscopic determination of kinetic parameters for frequency sweeping Alfvén eigenmodes. *Physics of Plasmas*, **17** (12) 122311 (2010).
- [80] M. Lesur. Effect of collisions on energetic particle-driven chirping bursts. *Physics of Plasmas*, **20** (5) 055905 (2013).
- [81] M. K. Lilley, B. N. Breizman, and S. E. Sharapov. Effect of dynamical friction on nonlinear energetic particle modes. *Physics of Plasmas*, **17** (9) 092305 (2010).
- [82] M. K. Lilley and R. M. Nyqvist. Formation of Phase Space Holes and Clumps. *Physical Review Letters*, **112** (15) 155002 (2014).

- [83] C. Z. Cheng. Kinetic extensions of magnetohydrodynamics for axisymmetric toroidal plasmas. *Physics Reports*, **211** (1) 1–51 (1992).
- [84] R. B. White and M. S. Chance. Hamiltonian guiding center drift orbit calculation for plasmas with arbitrary cross section. *The Physics of Fluids*, **27** (10) 2455–2467 (1984).
- [85] G. M. Staebler, J. E. Kinsey, and R. E. Waltz. A theory-based transport model with comprehensive physics. *Physics of Plasmas*, **14** (5) 055909 (2007).
- [86] He Sheng, R. E. Waltz, and G. M. Staebler. Alfvén eigenmode stability and critical gradient energetic particle transport using the Trapped-Gyro-Landau-Fluid model. *Physics of Plasmas*, **24** (7) 072305 (2017).
- [87] E. M. Bass and R. E. Waltz. Predictions of alpha-particle and neutral-beam heating and transport in ITER scenarios. TH/6-2. 27th IAEA Fusion Energy Conference (Gandhinagar, India) (2018). https://conferences.iaea.org/indico/event/151/papers/5860/files/4334-BASS_IAEA_FEC_2018_preprint.pdf (Link accessed 30 October 2018).
- [88] C. S. Collins, W. W. Heidbrink, M. E. Austin, G. J. Kramer, D. C. Pace, C. C. Petty, L. Stagner, M. A. Van Zeeland, R. B. White, Y. B. Zhu, *et al.* Observation of Critical-Gradient Behavior in Alfvén-Eigenmode-Induced Fast-Ion Transport. *Physical Review Letters*, **116** (9) 095001 (2016).
- [89] J. V. W. Reynders. *Gyrokinetic simulations of finite- β plasmas on parallel architectures*. Ph.D. thesis, Princeton University (1992).
- [90] J. C. Cummings. *Gyrokinetic simulation of finite-beta and self-generated sheared-flow effects on pressure-gradient-driven instabilities*. Ph.D. thesis, Princeton University (1995).
- [91] J. Stoer and R. Bulirsch. *Numerische Mathematik 2*. Springer-Lehrbuch, Third edition (1990).
- [92] Y. Chen and S. E. Parker. A δf particle method for gyrokinetic simulations with kinetic electrons and electromagnetic perturbations. *Journal of Computational Physics*, **189** (2) 463–475 (2003).
- [93] A. Mishchenko, M. Cole, R. Kleiber, and A. Könies. New variables for gyrokinetic electromagnetic simulations. *Physics of Plasmas*, **21** (5) 052113 (2014).
- [94] C. Slaby, R. Kleiber, and A. Könies. Combining electromagnetic gyro-kinetic particle-in-cell simulations with collisions. *Computer Physics Communications*, **218** 1–9 (2017).
- [95] W. Wan, Y. Chen, and S. E. Parker. Gyrokinetic δf simulation of the collisionless and semicollisional tearing mode instability. *Physics of Plasmas*, **12** (1) 012311 (2005).
- [96] M. N. Rosenbluth, W. M. MacDonald, and D. L. Judd. Fokker-Planck Equation for an Inverse-Square Force. *Physical Review*, **107** (1) 1–6 (1957).
- [97] A. Y. Aydemir. A unified Monte Carlo interpretation of particle simulations and applications to non-neutral plasmas. *Physics of Plasmas*, **1** (4) 822–831 (1994).
- [98] S. E. Parker and W. W. Lee. A fully nonlinear characteristic method for gyrokinetic simulations. *Physics of Fluids B: Plasma Physics*, **5** (1) 77–86 (1993).

- [99] I. G. Abel, M. Barnes, S. C. Cowley, W. Dorland, and A. A. Schekochihin. Linearized model Fokker–Planck collision operators for gyrokinetic simulations. I. Theory. *Physics of Plasmas*, **15** (12) 122509 (2008).
- [100] S. Satake, R. Kanno, and H. Sugama. Development of a Non-Local Neoclassical Transport Code for Helical Configurations. *Plasma and Fusion Research*, **3** S1062 (2008).
- [101] T. Vernay, S. Brunner, L. Villard, B. F. McMillan, S. Jolliet, T. M. Tran, A. Bottino, and J. P. Graves. Neoclassical equilibria as starting point for global gyrokinetic microturbulence simulations. *Physics of Plasmas*, **17** (12) 122301 (2010).
- [102] A. Könies. Private communication (2018).
- [103] S. P. Hirshman and J. C. Whitson. Steepest-descent moment method for three-dimensional magnetohydrodynamic equilibria. *The Physics of Fluids*, **26** (12) 3553–3568 (1983).
- [104] A. Könies and D. Eremin. Coupling of Alfvén and sound waves in stellarator plasmas. *Physics of Plasmas*, **17** (1) 012107 (2010).
- [105] M. Schneller, Ph. Lauber, and S. Briguglio. Nonlinear energetic particle transport in the presence of multiple Alfvénic waves in ITER. *Plasma Physics and Controlled Fusion*, **58** (1) 014019 (2016).
- [106] H. L. Berk and B. N. Breizman. Saturation of a single mode driven by an energetic injected beam. III. Alfvén wave problem. *Physics of Fluids B: Plasma Physics*, **2** (9) 2246–2252 (1990).
- [107] T. Hayward-Schneider and Ph. Lauber. Nonlinear energetic particle transport by Alfvén eigenmodes and sensitivity study of hybrid-gyrokinetic physics models. P-10. 15th IAEA TM on Energetic Particles in Magnetic Confinement Systems (Princeton, NJ, USA) (2017). <https://nucleus.iaea.org/sites/fusionportal/Shared%20Documents/EP%2017th/Posters/P-10.pdf> (Link accessed 23 October 2018).
- [108] J. A. Heikkinen, S. K. Sipilä, and T. J. H. Pättikangas. Monte Carlo simulation of runaway electrons in a toroidal geometry. *Computer Physics Communications*, **76** (2) 215–230 (1993).
- [109] S. P. Hirshman, K. C. Shaing, W. I. van Rij, C. O. Beasley, Jr., and E. C. Crume, Jr. Plasma transport coefficients for nonsymmetric toroidal confinement systems. *The Physics of Fluids*, **29** (9) 2951–2959 (1986).
- [110] M. Landreman, H. M. Smith, A. Mollén, and P. Helander. Comparison of particle trajectories and collision operators for collisional transport in nonaxisymmetric plasmas. *Physics of Plasmas*, **21** (4) 042503 (2014).

Appendix A

Thesis articles

In this appendix, all articles that constitute the main part of this thesis are included. They are listed in the same order as they appear in below. Furthermore, the individual contributions of each author to the respective article is given.

Contributions to the articles

1. C. Slaby (CS), R. Kleiber (RK), and A. Könies (AK). Combining electromagnetic gyrokinetic particle-in-cell simulations with collisions. *Computer Physics Communications*, **218** 1-9 (2017).

CS performed all simulations and wrote the manuscript. RK conceived the Legendre approach. It was implemented by RK and CS. All authors corrected the manuscript during the refereeing process.

2. C. Slaby (CS), A. Könies (AK), R. Kleiber (RK), and J. M. García-Regaña (JG). Effects of collisions on the saturation dynamics of TAEs in tokamaks and stellarators. *Nuclear Fusion*, **58** (8) 082018 (2018).

CS performed the CKA and EUTERPE simulations and wrote the manuscript. The implementation of the momentum-conservation scheme was jointly done by RK, JG, and CS. It was parallelized by RK and CS. All authors corrected the manuscript during the refereeing process.

3. C. Slaby (CS), A. Könies (AK), R. Kleiber (RK), S. Äkäslompolo (SA), and J. Kontula (JK). Numerical investigation of fast-ion-driven modes in Wendelstein 7-X. *Europhysics Conference Abstracts*, **42A** P4.1098 (2018) (non-refereed).

CS performed the CKA, EUTERPE, and STAE-K simulations and wrote the manuscript. SA provided the fast-ion distribution function and density profile calculated with the ASCOT code. JK contributed by writing tools that extract data relevant for the EUTERPE simulations from the ASCOT output. CS, AK, RK, and SA commented on and improved the manuscript.

4. C. Slaby (CS), A. Könies (AK), R. Kleiber (RK), S. Äkäslompolo (SA), and J. Kontula (JK). Parametric study of fast-ion-driven modes in Wendelstein 7-X. *Journal of Physics: Conference Series*, **1125** 012019 (2018)

CS performed the CKA and EUTERPE simulations and wrote the manuscript. CS and RK implemented the fast-ion collision operator into EUTERPE. SA provided the fast-ion distribution function and density profile calculated with the ASCOT code. JK contributed by writing tools that extract data relevant for the EUTERPE simulations from the ASCOT output. CS, AK, RK, and SA commented on and improved the manuscript.

5. C. Slaby (CS), A. Könies (AK), R. Kleiber (RK), and Henry Leyh (HL). On non-linear frequency chirping in connection with collisions. *submitted to Nuclear Fusion* (2018).

CS performed EUTERPE and CONTI simulations and wrote the manuscript. AK did the CKA simulations. HL and CS wrote and tested the diagnostics tool that calculates the spectrograms. All authors commented on and improved the manuscript.

6. C. Slaby (CS), A. Könies (AK), and R. Kleiber (RK). Numerical investigation of non-perturbative kinetic effects of energetic particles on toroidicity-induced Alfvén eigenmodes in tokamaks and stellarators. *Physics of Plasmas*, **23** (9) 092501 (2016).

CS wrote the STAE-K code from a pre-existing shooting code developed by RK. CS performed the STAE-K simulations and wrote the manuscript. All authors corrected the manuscript during the refereeing process.

7. J. M. García-Regaña (JG), T. Estrada (TS), I. Calvo (IC), J. L. Velasco (JV), J. A. Alonso (JA), D. Carralero (DC), R. Kleiber (RK), M. Landreman (ML), A. Mollén (AM), E. Sánchez (ES), C. Slaby (CS), and TJ-II Team, and W7-X Team. On-surface potential and radial electric field variations in electron root stellarator plasmas. *Plasma Physics and Controlled Fusion*, **60** (10) 104002 (2018).

The manuscript was written by JG. The implementation of the momentum-conservation scheme was jointly done by RK, JG, and CS. It was parallelized by RK and CS. CS also performed a benchmark (see App. B.4) to verify the correctness of the implementation. CS further contributed by commenting on and improving the manuscript during the refereeing process. The contributions of the other authors are as follows: TS and DC performed the experimental Doppler Reflectometry measurements at TJ-II. DKES simulations to compare the electric field to the measured value were done by JV. ML and AM performed SFINCS calculations that provided the electric field used in the EUTERPE simulations of W7-X. IC took part of numerous theoretical discussions essential for the development of the work.

Christoph Slaby

Prof. Dr. Per Helander

Combining electromagnetic gyro-kinetic particle-in-cell simulations with collisions (A.1)

Full citation:

C. Slaby, R. Kleiber, and A. Könies. Combining electromagnetic gyro-kinetic particle-in-cell simulations with collisions. *Computer Physics Communications*, **218** 1-9 (2017).

DOI:

10.1016/j.cpc.2017.04.011 (<https://doi.org/10.1016/j.cpc.2017.04.011>)

Reproduced with the permission of Elsevier and EUROfusion.

Appendix A. Thesis articles



Combining electromagnetic gyro-kinetic particle-in-cell simulations with collisions



Christoph Slaby*, Ralf Kleiber, Axel Könies

Max-Planck-Institut für Plasmaphysik, Wendelsteinstraße 1, 17491 Greifswald, Germany

ARTICLE INFO

Article history:

Received 17 January 2017
Received in revised form 20 April 2017
Accepted 24 April 2017
Available online 4 May 2017

Keywords:

PIC simulation
Pitch-angle collisions
Kinetic Alfvén waves

ABSTRACT

It has been an open question whether for electromagnetic gyro-kinetic particle-in-cell (PIC) simulations pitch-angle collisions and the recently introduced pullback transformation scheme (Mishchenko et al., 2014; Kleiber et al., 2016) are consistent.

This question is positively answered by comparing the PIC code EUTERPE with an approach based on an expansion of the perturbed distribution function in eigenfunctions of the pitch-angle collision operator (Legendre polynomials) to solve the electromagnetic drift-kinetic equation with collisions in slab geometry.

It is shown how both approaches yield the same results for the frequency and damping rate of a kinetic Alfvén wave and how the perturbed distribution function is substantially changed by the presence of pitch-angle collisions.

© 2017 EURATOM. Published by Elsevier B.V. All rights reserved.

1. Introduction

The numerical treatment of the gyro-kinetic equation including collisions and electromagnetic effects is, for instance, necessary for studying the interaction of Alfvén modes with fast particles. It has been shown analytically and numerically (see e.g. Refs. [1,2]) that collisions have a particularly strong influence on the non-linear saturation mechanism of the mode by detrapping resonant particles. Also the multi-phase simulations addressing bursting phenomena for JT 60-U [3] and profile flattening effects for D III-D [4] rely on the proper treatment of collisions for the fast particles. Furthermore, trapped electrons can contribute to the damping of Alfvén waves as has been shown in Ref. [5]. (A more elaborate discussion can be found in Ref. [6].)

Most computational approaches for solving the gyro-kinetic equations either rely on a grid-based discretization (Eulerian codes) or use a particle discretization (particle-in-cell (PIC) codes). Additionally, the electromagnetic gyro-kinetic equations can either be stated in the so-called v_{\parallel} -formulation or p_{\parallel} -formulation, where the former uses the physical parallel velocity while the latter adopts the parallel canonical momentum $p_{\parallel} = mv_{\parallel} + qA_{\parallel}$ as an independent variable [7]. For PIC simulations, the v_{\parallel} -formulation had serious problems related to the partial time derivative of the perturbed parallel vector potential (A_{\parallel}) in the equations of motion [8]. Therefore, the p_{\parallel} -formulation [9] became standard despite its notorious cancellation problem (see e.g. Ref. [10]), caused

by the appearance of a non-physical current in Ampère's law. This problem could be overcome by the adjustable control variate scheme [11]. A different approach, avoiding some problems of this method, is the recently proposed pullback transformation scheme (PT-scheme) [12,13]. This algorithm, loosely speaking, works in v_{\parallel} . Thus, it was conjectured that it may provide an optimal framework for implementing a (pitch-angle) collision operator, which is naturally formulated in v_{\parallel} .

Here, the gyro-kinetic PIC code EUTERPE is used to investigate the compatibility of collisions with the PT-scheme (and additionally with the two-weight scheme developed in Ref. [14]) as well as its convergence properties. In the past, electrostatic calculations including collisions, neoclassical impurity transport studies as well as electromagnetic simulations without collisions were successfully performed with EUTERPE [15–18].

In the present work, the PT-scheme is combined with a linearized electron pitch-angle collision operator. Since such a combination is reported for the first time, the main focus of this paper is on verification and not on validation. In order to concentrate on the essential properties of the numerical scheme, (drift-)kinetic Alfvén waves in a homogeneous slab are considered. Additionally, only electron pitch-angle collisions are included. Ion finite-Larmor-radius (FLR) effects are retained in the ion polarization density with a Padé approximation whereas the ion dynamics, electron FLR effects, and gyro-averaging of the fields over the gyro-ring are neglected. Gyro-averaging may contribute significantly to the damping from ion collisions when $k_{\perp}\rho_i \gtrsim 1$ (with k_{\perp} and ρ_i denoting the perpendicular wave vector of the mode and the ion gyro-radius, respectively). Notwithstanding the simplifications

* Corresponding author.
E-mail address: christoph.slaby@ipp.mpg.de (C. Slaby).

made for the collision operator, this problem is non-trivial and only few analytical results are available. Moreover, recent comparisons of frequencies and damping rates from analytical theory with direct measurements revealed striking discrepancies [19]. This additionally motivates the need for accurate algorithms to gain physical insight.

Since there are no reliable analytical theories available, the results of the PIC approach will be benchmarked against results from a numerical method (here called ‘Legendre approach’) using a decomposition of the perturbed distribution function into eigenfunctions of the pitch-angle scattering operator, which are Legendre polynomials.

2. Theory and algorithms

The theoretical description of kinetic Alfvén waves in a slab starts with the gyro-kinetic equation for the electrons

$$\frac{\partial f_e}{\partial t} + \dot{\mathbf{R}} \cdot \nabla f_e + \dot{v}_{\parallel} \frac{\partial f_e}{\partial v_{\parallel}} = \mathcal{L}(f_e) \quad (1)$$

in its v_{\parallel} -form. For simplicity, gyro-averaging and the dynamics of the ions have been neglected. The ions just provide a uniform background charge density to satisfy quasi-neutrality. $f_e = f_e(\mathbf{R}, \mathbf{v})$ is the electron distribution function, \mathbf{R} denotes the spatial position, and $v_{\parallel} = \mathbf{b} \cdot \mathbf{v}$ is the velocity along the magnetic field $\mathbf{B} = B\mathbf{b}$. To treat the collisional influence on the distribution function, a pitch-angle ($\xi = v_{\parallel}/v$) collision operator

$$\mathcal{L} = \frac{v}{2} \frac{\partial}{\partial \xi} (1 - \xi^2) \frac{\partial}{\partial \xi} \quad (2)$$

is used. This operator follows from transforming the full Fokker-Planck operator to guiding-centre coordinates (see e.g. Ref. [20]) followed by neglecting energy and guiding-centre diffusion. For the electron–electron pitch-angle collisions considered here, this is well justified.

In the collision operator, ν is the electron self-collision frequency [21]

$$\nu = \nu_0 \frac{\Phi(x) - G(x)}{x^2}, \quad x = \frac{v}{\sqrt{2}v_{\text{th},e}}, \quad (3)$$

where Φ and G denote the error function and the Chandrasekhar function, respectively. ($v_{\text{th},e} = \sqrt{k_B T_e/m_e}$ is the electron thermal velocity.)

The characteristics of the kinetic equation are

$$\dot{\mathbf{R}} = v_{\parallel} \mathbf{b} + \frac{1}{B_{\parallel}} \mathbf{b} \times \nabla [\phi - v_{\parallel} A_{\parallel}] \quad (4)$$

$$\dot{v}_{\parallel} = -\frac{q_e}{m_e} \left(\nabla_{\parallel} \phi + \frac{\partial A_{\parallel}}{\partial t} \right) \quad (5)$$

with

$$\mathbf{B}^* = \nabla \times \mathbf{A}^* \quad (6)$$

$$\mathbf{A}^* = \mathbf{A}_0 + \left(\frac{m_e}{q_e} v_{\parallel} + A_{\parallel} \right) \mathbf{b} \quad (7)$$

in a straight and constant magnetic field. (Here, q_e and m_e are the electron charge and mass, and \mathbf{A}_0 denotes the fixed background vector potential, respectively.) The electrostatic potential ϕ and the parallel component of the vector potential A_{\parallel} are denoted as usual.

Eqs. (1), (4), and (5) are solved together with the gyro-kinetic Poisson equation

$$-\nabla \cdot \left(\frac{m_i n_0}{B^2} \nabla_{\perp} \phi \right) = (1 - \nabla \cdot \rho_i^2 \nabla_{\perp}) q_e n_e \quad (8)$$

(with $\rho_i = \sqrt{k_B T_i m_i} / (q_i B)$ being the ion gyro-radius) and Ampère’s law

$$-\nabla_{\perp}^2 A_{\parallel} = \mu_0 j_{\parallel,e} \quad (9)$$

for the fields. Since collisions are expected to mainly influence high $k_{\perp} \rho_i$ modes, a Padé approximation for the ion polarization density was employed in Eq. (8). In the equations above, m_i is the ion mass, n_0 denotes the background density, μ_0 is the vacuum permeability, and j_{\parallel} stands for the parallel current density. The electron density and current are obtained by taking the appropriate moments of the distribution function

$$n_e(\mathbf{R}) = \int d^3 v f_e(\mathbf{R}, \mathbf{v}) \quad (10)$$

$$j_{\parallel,e}(\mathbf{R}) = q_e \int d^3 v v_{\parallel} f_e(\mathbf{R}, \mathbf{v}). \quad (11)$$

The kinetic equation together with the field equations will be solved in two different ways. Firstly, a particle-in-cell (PIC) method will be employed. Numerical marker particles, which move along the characteristics (Eqs. (4) and (5)) through phase-space, are used to represent the actual electrons. Secondly, the equations will be solved by employing a decomposition of the distribution function into Legendre polynomials (‘Legendre approach’), which are eigenfunctions of the collision operator \mathcal{L} . A similar strategy was recently used in Ref. [22] for an electrostatic system.

The following subsections elaborate on the individual approaches.

2.1. A short description of the pullback transformation scheme

The PT-scheme was introduced in Refs. [12,13] in the absence of collisions. Since those papers give a good overview of the general idea and of the implementation into a PIC code, only the key elements are repeated here. The implementation [23] of pitch-angle collisions into EUTERPE is discussed briefly.

The PT-scheme is based on an arbitrary splitting of A_{\parallel} into a Hamiltonian and a symplectic part, $A_{\parallel} = A_{\parallel}^h + A_{\parallel}^s$. Furthermore, an ‘incomplete’ transformation

$$\tilde{u}_{\parallel} = v_{\parallel} + \frac{q_e}{m_e} A_{\parallel}^h \quad (12)$$

is employed. This transformation is similar to the one transforming to the canonical momentum p_{\parallel} , but ‘incomplete’ in the sense that it only contains the Hamiltonian part of A_{\parallel} . The resulting equations of motion are

$$\dot{\mathbf{R}} = \left(\tilde{u}_{\parallel} - \frac{q_e}{m_e} A_{\parallel}^h \right) \mathbf{b} + \frac{1}{B_{\parallel}} \mathbf{b} \times \nabla [\phi - \tilde{u}_{\parallel} (A_{\parallel}^h + A_{\parallel}^s)] \quad (13)$$

$$\dot{\tilde{u}}_{\parallel} = -\frac{q_e}{m_e} \left\{ \nabla_{\parallel} [\phi - \tilde{u}_{\parallel} A_{\parallel}^h] + \frac{\partial A_{\parallel}^s}{\partial t} \right\} \quad (14)$$

with

$$\mathbf{A}^* = \mathbf{A}_0 + \left(\frac{m_e}{q_e} \tilde{u}_{\parallel} + A_{\parallel}^s \right) \mathbf{b} \quad (15)$$

for a plasma slab with constant magnetic field. While the Poisson equation for the PT-scheme is the same as Eq. (8), Ampère’s law changes to

$$-\nabla \cdot \nabla_{\perp} A_{\parallel}^h + A_{\parallel}^h \frac{\mu_0 n_0 q_e^2}{m_e} = \mu_0 j_{\parallel,e} + \nabla \cdot \nabla_{\perp} A_{\parallel}^s. \quad (16)$$

It is important to note that, because of the arbitrary splitting of A_{\parallel} , an additional equation is needed to close the system. One thus gains an additional degree of freedom to fix A_{\parallel}^s . This is done by postulating the equation

$$\frac{\partial A_{\parallel}^s}{\partial t} + \mathbf{b} \cdot \nabla \phi = 0, \quad (17)$$

which is similar to the ideal Ohm’s law from MHD (magneto-hydrodynamic) theory. The idea is that, when simulating MHD modes (such as shear Alfvén waves) the majority of A_{\parallel} will be

contained in A_{\parallel}^s . Hence, A_{\parallel}^h will be small. In this way the cancellation problem is mitigated.

In the simulation, A_{\parallel}^h is chosen to be zero at $t = 0$. However, as the simulation proceeds, A_{\parallel}^h increases, which could eventually lead to the reappearance of the cancellation problem. Therefore, after each time step, a resetting procedure (the actual pullback transformation) is performed: Before A_{\parallel}^h is reset to zero its value is added to A_{\parallel}^s , Eq. (12) is used to go back from \tilde{u}_{\parallel} to v_{\parallel} , and the distribution function is transformed $f_e(v_{\parallel}) = f_e(\tilde{u}_{\parallel})$.

Thus, at its core, the PT-scheme is a method for solving the gyro-kinetic equations in the v_{\parallel} -formulation. As the collision operator is given in v_{\parallel} , the PT-scheme should be well suited to incorporate collisions.

In EUTERPE, the collision step is performed after the advection step, in which a fourth-order Runge–Kutta is used for time integration. The collisions themselves change the pitch-angle and magnetic moment of each particle. This involves rotating the velocity vector on a spherical shell (the magnitude of the velocity remains unchanged) according to randomly generated numbers with specific statistical properties. Denoting the cosine of the pitch-angle before and after the collision by ξ_{in} and ξ_{out} one finds

$$\xi_{\text{out}} = \sin \chi \sin \lambda \sqrt{1 - \xi_{\text{in}}^2} + \xi_{\text{in}} \cos \chi, \quad (18)$$

where $\chi = R\sqrt{2\nu\Delta t}$ [23]. Both λ and R are random numbers. λ is drawn from a uniform distribution between 0 and 2π , while R comes from a Gaussian distribution with expectation value 0 and variance 1 [23]. This scheme was reported in Refs. [24,25] and can be regarded as a variant of the method presented in Ref. [26]. It is important to note that this particular collisional implementation corresponds to a first-order (weak convergence) scheme. The often-used Euler–Maruyama method (see e.g. Ref. [27]) for the integration of stochastic differential equations is also only of first order.

2.2. Solving the system by a decomposition into Legendre polynomials

While EUTERPE solves the kinetic equation in the mixed formalism, the p_{\parallel} -formalism will be used for the Legendre approach. This means that, in contrast to Eqs. (4) and (5), the characteristics of the kinetic equation are now given as

$$\dot{\mathbf{R}} = \left(u_{\parallel} - \frac{q_e}{m_e} A_{\parallel} \right) \mathbf{b} + \frac{1}{B_{\parallel}} \mathbf{b} \times \nabla \psi \quad (19)$$

$$\dot{u}_{\parallel} = -\frac{q_e}{m_e} \nabla_{\parallel} \psi \quad (20)$$

$$\dot{\psi} = \phi - u_{\parallel} A_{\parallel} \quad (21)$$

with

$$\mathbf{A}^* = \mathbf{A}_0 + \frac{m_e}{q_e} u_{\parallel} \mathbf{b}. \quad (22)$$

Note that in this formalism, $u_{\parallel} = p_{\parallel}/m_e = v_{\parallel} + (q_e/m_e)A_{\parallel}$ is not the physical velocity along the magnetic field lines.

Using the left-hand side of Eq. (1) in its p_{\parallel} -form and transforming it via

$$u = \sqrt{u_{\parallel}^2 + 2\mu B}, \quad \xi' = \frac{u_{\parallel}}{u} \quad (23)$$

to a (u, ξ') -coordinate system (μ denotes the magnetic moment per mass) yields

$$\frac{\partial f_e^{(1)}}{\partial t} + u \xi' \nabla_{\parallel} f_e^{(1)} - \frac{q_e}{m_e} \xi' \nabla_{\parallel} \psi \frac{\partial F}{\partial u} = \mathcal{L}(F) + \mathcal{L}(f_e^{(1)}). \quad (24)$$

The ansatz $f_e = F + f_e^{(1)}$, with F being the uniform Maxwellian background and $f_e^{(1)}$ denoting a small perturbation, has also been

used to linearize the kinetic equation. The ∇F -term vanishes, since there are no gradients in density and temperature.

Note that \mathcal{L} still acts in (v, ξ) -space. The term with the collision operator acting on the Maxwellian background is important as F has to be transformed from u_{\parallel} to v_{\parallel} as will be discussed below. With a plane-wave ansatz $f_e^{(1)} \sim \exp(ik_{\parallel}z)$ the kinetic equation becomes

$$\frac{\partial f_e^{(1)}}{\partial t} + u \xi' ik_{\parallel} f_e^{(1)} = -\frac{q_e}{m_e} \frac{u}{v_{\text{th},e}^2} \xi' F ik_{\parallel} \psi + \mathcal{L}(F) + \mathcal{L}(f_e^{(1)}) \quad (25)$$

using the representation

$$f_e^{(1)} = \sum_{l=0}^{N_l} f_l(u, t) P_l(\xi') F, \quad (26)$$

where P_l is the l th Legendre polynomial, and the f_l are coefficients of the decomposition which have yet to be determined. One arrives at

$$\sum_l \frac{\partial f_l}{\partial t} P_l F + u \xi' ik_{\parallel} \sum_l f_l P_l F = -\frac{q_e}{m_e} \frac{u}{v_{\text{th},e}^2} \xi' F ik_{\parallel} \psi + \mathcal{L}(F) + \sum_l f_l F \mathcal{L}(P_l), \quad (27)$$

where it still must be specified how the collision operator acts on the Maxwellian. In the p_{\parallel} -formulation F is given as

$$F = \frac{n_0}{(2\pi v_{\text{th},e}^2)^{3/2}} \exp\left(-\frac{u^2}{2v_{\text{th},e}^2}\right) \cong \frac{n_0}{(2\pi v_{\text{th},e}^2)^{3/2}} \exp\left(-\frac{v^2 + 2v\xi(q_e/m_e)A_{\parallel}}{2v_{\text{th},e}^2}\right). \quad (28)$$

Hence,

$$\mathcal{L}(F) = \frac{v}{2} \frac{\partial}{\partial \xi} (1 - \xi^2) \frac{\partial F}{\partial \xi} \cong v \frac{q_e}{m_e} \frac{v \xi}{v_{\text{th},e}^2} A_{\parallel} F \cong v \frac{q_e}{m_e} \frac{u \xi'}{v_{\text{th},e}^2} A_{\parallel} F, \quad (29)$$

where terms quadratic in A_{\parallel} have been neglected. Finally, this transformation of the Maxwellian leads to a correction proportional to the collision frequency and A_{\parallel} , a fact already reported in Ref. [28].

Next, the collision operator acting on the perturbation, $\mathcal{L}(f_e^{(1)})$, is transformed from ξ to ξ' neglecting all non-linear terms in A_{\parallel} and $f_e^{(1)}$. The result has the same form as the original \mathcal{L} but with ξ replaced by ξ' .

In summary, one thus arrives at a linear equation fully acting in (u, ξ') -space.

Eq. (27) is now multiplied by P_l and integrated over the pitch-angle variable ($\xi' \in [-1, 1]$). In this process the orthogonality relations of the Legendre polynomials are used. After some straightforward algebra one finds the final result

$$\frac{\partial f_l}{\partial t} + ik_{\parallel} u \left(\frac{l+1}{2l+3} f_{l+1} + \frac{l}{2l-1} f_{l-1} \right) = v \frac{q_e}{m_e} \frac{u}{v_{\text{th},e}^2} A_{\parallel} \delta_{l,1} - \frac{v}{2} l(l+1) f_l - \frac{q_e}{m_e} ik_{\parallel} \frac{u}{v_{\text{th},e}^2} \left[\phi \delta_{l,1} - \frac{u A_{\parallel}}{3} (\delta_{l,0} + 2\delta_{l,2}) \right]. \quad (30)$$

This is the electromagnetic extension of a very similar equation recently derived in Ref. [22].

The first term on the right-hand side of the above equation is the correction described by Eq. (29), the second and the third term result from the pitch-angle scattering operator and the parallel electric field, respectively.

An expression very similar to Eq. (30) can also be obtained for a simple Krook-type [29] collision operator C . In that particular case the numerical implementation of Eq. (30) and the correctness of its solution could be verified, since the dispersion relation can be solved analytically. It is noteworthy to mention that only in the v_{\parallel} -formulation the Krook operator has the simple $C_{v_{\parallel}} = -v f_e^{(1)}$ form. In the p_{\parallel} -formulation, however, the Krook operator still has to relax the whole distribution function towards a Maxwellian defined with the physical parallel velocity. This gives rise to a (linearized) correction,

$$C_{p_{\parallel}} = -v f_e^{(1)} + v \frac{q_e}{m_e} \frac{u_{\parallel}}{v_{\text{th},e}^2} A_{\parallel} F \quad (31)$$

in the p_{\parallel} -formulation, which is the same as the one associated with the pitch-angle collision operator.

The initial condition for Eq. (30) is chosen as $f_0(t=0) = 1$, $f_l(t=0) = 0$ for $l > 1$, which corresponds to $f_e^{(1)}(t=0) = F$.

The field equations for ϕ and A_{\parallel} in the p_{\parallel} -formulation, using a Padé approximation, are

$$\frac{m_i n_0}{B^2} \frac{k_{\perp}^2}{1 + k_{\perp}^2 \rho_s^2} \phi = q_e n_e, \quad \left(k_{\perp}^2 + \frac{\mu_0 n_e q_e^2}{m_e} \right) A_{\parallel} = \mu_0 j_{\parallel,e}. \quad (32)$$

The second term on the left-hand side of Ampère's law is the skin term only present in the p_{\parallel} -formulation. (Consequently, this term does not appear in Eq. (9).)

In Eq. (30) the variable u is simply a parameter, which will be defined on an equidistant grid in the numerical implementation. To obtain n_e and $j_{\parallel,e}$ integrals over (u, ξ') -space have to be performed. The results are

$$n_e = 4\pi \int du u^2 f_0 F \quad (33)$$

$$j_{\parallel,e} = \frac{4\pi}{3} q_e \int du u^3 f_1 F. \quad (34)$$

3. Case definition

A plasma slab (x, y, z) is simulated, with the magnetic field pointing in the z -direction and periodic boundary conditions applied in the x - and y -directions. EUTERPE was built to work in geometries topologically equivalent to a torus, hence also the slab has to be treated as if it were a torus. In the following, the usual nomenclature for a toroidal system will be used, i.e. (x, y, z) corresponds to the radial, poloidal and toroidal coordinates (r, θ, φ) .

All background quantities, such as temperatures, densities, and the magnetic field are chosen to be constant. The slab has a length $L = 2\pi$ m in z . Its cross-section is quadratic with the length of one side being $\Delta = 1.4$ m. The parallel and the perpendicular wave-vector, expressed through the toroidal and poloidal Fourier numbers n and m and the radial mode number o , are given by

$$k_{\parallel} = \frac{2\pi n}{L} = \frac{n}{100\rho_s} \quad (35)$$

$$k_{\perp}^2 = k_r^2 + k_{\theta}^2 = \frac{4\pi^2}{\Delta^2} (o^2 + m^2) = \frac{4\pi^2}{140^2 \rho_s^2} (o^2 + m^2) \quad (36)$$

with the normalization quantity $\rho_s = 1$ cm ($\rho_s = \sqrt{k_B T_e m_i} / (q_i B)$ denotes the sound gyro-radius). Slightly different kinetic Alfvén waves with a fixed value $n = 1$, but varying in their poloidal mode number m are considered in the numerical simulations. The radial mode number is chosen as $o = 1/2$, because the initial perturbation used in the EUTERPE runs is a half sine-wave in r . Several other parameters of this case are listed in Table 1. If collisions are used, the velocity-independent part of the collision frequency is $\nu_0 = 0.15 \Omega_i$ (with the ion gyration frequency $\Omega_i = q_i B / m_i$).

Table 1

Plasma parameters.	
Magnetic field B/T	1.0
Electron density n_e/m^{-3}	$1.037 \cdot 10^{19}$
Ion density n_i/m^{-3}	n_e
Electron temperature T_e/keV	9.579
Ion temperature T_i/keV	$20 T_e$
Gyration frequency Ω_i/s^{-1}	$9.579 \cdot 10^7$

All EUTERPE calculations are performed using a phase-factor, $\exp(im\theta + in\varphi)$, to extract the dominant poloidal and toroidal Fourier harmonics from all perturbed quantities. The spatial resolution was chosen as $n_r = 16$, $n_{\theta} = 8$, and $n_{\varphi} = 1$ (parallel direction). This leads to a radial resolution of 8.75 cm. This is circa 50 times larger than the electron skin depth $\delta_e = \rho_s \sqrt{2m_e} / (m_i \beta_e)$, which does not need to be resolved in the EUTERPE simulations. (β_e is the electron plasma beta defined as usual.)

For the Legendre approach, $f_e^{(1)}$ is decomposed into the first 20 (40 to obtain Fig. 4) Legendre polynomials. As for the EUTERPE simulations, a fourth-order Runge–Kutta method is used for the time-integration. The time step is $\Delta t \Omega_i = 0.02$ (0.005 to obtain Fig. 4). The integration over u -space is performed on an equidistant grid (400 grid points) with $u_{\text{max}} \approx 9.33 v_{\text{th},e}$ using the trapezoidal rule. All results are converged with respect to those parameters.

4. Results

4.1. Collisional influences on the dispersion relation

In the case of the EUTERPE simulations, the kinetic equation, Eq. (1), is solved by a PIC-method. The equations of motion (see Eqs. (13) and (14)) are advanced in time using a fourth-order Runge–Kutta method. At each time step, the field equations (8) and (16) are solved.

A very similar strategy is pursued for the Legendre approach, where the modified kinetic equation (30) is instead solved together with the field equations given by Eq. (32).

The real frequency ω and the damping rate γ of the mode can be seen in Fig. 1 for $\nu_0 = 0$. Different mode numbers m , corresponding to different $k_{\perp} \rho_s$, have been used to obtain this dispersion relation.

For $k_{\perp} \rho_s \gtrsim 3.5$ Fig. 1 shows frequencies that are larger than the ion cyclotron frequency which contradicts one of the basic assumptions of gyro-kinetics. However, since the focus of this paper is to verify the correctness of the numerical algorithm (and not to validate the physics) the benchmark can be performed in that parameter range to illustrate clearly the effect of collisions (see below).

As can be seen in the figure, the mode is Landau-damped with a maximum damping rate around $k_{\perp} \rho_s \approx 3$. While γ varies over three orders of magnitude, the change in ω is smaller. The dotted line corresponds to the Legendre approach. The full circles have been obtained by EUTERPE. As expected, the agreement between the two different approaches is very good.

Both numerical implementations have also been compared with analytical theory in the collision-less case. For $\nu_0 = 0$ it is straightforward to obtain the analytical dispersion relation

$$1 - \frac{m_i \beta_e}{m_e} \frac{1}{k_{\perp}^2 \rho_s^2} \left\{ \zeta^2 - \frac{m_e}{m_i \beta_e} \left(1 + \frac{T_i}{T_e} k_{\perp}^2 \rho_s^2 \right) \right\} [1 + \zeta Z(\zeta)] = 0 \quad (37)$$

that can be solved for ζ numerically. Here, $\zeta = (\omega + i\gamma) / (\sqrt{2} k_{\parallel} v_{\text{th},e})$ and Z denotes the plasma dispersion function. Both numerical approaches agree very well with Eq. (37) in the collision-less limit.

Having verified EUTERPE and the Legendre approach for $\nu_0 = 0$, a case where collisions are included ($\nu_0 = 0.15 \Omega_i$) may be

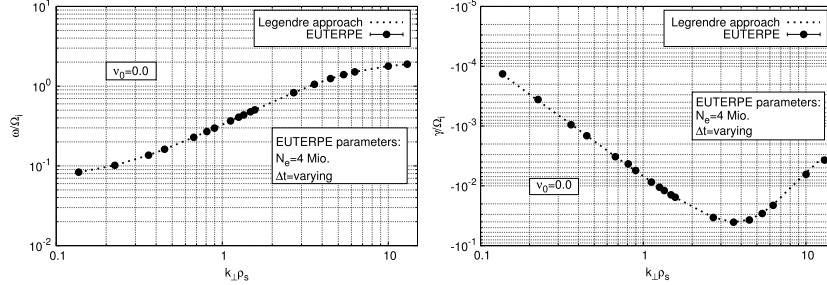


Fig. 1. Real frequency (left) and damping rate (right) of the kinetic Alfvén wave without collisions. EUTERPE and the decomposition of the perturbed electron distribution function into Legendre polynomials ('Legendre approach') yield virtually the same result.

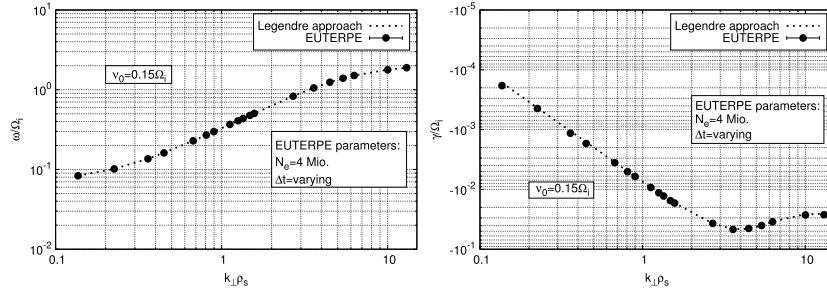


Fig. 2. Real frequency (left) and damping rate (right) of the kinetic Alfvén wave under the influence of collisions. The agreement between EUTERPE and the Legendre approach is still very good. Collisional damping mainly affects large $k_{\perp} \rho_s$. Compared with the case without collisions, the time step had to be reduced for small values of $k_{\perp} \rho_s$.

investigated next. Note that, in particular, the implementation of collisions is very different in the Legendre approach and the PIC-method.

Fig. 2 shows how the dispersion relation changes if collisions are taken into account. While there is no noticeable change in the frequency ω , the damping rate is modified substantially. γ is now a combination of pure Landau damping and collisional damping. In comparison with Fig. 1, the mode is a little bit stronger damped due to collisional damping for small $k_{\perp} \rho_s$. The largest differences, however, are seen at high $k_{\perp} \rho_s > 4$, where the mode is now much stronger damped than before. Pitch-angle collisions randomize the velocity distribution to a certain degree and thus have a smoothing effect on the perturbations. It is thus not surprising that the collisions have a larger effect on the small scales, i.e. high $k_{\perp} \rho_s$. Again, the agreement between the Legendre approach (dotted line) and EUTERPE (full circles) is very good for all values of $k_{\perp} \rho_s$.

It usually takes several collision times until the effects of collisions become apparent in a numerical simulation. Thus, a relatively high ν_0 was chosen. This leads to a short collision time $\tau_{\text{coll}} = 1/\nu_0$ and therefore to a reduced over-all time span required to be simulated.

A numerical study showing the effect of increasing collision frequency ν_0 on the damping rate is presented in Fig. 3. This has been done for a fixed mode number $m = 290$, which corresponds to $k_{\perp} \rho_s = 13$. Whereas the frequency stays roughly the same for different collision frequencies, the damping rate increases linearly with rising ν_0 . This is the expected behaviour as the collision operator \mathcal{L} also scales linearly with ν_0 .

Apart from the influence on the damping rate of the kinetic Alfvén wave, the effect of collisions becomes most apparent when investigating the perturbed distribution function $f_e^{(1)}$ in velocity-space (u, ξ') . Fig. 4 shows the results obtained by the Legendre

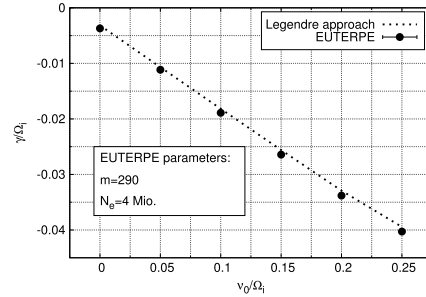


Fig. 3. Influence of an increasing collision frequency on the damping rate of the kinetic Alfvén wave. While the frequency (not shown) stays almost the same, the damping rate scales linearly with ν_0 .

approach. For this particular case the mode number $m = 25$ has been used, corresponding to an intermediate $k_{\perp} \rho_s \approx 1.12$. In Fig. 4, $f_e^{(1)}$ is plotted at different times in the simulation without (left-hand side) and with (right-hand side) collisions. In all diagrams the resonance condition

$$\omega - u_{\parallel} k_{\parallel} = 0 \quad (38)$$

is indicated as a solid black line using the ω obtained from the simulation.

Starting from the same initial condition, which is a Maxwellian and therefore isotropic in ξ' , it can be seen that collisions have a strong effect on the structure of $f_e^{(1)}$. Without collisions the

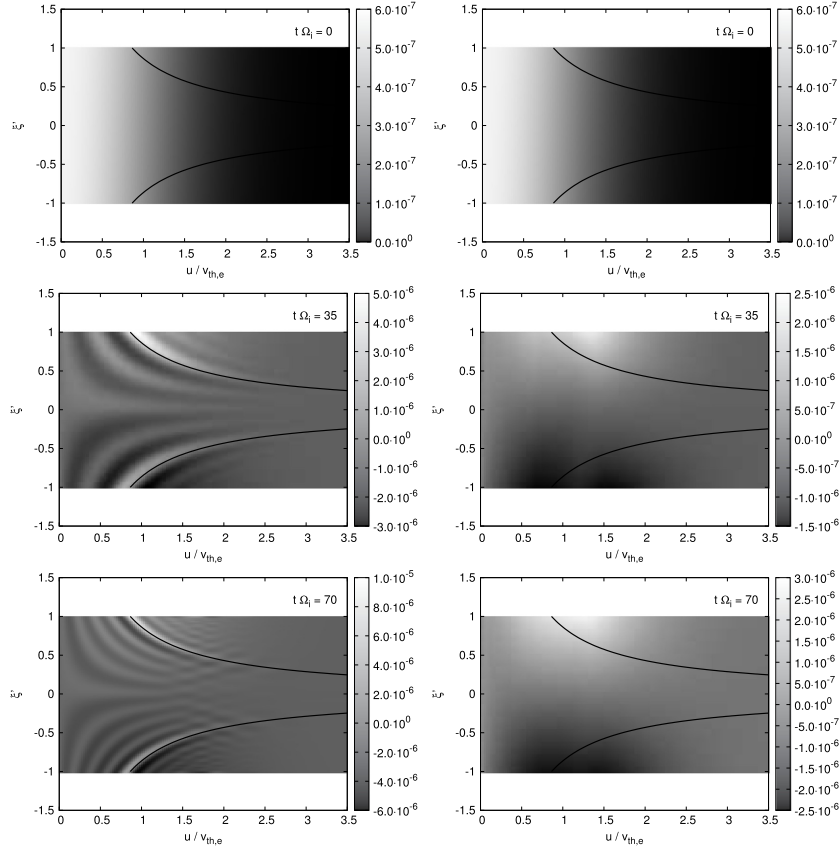


Fig. 4. The perturbed distribution function (at $k_{\perp}z = \pi/4$) in velocity-space at different simulation times. Collisions are included only on the right-hand side. While $f_e^{(1)}$ peaks around the resonant velocities (black line) without collisions, velocity-space becomes more isotropic in ξ' for the case including collisions. All solutions for $f_e^{(1)}$ were obtained by the Legendre approach.

perturbed distribution function becomes highly non-isotropic in pitch-angle. $f_e^{(1)}$ peaks around those velocities fulfilling Eq. (38), as expected. As time progresses, the structures in velocity-space become even finer.

When collisions are included, the velocity-space becomes more isotropic with respect to ξ' for $t\Omega_i \geq 35$. The strong peaking of $f_e^{(1)}$ around the resonant velocities has almost vanished, but the perturbed distribution function is still localized in the vicinity of the resonances. The small scales in velocity-space are effectively damped. Furthermore, the shape of $f_e^{(1)}$ in velocity space seems to have quickly reached a nearly converged state, nevertheless the amplitude is growing slightly (less than in the collision-less case) between $t\Omega_i = 35$ and $t\Omega_i = 70$.

Another feature of collisions is related to the long-time behaviour of $f_e^{(1)}$. Without collisions, the perturbed part of the distribution function never vanishes. The damping of the potentials ϕ and A_{\parallel} comes from the integration over velocity-space in combination with the developing fine-scale structure. Pitch-angle collisions, on the other hand, have the property of relaxing the distribution function towards a Maxwellian in this linear problem.

Hence (because of the splitting $f_e = F + f_e^{(1)}$) applied to the distribution function, $f_e^{(1)}$ has to vanish for $t \rightarrow \infty$.

It was observed in long-time simulations (about five times longer than the longest time shown in Fig. 4) that $f_e^{(1)}$ integrated over all velocities (using the L^2 -norm) saturates at a finite value in the collision-less case, but vanishes if collisions are included.

4.2. Convergence studies

4.2.1. Convergence study for Δt and small $k_{\perp}\rho_s$

As can be seen in Figs. 1 and 2, the frequency of the mode increases with rising values of $k_{\perp}\rho_s$. In order to fully resolve the ever-faster oscillatory behaviour, the time step had to be decreased with increasing values of the poloidal mode number m . Fig. 1 confirms that the time steps were chosen well for the cases without collisions. With collisions, however, Δt had to be chosen smaller at low values of $k_{\perp}\rho_s$ (at high values of $k_{\perp}\rho_s$ the time step was already small enough). This is due to the fact that, when collisions are included in the EUTERPE simulations, a stochastic scheme is chosen. As this scheme only has a weak convergence of order one

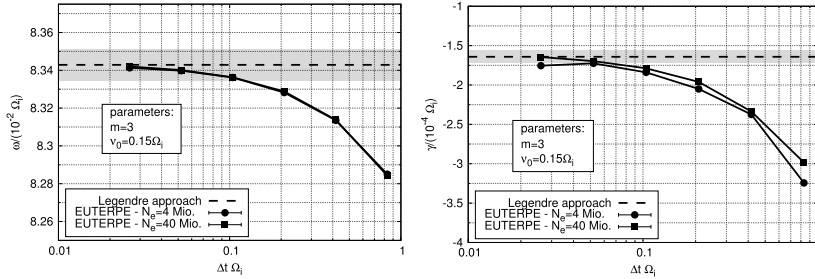


Fig. 5. Convergence of the real frequency (left) and of the damping rate (right) determined by EUTERPE with decreasing time step under the influence of collisions. The grey region on the left-hand side corresponds to an uncertainty level of 0.1%. Since it is more difficult to resolve the damping rate, the grey region indicates 5% uncertainty on the right-hand side. Since increasing the particle number by a factor of 10 leads to nearly the same behaviour, the convergence seems to be bound by Δt . The convergence with respect to Δt is of first order.

(in Δt) and is thus less accurate than the fourth-order Runge–Kutta, a smaller time step needs to be chosen.

A convergence scan with respect to the time step Δt was performed for the EUTERPE calculation including collisions at $m = 3$ ($k_{\perp} \rho_s \approx 0.14$). Fig. 5 shows the results. Using the same time step $\Delta t \Omega_i \approx 0.83$ with and without collisions does not lead to accurate results for ω and γ in the collisional case: The damping rate is for instance wrong by a factor of two. This is due to the aforementioned change in the time-integrator from a fourth-order Runge–Kutta to a first-order stochastic method. Note that for this small value of $k_{\perp} \rho_s$ collisions have nearly no influence on ω and γ (see Fig. 2), but they still determine the time step.

However, Fig. 5 also shows how EUTERPE converges to the result obtained by the Legendre approach with decreasing values of Δt . Thus, when including collisions into the simulations, it should be carefully checked if the result is converged with respect to the time step. Especially since the numerical error of the integration scheme increases that drastically.

4.2.2. Convergence study for N_e and high $k_{\perp} \rho_s$

Figs. 2 and 3 nicely demonstrate the correct implementation of collisions in the electromagnetic version of EUTERPE. However, to obtain the results presented in Fig. 2 rather high particle numbers have been chosen in order to ensure numerically converged results. Now, a convergence study (for the last point of Fig. 2 at $k_{\perp} \rho_s = 13$, $m = 290$) has been conducted with the aim to reduce the required particle number. Fig. 6 summarizes the results.

It can be seen that particle numbers greater than 4 million are not necessary for an accurate determination of ω and γ . Reducing the particle number by a factor of 2 to 2 million still gives a frequency that is approximately only 0.2% ($\approx 5\%$ for γ) off compared with the Legendre approach. For particle numbers greater than 2 million the agreement between both approaches is very good. This is even less than the 4 million numerical marker particles used in the case without collisions (Fig. 1). This hints on the fact that not the optimum particle number may have been used in that case.

Seeing how on the left-hand side of Fig. 6 nearly all points scatter around the 0.1% uncertainty interval emphasizes again that the frequency is more robust than the damping rate for this case.

4.3. Comparison of p_{\parallel} - and v_{\parallel} -formulation

All the EUTERPE results have been obtained using the PT-scheme. For the second strategy presented in this paper, using the Legendre approach to solve the kinetic equation, the p_{\parallel} -formalism has been used exclusively so far. This avoids the numerically difficult $\partial A_{\parallel} / \partial t$ -term inherent to the v_{\parallel} -formulation, but requires the introduction of a correction resulting from $\mathcal{L}(F)$.

It is not required to change the collision operator (given in v_{\parallel}) directly, because all corrections are non-linear in the perturbations and therefore negligible.

When comparing the results obtained with the Legendre approach with the EUTERPE results it should be pointed out that the collision step in EUTERPE is performed while being in the v_{\parallel} -frame. It is therefore worthwhile to examine what happens to the Legendre approach when going from p_{\parallel} to v_{\parallel} .

This transition requires the \dot{u}_{\parallel} equation to be replaced by

$$\dot{v}_{\parallel} = -\frac{q_e}{m_e} \left(\nabla_{\parallel} \phi + \frac{\partial A_{\parallel}}{\partial t} \right). \quad (39)$$

Consequently, the skin term in Ampère's law and $\mathcal{L}(F)$ do no longer appear. Hence, in the kinetic equation only the A_{\parallel} -terms change and Eq. (30) must be transformed to

$$\begin{aligned} \frac{\partial}{\partial t} \left(f_1 + \frac{q_e}{m_e} \frac{v}{v_{\text{th},e}^2} A_{\parallel} \delta_{l,1} \right) + ik_{\parallel} v \left(\frac{l+1}{2l+3} f_{l+1} + \frac{l}{2l-1} f_{l-1} \right) \\ = -\frac{v}{2} l(l+1) f_1 - \frac{q_e}{m_e} ik_{\parallel} \frac{v}{v_{\text{th},e}^2} \phi \delta_{l,1}. \end{aligned} \quad (40)$$

Contrary to the p_{\parallel} -formulation, f_1 is now integrated together with the vector potential, i.e.

$$\tilde{f}_1 = f_1 + \frac{q_e}{m_e} \frac{v}{v_{\text{th},e}^2} A_{\parallel} \quad (41)$$

and after each Runge–Kutta sub-step f_1 is computed from \tilde{f}_1 using the A_{\parallel} from the previous step. This emphasizes that the v_{\parallel} -formulation is numerically indeed more challenging.

In Fig. 7 it is shown that also for electromagnetic simulations including collisions the agreement between the p_{\parallel} - (dotted line) and v_{\parallel} -implementation (full circles) is very good. However, this comparison could only be carried out for three data points with high mode numbers, because the integration scheme became numerically unstable in v_{\parallel} for smaller values of $k_{\perp} \rho_s$. Using an implicit scheme for the time integration might prevent the numerical instability.

5. Summary and conclusions

The applicability of the pullback transformation scheme [12,13] to an electromagnetic system influenced by electron pitch-angle collisions has been investigated using the gyro-kinetic PIC code EUTERPE. For comparison, a decomposition of the perturbed electron distribution function into Legendre polynomials was used as a second strategy to solve the equations.

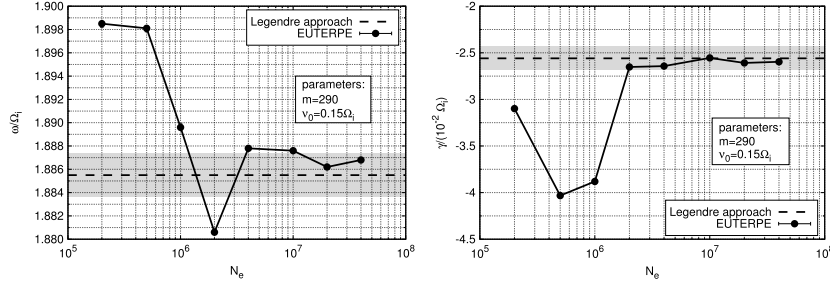


Fig. 6. Convergence of the real frequency (left) and of the damping rate (right) with increasing number of electron markers in EUTERPE. Collisions are present. The uncertainty levels are the same as in Fig. 5.

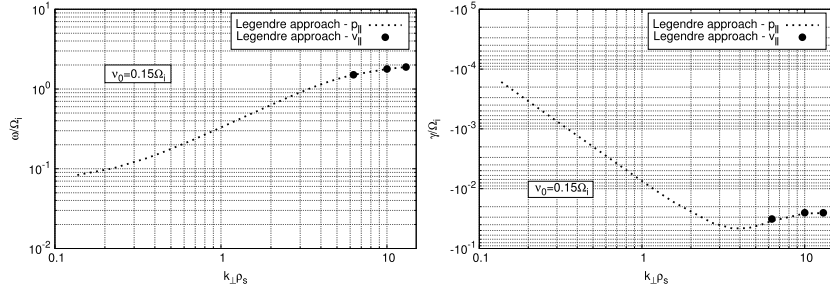


Fig. 7. Comparison of the $p_{||}$ - and $v_{||}$ -formulation of the equations. Good agreement is found for values of $k_{||}\rho_s$ for which the $v_{||}$ -formulation was numerically stable.

The widely used $p_{||}$ -approach has the drawback that the collisional and non-collisional parts of the kinetic equation operate in different coordinates. This is counter-intuitive and necessitates the introduction of a correction term. On the other hand, the PT-scheme, apart from its other advantages, operates in $v_{||}$ -space. Here we showed by comparing the PIC and the Legendre approach that this scheme is a natural choice for including collisional effects in electromagnetic PIC simulations and is compatible with a two-weight scheme.

After the successful benchmark between EUTERPE and the Legendre approach the effects of collisions on $f_e^{(1)}$ were studied in greater detail. It was found that because of collisions, the velocity-space becomes much more isotropic with respect to the pitch-angle. $f_e^{(1)}$ is completely different with and without collisions, which might be the reason why perturbative theories on this topic are scarce.

All simulations have been performed in slab geometry in order to concentrate on the essential properties of the numerical scheme. The parameters of this case were chosen in a way to facilitate a straightforward comparison between EUTERPE and the Legendre approach with the focus of the benchmark being on verification rather than on validation.

The convergence scans showed that, when collisions are included, choosing a small time step is more important than having a high particle number. This could easily be understood as the integration scheme changes from a fourth-order Runge–Kutta to a first-order (weak convergence) stochastic scheme. For more complex systems with higher constraints on the time step, it could be worthwhile to test stochastic integrators of higher order.

For simplicity, only results excluding the ion dynamics have been presented in this paper. A fully kinetic extension is straightforward.

The consequent next steps would be performing simulations in more interesting parameter regimes and in more realistic geometries, e.g. in tokamaks or stellarators. Moreover, since only electron–electron pitch-angle collisions were considered so far, the collision operator should be extended accordingly.

Acknowledgements

The authors gratefully acknowledge helpful discussions with Per Helander and Alessandro Zocco.

A part of this work was carried out using the HELIOS supercomputer system at the Computational Simulation Centre of International Fusion Energy Research Centre (IFERC–CSC), Aomori, Japan, under the Broader Approach collaboration between Euratom and Japan, implemented by Fusion for Energy and JAEA.

This work has been carried out within the framework of the EUROfusion Consortium and has received funding from the Euratom research and training programme 2014–2018 under Grant Agreement No. 633053. The views and opinions expressed herein do not necessarily reflect those of the European Commission.

References

- [1] H.L. Berk, B.N. Breizman, H. Ye, *Phys. Rev. Lett.* 68 (1992) 3563.
- [2] J. Lang, G.Y. Fu, Y. Chen, *Phys. Plasmas* 17 (2010) 042309.
- [3] A. Bierwage, Y. Todo, N. Aiba, K. Shinohara, *Nucl. Fusion* 54 (2014) 104001.
- [4] Y. Todo, M.A. Van Zeeland, A. Bierwage, W.W. Heidbrink, *Nucl. Fusion* 54 (2014) 104012.
- [5] N.N. Gorelenkov, S.E. Sharapov, *Phys. Scr.* 45 (1992) 163.
- [6] G.Y. Fu, C.Z. Cheng, K.L. Wong, *Phys. Fluids B* 5 (1993) 4040.
- [7] A.J. Brizard, T.S. Hahm, *Rev. Modern Phys.* 79 (2007) 421.
- [8] J.V.W. Reynders, *Cyroknetic Simulations of Finite- β Plasmas on Parallel Architectures* (Ph.D. thesis), Princeton University, 1992.
- [9] T.S. Hahm, W.W. Lee, A. Brizard, *Phys. Fluids* 31 (1988) 1940.

- [10] Y. Chen, S.E. Parker, J. Comput. Phys. 189 (2003) 463.
- [11] R. Hatzky, A. Könies, A. Mishchenko, J. Comput. Phys. 225 (2007) 568.
- [12] A. Mishchenko, A. Könies, R. Kleiber, M. Cole, Phys. Plasmas 21 (2014) 092110.
- [13] R. Kleiber, R. Hatzky, A. Könies, A. Mishchenko, E. Sonnendrücker, Phys. Plasmas 23 (2016) 032501.
- [14] E. Sonnendrücker, A. Wachter, R. Hatzky, R. Kleiber, J. Comput. Phys. 295 (2015) 402.
- [15] K. Kauffmann, R. Kleiber, R. Hatzky, M. Borchardt, J. Phys. Conf. Ser. 260 (2010) 012014.
- [16] J.M. García-Regaña, R. Kleiber, C.D. Beidler, H. Maaßberg, P. Helander, Y. Turkin, Plasma Phys. Control. Fusion 55 (2013) 074008.
- [17] J.M. García-Regaña, C.D. Beidler, R. Kleiber, P. Helander, A. Mollén, J.A. Alonso, M. Landreman, H. Maaßberg, H.M. Smith, Y. Turkin, L. Velasco, Nucl. Fusion 57 (2017) 056004.
- [18] A. Mishchenko, M. Borchardt, M. Cole, R. Hatzky, T. Fehér, R. Kleiber, A. Könies, A. Zocco, Nucl. Fusion 55 (2015) 053006.
- [19] D.J. Thuecks, C.A. Kletzing, F. Skiff, S.R. Bounds, S. Vincena, Phys. Plasmas 16 (2009) 052110.
- [20] E. Hirvijoki, A. Brizard, A. Snicker, T. Kurki-Suonio, Phys. Plasmas 20 (2013) 092505.
- [21] P. Helander, D.J. Sigmar, Cambridge University Press, 2002.
- [22] J.W. Banks, S. Brunner, R.L. Berger, T.M. Tran, Vlasov Simulations of Electron-Ion Collision Effects on Damping of Electron Plasma Waves, 2016. <http://www.arxiv.org/abs/1601.01002>.
- [23] K. Kauffmann, Including Collisions in Gyrokinetic Tokamak and Stellarator Simulations (Ph.D. thesis), Ernst-Moritz-Arndt-Universität Greifswald, 2011.
- [24] S. Brunner, E. Valeo, J.A. Krommes, Phys. Plasmas 6 (1999) 4504.
- [25] T. Vernay, Numerical Study of Electron-Ion Collision Effects on Trapped Electron Modes with the Gyrokinetic Code ORB5 (M.Sc. thesis), École Polytechnique Fédérale de Lausanne, 2008.
- [26] T. Takizuka, H. Abe, J. Comput. Phys. 25 (1977) 205.
- [27] P.E. Kloeden, E. Platen, Springer, 1999.
- [28] W. Wan, Y. Chen, S.E. Parker, Phys. Plasmas 12 (2005) 012311.
- [29] P.L. Bhatnagar, E.P. Gross, M. Krook, Phys. Rev. Lett. 94 (1954) 511–525.

Appendix A. Thesis articles

Effects of collisions on the saturation dynamics of TAEs in tokamaks and stellarators (A.2)

Full citation:

C. Slaby, A. Könies, R. Kleiber, and J. M. García-Regaña. Effects of collisions on the saturation dynamics of TAEs in tokamaks and stellarators. *Nuclear Fusion*, **58** (8) 082018 (2018).

DOI:

10.1088/1741-4326/aaaed3 (<https://doi.org/10.1088/1741-4326/aaaed3>)

Reproduced with the permission of the IAEA and EUROfusion.

Appendix A. Thesis articles

Effects of collisions on the saturation dynamics of TAEs in tokamaks and stellarators

Christoph Slaby¹, Axel Könies¹, Ralf Kleiber¹ and José Manuel García-Regaña²

¹ Max-Planck-Institut für Plasmaphysik, Wendelsteinstraße 1, 17491 Greifswald, Germany

² Laboratorio Nacional de Fusión Ciemat, Av. Complutense 40, 28040 Madrid, Spain

E-mail: christoph.slaby@ipp.mpg.de

Received 4 December 2017, revised 31 January 2018

Accepted for publication 13 February 2018

Published 29 June 2018



CrossMark

Abstract

The non-linear saturation dynamics of TAEs (toroidicity-induced Alfvén eigenmodes) is investigated numerically in tokamaks and stellarators. Special attention is given to the influence that pitch-angle collisions among the fast ions have in the non-linear regime.

For this investigation a perturbative model is used. We employ the 3D ideal reduced MHD eigenvalue code CKA to obtain the mode frequency and mode structure. This information is given to the non-linear gyro-kinetic particle-in-cell code EUTERPE, which calculates the growth rate of the mode and the temporal evolution of the mode amplitude. The mode structure remains fixed for the entire calculation.

In the tokamak, analytical predictions regarding the transition from periodic non-linear behaviour to a steady-state solution and the scaling of the saturated amplitude are available. Both are influenced by collisions. The numerical results are in agreement with the theoretical predictions within the validity range of the theory (Berk *et al* 1992 *Phys. Rev. Lett.* **68** 3563). Beyond the validity range of the theory different scaling laws are found numerically.

We show that using a momentum-conserving collision operator does not change the scaling significantly for small ν , but is important for high collision frequencies.

The stellarator case, a Wendelstein 7-X high-mirror configuration, shows some differences when compared with the tokamak. Most notably, the saturated perturbed magnetic field becomes a non-monotonic function of ν .

Keywords: non-linear simulations, pitch-angle collisions, shear Alfvén waves, tokamak, stellarator

(Some figures may appear in colour only in the online journal)

1. Introduction

In fusion devices, present-day experiments or future fusion reactors, there typically exists a supra-thermal population of fast ions. Today, these particles are created mainly by heating methods, such as neutral beam injection (NBI) or ion cyclotron resonance heating (ICRH). In future fusion reactors also self-generated alpha particles (coming from the fusion reaction) will be present. The fast ions are supposed to be confined for a time of the order of the slowing-down time (the time

it takes the fast particles to thermalize) in order to heat the plasma. However, the resonant interaction of fast ions with shear Alfvén modes can lead to their destabilization [11, 25] and to increased fast-ion transport with potentially dangerous consequences for plasma-facing components [7, 35]. Typical Alfvén eigenmodes excited in tokamaks are toroidicity-induced Alfvén eigenmodes (TAEs), beta-induced Alfvén eigenmodes (BAEs), or—at high fast-particle pressures—energetic-particle modes (EPMs). Because of the more complex geometry of stellarators, other classes of modes, e.g.

helicity-induced Alfvén eigenmodes (HAEs), can be destabilized in these devices.

In order to predict transport-induced losses, the non-linear saturation levels of Alfvén eigenmodes (AEs) need to be computed. This paper investigates TAEs as an example for the zoo of AEs in general. For tokamaks, it has been shown analytically [2, 3] and numerically [20] that the saturation amplitude is influenced by particle collisions. Recently, the influence of pitch-angle collisions on the saturation level of TAEs in NSTX [9] has been investigated [37].

In TJ-II the non-linear dynamics of Alfvén modes, in particular the transition between chirping and steady state, was recently investigated experimentally [22, 23]. It was found that the magnetic configuration plays a larger role for the transition than collisions. Large-scale numerical simulations, aimed at numerically reproducing bursts of AEs observed in the LHD experiment, have also been performed recently [30]. There, collisions are needed to restore the fast-ion gradient after it has been flattened by an AE burst. They are needed to accurately reproduce experimental measurements.

This paper reports on a systematic numerical study of the non-linear dynamics of TAEs in the saturated phase for various collision frequencies. The simulations are carried out for a tokamak and for a stellarator case. We use a well-established benchmark case devised for tokamaks to compare our numerical results to a theoretically predicted scaling law. The purpose of the tokamak case is two-fold: Firstly, it will serve as a benchmark for our numerical implementation in the parameter range where the analytical theory can be applied. Secondly, the effect of pitch-angle collisions on the saturation dynamics can be studied in other parameter regimes. We find, in particular, that the analytical theory is only applicable in the so-called resonance detuning regime and for low enough collision frequencies.

The numerical model can then be applied to stellarators. As an example, we use the optimized stellarator Wendelstein 7-X (W7-X)—the largest and most sophisticated stellarator in the world [24]. In part, this case is chosen to illustrate the capability of CKA-EUTERPE (described below) to also treat real geometries and realistic plasmas. One of the optimization goals of W7-X is good confinement of fast particles, in particular at high beta (plasma pressure divided by magnetic pressure). The NBI and ICRH systems are currently being installed at W7-X and will be ready for future experimental campaigns. Thus, now is a natural time to confirm the predictive capabilities of our numerical tools.

We use the CKA-EUTERPE code for our numerical simulations. It combines the eigenvalue code CKA (Code for Kinetic Alfvén waves) with the gyro-kinetic particle-in-cell (PIC) code EUTERPE. The coupling of the two codes is perturbative in the sense that an MHD mode is calculated by CKA and then passed to EUTERPE which calculates the motion of fast ions in the pre-calculated field and their power transfer to the mode. Knowing this, the amplitude of the mode can be advanced in time. The mode structure remains fixed throughout the simulation. It is well known that the MHD mode structure may react to the kinetic influence of the fast particles (see e.g. [28, 34]). Furthermore, the linear mode

structure can change in the non-linear phase since it may react to changes of the fast-particle drive [36]. Such effects are not included in the CKA-EUTERPE model. Fully gyro-kinetic simulations, that allow for mode structure variations, would provide a solution to the problem, but suffer from the fact that they are numerically very challenging and expensive. At the moment, they are not suited for parameter scans.

Being a PIC code, EUTERPE is very well suited to compute the collisions between the fast ions. The implementation of collisions into the electromagnetic version of EUTERPE has been benchmarked recently [27]. This reference also serves as a brief introduction to the EUTERPE code. We use a pitch-angle scattering operator acting on the fast-ion distribution function to capture the influence of collisions on the non-linear dynamics (spatial diffusion is neglected). Furthermore, we can choose whether or not the collision operator should conserve momentum. The analytical scaling laws were derived without taking momentum conservation into account. It will be investigated to what extent the inclusion of a momentum-conserving collision operator affects the scaling laws.

This paper is organized as follows. In section 2 we recapitulate the analytical theory available and briefly introduce the numerical scheme used by CKA-EUTERPE. Section 3 reports on our results for the tokamak case and for the stellarator case, respectively. Finally, conclusions are drawn in section 4.

2. Theory and algorithms

To compute the various aspects of (collisional) fast particles interacting with TAEs, the CKA-EUTERPE [10] code package is used. The eigenvalue code CKA [8] computes the real frequency and eigenmode structure of the TAE in the framework of ideal (zero resistivity) magneto-hydrodynamic (MHD) theory. This information is then given to the EUTERPE code which follows numerical marker particles and computes the power transfer from the fast ions to the mode. The wave-particle power transfer is used to calculate a (time-dependent) growth rate γ , which determines the time evolution of the electromagnetic potentials. Throughout the calculations, the spatial shape of the mode structure remains fixed. Only the complex amplitude is affected by the resonant interaction with the fast particles. In this sense, CKA-EUTERPE is a perturbative model that cannot capture non-linear mode structure modifications. However, this also means that no field equations for the potentials need to be solved, which accounts for the higher speed and the enhanced robustness of CKA-EUTERPE compared with fluid or fully gyro-kinetic approaches.

The individual codes are briefly described in the following sections. A more elaborate discussion can be found in [8, 16] and [15, 19] for CKA and for EUTERPE, respectively.

2.1. The CKA code

CKA (Code for Kinetic Alfvén waves) [8] is a 3D eigenvalue code solving the ideal and reduced MHD equations. It uses a B-spline discretization in all three directions (PEST coordinates), a phase factor to extract the dominant Fourier

harmonic, and the electrostatic potential is expressed as $\phi(\mathbf{r}, t) = \phi(\mathbf{r}) \exp(i\omega t)$ (ω is the frequency of the mode). The code solves an eigenvalue equation

$$\omega^2 D_2 \phi = D_1 \phi \quad (1)$$

where D_1 and D_2 are linear differential operators defined as [10]

$$D_2 \phi = \nabla \cdot \left(\frac{1}{v_A^2} \nabla_{\perp} \phi \right) + \nabla_{\perp}^2 \left[\frac{1}{v_A^2} \left(\frac{3}{4} \rho_i^2 + \rho_s^2 \right) \nabla_{\perp}^2 \phi \right] \quad (2)$$

$$D_1 \phi = \nabla \cdot \left\{ \mathbf{b} \nabla_{\perp}^2 \left[\left(1 - \frac{\mu_0 p^{(0)}}{B^2} \right) \mathbf{b} \cdot \nabla \phi \right] \right\} + \nabla \cdot \left\{ \mathbf{b} \times \boldsymbol{\kappa} \frac{2\mu_0 \mathbf{b} \times \nabla p^{(0)}}{B^2} \cdot \nabla \phi \right\} - \nabla \cdot \left\{ \frac{\mu_0 j_{\parallel}^{(0)}}{B} [\nabla \times (\mathbf{b} \cdot \nabla \phi)]_{\perp} \right\}. \quad (3)$$

The notation is conventional: $v_A = B/\sqrt{\mu_0 n_i m_i}$ denotes the Alfvén speed of the background plasma (characterized by density n_i and ion mass m_i). \mathbf{B} is the magnetic field with magnitude B and direction \mathbf{b} . The subscripts \parallel and \perp are used to denote vector components parallel and perpendicular to the background magnetic field, respectively. μ_0 is the vacuum permeability. $\rho_i = \sqrt{k_B T_i m_i}/(q_i B)$ and $\rho_s = \sqrt{k_B T_e m_i}/(q_i B)$ denote the ion gyro-radius and the sound gyro-radius, respectively. T and k_B are the temperature and Boltzmann's constant, respectively. The charge of a bulk-ion is denoted by q_i . The equilibrium pressure and current density are labeled as $p^{(0)}$ and $j_{\parallel}^{(0)}$, respectively. $\boldsymbol{\kappa} = (\nabla \times \mathbf{b}) \times \mathbf{b}$ denotes the curvature of the magnetic field lines.

After equation (1) has been solved for ϕ , the condition $E_{\parallel} = 0$ can be used to easily obtain the parallel component of the vector potential

$$A_{\parallel} = \frac{i}{\omega} \mathbf{b} \cdot \nabla \phi. \quad (4)$$

The solutions ϕ and A_{\parallel} together with ω are then passed to EUTERPE to calculate the growth rate of the mode in the presence of energetic particles.

2.2. The EUTERPE code

EUTERPE, a global non-linear delta-f particle-in-cell code suited for 3D geometries, solves the gyro-kinetic equation

$$\frac{\partial f_s}{\partial t} + \dot{\mathbf{R}} \cdot \nabla f_s + \dot{v}_{\parallel} \frac{\partial f_s}{\partial v_{\parallel}} + \dot{\mu} \frac{\partial f_s}{\partial \mu} = \mathcal{C}(f_s) \quad (5)$$

of a distribution function f_s for species s . μ denotes the specific magnetic moment, $\mu = v_{\perp}^2/(2B)$ and $\mathcal{C}(f_s)$ is a collision operator that will be specified later. Equation (5) is solved together with field equations for the potentials, where particle and current density are calculated by taking moments of the distribution function.

In CKA-EUTERPE, however, typically only one fast-ion species is simulated ($s = \text{fast}$). Therefore, the species index will be omitted for the remainder of the paper, except where needed to avoid confusion.

The equations of motion (characteristics of equation (5)) are solved in the so-called v_{\parallel} -formulation in the absence of collisions:

$$\dot{\mathbf{R}} = v_{\parallel} \mathbf{b} + \frac{m}{q} \left[\frac{\mu B + v_{\parallel}^2}{BB_{\parallel}^*} \mathbf{b} \times \nabla B + \frac{v_{\parallel}^2}{BB_{\parallel}^*} (\nabla \times \mathbf{B})_{\perp} \right] + \frac{v_{\parallel}}{BB_{\parallel}^*} [\mathbf{b} \times \nabla B + (\nabla \times \mathbf{B})_{\perp}] \langle A_{\parallel} \rangle + \frac{1}{B_{\parallel}^*} \mathbf{b} \times \nabla \langle \psi \rangle \quad (6)$$

$$\dot{v}_{\parallel} = -\mu \nabla B \cdot \left[\mathbf{b} + \frac{m}{q} \frac{v_{\parallel}}{BB_{\parallel}^*} (\nabla \times \mathbf{B})_{\perp} \right] - \frac{v_{\parallel}}{BB_{\parallel}^*} [\mathbf{b} \times \nabla B + (\nabla \times \mathbf{B})_{\perp}] \cdot \nabla \langle \phi \rangle - \frac{\mu}{B_{\parallel}^*} \left[\mathbf{b} \times \nabla B \cdot \nabla \langle A_{\parallel} \rangle + \frac{1}{B} \nabla B \cdot (\nabla \times \mathbf{B})_{\perp} \langle A_{\parallel} \rangle \right] \quad (7)$$

$$\dot{\mu} = 0 \quad (8)$$

with

$$\psi = \phi - v_{\parallel} A_{\parallel} \quad (9)$$

$$B_{\parallel}^* = B + \left[\frac{m}{q} v_{\parallel} + \langle A_{\parallel} \rangle \right] \mathbf{b} \cdot \nabla \times \mathbf{b}. \quad (10)$$

$\langle \dots \rangle$ denotes the gyro-average. The ideal Ohm's law

$$\frac{\partial \langle A_{\parallel} \rangle}{\partial t} + \mathbf{b} \cdot \nabla \langle \phi \rangle = 0 \quad (11)$$

has been used to eliminate the partial time derivative of the vector potential in the equation for \dot{v}_{\parallel} . Equations (6)–(8) are the full equations of motion with all non-linearities retained. Note that the structure of the potentials (ϕ and A_{\parallel}) is pre-calculated by CKA. Therefore, no field equations need to be solved. Instead, the amplitude equations

$$\frac{\partial \hat{\phi}(t)}{\partial t} = i\omega (\hat{A}_{\parallel} - \hat{\phi}) + 2(\gamma(t) - \gamma_d) \hat{\phi} \quad (12)$$

$$\frac{\partial \hat{A}_{\parallel}(t)}{\partial t} = i\omega (\hat{\phi} - \hat{A}_{\parallel}) \quad (13)$$

describe the temporal evolution of the potentials. $\hat{\phi}$ denotes a complex amplitude. The amplitude equations come from taking the time derivative of the quasi-neutrality condition, where the bulk plasma is described using the ideal and reduced MHD equations. The fast ions are treated gyro-kinetically. Furthermore, the ansatz $\phi(\mathbf{r}, t) = \hat{\phi}(t) \phi_0(\mathbf{r}) \exp(i\omega t)$ (and similar for A_{\parallel} and the pressure) has been used. Averaging over the fast oscillation of the mode (with frequency ω) yields equations (12) and (13) for the complex amplitudes that evolve on a much longer time scale. The details of the derivation are described in [8, 16]. Note that the amplitude

equation for $\hat{\phi}$ includes an ad-hoc damping rate γ_d used to summarize the various damping mechanisms that would be present in a fully gyro-kinetic simulation. The time-dependent growth rate $\gamma(t) = T(t)/(2W)$ is calculated from the wave-particle power transfer ($f^{(1)}$ denotes the perturbed part of the distribution function.)

$$T(t) = - \int d^3r \int d\Gamma B_{\parallel}^2 \left[\frac{m}{ZeB} \mathbf{b} \times (v_{\parallel}^2 \boldsymbol{\kappa} + \mu \nabla B) \cdot (Ze \nabla_{\perp} \phi^*(\mathbf{r}, t) f^{(1)}) \right] \quad (14)$$

and divided by the wave energy

$$W = \int d^3r \frac{\rho_{i+f}}{B^2} |\nabla_{\perp} \phi|^2. \quad (15)$$

2.3. Treatment of collisions

EUTERPE offers the possibility of including a collision operator on the right-hand side of the kinetic equation (5). Here, we study the influence of pitch-angle collisions on the saturation dynamics. Therefore, the (test-particle) collision operator is given as

$$\mathcal{C}_{\text{fp}} = \frac{\nu}{2} \frac{\partial}{\partial \xi} (1 - \xi^2) \frac{\partial}{\partial \xi} \quad (16)$$

with $\xi = v_{\parallel}/v$ being the pitch-angle variable. This collision operator is obtained by transforming the full Fokker–Planck operator to guiding-center coordinates and neglecting energy and guiding-center diffusion, as illustrated in e.g. [13]. The collision frequency ν is the self-collision frequency of the fast ions defined as [12]

$$\nu = \nu_0 \frac{\Phi(x) - G(x)}{x^3}, \quad (17)$$

where $x = v/(\sqrt{2}v_{\text{th}})$ and $v_{\text{th}} = \sqrt{k_B T/m}$. Φ and G denote the error function and the Chandrasekhar function, respectively. ν_0 is not calculated self-consistently from the temperature and density profile of the fast ions, but rather set as a constant. In a typical fusion experiment, the fast particles collide much more frequently with the background plasma than with themselves. We can therefore treat ν_0 as an ‘effective’ collision frequency that mainly includes collisions with the bulk.

The collisional process itself is easily implemented into a PIC code. After the ‘non-collisional’ part of the trajectories (the characteristics of the kinetic equation in the absence of a collision operator) are advanced in time using a fourth-order Runge–Kutta method, a Monte-Carlo collision step is performed. EUTERPE uses a scheme that was (first) reported in [5, 31] (an earlier version was published in [29]). The scheme employs a (random) rotation of the velocity vector on a spherical shell. This is done by changing the pitch-angle variable of a particle according to

$$\xi_{\text{out}} = \sin \chi \sin \lambda \sqrt{1 - \xi_{\text{in}}^2} + \xi_{\text{in}} \cos \chi. \quad (18)$$

Here, ξ_{in} and ξ_{out} denote the pitch-angle variable before and after the collision and $\chi = R\sqrt{2\nu\Delta t}$. λ is a random number drawn from a uniform distribution between 0 and 2π , whereas R is drawn from a Gaussian distribution with expectation

value 0 and variance 1 [14]. After the collision, the new values for v_{\parallel} and μ are calculated from ξ_{out} using the fact that the energy remains unchanged.

A collision operator constructed in such a fashion has the obvious drawback that it does not conserve linear momentum. Also the conservation of particle number and kinetic energy (guaranteed analytically) may be lost numerically due to rounding errors. The reason is that the test-particle term has been retained, but the field-particle term \mathcal{C}_{fp} , describing the reaction of the background particles, was neglected

$$\mathcal{C}(f) = \mathcal{C}_{\text{fp}}(f) + \mathcal{C}_{\text{fp}}(f) \cong \mathcal{C}_{\text{fp}}(f). \quad (19)$$

In EUTERPE a scheme, presented in detail in [1, 26, 32], that ensures the conservation of particle number, linear momentum, and kinetic energy to machine precision is implemented. The idea is that an appropriate ansatz for the field-particle term can be made such that the contribution of this term cancels exactly the errors made in the conservation laws. The field-particle term is written as

$$\mathcal{C}_{\text{fp}}(f^{(1)}) = [N(\mathbf{v})\mathcal{N} + P(\mathbf{v})\mathcal{P} + E(\mathbf{v})\mathcal{E}]F \quad (20)$$

with coefficients \mathcal{N} , \mathcal{P} , and \mathcal{E} that have to be determined. F is the Maxwellian background and

$$N(\mathbf{v}) = \nu - 3\sqrt{\frac{\pi}{8}}\nu_E x^2 \quad (21)$$

$$P(\mathbf{v}) = \nu_s \frac{v_{\parallel}}{v_{\text{th}}^2} \quad (22)$$

$$E(\mathbf{v}) = \nu_E x^2. \quad (23)$$

For self-collisions, with an externally prescribed collision frequency ν_0 , the slowing-down frequency and the energy-diffusion frequency are defined as

$$\nu_s = 4\nu_0 \frac{G(x)}{x} \quad (24)$$

$$\nu_E = -2\nu + \left(2 + \frac{1}{2x^2}\right)\nu_s. \quad (25)$$

The deflection frequency ν is given by equation (17).

Writing the field-particle operator in this form, the numerical conservation of the desired quantities can be ensured while keeping the self-adjointness of the collision operator. To determine the coefficients \mathcal{N} , \mathcal{P} , and \mathcal{E} the 3×3 linear system

$$- \begin{pmatrix} \Delta N \\ \Delta P \\ \Delta E \end{pmatrix} = \int d^3v \left[F \begin{pmatrix} N(\mathbf{v}) & P(\mathbf{v}) & E(\mathbf{v}) \\ v_{\parallel} N(\mathbf{v}) & v_{\parallel} P(\mathbf{v}) & v_{\parallel} E(\mathbf{v}) \\ v^2 N(\mathbf{v}) & v^2 P(\mathbf{v}) & v^2 E(\mathbf{v}) \end{pmatrix} \right] \begin{pmatrix} \mathcal{N} \\ \mathcal{P} \\ \mathcal{E} \end{pmatrix} \quad (26)$$

needs to be solved in each spatial bin. The size of one spatial bin is given naturally by the resolution in radial, poloidal, and toroidal direction needed for the representation of the potentials. The quantity ΔP , for example, denotes the ‘amount of non-conservation’ of momentum P , $\Delta P = P_{\text{after collision}} - P_{\text{before collision}}$ summed over all particles in the spatial bin (similar for particle number N and kinetic

energy E). Note that in order for the matrix in equation (26) to be regular and thus invertible at least two particles are needed in a spatial bin. The scheme can only be applied if this condition is satisfied. Since inverting the 3×3 -matrix is very fast, nearly no increase in runtime is noticeable when the conservation scheme is used.

3. Results

Here, we present the results of our non-linear simulations. First, results for a simple circular tokamak are presented. In the second part of this section we show results for a more realistic and more complex W7-X scenario.

3.1. A tokamak case

First, the influence of pitch-angle collisions on the saturation dynamics of a TAE in tokamak geometry is presented. We use the well-established ITPA benchmark case [17] for simplicity and because it has become a well-established source for comparison within the fast-particle community. This case therefore provides a link both to recent numerical work [4, 20, 33] as well as to analytical theory [2, 3], which we also use to benchmark our code. For this test, only pitch-angle collisions of the fast-ions with each other are kept. The collision frequency (meaning ν_0 in equation (17)) is considered a parameter and varied over several orders of magnitude (recall that this models also the collisions of fast particles with the background plasma) in order to clearly show all the various non-linear scenarios that may emerge. The non-linear dynamics and eventual saturation will be illustrated based on the temporal behaviour of the perturbed magnetic field of the mode δB (more precisely its poloidal component). The value of δB at saturation (first maximum) is denoted by δB^{sat} .

The magnetic equilibrium is that of a circular, large-aspect-ratio tokamak with concentric circular flux surfaces. The q -profile is given by $q(s) = 1.71 + 0.16s$, with s being the flux-surface label (normalized toroidal flux). In this geometry we investigate a TAE located near the avoided crossing of the $m = 10, n = -6$ and $m = 11, n = -6$ continuum branches. The mode amplitude is zero at $s = 0$ and $s = 1$. The TAE mode is driven unstable by the interaction with a Maxwellian population of fast ions (hydrogen) with a non-uniform density profile given by (see appendix A for the coefficients)

$$N_{\text{fast}}(s) = c_1 \cdot N_{\text{fast},0} \exp \left[-\frac{c_2}{c_3} \tanh \left(\frac{\sqrt{s} - c_4}{c_2} \right) \right]. \quad (27)$$

The density gradient is the source of free energy to drive the mode unstable. The temperature of the fast ions is uniform with $T_{\text{fast}} = 400$ keV. Numerical simulations are performed for three different values of the fast-ion peak density

$$N_{\text{fast},0} = \{0.721, 1.44, 7.21\} \cdot 10^{17} \text{ m}^{-3}. \quad (28)$$

Varying the fast-ion density corresponds to changing the linear growth rate γ_L , which is constant for a given case.

Without collisions we compute

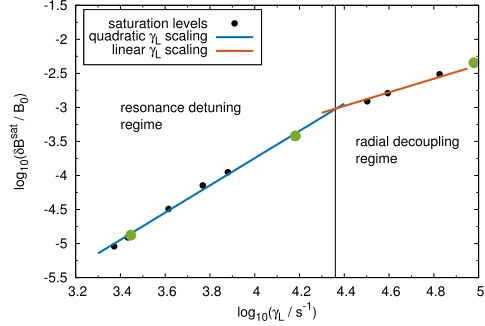


Figure 1. Transition from the resonance detuning regime to the radial decoupling regime without collisions as described in e.g. [4, 33]. The saturation levels indicated by the black dots have been taken from [16]. The green dots indicate the cases investigated in the present paper for various collision frequencies. We will refer to them as low-density, medium-density, and high-density case, respectively. Both the resonance detuning and the radial decoupling regime are covered.

$$\gamma_L \cong \{0.280, 1.52, 9.53\} \cdot 10^4 \text{ s}^{-1}. \quad (29)$$

Thus, both the resonance detuning and the radial decoupling regime [4, 33] are covered (see figure 1) in the simulations. It will be investigated if the change of the saturation mechanism ($\delta B^{\text{sat}} \propto \gamma_L^2$ transitions to $\delta B^{\text{sat}} \propto \gamma_L$) also changes the scaling of the saturated amplitude with respect to ν_0 .

Since the saturation mechanisms are different in the resonance detuning regime versus the radial decoupling regime, it cannot necessarily be expected that collisions will have the same influence on the saturation dynamics in both regimes. Saturation is reached in the resonance detuning regime, because the radial excursions of particles from a flux surface become comparable to the (finite) resonance width where wave-particle power transfer is possible. In the radial decoupling regime, the mode width limits the power transfer. We expect that collisions have a stronger impact on the saturation amplitude in the resonance detuning regime, because this is the regime in which the wave-particle resonance condition is important. The resonance condition includes the parallel velocity of a particle which is directly influenced by collisions. On the other hand, in the radial decoupling regime, saturation is reached because the resonance region becomes wider than the mode-localization region. This is a mechanism that is less sensitive to the individual particles and it should therefore be less influenced by collisions.

Figure 2 shows the perturbed component of the poloidal magnetic field for various collision frequencies and for the three different fast-ion densities investigated. (The fast-ion density, and therefore also the linear growth rate, increases from top to bottom.)

All sub-figures clearly show that the non-linear dynamics is influenced by collisions. This includes not only the saturation level itself, but also the dynamics in the saturated phase (saturated phase refers to all times after the first maximum of

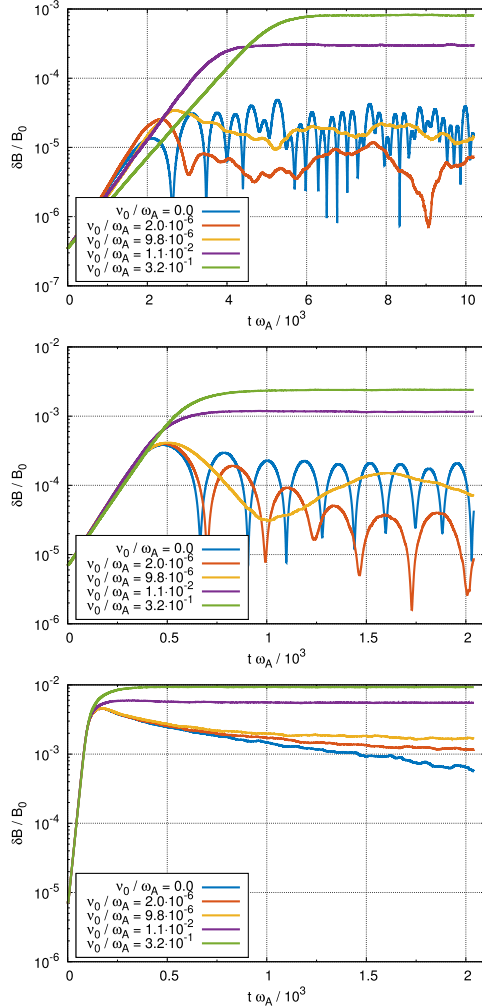


Figure 2. Time trace of the poloidal component of the perturbed magnetic field for the low-density (top), medium-density (middle), and high-density case (bottom) for various collision frequencies. Depending on the linear drive and collisionality either a steady-state or a periodic non-linear dynamics develops. The saturation levels (i.e. the first maxima of δB) increase monotonically with ν_0 .

δB). While the first and the second diagram of figure 2 show a similar non-linear dynamics, the high-density case on the bottom is different because any periodic non-linear behaviour is completely absent. Between the first two plots and the last one of figure 2 the saturation mechanism changes from resonance detuning to radial decoupling. In the high-density case the damping rate (a free input parameter in CKA-EUTERPE, $\gamma_d = 1.05 \cdot 10^4 \text{ s}^{-1}$ for all cases) is much smaller than the linear growth rate. Therefore a steady-state solution develops

after saturation. It was shown in [3] that a sufficiently high γ_d is required for a periodic scenario to develop.

For the two cases with lower $N_{\text{fast},0}$ that show periodic solutions in the non-linear phase, the transition to a more steady-state dynamics happens for a collision frequency ν_0 that is consistent with analytical theory [3]. Note that only for those two cases the analytical theory is valid in the first place. The transition from the periodic regime to the steady-state regime is determined by the relative strength of damping effects compared with the rate at which the distribution function is rebuilt, $\nu_{\text{eff},0} = \nu \omega^2 / \gamma_L^2$, [3]. Thus, a good indication of whether a steady-state or a periodic saturation should be expected is to compare $\nu_{\text{eff},0}$ with the damping rate γ_d . For $\nu_{\text{eff},0} > \gamma_d$ a steady state is expected, whereas the saturation should be periodic for $\nu_{\text{eff},0} < \gamma_d$ [3]. For the ITPA case investigated here, the damping rate equals $\nu_{\text{eff},0}$ for $\nu_0 \approx 3.35 \cdot 10^{-7} \omega_A$ (low-density case) and for $\nu_0 \approx 9.89 \cdot 10^{-6} \omega_A$ (medium-density case). ($\omega_A = v_A / R_0$ is the on-axis Alfvén frequency.) Hence, these are the collision frequencies for which the transition between the two regimes should be happening. Re-examining figure 2, this is exactly what is found by CKA-EUTERPE. For the low-density case the periodic solution is predicted to disappear for very low collision frequencies. Hence, even for the lowest frequency shown in the plot, $\nu_0 / \omega_A = 2.0 \cdot 10^{-6}$ (i.e. the red line), the oscillations have already vanished. For the medium-density case (middle plot of figure 2), the transition is nicely visible for $\nu_0 / \omega_A = 9.8 \cdot 10^{-6}$ (see the yellow line) which is close to the theoretically predicted value.

3.1.1. The scaling law. In order to extract a scaling law, $\delta B^{\text{sat}}(\nu_0)$, from the simulation data, we take the first maximum in the time-trace of the perturbed magnetic field (Note that, to account for the noisiness of the simulation and to calculate error bars, an average around the presumed location of the maximum is taken.). The analytical theory [3] has been derived for the value of the first maximum. The value $\delta B^{\text{sat}}(\nu_0 = 0)$ without collisions is subtracted, and the resulting quantity is plotted as a function of the collision frequency. This has been done in figure 3 for the three different fast-ion densities under investigation.

The figure shows the simulation results (black dots and diamonds) and numerical fits to the data (coloured lines). Note that numerical simulations for more collision frequencies than shown in figure 2 have been performed. The cases already presented in figure 2 are indicated as diamonds in figure 3. For all fits a function of the type

$$y = a \cdot x + b \quad (30)$$

with $y = \log[(\delta B^{\text{sat}}(\nu_0) - \delta B^{\text{sat}}(0)) / B_0]$ and $x = \log(\nu_0 / \omega_A)$ is used. The parameters a and b are determined by the fitting routine. The complete results for all fit parameters (showing also their uncertainties) are given in appendix B.

In all three cases different scaling laws emerge. The general trend is that small collision frequencies influence the saturation level more strongly if the linear growth rate is small (i.e. if the fast-ion density is small). In the opposite limit, for

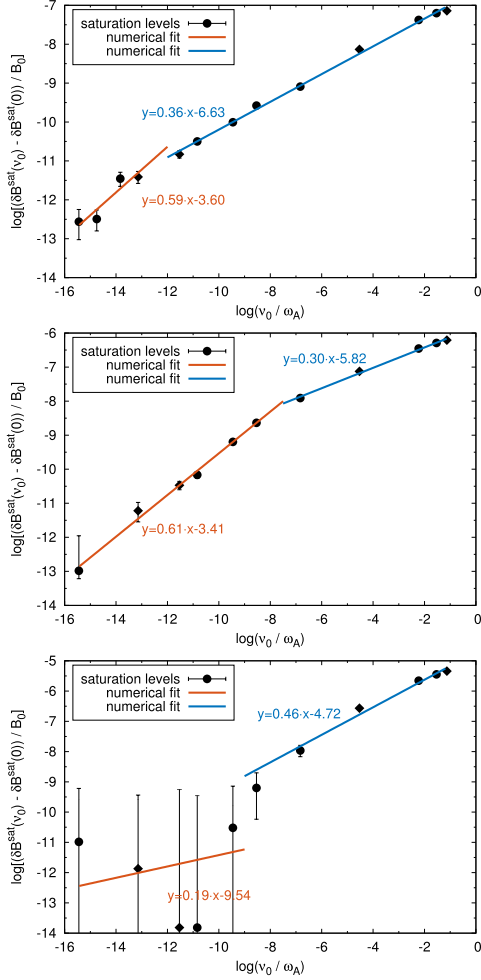


Figure 3. Scaling laws $\delta B^{\text{sat}}(\nu_0)$ extracted from the simulation data for the low-density (top), medium-density (middle), and high-density case (bottom). The theoretically predicted $\nu^{2/3}$ -scaling is confirmed in the resonance detuning regime (top two plots) for low enough collision frequencies (red curves) within the validity range of the theory. For higher collision frequencies different scaling laws are found numerically. The plot on the bottom (radial decoupling regime) shows a characteristic plateau for small ν_0 where the saturation level scales very weakly with collisionality.

high growth rates, a ‘plateau’ forms for small ν_0 indicating that in this regime the saturation level is almost independent of the collision frequency. This fact strengthens our initial assumption that the scaling $\delta B^{\text{sat}}(\nu_0)$ should be stronger in the resonance detuning regime. Note that if $\delta B^{\text{sat}}(\nu_0) - \delta B^{\text{sat}}(0)$ became negative, we took the absolute value in order to calculate the logarithm. Furthermore, the error bars are large if $\delta B^{\text{sat}}(\nu_0)$ and $\delta B^{\text{sat}}(0)$ are close together.

Analytical theory [3] predicts a $\nu^{2/3}$ -scaling of the saturated amplitude. Here, the term ‘saturated amplitude’ is used to refer to the first maximum after the linear phase. This scaling is valid for $\gamma_L \gg \gamma_d, \nu_{\text{eff}}$. ν_{eff} is the rate of reconstruction of the distribution function after it has been flattened by particle trapping in the wave [3]. Figure 2 confirmed that, depending on the value of $\nu_{\text{eff},0}$, either a steady state or a periodic scenario emerges. This, however, has no influence on the scaling law, since up until the first maximum of δB (corresponds to the first flattening of the distribution function) the physical processes in both regimes are similar and they only differ in the rate of reconstruction of the distribution function after the initial flattening.

Looking at the medium-density case, for which the saturation mechanism is resonance detuning (see figure 1), the analytically predicted scaling can be confirmed very well for low enough collision frequencies. For large collision frequencies, on the other hand, a different scaling is obvious. We speculate that the condition $\gamma_L \gg \nu_{\text{eff}}$ is violated before the mode reaches saturation in these cases and, therefore, the theory breaks down. It is intuitively clear that if ν_0 is arbitrarily high this is the case. A precise prediction of the collision frequency for which the scaling changes, hinges on a good estimate of ω_b , which is necessary to calculate $\nu_{\text{eff}} = \nu \omega^2 / \omega_b^2$ [3].

An instructive estimate for ω_b can be found in a cylindrical plasma. In the absence of a mode a particle just follows the magnetic field lines. On the other hand, if a mode with a high enough amplitude is present, the resulting $\mathbf{E} \times \mathbf{B}$ -drift may significantly influence the particle trajectory. A calculation, detailed in appendix C, provides the estimate

$$\omega_b^2 \cong -\frac{m^2 v_{\parallel}}{R_0 r B_0} \frac{\partial \iota}{\partial r} \phi_0 \quad (31)$$

for the bounce frequency of a particle trapped in the wave. ($\iota = 1/q$ is the rotational transform.) Substituting the parameters of the ITPA benchmark case (medium density) yields a critical collision frequency $\nu_{\text{crit}}/\omega_A \approx 1.3 \cdot 10^{-4}$ above which the analytical theory can no longer be valid. This critical collision frequency is in the same order of magnitude as the frequency for which the scaling changes in figure 3 (middle). Note that the simplified analytical model only provides a qualitative estimate for when the scaling law might change. For the low-density case we estimate $\nu_{\text{crit}}/\omega_A \approx 1.2 \cdot 10^{-6}$.

For the low-density case the estimated value for ν_{crit} is less successful in describing the numerical findings. The trend remains, however, that the region of validity of the analytical theory is much smaller since the linear growth rate is significantly reduced. Therefore, the transition from one scaling law to another happens on the very left of the curve for low collision frequencies. The scaling found numerically for small collision frequencies is still close to the analytical prediction albeit the large uncertainties in the numerical simulations.

Compared with the first two diagrams, the last plot in figure 3 is qualitatively different. Since the growth rate is high, the saturation mechanism is radial decoupling and is not described by the analytical theory. Therefore, the estimate for ν_{crit} is not applicable to that case. For these reasons, it is not

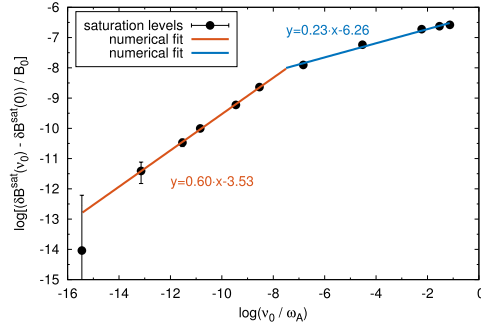


Figure 4. Same as figure 3 (middle plot), but taking into account also momentum conservation for the collision operator. Again, two regions with different scaling laws are observed. Momentum conservation is mainly important for the large collision frequencies. The lowest collision frequency was excluded from the numerical fit.

surprising that the scaling laws found numerically deviate significantly from theoretical predictions. As was shown in [4], the saturated amplitude of the perturbed magnetic field scales linearly with the growth rate in the radial decoupling regime. It remains to be investigated whether this is the reason why also the scaling law for δB^{sat} changes.

3.1.2. The influence of the conservation scheme. So far, all results presented in this section were obtained without the use of the parallel-momentum conservation scheme. Such a scheme is also absent in [3, 20, 37]. With the predicted $\nu^{2/3}$ -scaling confirmed for the medium-density case, it is worthwhile to investigate how the non-linear dynamics and the scaling law change when the conservation of momentum is properly taken into account. Figure 4 shows the scaling of the saturated amplitudes for the same collision frequencies investigated before for the medium-density case.

For small values of ν_0 , the saturated amplitudes are very similar with and without the conservation scheme. Consequently, also the scaling is only influenced slightly. On the other hand, for large ν_0 the conservation of momentum by the collision operator becomes important. The scaling changes in the sense that if the momentum correction is included in the collision operator, the saturation levels depend less on ν_0 . Neglecting the momentum correction leads to an overestimation of collisional effects just as it does in other areas of tokamak physics, such as neoclassical transport and micro-instability theory [14]. We find that conservation of momentum only changes the saturation levels, but does not affect the non-linear dynamics. For example, the transition from the periodic non-linear behaviour to the steady-state solution remains unchanged.

Note that the conservation scheme is designed for self-collisions. Even though ν_0 contains fast-fast collisions as well as fast-ion collisions, no momentum is transferred to the background ions.

3.1.3. Saturation mechanism—density flattening. All the numerical simulations share the feature that the mode amplitude saturates because the density profile of the fast ions

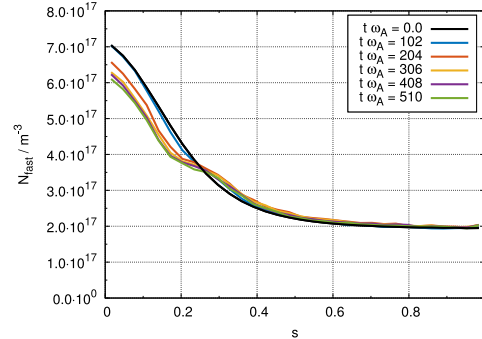


Figure 5. Flattening of the fast-ion density profile at various times in the simulation for the high-density case with the highest collision frequency. Since the saturation mechanism is radial decoupling flattening of the profile occurs in broad region comparable to the mode width. The flattening is significant because the saturation level is enhanced due to collisions.

flattens in the region of interest. The cases with non-vanishing collision frequency exhibit a stronger flattening of the density profile. We attribute this only to a ‘secondary’ effect of collisions. As has been shown, collisions lead to a higher saturation level, i.e. a larger mode amplitude, which in turn leads to enhanced fast-particle transport.

The high-density case with the highest ν_0 -value is taken as an example in figure 5, since this case has the highest saturation level of all cases investigated.

Flattening of the density profile over the region where the mode is localized (characteristic for the radial decoupling regime) is very obvious for later times in the simulation. Note that due to numerical inaccuracies, about 4% of the fast-ion density is lost over the course of the simulation.

For the medium-density case without collisions the initial profile and the saturated profile at the end of the simulation (in the time-asymptotic limit) are compared in figure 6 on the left-hand side.

Since the saturation level is low, transport is low and no significant changes can be seen in the saturated density profile. Note that in the resonance detuning regime the flattening of the density profile can be restricted to a very narrow region, which is challenging to resolve numerically. It is, however, possible to investigate the instantaneous change in the fast-ion density profile, as shown in figure 6 on the right-hand side, caused by the presence of the TAE. The change in particle density is investigated at the radial position $s = 0.25$ where the mode is peaked. Clearly, particles are transported away from the mode-localization region. By the end of the simulation, the particle density at $s = 0.25$ has decreased by approximately 0.6%. This is why the change is not visible by looking directly at the profile. The fast-ion density is oscillating in time in such a way that the fast-ion density is minimal (local minima in time) whenever the mode amplitude is largest (see the middle plot of figure 2). This corresponds to a flattening of the density gradient, followed by a phase of mode decay. In this phase, the density gradient can recover and the whole process starts anew.

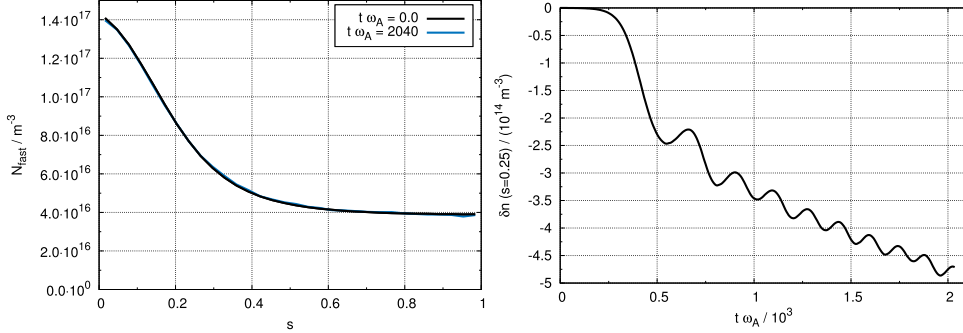


Figure 6. Left: Flattening of the fast-ion density profile for the medium-density case without collisions at a late time in the simulation. Since the saturation mechanism is resonance detuning flattening of the profile occurs in a narrow region. Right: Instantaneous fast-ion density at $s = 0.25$. Overall, particles are transported away from the mode-localization region. The particle density oscillates in time with the maxima and minima being correlated to the amplitude of the perturbed magnetic field as shown in figure 2 in the middle.

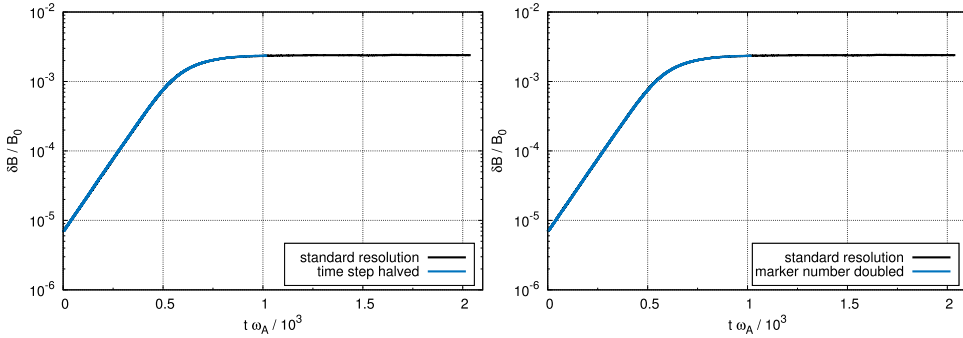


Figure 7. Convergence scan with respect to time step (left) and maker number (right). Since the deviations between the curves are below 1% (measuring γ_L), the standard resolution was chosen well.

3.2. Convergence scan

A convergence test with respect to time step and marker number has been performed for the medium-density case at the highest collision frequency. Figure 7 shows the results in terms of the perturbed magnetic field as calculated by the code. Both diagrams (time step halved on the left-hand side and numerical marker number doubled on the right-hand side) confirm that the standard resolution was chosen well. The standard time step for all tokamak calculations is $\Delta t \omega_A = 0.1$. We used $N_p = 10^6$ numerical marker particles in the standard runs.

It has been reported before that for the particular collisional scheme used in EUTERPE the time step is more critical than the number of markers [27]. Nevertheless, the relative deviations in the linear growth rate (compared with the standard resolution) are well below 1%, which is very acceptable.

3.3. A stellarator case

Having confirmed the theoretically predicted scaling law in tokamaks (in the resonance detuning regime and for low

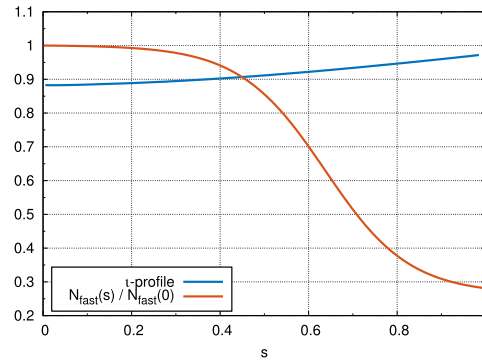
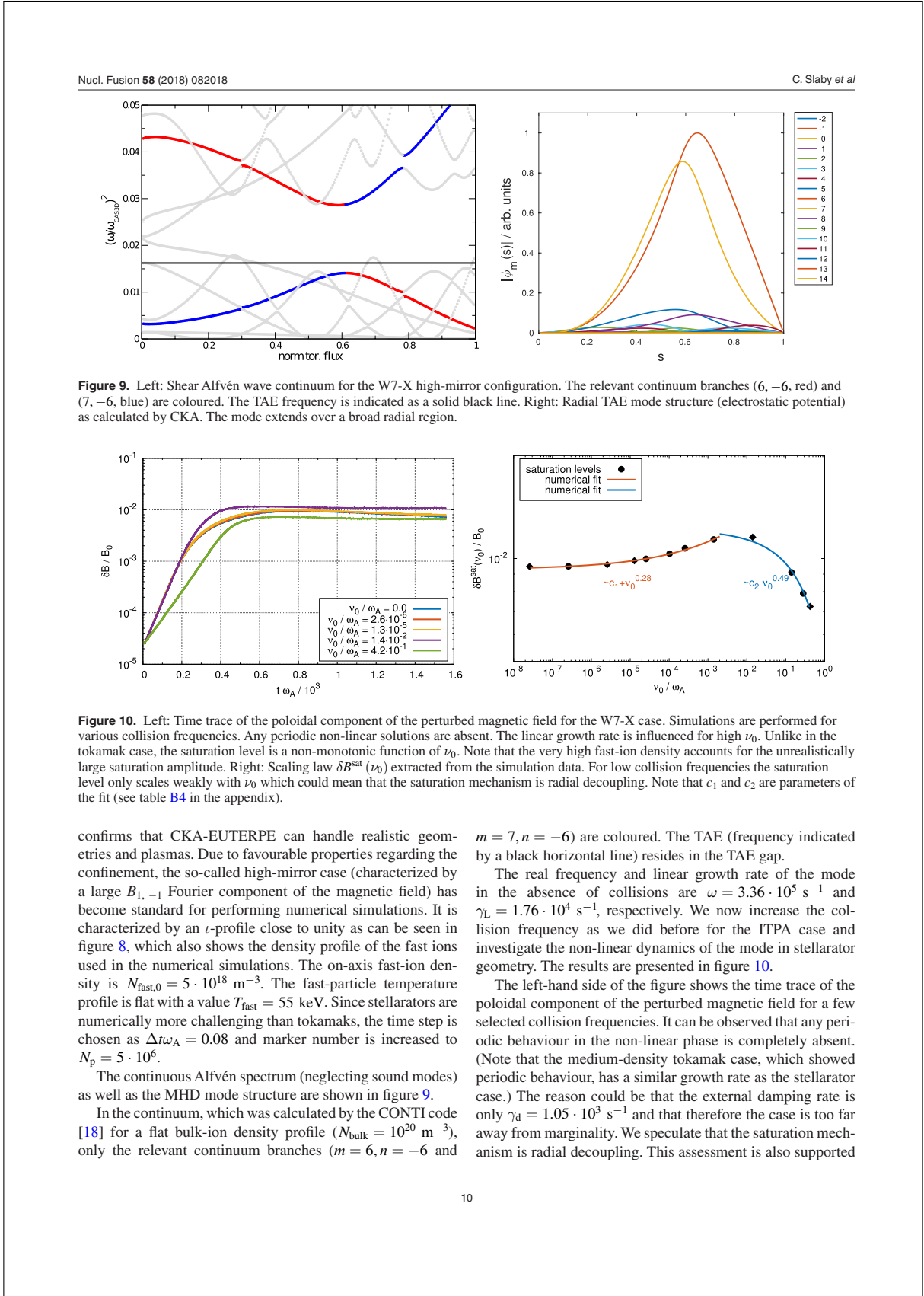


Figure 8. t -profile and fast-ion density profile (normalized to on-axis value) for the Wendelstein 7-X (W7-X) high-mirror configuration.

enough collision frequencies), we now apply the CKA-EUTERPE code to a Wendelstein 7-X (W7-X) high-mirror equilibrium with an on-axis magnetic field $B_0 = 2.44$ T. This



confirms that CKA-EUTERPE can handle realistic geometries and plasmas. Due to favourable properties regarding the confinement, the so-called high-mirror case (characterized by a large $B_{1,-1}$ Fourier component of the magnetic field) has become standard for performing numerical simulations. It is characterized by an ι -profile close to unity as can be seen in figure 8, which also shows the density profile of the fast ions used in the numerical simulations. The on-axis fast-ion density is $N_{\text{fast},0} = 5 \cdot 10^{18} \text{ m}^{-3}$. The fast-particle temperature profile is flat with a value $T_{\text{fast}} = 55 \text{ keV}$. Since stellarators are numerically more challenging than tokamaks, the time step is chosen as $\Delta t \omega_A = 0.08$ and marker number is increased to $N_p = 5 \cdot 10^6$.

The continuous Alfvén spectrum (neglecting sound modes) as well as the MHD mode structure are shown in figure 9.

In the continuum, which was calculated by the CONTI code [18] for a flat bulk-ion density profile ($N_{\text{bulk}} = 10^{20} \text{ m}^{-3}$), only the relevant continuum branches ($m = 6, n = -6$ and

$m = 7, n = -6$) are coloured. The TAE (frequency indicated by a black horizontal line) resides in the TAE gap.

The real frequency and linear growth rate of the mode in the absence of collisions are $\omega = 3.36 \cdot 10^5 \text{ s}^{-1}$ and $\gamma_L = 1.76 \cdot 10^4 \text{ s}^{-1}$, respectively. We now increase the collision frequency as we did before for the ITPA case and investigate the non-linear dynamics of the mode in stellarator geometry. The results are presented in figure 10.

The left-hand side of the figure shows the time trace of the poloidal component of the perturbed magnetic field for a few selected collision frequencies. It can be observed that any periodic behaviour in the non-linear phase is completely absent. (Note that the medium-density tokamak case, which showed periodic behaviour, has a similar growth rate as the stellarator case.) The reason could be that the external damping rate is only $\gamma_d = 1.05 \cdot 10^3 \text{ s}^{-1}$ and that therefore the case is too far away from marginality. We speculate that the saturation mechanism is radial decoupling. This assessment is also supported

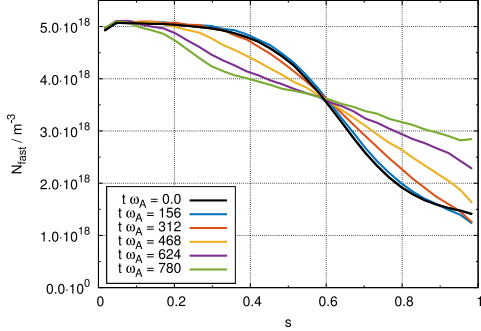


Figure 11. Flattening of the fast-ion density profile at various times in the simulation for the W7-X high-mirror case without collisions. The saturation mechanism resembles radial decoupling and a flattening of the profile over the whole mode-localization region is observed.

by the fact that the flattening of the density profile happens over an area of large radial extent comparable to the mode width, see figure 11. Shown is the case without collisions. Including collisions makes no qualitative difference.

About 5% of the fast-ion density is lost due to numerical errors.

Since the ι -profile of this specific W7-X configuration is very flat (low shear), there is very little variation in ω_{res} (as defined in [4]). Thus, even for very small growth rates, the resonance width can be of the same order as the mode width which then leads to radial decoupling.

It was found in the tokamak case that if the saturation mechanism is radial decoupling, the saturation level scales very weakly with collisionality for low values of ν_0 . Examining the right-hand side of figure 10, a similar observation can be made for W7-X. However, a striking difference between tokamak and stellarator is that δB^{sat} is a non-monotonic function of ν_0 . Large collision frequencies clearly lead to a reduction of the saturation level. It even drops below the collision-less value.

Unlike in the tokamak cases, the linear growth rate is reduced substantially by collisions (reduction of approx. 42% for the highest collision frequency compared with the collision-less case). In the tokamak cases, γ_L only changes by 20%, 7%, and 3% for the low-density, medium-density, and high-density cases, respectively.

The saturated amplitude of the magnetic field is a function of many parameters with γ_d , γ_L , and ν_0 being the most important ones. Disentangling the various contributions of the individual parameters to the overall scaling law proved to be successful for the ITPA case, since γ_d is an external parameter and γ_L was found to not depend significantly on ν_0 .

In the stellarator, γ_L and ν_0 cannot be varied independently (at least for high collision frequencies). This may be the reason why δB^{sat} is a non-monotonic function of ν_0 . This issue remains to be investigated.

4. Summary and conclusions

We have studied the non-linear saturation of TAEs in tokamaks and stellarators. Special emphasis is given to the role of pitch-angle collisions of the fast ions and how the collisions influence the saturation level and the subsequent non-linear dynamics in the saturated phase. As a tokamak representative, the ITPA benchmark case was chosen. We performed numerical simulations for the standard case as well as with half of the standard density and a five-times increased value. In doing so, we cover both the resonance detuning and the radial decoupling regime by the simulations.

It is seen that features predicted by analytical theory are recovered by the simulations, if they are performed in the validity range of the theory. We showed that the transition from a periodic dynamics in the non-linear phase to a steady-state solution occurs for a collision frequency that is consistent with analytical predictions. In the resonance detuning regime (i.e. for cases that are closer to marginal stability) the theoretically predicted $\nu^{2/3}$ -scaling of the saturation level is confirmed numerically. In this sense, this case also serves as a benchmark of the implementation of collisions into the non-linear and electromagnetic version of CKA-EUTERPE.

Outside the validity range of the theory (for $\gamma_L \lesssim \nu_{\text{eff}}$) scaling laws deviating from the $\nu^{2/3}$ -prediction are found numerically. The critical collision frequency ν_{crit} for which the scaling is supposed to change can (roughly) be estimated by calculating the bounce frequency ω_b of particles trapped in the potential of the wave. A simple cylindrical calculation for ω_b leads to an estimate for ν_{crit} that qualitatively matches the numerical findings.

Analytical theory and previous numerical simulations did not include a momentum-conserving collision operator. We investigated the implications that conserving linear momentum in the collision step has on the scaling law. It turns out that neglecting momentum conservation leads to an over-estimation of collisional effects. However, this only becomes important for large collision frequencies. As expected, for small values of ν_0 the scaling laws found numerically with and without the momentum-conservation scheme are the same.

After having confirmed the analytical predictions in tokamaks, the code was applied to a Wendelstein 7-X (W7-X) high-mirror equilibrium. Similarly to the ITPA case a TAE, now with a broader radial structure, is investigated in stellarator geometry. Several differences become apparent when comparing the tokamak and the stellarator case. The stellarator case shows no periodic non-linear behaviour, which might be a consequence of the relative values of γ_L and γ_d used for this simulation. The second difference is that the scaling of the saturation level with ν_0 is now non-monotonic. Again, this might be related to a closer entanglement of the various factors influencing the non-linear dynamics in stellarators. The weak scaling of $\delta B^{\text{sat}}(\nu_0)$ coupled with a flattening of the fast-ion density profile over the whole mode-localization region suggests that the saturation regime in W7-X is radial decoupling. Notwithstanding the above, the mode is found to saturate due to profile flattening in the tokamak and stellarator alike.

Finally, it must be pointed out that it is too soon to draw any final conclusions about the non-linear dynamics of shear Alfvén modes in W7-X. Many more gap modes existing in stellarator geometry (HAEs, EAEs, MAEs, but also EPMs) with different mode numbers and radial profiles need to be studied to determine if the findings reported here prevail in general. Especially with neutral beam injection becoming available at W7-X for the next operation phase, also the effect of using a slowing-down distribution function for the fast-ions and a proper slowing-down collision operator should be studied. The implementation of proper distribution functions for such scenarios is in progress.

All numerical simulations reported in this paper were performed in a perturbative sense with the mode structure held fixed throughout the simulations. Future investigations with fully gyro-kinetic models (allowing for the evolution of the mode structure) should be carried out in order to confirm the results of the perturbative models. Such simulations are, however, still very expensive and numerically challenging and at the moment not suited for parameter studies as the one reported in this paper.

Finite \mathbf{A}_\perp -effects have been neglected in this paper. While CKA as a reduced MHD code contains \mathbf{A}_\perp , the equations of motion in EUTERPE do not. A more complete coupling of CKA and EUTERPE in this regard is a matter of ongoing research.

As has been pointed out in [6, 21], when compared to models or numerical predictions, experimentally diagnosed properties of chirping solutions can provide information on plasma parameters which are otherwise difficult to diagnose. Hence, a next step should be to investigate stellarator cases that are closer to marginality and thus allow for chirping behaviour.

Acknowledgment

The simulations were performed on the MARCONI super-computer (CINECA), the HPC extension DRACO (MPCDF), and the local Linux cluster in Greifswald.

Christoph Slaby would like to thank Matthias Borchardt and Henry Leyh for their assistance with the parallel computing environment.

This work has been carried out within the framework of the EUROfusion Consortium and has received funding from the Euratom research and training programme 2014-2018 under grant agreement No 633053. The views and opinions expressed herein do not necessarily reflect those of the European Commission.

Appendix A. Parameters of the ITPA density profile

The coefficients of the density profile are listed in table A1.

Appendix B. Parameters of the numerical fits

Tables B1–B3 list all resulting parameters of the numerical fits shown in figure 3 in section 3. For all fits a function of the type

Table A1. Parameters of the ITPA fast-ion density profile.

coefficient	c_1	c_2	c_3	c_4
value	0.521 298	0.198 739	0.298 228	0.491 23

Table B1. Parameters of the numerical fits for the low-density case.

	a	b
small ν_0 (red curve)	0.59 ± 0.15	-3.60 ± 2.20
large ν_0 (blue curve)	0.36 ± 0.01	-6.63 ± 0.05

Table B2. Parameters of the numerical fits for the medium-density case.

	without conservation scheme		with conservation scheme	
	a	b	a	b
small ν_0 (red curve)	0.61 ± 0.03	-3.41 ± 0.30	0.60 ± 0.01	-3.53 ± 0.08
large ν_0 (blue curve)	0.30 ± 0.01	-5.82 ± 0.04	0.23 ± 0.02	-6.26 ± 0.06

Table B3. Parameters of the numerical fits for the high-density case.

	a	b
small ν_0 (red curve)	0.19 ± 0.36	-9.54 ± 4.17
large ν_0 (blue curve)	0.46 ± 0.03	-4.72 ± 0.14

Table B4. Parameters of the numerical fits for the W7-X case.

	a	b	c
small ν_0 (red curve)	0.28 ± 0.03	0.013 ± 0.002	$0.009 \pm 7.7 \cdot 10^{-5}$
large ν_0 (blue curve)	0.49 ± 0.16	$-0.008 \pm 8.0 \cdot 10^{-4}$	$0.012 \pm 6.0 \cdot 10^{-4}$

$$y = a \cdot x + b \quad (\text{B.1})$$

with $y = \log[(\delta B^{\text{sat}}(\nu_0) - \delta B^{\text{sat}}(0))/B_0]$ and $x = \log(\nu_0/\omega_A)$ is used.

In the case of W7-X (see figure 10) the data are fitted to

$$y = b \cdot x^a + c \quad (\text{B.2})$$

with $y = \delta B^{\text{sat}}(\nu_0)/B_0$ and $x = \nu_0/\omega_A$. Table B4 lists the results.

Appendix C. An analytical estimate for ω_b

Consider a particle moving in a cylindrical plasma. The magnetic field is given by

$$\mathbf{B} = B_1 \mathbf{e}_\Theta + B_0 \mathbf{e}_z, \quad (\text{C.1})$$

where \mathbf{e}_Θ and \mathbf{e}_z are unit vectors in cylindrical coordinates. The equations of motion are

$$\dot{\mathbf{R}} = v_\parallel \mathbf{b} + \frac{\mathbf{B} \times \nabla \phi}{B^2} \quad (\text{C.2})$$

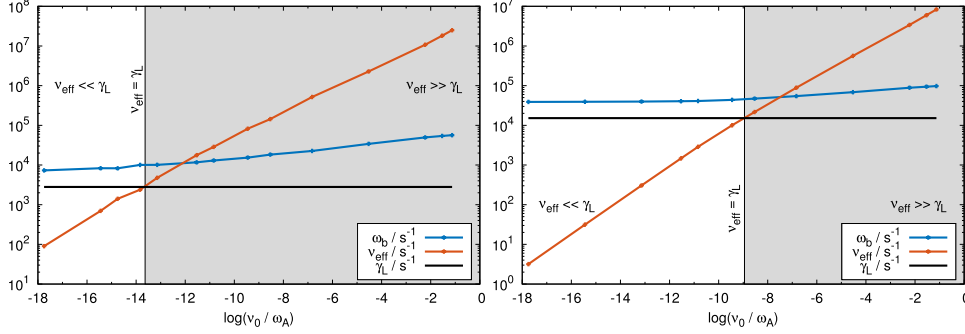


Figure C1. Resulting values of the cylindrical ω_b estimates (blue) for the low-density (left) and medium-density cases (right). The calculated values for ν_{eff} are shown in red. The primary assumptions of the analytical theory [3] exclude the gray region.

$$\dot{v}_{\parallel} = 0 \quad (\text{C.3})$$

if all ∇B terms are ignored. For the spatial coordinates of the particle one thus finds

$$\dot{r} = \frac{1}{B^2} \left(B_1 \phi_{,z} - \frac{B_0}{r} \phi_{,\Theta} \right) \quad (\text{C.4})$$

$$\dot{\Theta} = \frac{v_{\parallel} B_1}{Br} + \frac{B_0 \phi_{,r}}{B^2 r} \quad (\text{C.5})$$

$$\dot{z} = \frac{v_{\parallel} B_0}{B} - \frac{B_1 \phi_{,r}}{B^2}. \quad (\text{C.6})$$

Suppose that $B \approx B_0$ and introduce the rotational transform as

$$\iota = \frac{R_0 B_1}{r B_0}. \quad (\text{C.7})$$

The equations of motion then reduce to (terms that scale with the inverse aspect ratio can be neglected)

$$\dot{r} = \frac{r}{R_0} \iota \phi_{,z} - \frac{1}{r B_0} \phi_{,\Theta} \cong -\frac{1}{r B_0} \phi_{,\Theta} \quad (\text{C.8})$$

$$\dot{\Theta} = \frac{\iota v_{\parallel}}{R_0} + \frac{1}{r B_0} \phi_{,r} \quad (\text{C.9})$$

$$\dot{z} = v_{\parallel} - \frac{r}{R_0} \iota \phi_{,r} \cong v_{\parallel}. \quad (\text{C.10})$$

The z -equation is easily integrated. When transforming to a new coordinate $p = B_0 r^2 / 2$ it can be seen that the remaining system can be cast into Hamiltonian form

$$\dot{p} = -\frac{\partial H}{\partial \Theta} \quad (\text{C.11})$$

$$\dot{\Theta} = \frac{\partial H}{\partial p} \quad (\text{C.12})$$

with $H = v_{\parallel} \psi / R_0 + \phi$ and $\partial \psi / \partial p = \iota$. Obviously, the Hamiltonian of the co-moving frame,

$$\bar{H} = \left(\frac{v_{\parallel}}{R_0} n - \omega \right) p + mH, \quad (\text{C.13})$$

is an invariant of the (perturbed) motion. Suppose that the potential varies as $\phi = \phi_0 \cos(m\Theta + n/R_0 z - \omega t)$. Then, a phase

$$\chi = m\Theta + \frac{n}{R_0} z_0 + \left(\frac{n}{R_0} v_{\parallel} - \omega \right) t \quad (\text{C.14})$$

can be defined in the co-moving frame of the wave. The equations of motion in the reference frame of the wave are thus

$$\dot{p} = -\frac{\partial \bar{H}}{\partial \chi} = m\phi_0 \sin \chi \quad (\text{C.15})$$

$$\dot{\chi} = \frac{\partial \bar{H}}{\partial p} = \frac{n}{R_0} v_{\parallel} - \omega + \frac{m}{R_0} \iota v_{\parallel} + m \cos \chi \frac{\partial \phi_0}{\partial p}. \quad (\text{C.16})$$

Calculating the second time derivative of the phase and Taylor-expanding around $\chi = 0$ yields

$$\begin{aligned} \ddot{\chi} &= \left[\frac{m}{R_0} \frac{\partial \iota}{\partial p} v_{\parallel} + m \cos \chi \frac{\partial^2 \phi_0}{\partial p^2} \right] m\phi_0 \sin \chi - m \sin \chi \frac{\partial \phi_0}{\partial p} \\ &\quad \times \left[\frac{n}{R_0} v_{\parallel} - \omega + \frac{m}{R_0} \iota v_{\parallel} + m \cos \chi \frac{\partial \phi_0}{\partial p} \right] \end{aligned} \quad (\text{C.17})$$

$$\begin{aligned} &\cong \left[\frac{m^2}{R_0} \frac{\partial \iota}{\partial p} v_{\parallel} \phi_0 + m^2 \phi_0 \frac{\partial^2 \phi_0}{\partial p^2} \right. \\ &\quad \left. - m \frac{\partial \phi_0}{\partial p} (v_{\parallel} k_{\parallel} - \omega) - m^2 \left(\frac{\partial \phi_0}{\partial p} \right)^2 \right] \chi \end{aligned} \quad (\text{C.18})$$

$$\equiv -\omega_b^2 \chi. \quad (\text{C.19})$$

Using the resonance condition $v_{\parallel} k_{\parallel} = \omega$, the square of the bounce frequency is defined as

$$\omega_b^2 \equiv - \left[\frac{m^2}{R_0} \frac{\partial \iota}{\partial p} v_{\parallel} \phi_0 + m^2 \phi_0 \frac{\partial^2 \phi_0}{\partial p^2} - m^2 \left(\frac{\partial \phi_0}{\partial p} \right)^2 \right] \quad (\text{C.20})$$

and includes terms both linear and quadratic in the field amplitude. This is contrary to conventional Berk–Breizman theory and could hint on the transition from the resonance detuning regime (terms linear in ϕ_0) to the radial decoupling regime (quadratic terms). The estimate for ω_b presented in the main text (see equation (31)) is obtained by keeping only the linear term and transforming back to the radial coordinate r .

We can use that equation to try to estimate the validity range of the analytical theory [3]. In order to compare with the numerical simulations, we substitute the parameters of the ITPA benchmark and use $v_{\parallel} = v_A/3$. The results of this simple estimate for ω_b are shown in figure C1 in blue for the various collision frequencies using the value for ϕ_0 at saturation. Given the value for ω_b it is then possible to calculate ν_{eff} (red curve in figure C1). Two regimes are visible. For $\nu_{\text{eff}} \ll \gamma_L$ the assumptions of [3] are valid. In this regime the theoretically predicted scaling is confirmed numerically (in the resonance detuning regime). For $\nu_{\text{eff}} \gg \gamma_L$, on the other hand, the initial assumptions are violated and a new scaling law is found numerically. This simple cylindrical estimate is able to qualitatively predict the transition from one regime to the other. It fits fairly well with our simulation results.

References

- [1] Abel I.G., Barnes M., Cowley S.C., Dorland W. and Schekochihin A.A. 2008 Linearized model Fokker–Planck collision operators for gyrokinetic simulations. I. Theory *Phys. Plasmas* **15** 122509
- [2] Berk H.L. and Breizman B.N. 1990 Saturation of a single mode driven by an energetic injected beam. III. Alfvén wave problem *Phys. Fluids B* **2** 2246
- [3] Berk H.L., Breizman B.N. and Huanchun Y. 1992 Scenarios for the nonlinear evolution of alpha-particle-induced Alfvén wave instability *Phys. Rev. Lett.* **68** 3563
- [4] Briguglio S., Wang X., Zonca F., Vlad G., Fogaccia G., Troia C.D. and Fusco V. 2014 Analysis of the nonlinear behavior of shear-Alfvén modes in tokamaks based on Hamiltonian mapping techniques *Phys. Plasmas* **21** 112301
- [5] Brunner S., Valeo E. and Krommes J.A. 1999 Collisional delta-f scheme with evolving background for transport time scale simulations *Phys. Plasmas* **6** 4504
- [6] Duarte V.N., Berk H.L., Gorelenkov N.N., Heidbrink W.W., Kramer G.J., Nazikian R., Pace D.C., Podestà M., Tobias B.J. and Zeeland M.A.V. 2017 Prediction of nonlinear evolution character of energetic-particle-driven instabilities *Nucl. Fusion* **57** 054001
- [7] Duong H.H., Heidbrink W.W., Strait E.J., Petrie T.W., Lee R., Moyer R.A. and Watkins J.G. 1993 Loss of energetic beam ions during TAE instabilities *Nucl. Fusion* **33** 749
- [8] Könies A. et al 2007 A code for the calculation of kinetic Alfvén waves in three-dimensional geometry *10th IAEA Technical Meeting on Energetic Particles in Magnetic Confinement Systems (Kloster Seeon, 8–10 October 2007)*
- [9] Kaye S.M. et al 2005 Progress towards high performance plasmas in the national spherical torus experiment (NSTX) *Nucl. Fusion* **45** S168
- [10] Fehér T.B. 2013 Simulation of the interaction between Alfvén waves and fast particles *PhD Thesis Ernst-Moritz-Arndt-Universität Greifswald*
- [11] Fu G.Y. and van Dam J.W. 1989 Excitation of the toroidicity-induced shear Alfvén eigenmode by fusion alpha particles in an ignited tokamak *Phys. Fluids B* **1** 1949
- [12] Helander P. and Sigmar D.J. 2002 *Collisional Transport in Magnetized Plasmas* (Cambridge: Cambridge University Press)
- [13] Hirvijoki E., Brizard A., Snicker A. and Kurki-Suonio T. 2013 Monte Carlo implementation of a guiding-center Fokker–Planck kinetic equation *Phys. Plasmas* **20** 092505
- [14] Kauffmann K. 2011 Including collisions in gyrokinetic tokamak and stellarator simulations *PhD Thesis Ernst-Moritz-Arndt-Universität Greifswald*
- [15] Kleiber R., Hatzky R., Könies A., Mishchenko A. and Sonnendrücker E. 2016 An explicit large time step particle-in-cell scheme for nonlinear gyrokinetic simulations in the electromagnetic regime *Phys. Plasmas* **23** 032501
- [16] Könies A. Paper on the model of CKA-EUTERPE in preparation
- [17] Könies A. et al 2012 Benchmark of gyrokinetic, kinetic MHD and gyrofluid codes for the linear calculation of fast particle driven TAE dynamics *24th IAEA Int. Conf. on Fusion Energy (San Diego, CA, 8–13 October 2012)* (www.naweb.iaea.org/naweb/FEC/FEC2012/papers/437_ITRP134.pdf)
- [18] Könies A. and Eremin D. 2010 Coupling of Alfvén and sound waves in stellarator plasmas *Phys. Plasmas* **17** 012107
- [19] Kornilov V., Kleiber R., Hatzky R., Villard L. and Jost G. 2004 Gyrokinetic global three-dimensional simulations of linear ion-temperature-gradient modes in Wendelstein 7-X *Phys. Plasmas* **11** 3196
- [20] Lang J., Fu G. and Chen Y. 2010 Nonlinear simulation of toroidal Alfvén eigenmode with source and sink *Phys. Plasmas* **17** 042309
- [21] Lesur M., Idomura Y., Shinohara K., Garbet X. and The JT-60 Team 2010 Spectroscopic determination of kinetic parameters for frequency sweeping Alfvén eigenmodes *Phys. Plasmas* **17** 122311
- [22] Melnikov A.V. et al 2016 Transition from chirping to steady NBI-driven Alfvén modes caused by magnetic configuration variations in the TJ-II stellarator *Nucl. Fusion* **56** 076001
- [23] Melnikov A.V. et al 2016 Study of NBI-driven chirping mode properties and radial location by the heavy ion beam probe in the TJ-II stellarator *Nucl. Fusion* **56** 112019
- [24] Pedersen T.S., Otte M., Lazerson S., Helander P., Bozhenkov S., Biedermann C., Klingert T., Wolf R.C., Bosch H.S. and The Wendelstein 7-X Team 2016 Confirmation of the topology of the Wendelstein 7-X magnetic field to better than 1:100,00 *Nat. Commun.* **7** 13493
- [25] Rosenbluth M.N. and Rutherford P.H. 1975 Excitation of Alfvén waves by high-energy ions in a tokamak *Phys. Rev. Lett.* **34** 1428
- [26] Satake S., Kanno R. and Sugama H. 2008 Development of a non-local neoclassical transport code for helical configurations *Plasma Fusion Res.* **3** S1062
- [27] Slaby C., Kleiber R. and Könies A. 2017 Combining electromagnetic gyro-kinetic particle-in-cell simulations with collisions *Comput. Phys. Commun.* **218** 1
- [28] Slaby C., Könies A. and Kleiber R. 2016 Numerical investigation of non-perturbative kinetic effects of energetic particles on toroidicity-induced Alfvén eigenmodes in tokamaks and stellarators *Phys. Plasmas* **23** 092501
- [29] Takizuka T. and Abe H. 1977 A binary collision model for plasma simulation with a particle code *J. Comput. Phys.* **25** 205
- [30] Todo Y., Seki R., Spong D.A., Wang H., Suzuki Y., Yamamoto S., Nakajima N. and Osakabe M. 2017 Comprehensive magnetohydrodynamic hybrid simulations of fast ion driven instabilities in a large helical device experiment *Phys. Plasmas* **24** 081203
- [31] Vernay T. 2008 Numerical study of electron-ion collision effects on trapped electron modes with the gyrokinetic code ORB5 *Master's Thesis École Polytechnique Fédérale de Lausanne*
- [32] Vernay T., Brunner S., Villard L., McMillan B.F., Jolliet S., Tran T.M., Bottino A. and Graves J.P. 2010 Neoclassical equilibria as starting point for global gyrokinetic microturbulence simulations *Phys. Plasmas* **17** 122301

- [33] Wang X., Briguglio S., Lauber P., Fusco V. and Zonca F. 2016 Structure of wave-particle resonances and Alfvén mode saturation *Phys. Plasmas* **23** 012514
- [34] Wang Z., Lin Z., Holod I., Heidbrink W.W., Tobias B., Zeeland M.V. and Austin M.E. 2013 Radial localization of toroidicity-induced Alfvén eigenmodes *Phys. Rev. Lett.* **111** 145003
- [35] White R.B., Fredrickson E., Darrow D., Zarnstorff M., Wilson R., Zweben S., Hill K., Chen Y. and Fu G. 1995 Toroidal Alfvén eigenmode-induced ripple trapping *Phys. Plasmas* **2** 2871
- [36] Zhang H.S., Lin Z., Deng W., Holod I., Wang Z.X., Xiao Y. and Zhang W.L. 2013 Nonlinear dynamics of beta-induced Alfvén eigenmodes in tokamak *Phys. Plasmas* **20** 012510
- [37] Zhou M. and White R. 2016 Collisional dependence of Alfvén mode saturation in tokamaks *Plasma Phys. Control. Fusion* **58** 125006

Appendix A. Thesis articles

Numerical investigation of fast-ion-driven modes in Wendelstein 7-X (non-refereed) (A.3)

Full citation:

C. Slaby, A. Könies, R. Kleiber, S. Äkäslompolo, and J. Kontula. Numerical investigation of fast-ion-driven modes in Wendelstein 7-X. *Europhysics Conference Abstracts*, **42A** P4.1098 (2018) (non-refereed).

URL:

<http://ocs.ciemat.es/EPS2018PAP/pdf/P4.1098.pdf>

Reproduced under CC BY 3.0 License (<https://creativecommons.org/licenses/by/3.0/>).

Appendix A. Thesis articles

Numerical investigation of fast-ion-driven modes in Wendelstein 7-X

C. Slaby¹, A. Könies¹, R. Kleiber¹, S. Äkäslompolo¹, and J. Kontula²

¹ Max-Planck-Institut für Plasmaphysik, Greifswald, Germany

² Aalto University, Aalto, Finland

Introduction

Heating methods such as neutral beam injection (NBI) or ion cyclotron resonance heating (ICRH) generate fast ions in fusion plasmas. In order to effectively heat the plasma, the fast ions need to remain confined for a time period on the order of the slowing-down time. While slowing down, the fast ions may resonantly interact with Alfvénic perturbations, which can lead to enhanced fast-ion transport [1] and premature ejection of fast ions from the plasma.

Here, we numerically investigate the interaction of Alfvén waves and fast ions in a Wendelstein 7-X (W7-X) high-mirror configuration. Note that one of the optimization goals of W7-X is good fast-ion confinement [2].

The simulations are performed using the non-linear CKA-EUTERPE code package [3]. It combines the ideal MHD code CKA, which provides a mode structure, and the gyro-kinetic code EUTERPE, which computes the power transfer from the fast ions to the mode. This approach is perturbative since the mode structure remains fixed for the entire calculation.

Even though non-linear simulations, using CKA-EUTERPE, have been conducted in the past for W7-X [4], this is the first time that a realistic fast-ion distribution function and density profile, as expected for plasmas in operation phase 1.2b (July-October 2018), are considered. Both are obtained using the ASCOT code [5, 6]. As can be seen in Fig. 1 (top), we use a slowing-down distribution function with two intermediate steps to describe the fast ions. Those steps are at $E_{\max}/2$ and $E_{\max}/3$ and come from the acceleration of molecular hydrogen. The black circles are computed by ASCOT while

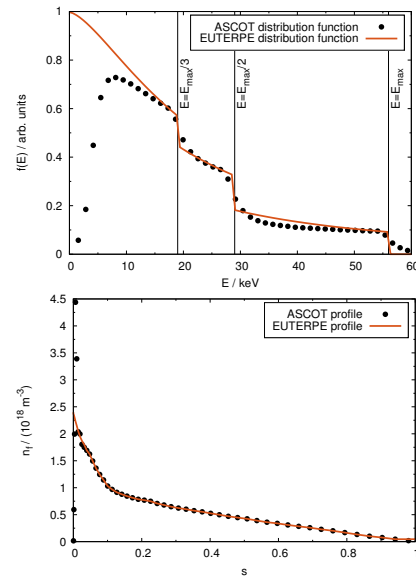


Figure 1: Fast-ion distribution function (top) and density profile (bottom) provided by ASCOT (black dots) and used in EUTERPE (red line).

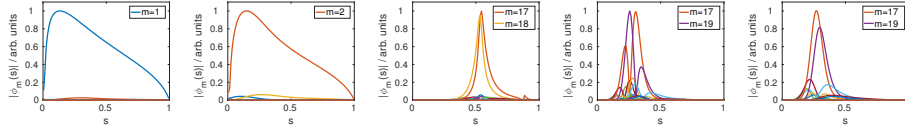


Figure 2: Alfvén eigenmodes found in the W7-X high-mirror configuration. From left to right: GAE ($m = 1; n = -1$), GAE ($m = 2; n = -2$), TAE ($m = 17, 18; n = -16$), even EAE ($m = 17, 19; n = -16$), odd EAE ($m = 17, 19; n = -16$).

the red line is the fit that is used in EUTERPE. The distribution function provided by ASCOT is non-uniform in the pitch-angle variable $\xi = v_{\parallel}/v$. For our EUTERPE simulations, on the other hand, a uniform distribution is used as a first approximation. The generalization to a pitch-angle-dependent distribution function is straightforward and will be reported elsewhere.

The fast-ion density profile used in all simulations is shown in Fig. 1 (bottom). The density gradient provides the source of free energy that can potentially drive Alfvén eigenmodes (AEs) unstable. Note that the density profile computed by ASCOT is noisy close to the magnetic axis. Therefore, the density profile is smoothed for usage in EUTERPE. Since the AEs that will be studied later are localized at larger radii (see Fig. 2), it is a reasonable assumption that the growth rates are independent of the exact shape of the density profile in the core of the plasma.

The profiles of the background plasma are determined by NTSS [7] calculations. The on-axis values $n_{i,0} = n_{e,0} = 5.0 \cdot 10^{19} \text{ m}^{-3}$ (hydrogen), $T_{i,0} \cong 2.5 \text{ keV}$, $T_{e,0} \cong 4.5 \text{ keV}$ are close to the parameters envisaged for W7-X OP 1.2b plasmas where NBI will be available.

Eigenmodes found by CKA

Several AEs – possible candidates for the destabilization by fast ions – are found in this W7-X high-mirror configuration using CKA. The radial mode structures (indicating also the mode numbers) are shown in Fig. 2. Of lowest frequency are two global Alfvén eigenmodes (GAEs) that fulfil $|m| = |n|$. Therefore, they are classified as so-called isomon modes [8]. At higher frequencies, a toroidicity-induced Alfvén eigenmode (TAE) and two ellipticity-induced Alfvén eigenmodes (EAEs)

are found by CKA. All these AEs are located at different radial positions and have different frequencies. It is therefore expected that they will react differently to the fast-ion drive. The

Table 1: Frequencies and linear growth rates of the Alfvén eigenmodes shown in Fig. 2.

	ω/s^{-1}	γ/s^{-1}
$m = 1$ GAE	$2.772 \cdot 10^5$	$1.149 \cdot 10^3$
$m = 2$ GAE	$3.029 \cdot 10^5$	$2.505 \cdot 10^3$
TAE	$4.436 \cdot 10^5$	$1.008 \cdot 10^3$
even EAE	$8.306 \cdot 10^5$	$5.033 \cdot 10^2$
odd EAE	$8.522 \cdot 10^5$	$5.852 \cdot 10^2$

mode frequencies ω and growth rates γ_L obtained from a linear calculation are listed in Tab. 1. Since the growth rate is predicted to scale as [9, 10]

$$\gamma_L \sim m \frac{\omega_*}{\omega} - 1, \quad (1)$$

where ω_* denotes the diamagnetic drift frequency of the fast ions, it is not surprising that modes at higher frequency have a smaller linear growth rate. Finite-Larmor-radius effects reduce the growth rate and become more important for high- m modes.

Non-linear results

In order to numerically determine the saturation levels of the modes in non-linear calculations, a damping rate γ_d must be present. For $\gamma_d = 0$, a sub-exponential drift after the initial linear phase is observed. Note that in CKA-EUTERPE, γ_d is an externally specified parameter.

Since the growth rates of the modes are small, and still we want to save computation time, the following approach is pursued: We artificially increase the growth rate by a factor $\alpha > 1$. We then specify a damping rate $\gamma_d = (\alpha - 1)\gamma_L$, such that $\alpha\gamma_L - \gamma_d = \alpha\gamma_L - (\alpha - 1)\gamma_L = \gamma_L$ is the original linear growth rate. For practical purposes, $\alpha = 5.5$ has been chosen. Since the physical damping rate is missing, this approach corresponds to a maximal estimate of the saturation levels.

Fig. 3 shows the time traces of the perturbed poloidal magnetic field associated with the mode. A fast-ion collision operator was present in the numerical simulations, since collisions play an important role in the formation of the distribution function and can also influence the non-linear dynamics of AEs [4]. At $s = 0.5$, the critical velocity and slowing-down time are $v_c \cong 2.23 \cdot 10^6$ m/s and $\tau_s \cong 60$ ms, respectively. All modes saturate in the range of $\delta B/B_0 = 10^{-4} - 10^{-3}$.

The modes cause radial transport of fast ions as is indicated in Fig. 4. The flattening of the fast-ion

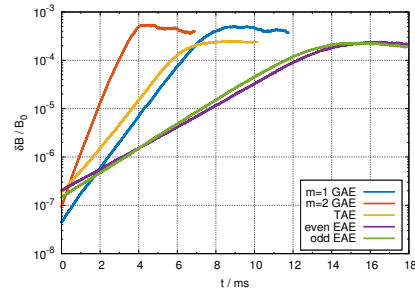


Figure 3: Time traces of the perturbed poloidal magnetic field associated with the modes shown in Fig. 2. The non-linear simulations include a fast-ion collision operator.

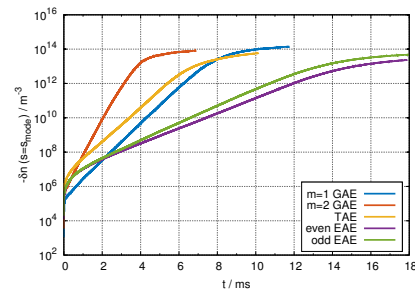


Figure 4: Change of the fast-ion density profile at the radial positions where the modes shown in Fig. 2 have their respective maximum.

density profile is on the order of $\delta n \cong -10^{14} \text{ m}^{-3}$

at the maximum position of the mode and thus four orders of magnitude lower than the value of the fast-ion density profile at this point. Higher saturation levels lead to an increased fast-ion transport. A similar observation has been made in Ref. [4].

So far only the drive of the modes due the presence of fast ions has been addressed. However, to make a prediction whether the modes will be unstable in the experiment requires also knowledge of the damping rates. The radiative damping rates of the gap modes have been estimated using the reduced model of STAE-K [10]. The GAEs cannot be addressed using STAE-K. For the TAE we find $\gamma_d/\omega = -6\%$. The even and odd EAEs have lower normalized damping rates of -0.7% and -0.5% , respectively. In any case, the damping rate exceeds the linear growth rate which means that, for the case studied, the fast-ion drive is likely not sufficient to destabilize gap modes.

Summary

We have investigated possible fast-ion driven modes in a Wendelstein 7-X high-mirror configuration for plasmas expected in the up-coming operation phase 1.2b.

Of all AEs investigated here the GAEs have the highest saturation levels and normalized growth rates. Our results are in agreement with the value of $\gamma_r/\omega = 10^{-3} - 10^{-2}$ given in Ref. [8]. Due to their radially extended mode structure, they might be the easiest to be excited by fast ions. In order to predict which modes will be unstable in the experiment, more work is needed to accurately compute damping rates.

Acknowledgement

The simulations were partly performed on the MARCONI supercomputer (CINECA).

This work has been carried out within the framework of the EUROfusion Consortium and has received funding from the Euratom research and training programme 2014-2018 under grant agreement No 633053. The views and opinions expressed herein do not necessarily reflect those of the European Commission.

References

- | | |
|---|---|
| [1] H. H. Duong <i>et al.</i> , Nucl. Fusion 33 , 749 (1993) | [6] E. Hirvijoki <i>et al.</i> , Comp. Phys. Comp. 185 , 1310 (2014) |
| [2] G. Grieger <i>et al.</i> , Phys. Fluids B (7), 2081 (1992) | |
| [3] T. B. Fehér, Ph.D. thesis, University Greifswald, 2013 | [7] Y. Turkin <i>et al.</i> , Phys. Plasmas 18 , 022505 (2011) |
| [4] C. Slaby <i>et al.</i> , Nucl. Fusion, accepted (2018) | [8] Ya. I. Kolesnichenko <i>et al.</i> Nucl. Fusion 56 , 066004 (2016) |
| [5] J. A. Heikkinen, S. K. Sipilä, Phys. Plasmas 2 , 3724 (1995) | [9] G. Y. Fu <i>et al.</i> , Phys. Fluids B (11), 3722 (1992) |
| | [10] C. Slaby <i>et al.</i> , Phys. Plasmas 23 , 092501 (2016) |

Parametric study of fast-ion-driven modes in Wendelstein 7-X (A.4)

Full citation:

C. Slaby, A. Könies, R. Kleiber, S. Äkäslompolo, and J. Kontula. Parametric study of fast-ion-driven modes in Wendelstein 7-X. *Journal of Physics: Conference Series*, **1125** 012019 (2018).

DOI:

10.1088/1742-6596/1125/1/012019 (<https://doi.org/10.1088/1742-6596/1125/1/012019>)

Reproduced under CC BY 3.0 License (<https://creativecommons.org/licenses/by/3.0/>).

Appendix A. Thesis articles

Parametric study of fast-ion-driven modes in Wendelstein 7-X

C Slaby¹, A Könies¹, R Kleiber¹, S Äkäslompolo¹ and J Kontula²

¹ Max-Planck-Institut für Plasmaphysik, Greifswald, Germany

² Aalto University, Aalto, Finland

E-mail: christoph.slaby@ipp.mpg.de

Abstract. In the 2018 experimental campaign, fast ions in the stellarator Wendelstein 7-X will be generated by neutral beam injection. Later operation phases will also include ion cyclotron resonance heating. The fast ions may excite instabilities in the plasma which can lead to enhanced fast-ion transport and can, in severe cases, cause damage to plasma-facing components.

We present a numerical study of fast-ion-driven Alfvén eigenmodes in a Wendelstein 7-X high-mirror equilibrium. Realistic fast-ion parameters are obtained using the ASCOT code. To model the instabilities, we use the CKA-EUTERPE code package. This model is perturbative, since a fixed mode structure – computed by the ideal-MHD code CKA – is used throughout the calculation. The non-linear gyro-kinetic code EUTERPE computes the power transfer from the fast particles to the mode which defines the growth rate of the instability.

We show that having a fast-ion collision operator present in the simulations is required to accurately predict the non-linear saturation level of the mode. The scaling of the saturated amplitude with respect to fast-ion drag and the pitch-angle collision frequency is investigated and found to vary for different Alfvén eigenmodes.

Furthermore, we study the impact of several other actuators that might be of experimental relevance for finding operation windows that show Alfvén-eigenmode activity. Examples are the effects of a radial electric field and the composition of the background plasma (hydrogen versus helium). While growth rates are found to be reduced in helium plasmas, including a radial electric field, typically present in Wendelstein 7-X, seems to have little influence on the modes.

1. Introduction

The 2018 experimental campaign of Wendelstein 7-X (W7-X), for the first time, includes neutral beam injection (NBI). This system supplies energetic ions, which heat the plasma via collisional energy exchange. The fast ions thermalize and eventually become part of the background plasma, thus contributing to fuelling. While slowing down, the parallel velocity of a fast ion can become resonant with the phase velocity of Alfvén eigenmodes (AEs) present in the plasma. In that case a resonant transfer of energy from the fast ion to the mode takes place [1]. The mode can grow in amplitude and influence the particle trajectories. This re-distribution of highly energetic ions could potentially damage the device [2].

A number of AEs, and their possible destabilization by fast ions, was recently investigated [3] (see that reference for details). We used a realistic fast-ion density profile and a slowing-down distribution function in energy space, both calculated by the ASCOT code [4, 5] for plasma parameters expected for the 2018 experimental campaign. While Ref. [3] reported on first



Content from this work may be used under the terms of the [Creative Commons Attribution 3.0 licence](https://creativecommons.org/licenses/by/3.0/). Any further distribution of this work must maintain attribution to the author(s) and the title of the work, journal citation and DOI.

Published under licence by IOP Publishing Ltd

results, we now aim to investigate further effects and possible experimental actuators that could influence the non-linear behaviour of the modes.

Firstly, we will describe the CKA-EUTERPE model used for the simulations. Secondly, we will investigate the wave-particle power transfer in phase space and compare the linear growth rates of the modes in hydrogen and helium plasmas. We will then study the effects of pitch-angle collisions and fast-ion drag on the non-linear saturation. Furthermore we investigate the effects of a radial electric field on the mode evolution, with emphasis on the non-linear phase. Finally, conclusions will be drawn.

2. The CKA-EUTERPE model

The CKA-EUTERPE code package [6] has recently been described in detail in Ref. [7]. For the sake of brevity, only the key aspects are repeated here.

CKA-EUTERPE combines the ideal-MHD eigenvalue code CKA and the global non-linear gyro-kinetic particle-in-cell code EUTERPE. A spatial mode structure and frequency are calculated using CKA by solving the eigenvalue problem

$$\omega^2 D_2 \phi_0(\mathbf{r}) = D_1 \phi_0(\mathbf{r}) \quad (1)$$

with linear differential operators D_1 and D_2 defined in Refs. [6, 7]. ω_0 and ϕ_0 denote the mode frequency and its electrostatic potential (spatial part), respectively. \mathbf{r} is the spatial position. Since ideal-MHD theory is employed, we can use the fact that the parallel electric field has to vanish in order to determine the vector potential

$$A_{\parallel,0} = \frac{i}{\omega} \mathbf{b} \cdot \nabla \phi_0, \quad (2)$$

where \mathbf{b} is a unit vector tangent to the background magnetic field.

ϕ_0 , $A_{\parallel,0}$, and ω are given to EUTERPE, which solves the gyro-kinetic equation

$$\frac{\partial f}{\partial t} + \dot{\mathbf{R}} \cdot \nabla f + v_{\parallel} \frac{\partial f}{\partial v_{\parallel}} + \dot{\mu} \frac{\partial f}{\partial \mu} = \mathcal{C}(f) \quad (3)$$

for the distribution function f of the fast particles (if the species index is omitted, fast ions are meant) moving in the external magnetic field as well as in the self-excited electromagnetic fields. Thus, the model is non-linear. The right-hand side of the kinetic equation includes a collision operator, which will be specified below. μ is the specific magnetic moment defined as $\mu = v_{\perp}^2 / (2B)$. The distribution function is split, $f = f^{(0)} + f^{(1)}$, with $f^{(0)}$ being the slowing-down distribution function of the fast ions and $f^{(1)}$ denoting the perturbation.

In the framework of CKA-EUTERPE no field equations need to be solved. The fast ions simply contribute to a time-dependent power transfer (see below), which is used to calculate the time development of the mode with a fixed spatial structure. Therefore, we can use the so-called v_{\parallel} -formulation of gyro-kinetic theory. The corresponding equations of motion for the marker particles can be found in Ref. [7].

Note that in the CKA-EUTERPE model the mode structure remains fixed, and only a complex amplitude is allowed to evolve in time. Thus, the model is perturbative and cannot capture fast-ion-induced mode structure modifications, but is much faster and more stable than fully gyro-kinetic approaches. The equations for the amplitudes of the electromagnetic potentials (denoted by a hat symbol) are

$$\frac{\partial \hat{\phi}}{\partial t} = i\omega (\hat{A}_{\parallel} - \hat{\phi}) + 2(\gamma(t) - \gamma_d) \hat{\phi} \quad \text{and} \quad \frac{\partial \hat{A}_{\parallel}}{\partial t} = i\omega (\hat{\phi} - \hat{A}_{\parallel}). \quad (4)$$

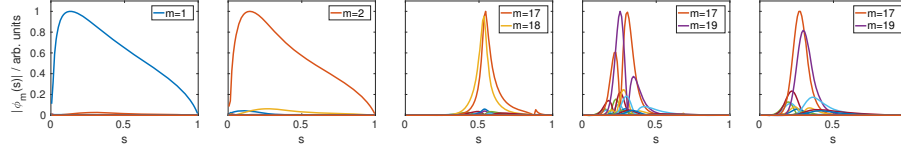


Figure 1. A selection of modes found by CKA. From left to right: ($m = 1/n = -1$) GAE, ($m = 2/n = -2$) GAE, ($m = 17, 18/n = -16$) TAE, ($m = 17, 19/n = -16$) EAE (even), ($m = 17, 19/n = -16$) EAE (odd). s is the normalized toroidal flux. Reproduced from Ref. [3].

They are derived from the quasi-neutrality equation – describing the background plasma with MHD theory and the fast ions gyro-kinetically – and Ampère’s law. Ref. [8] will describe the details of the model. The frequency of the mode may change as long as $\delta\omega/\omega \ll 1$ is fulfilled. This separation of time scales, where the oscillation of the mode is faster than the evolution of the amplitudes, has been used in the derivation of Eqs. (4). The time-dependent growth rate $\gamma(t) = T(t)/(2W)$ is defined as the quotient of the resonant wave-particle power transfer

$$T(t) = - \int d\Gamma B_{\parallel}^* \left[\frac{m}{ZeB} \mathbf{b} \times (v_{\parallel}^2 \boldsymbol{\kappa} + \mu \nabla B) \cdot (Ze \nabla_{\perp} \phi^*(\mathbf{r}, t) f^{(1)}) \right] \quad (5)$$

and the wave energy

$$W = \int d^3r \frac{\rho}{B^2} |\nabla_{\perp} \phi|^2. \quad (6)$$

The notation is conventional: B_{\parallel}^* denotes the Jacobian, $\boldsymbol{\kappa}$ is the curvature of the magnetic field \mathbf{B} with magnitude B , and ρ is the mass density of the plasma. The particle mass and charge are denoted by m and Ze , respectively. Finally, $d\Gamma$ indicates the integration over all of phase space. Note that the electrostatic potential (and similarly the parallel vector potential) is written as $\phi(\mathbf{r}, t) = \hat{\phi}(t) \phi_0(\mathbf{r}) \exp(i\omega t)$. The damping rate γ_d , describing continuum, radiative, and Landau damping, is a free parameter of the model. The choice of γ_d is outlined in Ref. [3].

The collision operator

$$\mathcal{C}(f) = \nu_D^{\text{fi}} \mathcal{L}(f) + \frac{1}{v^2} \frac{\partial}{\partial v} \left[v^3 \frac{m_f}{m_f + m_i} \nu_s^{\text{fi}} f \right] + \frac{1}{v^2} \frac{\partial}{\partial v} \left[v^3 \frac{m_f}{m_f + m_e} \nu_s^{\text{fe}} f \right] \quad (7)$$

used in this paper is a fast-ion collision operator that describes pitch-angle collisions with the background ions (the first term, \mathcal{L} , is the Lorentz operator) and friction with the entire background plasma (second and third term), respectively. In Eq. (7), ν_D labels the deflection frequency and ν_s is the slowing-down frequency. Energy diffusion is neglected. The labels i, e, f are used to denote ions, electrons, and fast ions, respectively.

This collision operator is the same as the one used in Ref. [3]. The implementation of the Lorentz operator into the electromagnetic version of EUTERPE has been benchmarked in Ref. [9] and was used for non-linear simulations in Ref. [7].

3. Modes

As in Ref. [3], we investigate a W7-X high-mirror equilibrium with plasma profiles as expected for the 2018 experimental campaign. In this magnetic configuration, five different AEs are studied, which are possible candidates to be destabilized by fast ions generated by the NBI system. The same modes have been investigated in Ref. [3], with the focus on the linear growth rates and non-linear saturation levels. Ref. [3] showed that the fast-ion drive could be insufficient

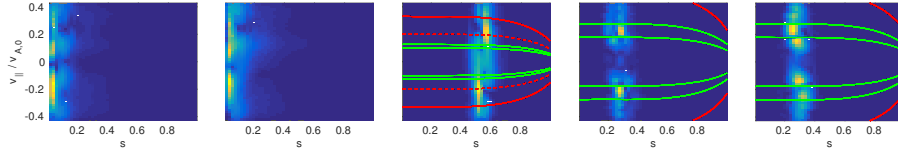


Figure 2. Absolute value of the wave-particle power transfer (arb. units) in the s - v_{\parallel} -plane for the modes shown in Fig. 1. The power transfer is strong where the gradient of the mode is large. The toroidal and helical resonances are shown as solid red and green lines for the gap modes. As shown for the TAE, the higher-order resonances (dashed red line) can play an important role.

to destabilize those modes. However, also the background plasma may contribute to the drive of the mode [10].

The radial mode structures are shown in Fig. 1. We study GAEs, EAEs, and a TAE. The latter two are gap modes (little continuum damping), but the GAEs could be subject to continuum damping. They are nevertheless added to our investigation, because they are expected to be easily destabilized in W7-X plasmas [11]. Since they fulfil $|m| = |n|$, they are called Isomon modes in Ref. [11].

4. Power transfer

It can be seen in Fig. 1 that especially the GAEs have a broad radial mode structure. In order to assess at which spatial position the drive is strongest, we investigate the wave-particle power-transfer in the s - v_{\parallel} -plane (integrating over poloidal and toroidal angle, and the magnetic moment). The results are shown in Fig. 2 for the same modes that were presented in Fig. 1. For the narrow gap modes, the drive is localized at the same radial position as the mode itself, which is expected. The broad GAEs, on the other hand, are not uniformly driven over their entire extent. Rather, the power transfer is restricted to a region where the mode structure exhibits the largest gradient. Comparing with Eq. (5), this is the expected behaviour.

In Fig. 2, the resonances (toroidal and helical Fourier components of the background magnetic field) are shown as solid red and green lines. They can be computed using

$$\frac{v_{\parallel}}{v_{A,\star}} = \left| 1 \pm 2 \frac{\iota_{\star} - \nu N}{\mu_0 \iota_{\star} - \nu_0 N} \right|^{-1} \quad (8)$$

for the well-localized gap modes [12]. Eq. (8) is not applicable to the GAEs, since for them a local approximation fails. Here, ι is the rotational transform, N denotes the number of field periods, μ_0, ν_0 determine the mode coupling, and ν relates to either the toroidal or helical resonance. Values that have to be taken at the mode localization region are indicated by a star.

For the TAE, the agreement with the simulated power transfer is not perfect. A possible explanation is that the drive could also come from higher-order resonances. This is shown for the TAE (middle plot), where the $v_{\parallel}/v_A = 1/5$ resonance (dashed red line) is found to agree well with the simulation.

It needs to be pointed out that the destabilization of the EAEs is particular to W7-X being a stellarator. The usual tokamak resonance of $v_{\parallel}/v_A = 1/2$ is not reached. Only the helical structure of the magnetic field provides additional resonances at lower velocities.

5. Growth rates in helium plasmas

While previous operation phases of W7-X relied on helium plasmas for high-density operation the 2018 experimental campaign will feature mostly hydrogen plasmas. There are however

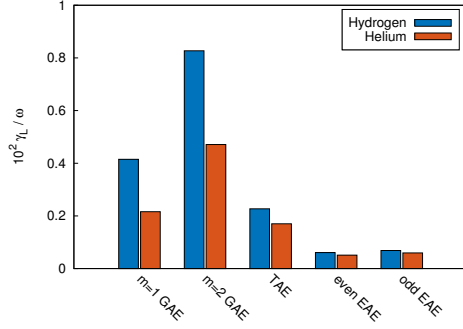


Figure 3. Linear growth rates (for $\gamma_d = 0$) of the five AEs shown in Fig. 1 normalized to their respective mode frequency. Lower normalized growth rates are observed in helium plasmas. The composition of the background plasma more strongly influences the low-frequency GAEs than the high-frequency EAEs.

proposals to study the effects of the background-plasma mass density on Alfvén-wave activity.

Fig. 3 shows the linear growth rates of the five AEs shown in Fig. 1 normalized to their respective mode frequency for hydrogen as well as helium plasmas. The fast ions injected into those plasmas are always protons. It can be seen that the normalized growth rates are generally reduced in helium plasmas. This effect is most pronounced for the GAEs. The EAEs, on the other hand, are barely influenced.

The reduction of the normalized growth rates in helium plasmas can be explained by a shift of the resonances. Given the injection parameters of the NBI system, at most $v_{\parallel}/v_A \approx 0.43$ can be reached for hydrogen. Taking the TAE as an example, $v_{\parallel}/v_A = 1/3$ and $v_{\parallel}/v_A = 1/5$ (higher-order resonance) are included, but the primary $v_{\parallel}/v_A = 1$ resonance is not. If helium is used instead, the Alfvén velocity drops, and the $v_{\parallel}/v_A = 1$ resonance becomes almost reachable. This mechanism would increase the drive in a tokamak. In a stellarator, however, the magnetic field also has helical Fourier harmonics, which in W7-X are larger than the toroidal Fourier harmonic. The additional helical resonances modify the shape of the resonance curve [13, 14]

$$\frac{\gamma}{\omega} \sim \sum_{j=\pm 1} \left[\epsilon_t^2 F(w_t^{(j)}) + \epsilon_h^2 F(w_h^{(j)}) \right] \quad (9)$$

$$F = w(1 + 2w^2 + 2w^4) \exp[-w^2] \quad (10)$$

so that the modes are more stable in helium than they are in hydrogen. Here, w is the resonant velocity and ϵ_t and ϵ_h denote the toroidal and helical Fourier components of the magnetic field, respectively.

This finding suggests that hydrogen plasmas could be more suitable for observing AE activity in W7-X in up-coming experimental campaigns.

6. The influence of collisions

It was reported in the past (see e.g. Refs. [7, 15, 16]) that collisions can influence the non-linear saturation levels of AEs. The fast-ion collision operator used here includes the effects of pitch-angle scattering and drag. In order to disentangle their contributions to the non-linear saturation, we vary the strength of both terms individually for the $m = 2$ GAE and the TAE. The results can be seen in Figs. 4 and 5, respectively. Both figures confirm the potentially strong influence of collisions on the saturation level. For the GAE, a 50% increase is possible. For the TAE, it is even possible to increase δB^{sat} (value of δB at the first maximum) by a factor of approximately 10. This emphasizes the tremendous importance of having a fast-ion collision operator present in non-linear simulations. At the radial position where the TAE is localized,

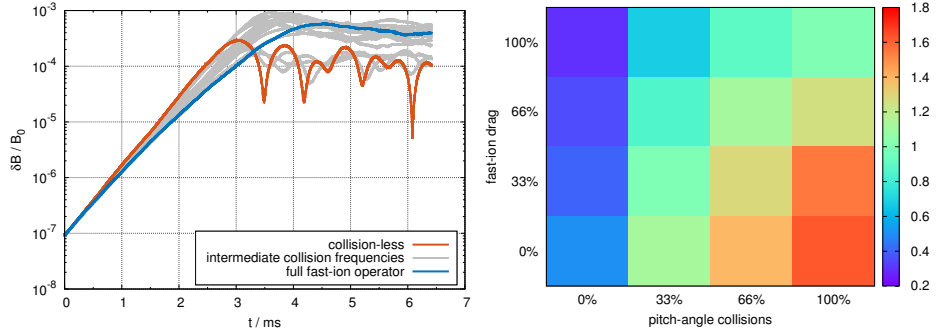


Figure 4. Time trace of the perturbed poloidal magnetic field of the $m = 2$ GAE for various strengths of the fast-ion collision operator (left). The right-hand side shows the value of $\delta B/B_0$ at saturation (normalized to the saturation level including the full collision operator) in colour code. Pitch-angle collisions increase the saturation level, while fast-ion drag lowers it.

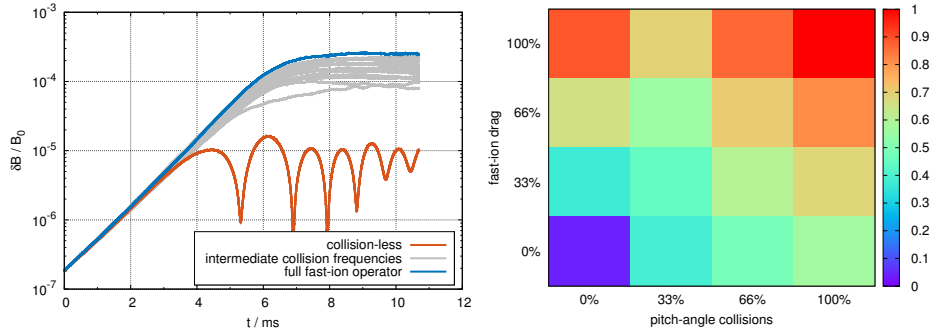


Figure 5. Same as Fig. 4, but for the TAE. Contrary to Fig. 4 ($m = 2$ GAE) both pitch-angle collisions and fast-ion drag increase the saturation level.

the basic collision frequencies (see Ref. [17] for their definition and relation to ν_D and ν_s) are $\nu_0^i = 48.8 \text{ s}^{-1}$ and $\nu_0^e = 38.3 \text{ s}^{-1}$.

Fast-ion drag and pitch-angle scattering are found to act differently on different AEs. In case of the GAE, there is a clear division: Pitch-angle scattering increases the saturation level while fast-ion drag lowers it, which means that the highest saturation level is not achieved with the self-consistent collision operator. The role of drag is different for the TAE, where it also acts to increase δB^{sat} . There seems to be a synergy between pitch-angle scattering and fast-ion drag, which is weakest at intermediate values of the pitch-angle collision frequency. The highest saturation level is obtained with the full fast-ion collision operator.

Pitch-angle scattering counteracts wave-particle trapping [15], the mechanism for saturation [15, 18], and thus allows for a higher saturation level. For the TAE, fast-ion drag has a similar effect. It needs to be pointed out that the radial positions of the $m = 2$ GAE and TAE are different. In this realistic scenario the density and temperature profiles are not flat, which makes the collision frequencies strong functions of the radial position. This could explain why fast-ion

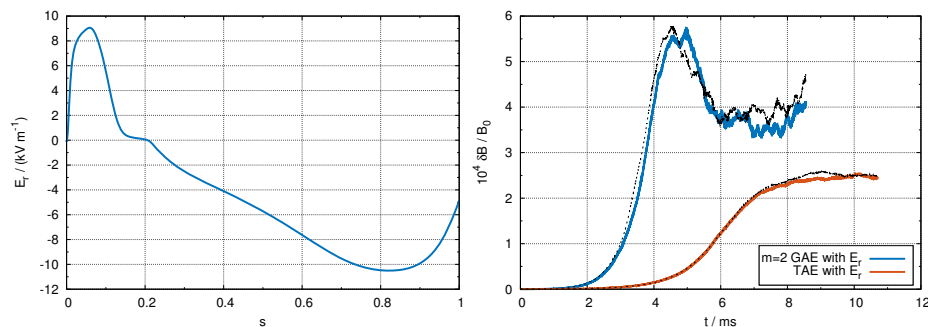


Figure 6. Radial structure of the radial electric field as determined by NTSS [19] calculations consistent with the input plasma profiles (left). On the right: E_r slightly modifies the non-linear dynamics of the TAE mode. The $m = 2$ GAE is also influenced in the linear phase. For reference, the black dashed lines are the cases without E_r . Overall, the impact of a radial electric field is very small.

drag acts differently on the two AEs. Another possibility is that the behaviour is due to the differences in the resonances.

7. The influence of a radial electric field

We would also like to investigate the impact of a radial electric field on the non-linear dynamics of the $m = 2$ GAE and the TAE. Here, we combine the calculations including E_r with the fully self-consistent fast-ion collision operator in order to progress to a more realistic case. Note however that the $\mathbf{E} \times \mathbf{B}$ Doppler shift of the mode frequency and a possible change of the MHD mode structure due to the radial electric field are neglected. Here, we just retain the influence of E_r on the particle motion. A more accurate treatment will be left for future work.

The radial shape of E_r is shown in Fig. 6 on the left-hand side. Over a wide radial range the radial electric field is negative (ion root). In the core, however, the radial electric field is positive, which corresponds to electron-root conditions. This is characteristic for low-plasma-density discharges in first operation phases of W7-X, in which core-localized electron heating usually dominates. The radial electric field leads via the $\mathbf{E} \times \mathbf{B}$ -drift to a further modification of the particle trajectories. This could potentially alter the wave-particle trapping mechanism and thus influence the saturation. How a radial electric field influences fast-ion-driven AEs has been considered in the past [20] for linear simulations. Here, we also consider the non-linear development of the mode.

The right-hand side of Fig. 6 shows the non-linear development of the amplitudes of the $m = 2$ GAE and of the TAE, respectively. Simulations including E_r are shown as solid lines, the ones without the radial electric field as black dashed lines. The figure shows that the saturation level stays nearly identical. (The other modes shown in Fig. 1 are found to behave similarly.) The linear growth rate reduces by 5% for the $m = 2$ GAE if the radial electric field is included. Overall, the impact of E_r on the mode dynamics is very small.

8. Summary and Conclusions

In this paper we studied several possible actuators that could be of experimental relevance for finding (or avoiding) operational conditions that show Alfvén-wave activity in Wendelstein 7-X (W7-X). Among the actuators investigated are the composition of the background plasma

(hydrogen vs. helium), fast-ion collisions, and the presence of a radial electric field. The present paper can be viewed as a continuation of Ref. [3] with the aim of testing the sensitivity of the results to the specifics of the input.

Five different Alfvén eigenmodes (AEs) in a W7-X high-mirror configuration were investigated. They are driven unstable by fast ions generated by neutral beam injection. The fast-ion density profile and distribution function in energy space were computed using the ASCOT code [4, 5]. The profiles of the background plasma were calculated by NTSS [19] for plasmas expected in the 2018 operational campaign of W7-X.

When looking at the power transfer in phase space, we saw that for the gap modes the drive comes from regions where the mode is localized. For the GAEs, the region of the drive coincides with the strongest gradient of the mode. We found that, due to the limited injection energy of the fast ions, EAEs can only be excited via the helical couplings present in a stellarator such as W7-X.

We also showed that the normalized growth rates of all AEs are lower in helium than in hydrogen. This could be explained by a shift of the resonances coupled with the existence of stellarator-specific helical Fourier components in W7-X. This result indicates that hydrogen plasmas might be a better candidate for observing AE activity. Furthermore, we could confirm that the role of the fast-ion collision operator is different for different AEs. Fast-ion drag increases the saturation level for the TAE, but decreases it for the $m = 2$ GAE. Since the collision frequencies are a strong function of density and temperature, this is a mechanism which could select a specific AE to be visible in specific experimental conditions. Finally, the role of a radial electric field was investigated. We found that for the specific case looked at, the presence of E_r does not affect the non-linear dynamics significantly. This may change if the full effect of the radial electric field is taken into account in CKA, which we plan for the future.

All simulations were carried out using the CKA-EUTERPE model [6]. It is a perturbative model that does not include fast-ion-induced mode-structure modifications. But since the fast-ion beta is low, such an approach seems justified. In a future work, the present results should nevertheless be compared to a fully gyro-kinetic simulation.

Acknowledgments

This work has been carried out within the framework of the EUROfusion Consortium and has received funding from the Euratom research and training programme 2014-2018 under grant agreement No 633053. The views and opinions expressed herein do not necessarily reflect those of the European Commission.

The simulations were performed on the MARCONI supercomputer (CINECA).

References

- [1] Heidbrink W W 2008 *Phys. Plasmas* **15** 055501
- [2] Duong H H, Heidbrink W W, Strait E J, Petrie T W, Lee R, Moyer R A and Watkins J G 1993 *Nucl. Fusion* **33** 749–765
- [3] Slaby C, Könies A, Kleiber R, Äkäslompolo S and Kontula J 2018 *Europhysics Conference Abstracts* **42A** P4.1098 URL <http://ocs.ciemat.es/EPS2018PAP/pdf/P4.1098.pdf>
- [4] Heikkinen J A and Sipilä S K 1995 *Phys. Plasmas* **2** 3724–3733
- [5] Hirvijoki E, Asunta O, Koskela T, Kurki-Suonio T, Miettunen J, Sipilä S, Snicker A and Äkäslompolo S 2014 *Comput. Phys. Commun.* **185** 1310–1321
- [6] Fehér T B 2013 *Simulation of the interaction between Alfvén waves and fast particles* Ph.D. thesis Ernst-Moritz-Arndt-Universität Greifswald
- [7] Slaby C, Könies A, Kleiber R and García-Regaña J M 2018 *Nucl. Fusion* **58** 082018
- [8] Könies A et al 2018 in preparation
- [9] Slaby C, Kleiber R and Könies A 2017 *Comput. Phys. Commun.* **218** 1–9
- [10] Könies A, Mishchenko A and Hatzky R 2008 *Theory of Fusion Plasmas* vol 1069 ed Garbet X, Sauter O and Sindoni E (New York: American Institute of Physics) pp 133–143

- [11] Kolesnichenko Y I, Könies A, Lutsenko V V, Drevlak M, Turkin Y and Helander P 2016 *Nucl. Fusion* **56** 066004
- [12] Kolesnichenko Y I, Lutsenko V V, Wobig H and Yakovenko Y V 2002 *Nucl. Fusion* **42** 949–958
- [13] Fu G Y and Dam J W V 1989 *Phys. Fluids B* **1** 1949–1952
- [14] Kolesnichenko Y I, Lutsenko V V, Wobig H and Yakovenko V 2002 *Phys. Plasmas* **9** 517–528
- [15] Berk H L, Breizman B N and Huanchun Y 1992 *Phys. Rev. Lett.* **68** 3563–3566
- [16] Lang J, Fu G and Chen Y 2010 *Phys. Plasmas* **17** 042309
- [17] Helander P and Sigmar D J 2002 *Collisional Transport in Magnetized Plasmas* (Cambridge University Press)
- [18] Briguglio S, Wang X, Zonca F, Vlad G, Fogaccia G, Troia C D and Fusco V 2014 *Phys. Plasmas* **21** 112301
- [19] Turkin Y, Beidler C D, Maaßberg H, Murakami S, Tribaldos V and Wakasa A 2011 *Phys. Plasmas* **18** 022505
- [20] Mishchenko A, Könies A, Fehér T, Kleiber R, Borchardt M, Riemann J, Hatzky R, Geiger J and Turkin Y 2014 *Nucl. Fusion* **54** 104003

Appendix A. Thesis articles

On non-linear frequency chirping in connection with collisions (A.5)

Full citation:

C. Slaby, A. Könies, R. Kleiber, and H. Leyh. On non-linear frequency chirping in connection with collisions. *submitted to Nuclear Fusion* (2018).

DOI:

10.1088/1741-4326/aafe31 (<https://doi.org/10.1088/1741-4326/aafe31>)

(for the published version of this article)

Reproduced with the permission of the IAEA and EUROfusion.

Appendix A. Thesis articles

On non-linear frequency chirping in connection with collisions

Christoph Slaby*, Axel Könies, Ralf Kleiber, and Henry Leyh

*Max-Planck-Institut für Plasmaphysik,
Wendelsteinstraße 1, 17491 Greifswald, Germany*

(Dated: December 10, 2018)

Abstract

The non-linear behaviour of toroidicity-induced Alfvén eigenmodes, destabilized by fast ions, is investigated in tokamak geometry and for a Wendelstein 7-X high-mirror equilibrium. Both cases show frequency chirping in the non-linear phase. The focus of this paper is on how particle collisions influence the non-linear dynamics and the associated frequency chirping. Pitch-angle scattering and fast-ion drag, which together are described by the fast-ion collision operator, are considered. We study the effect of a Krook operator, relaxing the distribution function to its unperturbed value, on the non-linear dynamics. The Krook operator leads to a periodic re-appearance of the chirping. This is also observed in experiments in which a fast-particle source is usually present.

The simulations are carried out using the non-linear and fully three-dimensional CKA-EUTERPE model. The model is perturbative in the sense that a fixed mode structure is used. Since such an investigation is undertaken for the first time for the stellarator Wendelstein 7-X, the tokamak case as well as analytical theory are used for comparison. The parameters of the fast-ion distribution function in Wendelstein 7-X are inspired by the 2018 experimental campaign which, for the first time, includes neutral beam injection to supply fast ions.

* E-mail address: christoph.slaby@ipp.mpg.de

I. INTRODUCTION

In plasmas that are relevant for nuclear fusion, there typically exists a small population of fast ions that are much hotter than the bulk of the plasma. In today's fusion experiments such particles are created by neutral beam injection (NBI) or ion cyclotron resonance heating (ICRH). In future fusion reactors, alpha particles created by the deuterium-tritium fusion reaction will be present. In order to heat the plasma, the fast ions need to remain in the plasma long enough to thermalize.

However, in the process of slowing down, the fast ions may resonantly interact with Alfvénic perturbations [15, 34]. This can lead to enhanced fast-ion transport and also to the ejection of fast ions from the confinement region, which implies energy losses [11, 37]. In severe cases, damage to plasma-facing components is possible [10, 11].

It depends on the magnetic equilibrium as well as on the fast-ion distribution function which Alfvén eigenmode (AE) in particular is most easily destabilized by the fast particles. A good overview is given in Ref. [18]. Typically, so-called gap modes that reside in frequency gaps of the shear Alfvén spectrum are likely to be unstable, because they experience only small continuum damping.

Especially with regard to future fusion reactors, an understanding of AE-induced fast-ion transport and redistribution has to be developed. Since the modes responsible for the redistribution are excited by the energetic ions themselves, the problem is non-linear. Analytical theory is available in the form of the simplified Berk-Breizman paradigm [1–4] which shows that a variety of non-linear behaviours – ranging from explosive, chirping, and periodic solutions to a steady-state dynamics – are possible. The analytical theory is able to identify some key parameters that govern the non-linear dynamics: The relative strength of damping and drive as well as diffusion and drag (i.e. collisions) are found to be important. Also the presence of particle sources can change the non-linear dynamics.

Frequency chirping has also been investigated experimentally in stellarators and tokamaks. AEs chirping in frequency are seen in the TJ-II stellarator in discharges that combine NBI and electron cyclotron resonance heating [31, 32]. A transition from a chirping state to a steady state is linked to variations of the magnetic configuration [31], i.e. equilibrium changes. The fast-ion transport induced by frequency-chirping AEs has been investigated in the ASDEX Upgrade tokamak [16]. Comprehensive non-linear simulations of chirping AEs, including equilibrium changes and collisions, have been carried out for JT-60U plasmas [6].

This paper reports on non-linear simulations of toroidicity-induced Alfvén eigenmodes (TAEs) in tokamak and stellarator plasmas. We choose the TAE modes destabilized by fast particles as an example, standing in for the class of all AEs. We focus on the frequency chirping of TAEs excited in realistic geometry. All cases chosen for this investigation show frequency chirping in the absence of collisions. We will then investigate the impact of various collision operators on the frequency chirping. This is the first time that such an investigation is undertaken for Wendelstein 7-X (W7-X). This study is of practical relevance for W7-X, since it is one step needed towards the development of a full fast-ion transport model, which is still lacking.

We use the CKA-EUTERPE code package [14] for our numerical simulations. The re-

duced ideal-magnetohydrodynamic (MHD) code CKA [13, 21] calculates the eigenmode (frequency and mode structure). In a separate step, the global non-linear gyro-kinetic electromagnetic particle-in-cell (PIC) code EUTERPE [20, 24] is used to compute the motion of marker particles in the pre-calculated field and the power transfer of the fast particles to the mode, which determines the temporal evolution of the mode amplitude. This approach is applied to two different magnetic configurations: We start by investigating how collisions influence the chirping in tokamaks. As an example, the ITPA benchmark case [22, 23] is used. Secondly, chirping TAEs influenced by collisions are simulated in a Wendelstein 7-X high-mirror equilibrium.

Various collision operators are explored in the paper. We start by using a simple pitch-angle scattering operator. The effect of pitch-angle scattering on the saturation amplitudes of TAEs in the ITPA tokamak and in W7-X was recently computed in Ref. [36]. The pitch-angle-scattering operator is, of course, just a first approximation of the full fast-ion collision operator, which also includes slowing-down drag. The effect of drag will be studied separately from the pitch-angle collisions. Finally, we will use a Krook term [5], emulating a particle source, to relax the distribution function towards its initial state. The Krook operator is linked to periodic, well separated chirping events that are routinely observed in experiments [16, 31, 32] and numerical simulations [25–27, 29].

Note that the effects of collisions on chirping have been studied extensively [3, 4, 25–30] in one-dimensional models that are related to the original Berk-Breizman paradigm. Relatively little work has been invested to study non-linear frequency chirping in two-dimensional (see e.g. Ref. [6] for simulation results on frequency chirping in JT-60U plasmas) or even three-dimensional devices. This is the reason why we start this investigation with the (relatively simple) ITPA benchmark case: We recover many features predicted by the Berk-Breizman theory, but now in a two-dimensional system. The magnetic geometry is still simple enough that this case can bridge the gap to the complex W7-X case, where it is investigated whether the fully three-dimensional system leads to differences compared with the analytical theory.

The paper is organized as follows: Sec. II elaborates on the existing theory and introduces our numerical tools. Sec. III describes both the tokamak and the W7-X case. The non-linear dynamics in the collisionless limit is, for comparison, given in this section. How these results change when collisions are taken into account is shown in Secs. IV and V. Finally, conclusions are drawn in Sec. VI.

II. THEORY AND ALGORITHMS

A. The numerical model of CKA-EUTERPE

The theory behind the model of CKA-EUTERPE has recently been described in Ref. [36]. Therefore, only the defining characteristics of the model will be repeated here.

The CKA-EUTERPE code package combines the reduced ideal MHD code CKA (Code for Kinetic Alfvén waves) with the global non-linear δf particle-in-cell code EUTERPE. Both are suited for fully three-dimensional geometries.

CKA is an eigenvalue code used to solve for the frequency ω of the mode as well as the mode structure (in terms of the electrostatic potential ϕ). Note that for vanishing

parallel electric field, the electrostatic potential and the parallel component of the vector potential, A_{\parallel} , are linked via

$$A_{\parallel} = \frac{i}{\omega} \mathbf{b} \cdot \nabla \phi. \quad (1)$$

(\mathbf{b} denotes a unit vector in the direction of the magnetic field, $\mathbf{B} = B\mathbf{b}$.) The Coulomb gauge is used and the perpendicular component of the vector potential (related to compression of the magnetic field) is neglected. No kinetic fast-ion effects are considered in CKA.

The mode frequency, electrostatic potential, and vector potential are passed to EUTERPE, which solves the gyro-kinetic equation

$$\frac{\partial f_s}{\partial t} + \dot{\mathbf{R}} \cdot \nabla f_s + \dot{v}_{\parallel} \frac{\partial f_s}{\partial v_{\parallel}} + \dot{\mu} \frac{\partial f_s}{\partial \mu} = C^{s\bar{s}}(f_s, f_{\bar{s}}) \quad (2)$$

for the distribution function of a species s including a collision operator $C^{s\bar{s}}(f_s, f_{\bar{s}})$. In the CKA-EUTERPE model only the fast ions are treated gyro-kinetically. Therefore the species index will be omitted hereafter. μ denotes the specific magnetic moment $\mu = v_{\perp}^2 / (2B)$. EUTERPE as a PIC code solves the kinetic equation by following numerical marker particles that move along the characteristics of Eq. (2). We split the distribution function into two parts, $f = f^{(0)} + f^{(1)}$, where $f^{(0)}$ is a time-independent background and $f^{(1)}$ denotes a perturbation, respectively. CKA-EUTERPE uses the so-called v_{\parallel} -formulation of gyro-kinetics. Hence, in the collisionless limit and with the non-linear terms retained the equations of motion for the particles (characteristics of Eq. (2)) are

$$\begin{aligned} \dot{\mathbf{R}} = & v_{\parallel} \mathbf{b} + \frac{m}{q} \left[\frac{\mu B + v_{\parallel}^2}{BB_{\parallel}^*} \mathbf{b} \times \nabla B + \frac{v_{\parallel}^2}{BB_{\parallel}^*} (\nabla \times \mathbf{B})_{\perp} \right] \\ & + \frac{v_{\parallel}}{BB_{\parallel}^*} [\mathbf{b} \times \nabla B + (\nabla \times \mathbf{B})_{\perp}] \langle A_{\parallel} \rangle + \frac{1}{B_{\parallel}^*} \mathbf{b} \times \nabla \langle \phi - v_{\parallel} A_{\parallel} \rangle \end{aligned} \quad (3)$$

$$\begin{aligned} \dot{v}_{\parallel} = & -\mu \nabla B \cdot \left[\mathbf{b} + \frac{m}{q} \frac{v_{\parallel}}{BB_{\parallel}^*} (\nabla \times \mathbf{B})_{\perp} \right] \\ & - \frac{v_{\parallel}}{BB_{\parallel}^*} [\mathbf{b} \times \nabla B + (\nabla \times \mathbf{B})_{\perp}] \cdot \nabla \langle \phi \rangle \end{aligned} \quad (4)$$

$$- \frac{\mu}{B_{\parallel}^*} \left[\mathbf{b} \times \nabla B \cdot \nabla \langle A_{\parallel} \rangle + \frac{1}{B} \nabla B \cdot (\nabla \times \mathbf{B})_{\perp} \langle A_{\parallel} \rangle \right]$$

$$\dot{\mu} = 0 \quad (5)$$

with

$$B_{\parallel}^* = B + \left[\frac{m}{q} v_{\parallel} + \langle A_{\parallel} \rangle \right] \mathbf{b} \cdot \nabla \times \mathbf{b}. \quad (6)$$

Here, m and q denote the particle mass and charge, respectively. The angular brackets, $\langle \dots \rangle$, denote the gyro-average. Note that the equation for \dot{v}_{\parallel} does not contain a time derivative of A_{\parallel} as we have used the $E_{\parallel} = 0$ constraint to replace this time derivative with the parallel gradient of ϕ .

We emphasize again that the mode structure is fixed throughout the calculation. Therefore, neither Poisson's equations nor Ampère's law have to be solved. We only need to consider the temporal evolution of the amplitudes (denoted by a circumflex below) of the electromagnetic potentials. The equations for the amplitudes are given as (We refer to Refs. [21, 36] for details.)

$$\frac{\partial \hat{\phi}(t)}{\partial t} = i\omega \left(\hat{A}_{\parallel} - \hat{\phi} \right) + 2(\gamma(t) - \gamma_d) \hat{\phi} \quad (7)$$

$$\frac{\partial \hat{A}_{\parallel}(t)}{\partial t} = i\omega \left(\hat{\phi} - \hat{A}_{\parallel} \right), \quad (8)$$

where $\gamma(t) = P/(2W)$ is a time-dependent growth rate that is computed from the wave-particle power transfer

$$P = - \int d\Gamma B_{\parallel}^* \left[\frac{m}{ZeB} \mathbf{b} \times \left(v_{\parallel}^2 \boldsymbol{\kappa} + \mu \nabla B \right) \cdot \left(Ze \nabla_{\perp} \phi^*(\mathbf{r}, t) f^{(1)} \right) \right] \quad (9)$$

and wave energy

$$W = \int d^3r \frac{\rho}{B^2} |\nabla_{\perp} \phi|^2. \quad (10)$$

Here, ρ is the mass density of the plasma, the particle charge is denoted by Ze , $\boldsymbol{\kappa}$ is the curvature of the magnetic field, and $d\Gamma$ denotes an infinitesimal phase-space element. The electrostatic potential is given by $\phi(\mathbf{r}, t) = \hat{\phi}(t) \phi_0(\mathbf{r}) \exp(i\omega t)$, where ϕ_0 denotes the MHD eigenfunction of the electrostatic potential calculated by CKA (similar for A_{\parallel}). In Eqs. (3) and (4), the real parts of the potentials are taken to compute the particle trajectories. γ_d is an externally specified damping rate. Note that while the mode varies on a short time scale, the amplitudes in Eqs. (7) and (8) evolve much more slowly. This fact has been used in the derivation of the amplitude equations. Thus the model is only applicable for chirping which satisfies $\delta\omega/\omega \ll 1$.

B. Collision operators

Throughout this paper various collision operators will be used and compared with each other. Since the focus is on TAEs excited by fast ions, we start with the general expression for a collision operator of test particles a colliding with a Maxwellian background [19] of particles b

$$C^{ab} \left(f_a^{(1)}, f_b^M \right) = v_D^{ab} \mathcal{L} \left(f_a^{(1)} \right) + \frac{1}{v^2} \frac{\partial}{\partial v} \left[v^3 \left(\frac{m_a}{m_a + m_b} v_s^{ab} f_a^{(1)} + \frac{1}{2} v_{\parallel}^{ab} v \frac{\partial f_a^{(1)}}{\partial v} \right) \right]. \quad (11)$$

The first term in this general collision operator describes pitch-angle scattering of species a with species b

$$v_D^{ab} \mathcal{L} = C_{\text{pitch}}^{ab} = \frac{v_D^{ab}}{2} \frac{\partial}{\partial \bar{\zeta}} \left(1 - \bar{\zeta}^2 \right) \frac{\partial}{\partial \bar{\zeta}}. \quad (12)$$

$\bar{\zeta} = v_{\parallel}/v$ denotes the pitch-angle variable,

$$v_D^{ab} = v_0^{ab} \frac{\Phi(x_b) - G(x_b)}{x_b^3} \quad (13)$$

is the deflection frequency of species a colliding with species b [19], and $x_s = v/(\sqrt{2}v_{\text{th},s})$ with $v_{\text{th},s} = \sqrt{k_B T_s/m_s}$. T denotes the temperature. Φ and G are the error function and the Chandrasekhar function, respectively. With n being the density, Z the charge number, e the electron charge, ϵ_0 the vacuum permittivity, and $\ln \Lambda$ the Coulomb logarithm, we will use [19]

$$\nu_0^{ab} = \frac{n_b Z_a^2 Z_b^2 e^4 \ln \Lambda}{4\pi\epsilon_0^2 m_a^2 2^{3/2} v_{\text{th},a}^3}, \quad (14)$$

with the density and temperature evaluated at the particle position, to determine the collision frequencies from the profiles. We will call this the self-consistent approach. However, in some cases it is enlightening to modify ν_0^{ab} in order to enforce a different non-linear behaviour of the system. Cases where this approach is pursued are indicated below. Note that in a realistic setting, the fast particles do not just collide among themselves. For typical fusion plasmas, the collision frequency with the bulk is many orders of magnitude larger, i.e. $\nu_0^{\text{fi}} \ll \nu_0^{\text{fi}}$. This motivates our approach to treat $\nu_0 = \sum_{\bar{s}} \nu_0^{\bar{s}}$ as an ‘effective’ collision frequency that contains different physics, depending on the case and which species are considered collisional. The letters ‘i’, ‘e’, and ‘f’ are used to label ions, electrons, and fast ions, respectively.

The implementation of the pitch-angle collision operator into EUTERPE is described in detail in Refs. [9, 36].

Furthermore, going back to Eq. (11), ν_s^{ab} is the slowing-down frequency defined as [19]

$$\nu_s^{ab} = \nu_0^{ab} \frac{2T_a}{T_b} \left(1 + \frac{m_b}{m_a}\right) \frac{G(x_b)}{x_a}, \quad (15)$$

and ν_{\parallel}^{ab} denotes the parallel velocity diffusion frequency [19]. To arrive at a fast-ion collision operator, we employ the following approximations:

1. The combination $a = \text{f}, b = \text{f}$ can be neglected due to the high temperature and small density of the fast particles.
2. Parallel velocity diffusion can be neglected in general, since its frequency is typically very small.
3. Pitch-angle scattering of the fast ions off electrons can be neglected due to the mass difference.

Under these circumstances the original operator can be significantly simplified to

$$\mathcal{C}_{\text{fast}}(f_{\text{f}}^{(1)}) = \sum_{\bar{s}=\text{i,e}} \mathcal{C}^{f\bar{s}}(f_{\text{f}}^{(1)}, f_{\bar{s}}^{\text{M}}) \quad (16)$$

$$\cong \nu_{\text{D}}^{\text{fi}} \mathcal{L}(f_{\text{f}}^{(1)}) + \frac{1}{v^2} \frac{\partial}{\partial v} \left[v^3 \frac{m_{\text{f}}}{m_{\text{f}} + m_{\text{i}}} \nu_{\text{s}}^{\text{fi}} f_{\text{f}}^{(1)} \right] + \frac{1}{v^2} \frac{\partial}{\partial v} \left[v^3 \frac{m_{\text{f}}}{m_{\text{f}} + m_{\text{e}}} \nu_{\text{s}}^{\text{fe}} f_{\text{f}}^{(1)} \right]. \quad (17)$$

The first term describes pitch-angle collisions between fast and bulk ions. The second and the third term describe the drag that the fast ions experience with the background ions and electrons, respectively.

It is tempting to further simplify the operator by using the fact that in fusion plasmas the fast particles are faster than the bulk ions, but still slower than the electrons. Therefore, one often uses the large-argument expansion of the Chandrasekhar function in the second term of Eq. (17). Accordingly, the third term is treated using the small-argument expansion, so that the operator can finally be written in the well-known form

$$\mathcal{C}_{\text{fast}}(f_f^{(1)}) \approx \nu_D^{\text{fi}} \mathcal{L}(f_f^{(1)}) + \frac{1}{v^2 \tau_s} \frac{\partial}{\partial v} \left[(v^3 + v_c^3) f_f^{(1)} \right], \quad (18)$$

where τ_s and v_c denote the slowing-down time and the critical velocity (below which ion drag is stronger than electron drag), respectively:

$$\tau_s = \frac{3(2\pi)^{3/2} \epsilon_0^2 m_f k_B^{3/2} T_e^{3/2}}{Z_f^2 e^4 \sqrt{m_e} n_e \ln \Lambda} \quad (19)$$

$$v_c = \sqrt{2} v_{\text{th},e} \left(\frac{n_i Z_i^2 3\sqrt{\pi} m_e}{n_e 4m_i} \right)^{1/3}. \quad (20)$$

However, the approximated operator given in Eq. (18) presents certain challenges in practical applications. The approximation is only valid as long as $v_{\text{th},e} \gg v_{\text{th},f} \gg v_{\text{th},i}$ is fulfilled. In a PIC code, however, the particles are loaded with a velocity distribution where some ‘fast’ particles will have velocities comparable to the bulk ions making the classification as fast particles misleading. Especially for those slow particles, the effect of drag is greatly enhanced by the approximations. In a stellarator this can lead to a localization (trapping) of particles in regions of low magnetic field strength. This localization of particles with respect to the toroidal angle of the device conflicts with the parallelization scheme (domain decomposition) and can lead to a severe load imbalance. This is the reason why we do not use the simplified fast-ion collision operator often cited in the literature, but instead use the one given by Eq. (17).

Recall that this operator is composed of a pitch-angle part and a drag part. In the code, an operator splitting is employed. The pitch-angle part can be treated in the way described in Refs. [9, 36]. The drag part, which contains only a first-order derivative with respect to velocity, can be incorporated into the regular equations of motion, i.e. the derivative $\partial/\partial v$ is translated into $\partial/\partial v_{\parallel}$ and $\partial/\partial \mu$ derivatives that are added to Eqs. (4) and (5). One finds that the changes of v_{\parallel} and μ due to drag are

$$\dot{v}_{\parallel, \text{drag}} = -2^{3/2} T_f v_{\text{th},f} \left[\frac{v_0^{\text{fi}}}{T_i} G(x_i) + \frac{v_0^{\text{fe}}}{T_e} G(x_e) \right] \zeta \quad (21)$$

$$\dot{\mu}_{\text{drag}} = -2^{3/2} T_f v_{\text{th},f} \left[\frac{v_0^{\text{fi}}}{T_i} G(x_i) + \frac{v_0^{\text{fe}}}{T_e} G(x_e) \right] \frac{v(1-\zeta^2)}{B}. \quad (22)$$

The last operator that will be used in this paper is a simple Krook operator [5]. The role of this operator is to relax the distribution function to its unperturbed state by damping the perturbation at rate ν_{Krook} .

Since we use the so-called v_{\parallel} -formulation of gyro-kinetics, the Krook operator is defined as

$$\mathcal{C}_{\text{Krook}}(f^{(1)}) = -\nu_{\text{Krook}} f^{(1)} = -\nu_{\text{Krook}} (f - f^{(0)}). \quad (23)$$

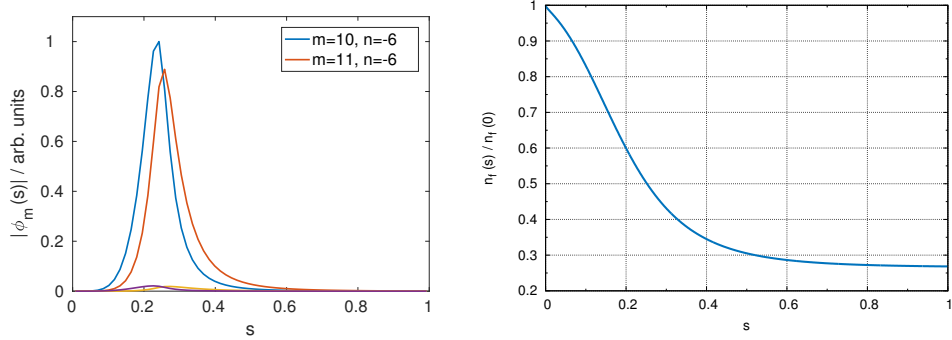


Figure 1: Mode structure (left) and normalized fast-ion density profile (right) for the ITPA case.

The motivation of using a Krook operator is as follows: Recall that in the one-dimensional Berk-Breizman paradigm a gradient in velocity space is the source of the instability. This explains the very strong influence of pitch-angle collisions (acting in velocity space) within that model. In our case, the TAE is destabilized by a density gradient in real space. Accordingly, pitch-angle collisions will have a different effect on the non-linear dynamics in the present case. Therefore, we use a Krook operator to relax the distribution function to its initial state and thus to rebuild the gradients in real space. In this way the Krook operator can play a comparable role in our model as pitch-angle collisions do in the Berk-Breizman framework.

Throughout the paper, guiding-centre diffusion due to collisions is neglected.

III. CASES AND COLLISIONLESS RESULTS

In this section, we investigate the non-linear chirping behaviour of the ITPA tokamak case [22, 23] as well as that of a Wendelstein 7-X high-mirror case. The magnetic equilibrium and properties of the fast-particle distribution function are described briefly in this section. For later comparison, we will present the collisionless results here.

A. Case description

The ITPA tokamak case [22, 23] has been studied extensively in the past. The radial mode structure and the fast-ion density profile are shown in Fig. 1. The radial coordinate s denotes the normalized toroidal flux. The background-plasma density and temperature profiles are flat with $n_i = n_e = 2.0 \cdot 10^{19} \text{ m}^{-3}$ and $T_i = T_e = 1 \text{ keV}$, respectively. We take the usual TAE mode, but vary the fast-ion content in the plasma in order to change the linear growth rate $\gamma_L = \gamma(t) + \gamma_d$ and thus cause different non-linear scenarios. $\gamma(t)$ is the instantaneous growth rate as measured by the code. It is constant in the linear phase and drops when saturation is reached. Thus, γ_L is only meaningful in the linear phase and corresponds to the growth rate without damping. The on-axis

Table I: Fast-ion densities and resulting linear growth rates for the tokamak cases.

case	Density $n_f(0) / \text{m}^{-3}$	Linear growth rate γ_L / s^{-1}
tokamak case 1	$7.24 \cdot 10^{16}$	$1.25 \cdot 10^4$
tokamak case 2	$2.51 \cdot 10^{17}$	$4.05 \cdot 10^4$
tokamak case 3	$5.03 \cdot 10^{17}$	$7.53 \cdot 10^4$

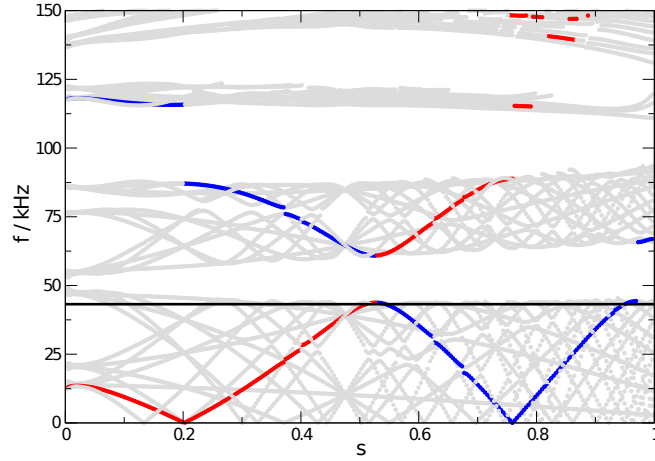


Figure 2: The shear Alfvén continuum for the W7-X high-mirror configuration. While most of the continuum branches are shown in grey, the relevant branches have been coloured. The TAE frequency is shown as a solid black horizontal line and lies at the lower edge of the TAE gap. The mode is radially located near the avoided crossing of the coloured branches.

values of the fast-ion density and the resulting linear growth rates γ_L for the different cases (denoted as tokamak case 1, 2, and 3) are given in Tab. I. They all share a common value for the damping rate $\gamma_d = 1.05 \cdot 10^4 \text{ s}^{-1}$. This value for γ_d is chosen, because it is the standard value for the ITPA benchmark case.

For W7-X, a high-mirror configuration is studied. The shear Alfvén wave continuum for this equilibrium is shown in Fig. 2. The relevant continuum branches ($m = 17$ in blue and $m = 18$ in red) are coloured and the TAE frequency is indicated as a solid horizontal line. The toroidal mode number is $n = -16$. Note that, while the magnetic equilibrium is the same as in Ref. [36], not the same mode is investigated. We follow Ref. [21] and study a slightly more core-localized TAE with higher mode numbers (which leads to a more narrow radial mode structure) that is more readily comparable with the tokamak case. The radial mode structure and fast-ion density profile for W7-X are shown in Fig. 3. For simplicity, the background-plasma density and temperature profiles are flat. We choose $n_i = n_e = 10^{20} \text{ m}^{-3}$ and $T_i = T_e = 3 \text{ keV}$, respectively.

Also for W7-X, two cases are compared with each other. They are denoted as W7-X

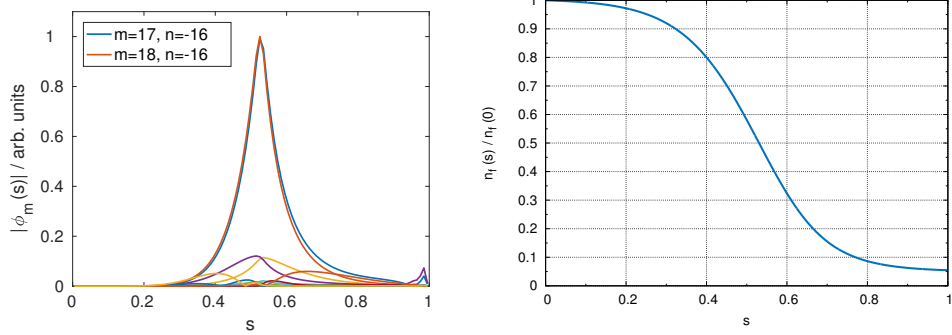


Figure 3: Mode structure (left) and normalized fast-ion density profile (right) for the W7-X case.

Table II: Fast-ion densities and resulting linear growth rates for the W7-X cases.

case	Density $n_f(0) / \text{m}^{-3}$	Linear growth rate γ_L / s^{-1}
W7-X case 1	$1.2 \cdot 10^{19}$	$1.19 \cdot 10^4$
W7-X case 2	$6.0 \cdot 10^{18}$	$5.90 \cdot 10^3$

case 1 and 2. Again, the on-axis values of the fast-ion density as well as the linear growth rates are given in Tab. II. The damping rates are chosen as $\gamma_d = 9.6 \cdot 10^3 \text{ s}^{-1}$ and $\gamma_d = 4.8 \cdot 10^3 \text{ s}^{-1}$ for cases 1 and 2, respectively. Choosing these values is motivated by trying to make the ratio γ_L/γ_d similar to the tokamak case 1. Note that the fast-ion density is very high for the W7-X cases. This is done to make the drive comparable to the ITPA tokamak case in which a high fast-ion temperature of 400 keV is used. Since the fast-ion temperature in W7-X is much lower (see below), the density needs to be increased accordingly.

Note that the velocity-dependent part of the fast-ion distribution function is different for the ITPA case and the W7-X case: We use a Maxwellian distribution function for the ITPA case. The fast particles, which are deuterium ions, have the standard temperature of $T_f = 400 \text{ keV}$. The fast-ion temperature profile is flat so that the density gradient is the only source of free energy for the instability.

For the W7-X case, on the other hand, a more realistic slowing-down distribution function with three distinct energy levels

$$f^{(0)} = C \sum_{i=1}^3 \frac{w_i}{v^3 + v_c^3} H(v_{b,i} - v) \quad (24)$$

is used (H denotes the Heaviside step function). As is well known, not only atomic hydrogen, but also molecules can be accelerated in the NBI system. This leads to the step-like shape of the distribution function, whose parameters (beam velocity levels and corresponding weights) are listed in Tab. III. The highest beam velocity corresponds to an energy of 55 keV of the injected protons. The critical velocity v_c is computed

Table III: Parameters of the fast-ion distribution function for the W7-X cases.

i	Velocities $v_{b,i} / \text{ms}^{-1}$	Weights w_i
1	$3.28 \cdot 10^6$	0.398
2	$2.34 \cdot 10^6$	0.347
3	$1.92 \cdot 10^6$	0.255

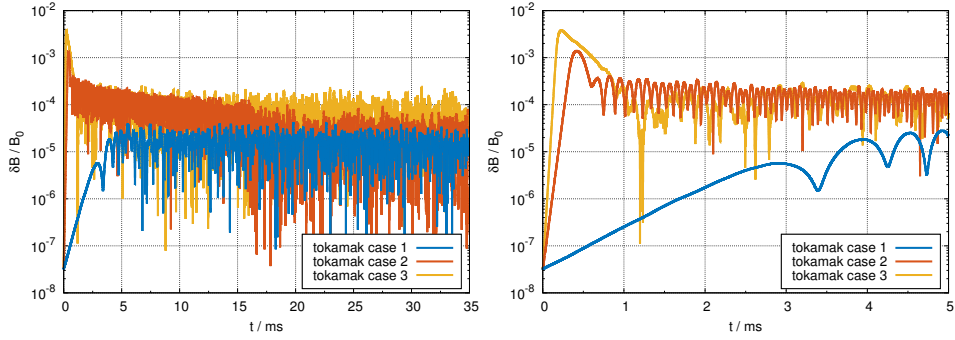


Figure 4: Time traces of the perturbed poloidal magnetic field for the tokamak cases investigated. Calculations are carried out for a long time into the non-linear phase. The left-hand side shows the whole simulation, while the right-hand side shows a zoomed-in view at the time when the initial saturation occurred.

according to Eq. (20) taking into account the temperature and density dependencies. The normalization constant C is determined numerically. Again, the fast-ion density gradient is the source of free energy that drives the instability.

It has to be mentioned here that the collision frequencies are very different for the ITPA case and for W7-X, respectively. To illustrate this fact, we give here the fast-ion self-collision frequencies (see Eq. (14)) at the respective mode maxima. While for the ITPA case the collision frequency is $\nu_0^{\text{ff}} = 2.8 \cdot 10^{-4} \text{ s}^{-1}$, the collision frequency is about four orders of magnitude higher for W7-X, $\nu_0^{\text{ff}} = 7.1 \text{ s}^{-1}$. This is due to the higher density and lower temperature of the fast ions.

B. Collisionless results

All these cases have been chosen because they exhibit frequency chirping in the non-linear phase of a collision-less simulation. Before showing how collisions can potentially alter the behaviour of the mode in the non-linear phase and how this affects the chirping, we will present the collisionless results for later comparison.

The temporal evolution of the perturbed magnetic field attributed to the mode (δB is defined as global maximum of the perturbed poloidal magnetic field) is shown in Fig. 4 for the ITPA case. Fig. 5 depicts the W7-X high-mirror case. In either case, the simu-

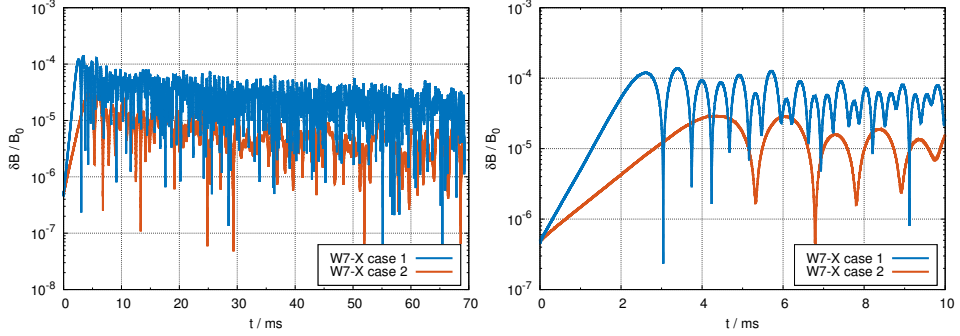


Figure 5: Same as Fig. 4, but for W7-X.

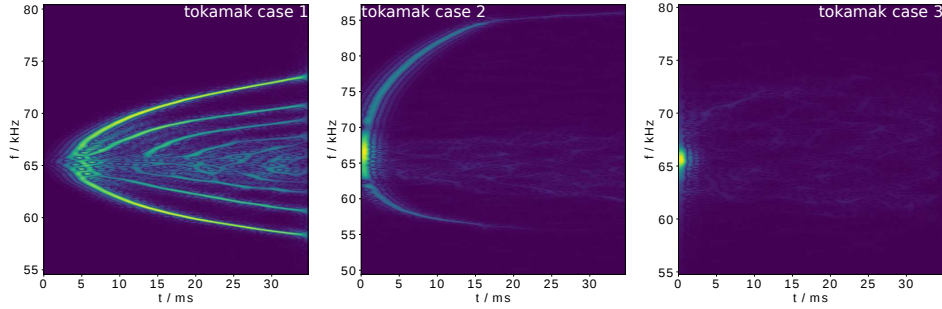


Figure 6: Spectrograms of the perturbed electrostatic potential for the different tokamak cases. The linear growth rate increases from case 1 to 3. This clearly influences the frequency chirping. While the chirping is only slightly asymmetric for case 1, it becomes very asymmetric for case 2 and has finally completely vanished for case 3.

lations extend for a long time into the non-linear phase. This is necessary in order to capture the frequency chirping with sufficient accuracy. Note that especially for W7-X it is crucial to check the time step for convergence.

The time trace of the perturbed electrostatic potential (whose envelope is directly proportional to $\delta B(t)$ for CKA-EUTERPE) is used to generate the spectrograms shown in Figs. 6 and 7 for the ITPA case and the W7-X case, respectively. Throughout this work the so-called S-method [7] is used to generate the spectrograms. This method includes a parameter λ , which can be used to ‘interpolate’ between a short-time Fourier transform ($\lambda \rightarrow 0$) and the Wigner distribution ($\lambda \rightarrow \infty$). For the ITPA case, we use every 5th value in the time trace of the electrostatic potential and $\lambda = 10$ to generate the spectrograms. For W7-X, since the time step is smaller, we use every 10th value and $\lambda = 5$ instead.

Even though the time traces of the perturbed magnetic field (see Figs. 4 and 5) do not look very different in the non-linear phase, the frequency chirping is strikingly different (see Figs. 6 and 7). Symmetric, asymmetric, and vanishing chirping are possible for

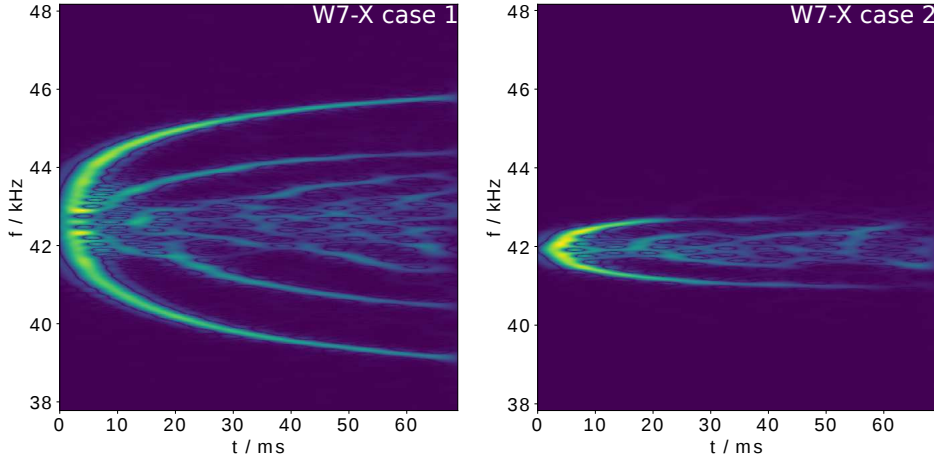


Figure 7: Spectrograms of the perturbed electrostatic potential for the different W7-X cases. Case 1 has twice the linear growth rate and twice the damping rate compared to case 2. It therefore shows a wider chirping parabola.

both the tokamak and the stellarator. Which chirping scenario is realized depends on the linear growth rate and the damping rate. (That all the cases have a different linear growth rate is clearly visible on the right-hand side of Figs. 4 and 5.) Ref. [21] will discuss the influence of γ_L and γ_d on the frequency chirping in greater detail. In the following, we pick only the cases that showed the most symmetric chirping (tokamak case 1 and W7-X case 1) in order to assess the influence of different collision operators on the non-linear dynamics.

IV. NON-LINEAR BEHAVIOUR INCLUDING COLLISIONS – ITPA TOKAMAK CASE

A. Changes induced by pitch-angle collisions

After having established a solid baseline of what scenarios to expect non-linearly without collisions, we now include pitch-angle collisions in the simulations and investigate how the frequency chirping changes. Different cases are considered: Firstly, we will use the self-consistently calculated self-collision frequency of the fast ions given by Eqs. (13) and (14). Subsequently, in order to emulate the fact that the fast ions do not only collide with themselves, but mainly with background ions and electrons, we will multiply the self-consistent value by 10 and by 100.

As a representative of the ITPA case, we investigate the symmetric tokamak case 1. Fig. 8 shows how the time trace of the perturbed magnetic field changes when pitch-angle collisions with varying collision frequency are taken into account. The right-hand side of Fig. 8 shows a zoomed-in view on the initial saturation. Several observations

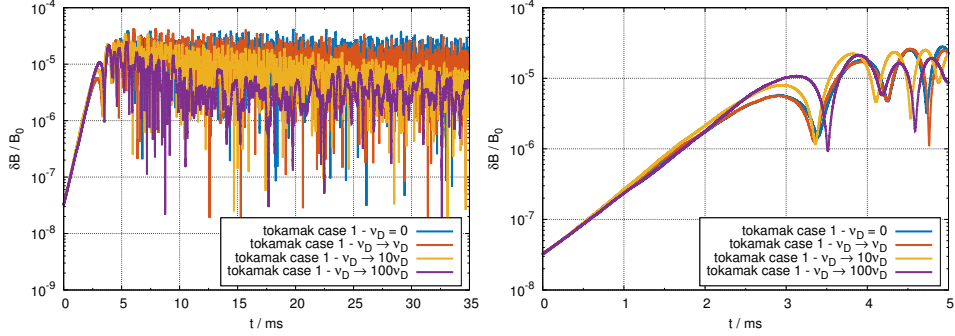


Figure 8: Similar as Fig. 4, but only for tokamak case 1 with a varying pitch-angle collision frequency. ν_D denotes the self-consistent value. Higher collision frequencies tend to lead to lower average δB values in the long-term non-linear phase. The right-hand side shows a zoomed-in view on the initial saturation.

can be made: Firstly, the linear phases in each simulation are very similar. Therefore, any changes in the frequency chirping can directly be attributed to the presence of the pitch-angle scattering operator and not to changes of γ_L . Furthermore, as predicted by analytical theory [1] (and numerically confirmed for the same magnetic equilibrium in Ref. [36]), the first maximum of δB after the linear phase increases with ν_D due to the prevention of wave-particle trapping.

The non-linear phases are completely different. Even when the fast-ion self-collision frequency is multiplied by 100, the collision frequency is still small enough to allow for a periodic non-linear behaviour of the mode. It is striking that even though the initial saturation level (first maximum of δB) increases with ν_D , this is not true for the long-term non-linear saturation level: It clearly decreases with ν_D .

Fig. 9 shows the spectrograms for the self-consistent case and two cases with artificially increased collision frequency by either a factor 10 or 100. Recall that in the standard ITPA tokamak case the fast-ion temperature is high ($T_f = 400$ keV). Hence, the fast-ion self-collision frequency is very low. This is reflected in the spectrograms, where the self-consistent case still very closely resembles its collisionless counterpart in Fig. 6. For increased collision frequencies, pitch-angle collisions tend to blur the ‘internal structure’ within the chirping parabola. Furthermore, they lead to a more narrow chirping in general. Fig. 8 shows that high pitch-angle collision frequencies significantly reduce the mode amplitude for long times, which is also visible in Fig. 9 where the chirping fades out in the high-collisionality case.

B. Changes induced by a fast-ion collision operator

We will now discuss the influence of a fast-ion collision operator on the non-linear dynamics. Still, a Maxwellian background is used, since the ITPA benchmark is defined that way.

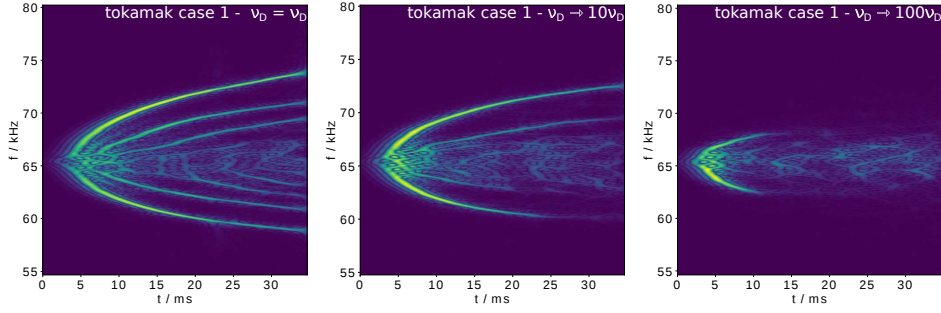


Figure 9: Different non-linear chirping scenarios for tokamak case 1 with varying collisionality (only pitch-angle collisions are considered). The self-consistent value for ν_D is rather low (fast-ion temperature is high and density is low), so that the first plot shows no significant deviation from its counterpart in Fig. 6. Higher collision frequencies damp the mode and lead to a more narrow chirping.

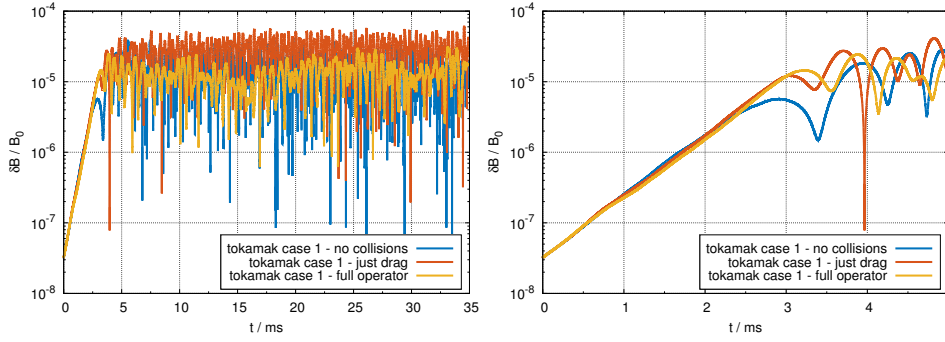


Figure 10: Time traces of the perturbed magnetic field for the reference case without collisions, a case where only the drag-part of the fast-ion collision operator was included, and for the full fast-ion collision operator. The non-linear dynamics is different in each case. The right-hand side shows a zoomed-in view on the time of initial saturation.

Fig. 10 shows how the time trace of the perturbed magnetic field changes when the fast-ion collision operator (either just drag or the full operator including also pitch-angle collisions) is taken into account. One can see that the non-linear phases are different, both with respect to the long-term averaged saturation level and the period of the non-linear oscillations. As shown in the expanded view on the right-hand side, the linear phases are still similar. However, the first maximum of δB after the linear phase increases due to fast-ion drag. We speculate that the friction force experienced by the fast ions pushes them in and out of the resonance. This could be a mechanism that prevents (or at least impedes) wave-particle trapping. While the addition of pitch-angle collisions in the case of the full fast-ion operator very slightly increases the initial saturation am-

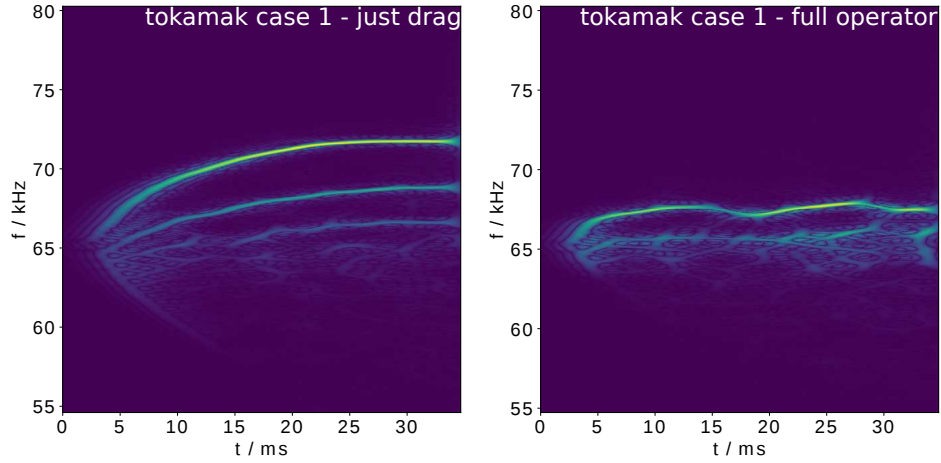


Figure 11: Spectrograms of the perturbed electrostatic potential for a case where just drag is included (left-hand side) and for the full fast-ion collision operator (right-hand side). Comparing with the collision-less result shown on the left-hand side of Fig. 6, we find that, as soon as drag is included, only the up-chirping branches remain.

plitude (first maximum), the just-drag case (without any pitch-angle collisions) shows the highest saturation level for long times.

The spectrograms of the perturbed electrostatic potential, including only drag on the left-hand side and the full fast-ion collision operator on the right-hand side, are shown in Fig. 11. In these spectrograms, the effects of the drag term are visible with their characteristic signature (see, for example, Refs. [25, 29]) and only the branches that show an up-chirping frequency remain. This is due to the fact that the fast-ion collision operator is not symmetric around the resonant velocity. The non-linear frequency evolution changes significantly in the case with the full fast-ion collision operator. As in the drag-only case, the frequency is just (slightly) chirping up, but pitch-angle collisions now lead to a ‘modulated’ behaviour after some time. As discussed before, they again reduce the width of the chirping parabola. Pitch-angle scattering leads to the de-trapping of particles from the phase-space structure, which reduced the overall chirping. Note that the pitch-angle collision frequency used in this case is close to the $\nu_D \rightarrow 100\nu_D$ -case shown in Fig. 9 on the far right. Therefore, the width of the chirping parabola is comparable. Nevertheless, the non-linear behaviour is different in the sense that now the mode amplitude does not decrease for long times, which can only be attributed to the presence of the drag term.

C. Using a time-dependent damping rate $\gamma_d(t)$

It has been studied in the literature (see, for example, Refs. [3, 25, 29]) how the choice of γ_d influences the non-linear dynamics and frequency chirping. However, these investigations were done with a fixed, but different, value for γ_d in each simulation. Here, we investigate the influence of a time-dependent damping rate $\gamma_d(t)$ on the non-linear dynamics in a single simulation.

The reason for this investigation is that two effects have to be distinguished: Firstly, the frequency of the mode may change on a short time scale, much shorter than the evolution of the equilibrium. This is the effect that is traditionally referred to as chirping. Secondly, the equilibrium may change on a longer time scale. Such equilibrium changes could, for instance, lead to a change in the shear Alfvén continuum gap structure, which could influence γ_L/γ_d , a critical parameter that determines the frequency chirping. Distinguishing these effects is important, especially for future comparisons with experimental measurements. Below, we use a time-dependent damping rate in order to simulate possible equilibrium changes.

We perform the substitution $\gamma_d \rightarrow \gamma_d f(t)$ in the amplitude equations of CKA-EUTERPE (see Eqs. (7) and (8)) with a time-dependent function

$$f(t) = -\varepsilon_{\gamma_d} \sin[\omega_{\gamma_d}(t - \Delta t_{\gamma_d})] \left(\frac{\operatorname{erfc}\left[\frac{t - \Delta t_{\gamma_d}}{2}\right] - 1}{2} \right) + 1. \quad (25)$$

The parameters in $f(t)$ are chosen as

$$\varepsilon_{\gamma_d} = 0.8 \quad (26)$$

$$\omega_{\gamma_d} = 430.1 \text{ s}^{-1} \quad (27)$$

$$\Delta t_{\gamma_d} = 3.14 \text{ ms}. \quad (28)$$

With this choice of parameters, γ_d will not vary in the linear phase. This ensures that the linear growth rate will be the same as in the regular collisionless reference case. This way, any changes in the non-linear phase cannot have their origin in a different linear phase. The resulting time trace of the perturbed magnetic field, including the time-dependent damping rate, is shown in Fig. 12. The figure shows that, in the non-linear phase, the average value of δB now oscillates with $\gamma_d(t)$. Even when $\gamma_d(t)$ is at its maximum (see maxima of red curve), the mode does not return to its initial value so that a new linear phase may start.

Analytical theory [3, 25] predicts that the frequency change scales as $\delta\omega(t) = \omega(t) - \omega(0) = \pm\alpha\gamma_L\sqrt{\gamma_d t}$ with $\alpha \approx 0.44$ (for the one-dimensional Berk-Breizman paradigm). Substituting the parameters of the collisionless reference case, $\gamma_L = \gamma + \gamma_d = 1.25 \cdot 10^4 \text{ s}^{-1}$, $\gamma_d = 1.05 \cdot 10^4 \text{ s}^{-1}$, and $\alpha = 0.25$, one arrives at the red curves in Fig. 13 (left-hand side). One can see that the fit works rather well for the upper branch for the case where γ_d is constant. The fit is worse for the lower branch, since the chirping parabola is slightly asymmetric. When γ_d changes over time, the analytical theory does not apply. This may be due to the fact that one of the assumptions of the Berk-Breizman model, that the mode is close marginal stability, is violated when $\gamma_d(t)$ is at its minimal values. Hence, the theory predicts a non-monotonic behaviour of $\delta\omega$, whereas we find a slightly modulated, but always monotonic behaviour in the simulations.

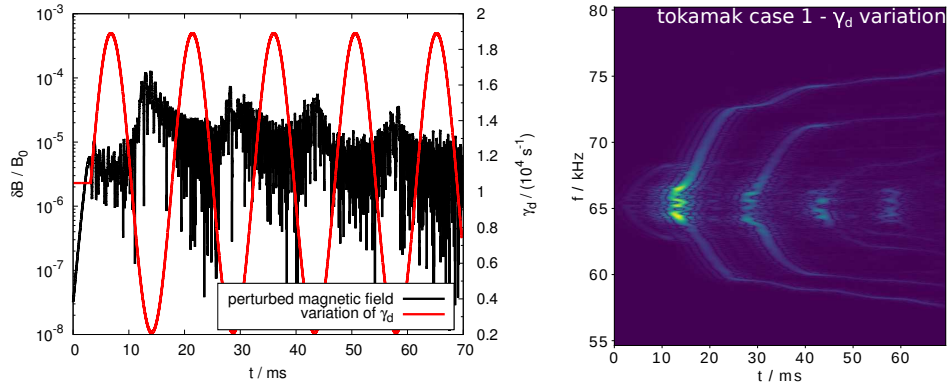


Figure 12: Temporal evolution of γ_d and the induced temporal behaviour of the perturbed magnetic field (left-hand side). The right-hand side shows the spectrogram of the perturbed electrostatic potential, which is now also modulated (parabola is either narrow or wide) with the same period as γ_d .

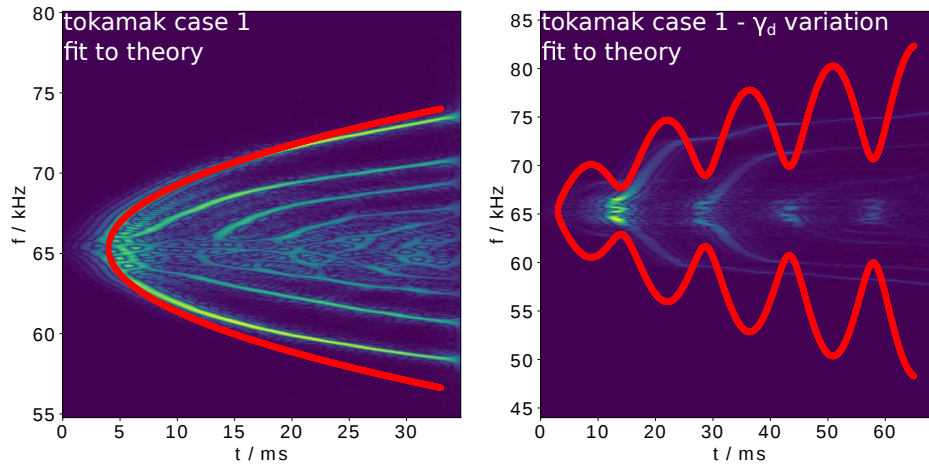


Figure 13: Fits of $\delta\omega(t) = \omega(t) - \omega(0)$ using analytical theory [3, 25]. The standard case is shown on the left-hand side. While the upper branch is fitted rather well, the chirping is slightly asymmetric so that the fit works less well for the lower branch. The right-hand side shows the case in which γ_d is not a constant. For a time-dependent $\gamma_d(t)$, the analytical theory fails to predict the numerically observed behaviour.

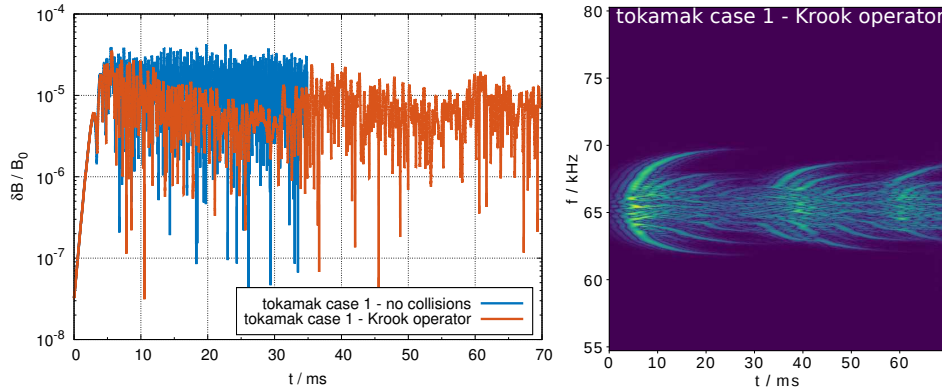


Figure 14: Influence of a Krook operator on the non-linear dynamics. The left-hand side shows the time trace of the perturbed magnetic field. The Krook operator periodically rebuilds the distribution function such that δB becomes modulated. The effect on the chirping can be seen on the right-hand side. The Krook operator leads to periodic chirping events.

D. The influence of a Krook operator

We now study the influence of a Krook operator on the non-linear dynamics. Since this operator acts to rebuilds the initial distribution function, it should lead to periodic chirping events.

It was shown in Ref. [30] that such events are linked to a local flattening of phase-space gradients, followed by the emission of holes and clumps [4], and finally a restoration of the initial gradient so that the process can repeat again. Note that our case is different from the simple Berk-Breizman paradigm: In the Berk-Breizman model a gradient in velocity space is the source of the instability. After this gradient in velocity space is flattened non-linearly, pitch-angle collisions (acting in velocity space) can rebuild it and thus restore the initial distribution function. In the present case, instead of velocity-space gradients, the spatial fast-particle density gradient is the source of instability. We found previously in Sec. IV A that pitch-angle collisions cannot (sufficiently) rebuild the gradient of the density profile and therefore we do not observe periodic chirping. What would be needed is a source of particles in real space. Therefore, a Krook operator is now used to emulate such a source (as would be present in a real experiment via e.g. neutral beam injection), which acts to restore the distribution function to its initial value. This leads to a periodic re-appearance of the mode with intermediate phases of lower mode amplitude, which is a common feature of non-linear systems in general. For instance, the fishbone burst cycle [8] is closely related.

Fig. 14 shows the resulting non-linear dynamics for $\nu_{\text{Krook}} = 114.7 \text{ s}^{-1}$. This value is chosen since it should guarantee several chirping events during a 60-ms-long simulation. Even though the Krook operator is present from the beginning of the simulation, it does not significantly change the first maximum of δB , frequency and growth rate of the

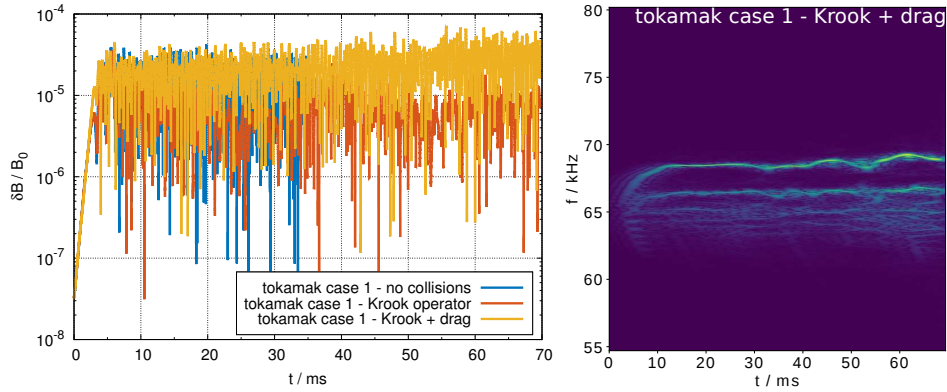


Figure 15: Influence of both Krook collisions and fast-ion drag on the non-linear dynamics. As before, the left-hand side shows the time trace of the perturbed magnetic field. When the drag term is included, the mode amplitude rises on average and is no longer modulated (even though the Krook term is still present). On the right-hand side, which shows the spectrogram of the perturbed electrostatic potential, the drag term now prevents individual, periodic events. The chirping is more narrow.

mode compared with the reference case. (For example, the linear growth rate is reduced by less than 0.1 %.) Clearly, the presence of the Krook operator lowers the long-term saturation level. But, as expected, it also leads to a periodic modulation of δB and therefore to periodic chirping events as can be seen on the right-hand side of Fig. 14. The initial chirping parabola fades away such that individual chirping events become visible. The average period in between the major chirping events is roughly 27.5 ms. This is about three times longer than ν_{Krook}^{-1} , which indicates that in this complex system other processes, such as the particle motion itself, influence the rate of construction of the distribution function. In the Berk-Breizman model, the Krook operator can be connected to the diffusive processes taking place at the phase-space resonance surface separating the fast ions trapped by the wave from passing particles. In that case, ν_{Krook} should reflect the characteristic de-trapping frequency of fast ions.

It may now be attempted to combine the Krook operator with a fast-ion collision operator. We already showed (see also Fig. 11) that the pitch-angle-scattering part of the full fast-ion collision operator leads to a narrowing chirping parabola. Otherwise, pitch-angle collisions do not significantly change the non-linear behaviour. Therefore, we restrict ourselves to the combination of the Krook operator and the drag term. The results can be seen in Fig. 15. As observed before (see Fig. 10), the inclusion of drag leads, on average, to a rising mode amplitude in the non-linear phase. Somewhat surprisingly, the long-term oscillations in the signal – induced by the presence of the Krook term that acts to rebuild the distribution function – are no longer present when fast-ion drag is included. We may again speculate that this is because particles are shifted in and out of the resonance as the simulation progresses. The absence of these long-term non-linear

oscillations also manifests itself in the spectrogram (see right-hand side of Fig. 15). The chirping does no longer ‘tear off’ in such a way that individual events are visible. On the other hand, the drag term presents itself with its usual signature (only up-chirping remains). After chirping initially, the frequency stays roughly constant in the non-linear phase. Ref. [33] argues that this corresponds to a state in which the effects of drag and relaxation of the distribution function due to the Krook term, balance each other.

V. NON-LINEAR BEHAVIOUR INCLUDING COLLISIONS – WENDELSTEIN 7-X CASE

The stellarator cases have been introduced in Sec. III. We will only focus on W7-X case 1 as it nicely showed almost symmetrical frequency chirping in the absence of collisions. Now we will investigate how the non-linear dynamics changes when particle collisions are included.

A. Changes induced by pitch-angle collisions

We now investigate for W7-X how pitch-angle collisions between the fast particles influence the frequency chirping and the non-linear dynamics in general. The results are compared to the collisionless reference case. The self-consistently calculated pitch-angle collision frequency ν_D is given by Eqs. (13) and (14). Since for W7-X the fast-ion temperature is much lower than for the ITPA tokamak case (and, simultaneously, the fast-ion density is much higher), the collision frequency is also larger. (Recall that we use a slowing-down distribution function. The temperature is therefore computed by calculating the pressure from the distribution function and then dividing by the density. Note that a Maxwellian with roughly the same shape as the slowing-down distribution function would have an equivalent temperature of approximately 20 keV.) The effect of the high collision frequency is, as can be seen in Fig. 16, that a steady-state develops after the initial saturation. This is in line with Refs. [35, 36] where it was shown recently that a steady-state develops in the non-linear phase for high collision frequencies. Further simulations are performed at one tenth and one hundredth of the original value of the collision frequency. The results are summarized in Fig. 16. The figure shows the time traces of the perturbed magnetic field for the reference case and for the collisional cases. The long-term saturation level is periodic only for the collisionless case. For the lowest collision frequency investigated, the behaviour is still close to being periodic. In that case, however, the damping of the wave in the early non-linear phase is severe. The first maximum of δB increases with increasing collision frequency ν_D (see Fig. 16 right-hand side).

Fig. 17 shows the associated spectrograms of the perturbed electrostatic potential for the cases including collisions. (The collisionless reference case is depicted in Fig. 7 on the left-hand side.) Note that the spectrograms contain less data for the collisional cases, since the time simulated is much shorter. Recall that the collisionless reference case nicely shows almost symmetric chirping (although, comparing $\delta\omega/\omega$, on a much smaller level than the ITPA case). However, as soon as collisions are added, the frequency basically becomes constant in time (see Fig. 17). Only for the lowest collision

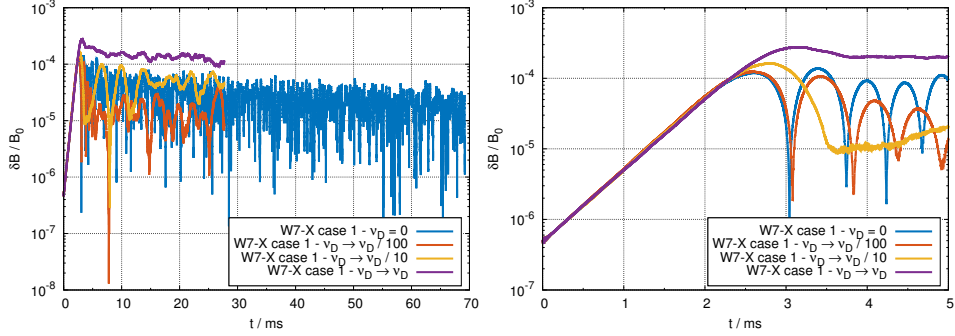


Figure 16: Time traces of the perturbed magnetic field of a TAE mode in Wendelstein 7-X geometry. The pitch-angle collision frequency is varied. ν_D denotes the self-consistent value. Except for the lowest collision frequency at early times, the non-linear dynamics resembles a steady-state when collisions are added. Contrary to the ITPA case, higher collision frequencies lead to a higher long-term-average saturation level. The right-hand side shows a zoomed-in view on the initial saturation.

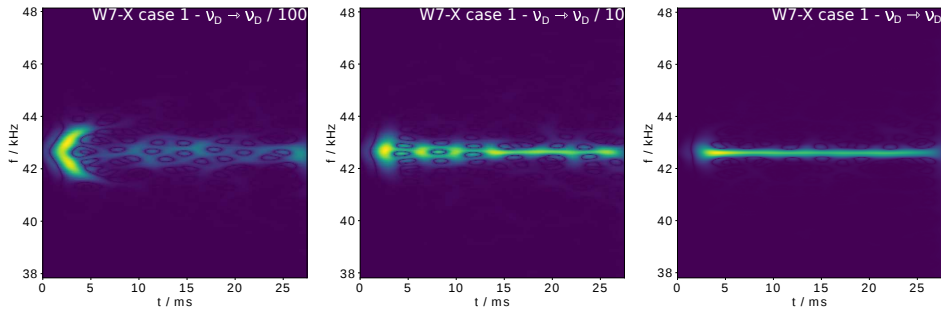


Figure 17: Effect of pitch-angle collisions on the non-linear chirping behaviour for the W7-X case 1. The self-consistent value for ν_D is high (low fast-ion temperature), so that the frequency becomes constant. Reducing the collision frequency (left-most sub-figure) leads to a re-appearance of the initial chirping, but significantly damps the mode.

frequency in this set (the left-most sub-figure) are traces of frequency chirping still visible in the early non-linear phase. Nevertheless, because the mode amplitude strongly decreases after the linear phase (see Fig. 16), the chirping eventually disappears.

B. The influence of fast-ion drag

It is a major goal of the W7-X physics program to assess the influence of fast particles on plasma performance, especially since good fast-ion confinement is an optimization criterion of W7-X [12, 17]. A realistic treatment of the fast ions requires not only realistic

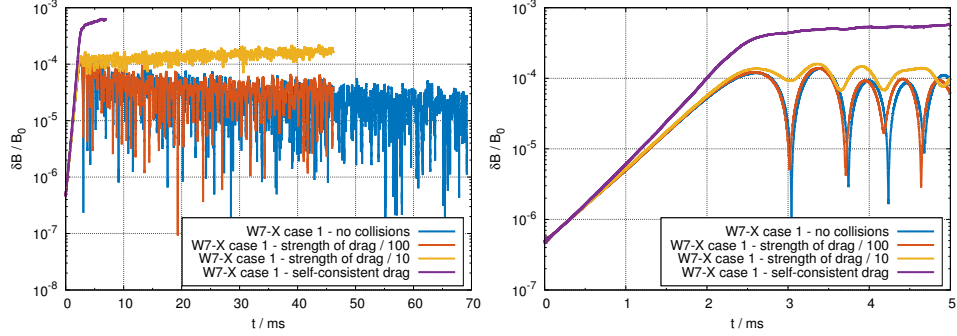


Figure 18: Time traces of the perturbed magnetic field for the W7-X case including a drag term of various strengths. The self-consistent case shows a very high saturation level. Reducing the strength of the drag term brings the curves closer to the collisionless reference. The right-hand side shows a zoomed-in view on the time of initial saturation.

distribution functions, but also the inclusion of a fast-ion collision operator. This is in particular important for non-linear simulations as they are performed here. As described in Sec. II, the fast-ion collision operator combines pitch-angle collisions and drag. Since the influence of pitch-angle collisions has already been addressed, we will now focus on drag only.

The effect of fast-ion drag on the frequency chirping in tokamaks was already discussed in Sec. IV B. This section aims at showing the differences and similarities in stellarators. The slowing-down distribution function described by Eq. (24) is the steady-state solution of the gyro-kinetic equation including a fast-ion collision operator and a beam-like fast-ion source. The formation of such a distribution function happens on a time scale that is much longer than the Alfvén wave dynamics. Therefore, we use the aforementioned Eq. (24) as a static background and simulate only the deviations from this distribution function caused by the presence of the mode.

The time traces of the perturbed magnetic field, while varying the strength of the drag term, are shown in Fig. 18. If the fast-ion drag is computed self-consistently, the non-linear saturation level is increased substantially compared with the collisionless reference case. This strong influence of the drag term is, again, due to the high collision frequencies in W7-X compared with the tokamak case. Note that self-consistently calculated drag quickly leads to a steady state with no signs of periodic behaviour. It is therefore excluded from further analysis.

Reducing the drag term by a factor of 10 or 100 leads to results that preserve the chirping nature of the solution in the non-linear phase. After the mode has initially saturated, there is still a sub-exponential drift. The same behaviour was seen before in the tokamak case.

The frequency spectrograms associated to these time traces are shown in Fig. 19. They show the expected behaviour: The chirping becomes asymmetric with the upper branch dominating in intensity over the lower branch. On the right-hand side of the figure, where the strength of the drag term is higher, the lower branch vanishes completely

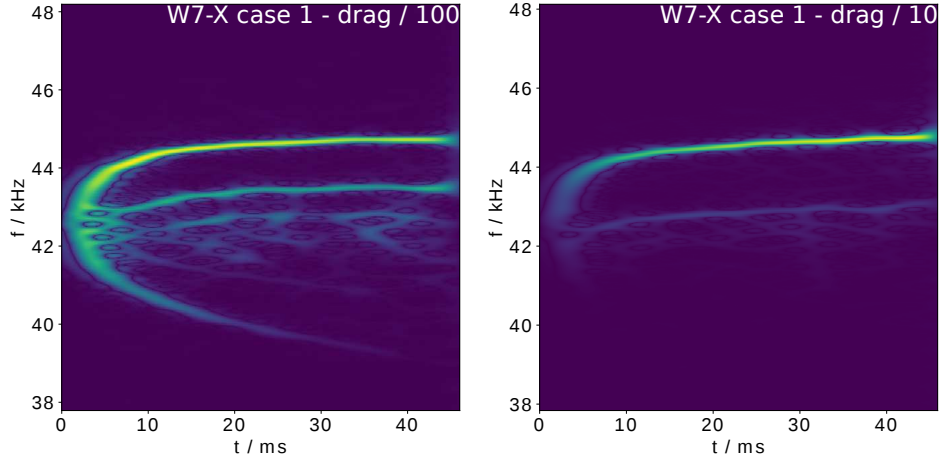


Figure 19: Spectrograms of the perturbed electrostatic potential for the W7-X cases that include fast-ion drag. Compared with Fig. 18, only the cases with reduced strength of the drag term are shown as they preserve the chirping behaviour. As before in the tokamak, drag leads to the disappearance of the down-chirping branches.

and the upper branch, after chirping initially, transitions to a new steady state. This is very similar to Fig. 14 of Ref. [29], even though the the dimension-less parameters that determine the frequency chirping (normalized growth rate and collision frequencies) are different in this publication.

C. The influence of a Krook operator

Finally, we want to demonstrate the effect of a Krook operator in stellarator geometry. We choose $\nu_{\text{Krook}} = 86.7 \text{ s}^{-1}$. The results are shown in Fig. 20. The linear phase remains nearly unaffected (the growth rate changes by less than 0.05 %). As before in the tokamak case (see Fig. 14 for comparison) the average saturation level in the non-linear phase is lower when the Krook operator is included. This is most clearly visible up until $t \cong 20 \text{ ms}$. Especially in the late non-linear phase ($t > 30 \text{ ms}$) a modulation of the δB signal due to the presence of the Krook term is visible. These modulations translate into individual chirping events as shown in the spectrogram on the right-hand side of Fig. 20. The average period between the major chirping events is approximately 19.7 ms, which is about twice ν_{Krook}^{-1} . It has to be pointed out that the reduction of the average saturation level and the modulation of the δB signal is less pronounced compared with the tokamak case. Note, furthermore, that this one choice of ν_{Krook} corresponds to a proof-of-principle calculation aimed at showing that periodic chirping is possible in W7-X. Details about this process (e.g. how the time in between chirping events is influenced by γ_L and ν_{Krook}) will be investigated in a future publication.

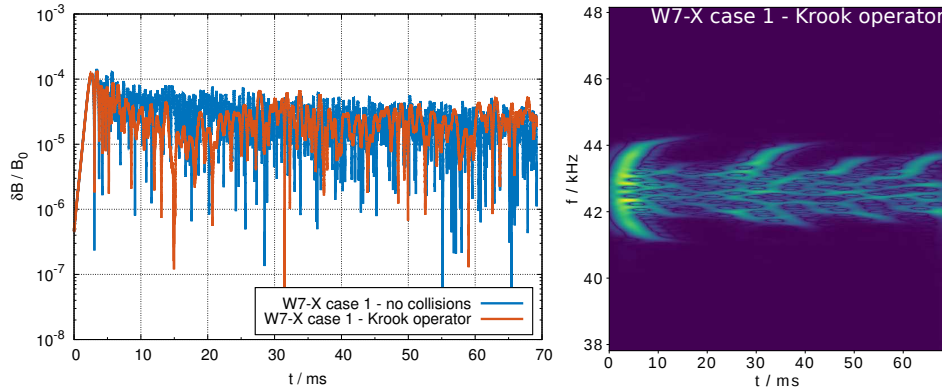


Figure 20: Influence of a Krook operator on the non-linear dynamics of a TAE in W7-X. The left-hand side shows the time trace of the perturbed magnetic field. As for the tokamak case, the Krook operator leads to a periodic modulation of δB via rebuilding of the distribution function. In the spectrogram on the right-hand side the Krook operator leads to periodic (and separated) chirping events.

VI. SUMMARY AND CONCLUSIONS

In this paper, we have investigated the influence of various collision operators on the non-linear frequency chirping of fast-ion-driven TAEs in two different magnetic geometries. A tokamak case as well as a Wendelstein 7-X (W7-X) high-mirror equilibrium have been considered. The effects of pitch-angle collisions and fast-ion drag on the non-linear dynamics of the mode were discussed separately. Pitch-angle collisions together with fast-ion drag constitute the fast-ion collision operator. A particle source was emulated using a Krook operator.

Starting with the tokamak case, we found that pitch-angle collisions lead to a reduction of the long-term saturation level and a more narrow frequency chirping compared with the collisionless case. The situation is different for the W7-X case, where the fast-ion temperature is lower while, at the same time, the fast-ion density is higher. Both effects lead to higher collision frequencies. Consequently, the non-linear dynamics of the TAE in W7-X becomes stationary for self-consistently calculated pitch-angle scattering frequencies. Contrary to the tokamak case, the long-term saturation level is enhanced in W7-X, when (self-consistently calculated) pitch-angle collisions are considered. This could be of practical relevance for the operation of the machine.

Many of the features we see in our simulations (in the tokamak as well as in the stellarator) are very similar to features observed in the one-dimensional Berk-Breizman paradigm. The drag term, for example manifests itself in the usual way that only up-chirping frequency branches (also dubbed holes in phase space [4]) remain. The so-called clumps disappear. For some collision operators, however, differences become apparent. This concerns the influence of pitch-angle collisions on the non-linear devel-

opment of the mode. It makes a difference whether a phase-space gradient or a density gradient in real space is considered. Furthermore, the Berk-Breizman model was found to not be applicable when a time-dependent damping rate $\gamma_d(t)$ is used, which is likely caused by violating the assumption of a marginal mode.

In order to simulate periodic chirping events, a particle source that restores the original distribution function needs to be present. Since the inclusion of a ‘real’ particle source into EUTERPE is a matter of on-going research, we use a Krook operator to emulate a particle source in the present work. The rate of reconstruction of the distribution function, ν_{Krook} , was chosen in a way to have periodic chirping events nicely visible in proof-of-principle calculations. Experimental measurements are needed to constrain this parameter. The Krook operator is found to have the same effect in the tokamak and in the stellarator.

The issue of frequency chirping is of practical relevance for operation phases of W7-X that include NBI heating. We hope that, when experimentally measured time traces of δB become available, we can spectroscopically determine γ_L , γ_d , and collision frequencies in W7-X by choosing critical input parameters of the simulations such that they fit the measurements. Such an approach has, for instance, been suggested in Ref. [27].

There could, however, be a number of problems: The Berk-Breizman model predicts [3, 25] that during a frequency chirp the frequency changes as $\delta\omega = \pm\alpha\gamma_L\sqrt{\gamma_d t}$. This means that, in order for the chirping to be nicely visible, both γ_L and γ_d should be large. However, the simulations presented in this paper indicate that the fast-ion drive in W7-X is rather small (and smaller than for the ITPA tokamak case). This leads to a narrow chirping parabola, which could be hard to resolve experimentally.

Furthermore, it was found that the collision frequencies in W7-X are high. For that reason, the periodic non-linear behaviour of δB is suppressed. Finding parameter regimes that allow for frequency chirping could be an experimental challenge. Nevertheless, this paper shows that collisions, especially in dense W7-X plasmas with a low fast-ion temperature, significantly influence the non-linear dynamics and the saturation level. They have thus to be included in the non-linear modelling of any AE instability.

From a numerical and theoretical standpoint, this paper confirms that CKA-EUTERPE can routinely be used to perform non-linear simulations for W7-X.

Finally, we want to point out that here we considered the interaction of fast ions with a single mode. In realistic experiments, however, multiple modes – possibly close together in frequency – may be present. In that case the assumption of a fixed mode structure would need to be revisited. Work on a multi-mode version of CKA-EUTERPE is currently in progress. Thus, frequency chirping in more complex systems will be investigated in the future, once this version is operational.

VII. ACKNOWLEDGEMENT

We would like to thank Udo von Toussaint for pointing out the benefits of modern signal processing tools. Further, we would like to acknowledge the useful comments and suggestions from the anonymous referees.

The simulations were performed on the MARCONI supercomputer (CINECA).

This work has been carried out within the framework of the EUROfusion Consortium and has received funding from the Euratom research and training programme 2014-2018 under grant agreement No 633053. The views and opinions expressed herein do not necessarily reflect those of the European Commission.

References

- [1] H. L. Berk, B. N. Breizman, and Ye. Huanchun. Scenarios for the nonlinear evolution of alpha-particle-induced Alfvén wave instability. *Physical Review Letters*, 68:3563, 1992.
- [2] H. L. Berk, B. N. Breizman, and M. Pekker. Nonlinear Dynamics of a Driven Mode near Marginal Stability. *Physical Review Letters*, 76:1256, 1996.
- [3] H. L. Berk, B. N. Breizman, and N. V. Petviashvili. Spontaneous hole-clump pair creation in weakly unstable plasmas. *Physics Letters A*, 234:213, 1997.
- [4] H. L. Berk, B. N. Breizman, J. Candy, M. Pekker, and N. V. Petviashvili. Spontaneous hole-clump pair creation. *Physics of Plasmas*, 6:3102, 1999.
- [5] P. L. Bhatnagar, E. P. Gross, and M. Krook. A Model for Collision Processes in Gases. I. Small Amplitude Processes in Charged and Neutral One-Component Systems. *Physical Review*, 94:511, 1954.
- [6] A. Bierwage, K. Shinohara, Y. Todo, N. Aiba, M. Ishikawa, G. Matsunaga, M. Takechi, and M. Yagi. Self-consistent long-time simulation of chirping and beating energetic particle modes in JT-60U plasmas. *Nuclear Fusion*, 57:016036, 2017.
- [7] Boualem Boashash. *Time-Frequency Signal Analysis and Processing, A Comprehensive Reference*. Academic Press, 2016.
- [8] Liu Chen, R. B. White, and M. N. Rosenbluth. Excitation of Internal Kink Modes by Trapped Energetic Beam Ions. *Physical Review Letters*, 52:1122–1125, 1984.
- [9] Christoph Slaby and Ralf Kleiber and Axel Könies. Combining electromagnetic gyro-kinetic particle-in-cell simulations with collisions. *Computer Physics Communications*, 218:1–9, 2017.
- [10] D. S. Darrow, S. J. Zweben, S. Batha, R. V. Bundy, C. E. Bush, Z. Chang, C. Z. Cheng, H. H. Duong, J. Fang, N. J. Fisch, R. Fischer, E. D. Fredrickson, G. Y. Fu, R. F. Heeter, W. W. Heidbrink, H. W. Herrmann, M. C. Herrmann, K. Hill, E. F. Jaeger, R. James, R. Majeski, S. S. Medley, M. Murakami, M. Petrov, C. K. Phillips, M. H. Redi, E. Ruskov, D. A. Spong, E. J. Strait, G. Taylor, R. B. White, J. R. Wilson, K.-L. Wong, and M. C. Zarnstorff. Alpha particle losses from Tokamak Fusion Test Reactor deuterium–tritium plasmas. *Physics of Plasmas*, 3:1875–1880, 1996.
- [11] H. H. Duong, W. W. Heidbrink, E. J. Strait, T. W. Petrie, R. Lee, R. A. Moyer, and J. G. Watkins. Loss of energetic beam ions during TAE instabilities. *Nuclear Fusion*, 33:749, 1993.
- [12] V. Erckmann, H.-J. Hartfuß, M. Kick, H. Renner, J. Sapper, F. Schauer, E. Speth, F. Wesner, F. Wagner, M. Wanner, A. Weller, H. Wobig, the W7-AS team, and the W7-X teams at IPP Garching, FZK Karlsruhe and IPF Stuttgart. The W7-X project: scientific basis and technical realization. In *17th IEEE/NPSS Symposium Fusion Engineering (Cat. No.97CH36131)*, volume 1, pages 40–48, San Diego, CA, USA, 1998. IEEE.
- [13] A. Könies et al. 10th IAEA Technical Meeting on Energetic Particles in Magnetic Confinement Systems (Kloster Seeon), 2007.
- [14] T. B. Fehér. *Simulation of the interaction between Alfvén waves and fast particles*. PhD thesis, Ernst-Moritz-Arndt-Universität Greifswald, 2013.
- [15] G. Y. Fu and J. W. van Dam. Excitation of the toroidicity-induced shear Alfvén eigenmode

- by fusion alpha particles in an ignited tokamak. *Physics of Fluids B*, 1:1949, 1989.
- [16] M. García-Muñoz, N. Hicks, R. van Voornveld, I. G. J. Classen, R. Bilato, V. Bobkov, M. Bruedgam, H.-U. Fahrbach, V. Igochine, S. Jaemsae, M. Maraschek, K. Sassenberg, and ASDEX Upgrade Team. Convective and Diffusive Energetic Particle Losses Induced by Shear Alfvén Waves in the ASDEX Upgrade Tokamak. *Physical Review Letters*, 104:185002, 2010.
- [17] G. Grieger, W. Lotz, P. Merkel, J. Nührenberg, J. Sapper, E. Sturmberger, H. Wobig, the W7-X Team, R. Burhenn, V. Erckmann, U. Gasparino, L. Giannone, H. J. Hartfuss, R. Jaenicke, G. Kühner, H. Ringler, A. Weller, F. Wagner, and the W7-AS Team. Physics optimization of stellarators. *Physics of Fluids B*, 4:2081, 1992.
- [18] W. W. Heidbrink. Basic physics of Alfvén instabilities driven by energetic particles in toroidally confined plasmas. *Physics of Plasmas*, 15:055501, 2008.
- [19] P. Helander and D. J. Sigmar. *Collisional Transport in Magnetized Plasmas*. Cambridge University Press, 2002.
- [20] R. Kleiber, R. Hatzky, A. Könies, A. Mishchenko, and E. Sonnendrücker. An explicit large time step particle-in-cell scheme for nonlinear gyrokinetic simulations in the electromagnetic regime. *Physics of Plasmas*, 23:032501, 2016.
- [21] A. Könies. paper on the CKA-EUTERPE model, in preparation.
- [22] A. Könies, S. Briguglio, N. Gorelenkov, T. Fehér, M. Isaev, Ph. Lauber, A. Mishchenko, D. A. Spong, Y. Todo, W. A. Cooper, R. Hatzky, R. Kleiber, M. Borchardt, G. Vlad, A. Biancalani, A. Bottino, and ITPA EP TG. Benchmark of gyrokinetic, kinetic MHD and gyrofluid codes for the linear calculation of fast particle driven TAE dynamics. *Nuclear Fusion*, 58:126027, 2018.
- [23] A. Könies, S. Briguglio, N. Gorelenkov, T. Fehér, M. Isaev, Ph. Lauber, A. Mishchenko, D. A. Spong, Y. Todo, W. A. Cooper, R. Hatzky, R. Kleiber, M. Borchardt, G. Vlad, and ITPA EP TG. Benchmark of gyrokinetic, kinetic MHD and gyrofluid codes for the linear calculation of fast particle driven TAE dynamics. 24th IAEA Int. Conf. on Fusion Energy (San Diego, CA), 2012. http://www-naweb.iaea.org/naweb/physics/FEC/FEC2012/papers/437_ITRP134.pdf.
- [24] V. Kornilov, R. Kleiber, R. Hatzky, L. Villard, and G. Jost. Gyrokinetic global three-dimensional simulations of linear ion-temperature-gradient modes in Wendelstein 7-X. *Physics of Plasmas*, 11:3196, 2004.
- [25] M. Lesur. Effect of collisions on energetic particle-driven chirping bursts. *Physics of Plasmas*, 20:055905, 2013.
- [26] M. Lesur, Y. Idomura, and X. Garbet. Fully nonlinear features of the energetic beam-driven instability. *Physics of Plasmas*, 16:092305, 2009.
- [27] M. Lesur, Y. Idomura, K. Shinohara, X. Garbet, and the JT-60 Team. Spectroscopic determination of kinetic parameters for frequency sweeping Alfvén eigenmodes. *Physics of Plasmas*, 17:122311, 2010.
- [28] M. K. Lilley and B. N. Breizman. Convective transport of fast particles in dissipative plasmas near an instability threshold. *Nuclear Fusion*, 52:094002, 2012.
- [29] M. K. Lilley, B. N. Breizman, and S. E. Sharapov. Effect of dynamical friction on nonlinear energetic particle modes. *Physics of Plasmas*, 17:092305, 2010.
- [30] M. K. Lilley and R. M. Nyqvist. Formation of Phase Space Holes and Clumps. *Physical*

- Review Letters*, 112:155002, 2014.
- [31] A. V. Melnikov, L. G. Eliseev, E. Ascasíbar, A. Cappa, F. Castejón, C. Hidalgo, T. Ido, J. A. Jiménez, A. S. Kozachek, L. I. Krupnik, M. Liniers, S. E. Lysenko, K. Nagaoka, J. L. de Pablos, A. Shimizu, S. E. Sharapov, M. V. Ufimtsev, S. Yamamoto, HIBP group, and TJ-II team. Transition from chirping to steady NBI-driven Alfvén modes caused by magnetic configuration variations in the TJ-II stellarator. *Nuclear Fusion*, 56:076001, 2016.
- [32] A. V. Melnikov, L. G. Eliseev, F. Castejón, C. Hidalgo, P. O. Khabanov, A. S. Kozachek, L. I. Krupnik, M. Liniers, S. E. Lysenko, J. L. de Pablos, S. E. Sharapov, M. V. Ufimtsev, V. N. Zenin, HIBP Group, and TJ-II Team. Study of NBI-driven chirping mode properties and radial location by the heavy ion beam probe in the TJ-II stellarator. *Nuclear Fusion*, 56:112019, 2016.
- [33] R. M. Nyqvist, M. K. Lilley, and B. N. Breizman. Adiabatic description of long range frequency sweeping. *Nuclear Fusion*, 52:094020, 2012.
- [34] M. N. Rosenbluth and P. H. Rutherford. Excitation of Alfvén Waves by High-Energy Ions in a Tokamak. *Physical Review Letters*, 34:1428, 1975.
- [35] C. Slaby, A. Könies, R. Kleiber, S. Äkäslompolo, and J. Kontula. Parametric study of fast-ion-driven modes in Wendelstein 7-X. *Journal of Physics: Conference Series*, 1125:012019, 2018.
- [36] Christoph Slaby, Axel Könies, Ralf Kleiber, and José Manuel García-Regaña. Effects of collisions on the saturation dynamics of TAEs in tokamaks and stellarators. *Nuclear Fusion*, 58:082018, 2018.
- [37] R. B. White, E. Fredrickson, D. Darrow, M. Zarnstorff, R. Wilson, S. Zweben, K. Hill, Yang Chen, and Guoyong Fu. Toroidal Alfvén eigenmode-induced ripple trapping. *Physics of Plasmas*, 2:2871, 1995.

Numerical investigation of non-perturbative kinetic effects of energetic particles on toroidicity-induced Alfvén eigenmodes in tokamaks and stellarators (A.6)

Full citation:

C. Slaby, A. Könies, and R. Kleiber. Numerical investigation of non-perturbative kinetic effects of energetic particles on toroidicity-induced Alfvén eigenmodes in tokamaks and stellarators. *Physics of Plasmas*, **23** (9) 092501 (2016).

DOI:

10.1063/1.4961916 (<https://doi.org/10.1063/1.4961916>)

Reproduced with the permission of AIP Publishing and EUROfusion.

Appendix A. Thesis articles



Numerical investigation of non-perturbative kinetic effects of energetic particles on toroidicity-induced Alfvén eigenmodes in tokamaks and stellarators

Christoph Slaby, Axel Könies, and Ralf Kleiber

Max-Planck-Institut für Plasmaphysik, D-17491 Greifswald, Germany

(Received 11 April 2016; accepted 8 August 2016; published online 1 September 2016)

The resonant interaction of shear Alfvén waves with energetic particles is investigated numerically in tokamak and stellarator geometry using a non-perturbative MHD-kinetic hybrid approach. The focus lies on toroidicity-induced Alfvén eigenmodes (TAEs), which are most easily destabilized by a fast-particle population in fusion plasmas. While the background plasma is treated within the framework of an ideal-MHD theory, the drive of the fast particles, as well as Landau damping of the background plasma, is modelled using the drift-kinetic Vlasov equation without collisions. Building on analytical theory, a fast numerical tool, STAE-K, has been developed to solve the resulting eigenvalue problem using a Riccati shooting method. The code, which can be used for parameter scans, is applied to tokamaks and the stellarator Wendelstein 7-X. High energetic-ion pressure leads to large growth rates of the TAEs and to their conversion into kinetically modified TAEs and kinetic Alfvén waves via continuum interaction. To better understand the physics of this conversion mechanism, the connections between TAEs and the shear Alfvén wave continuum are examined. It is shown that, when energetic particles are present, the continuum deforms substantially and the TAE frequency can leave the continuum gap. The interaction of the TAE with the continuum leads to singularities in the eigenfunctions. To further advance the physical model and also to eliminate the MHD continuum together with the singularities in the eigenfunctions, a fourth-order term connected to radiative damping has been included. The radiative damping term is connected to non-ideal effects of the bulk plasma and introduces higher-order derivatives to the model. Thus, it has the potential to substantially change the nature of the solution. For the first time, the fast-particle drive, Landau damping, continuum damping, and radiative damping have been modelled together in tokamak- as well as in stellarator geometry. [<http://dx.doi.org/10.1063/1.4961916>]

I. INTRODUCTION

In a burning fusion plasma, alpha particles are produced with a velocity that exceeds the typical Alfvén speed. In the process of slowing down, these fast particles may transfer energy to Alfvén waves, which thus become unstable.^{1,2} Also heating methods, such as ion cyclotron resonance heating (ICRH) and neutral beam injection (NBI), can supply energetic particles with similar consequences. The resonant interaction of the fast particles with Alfvén waves, in particular, with toroidicity-induced Alfvén eigenmodes (TAEs), may lead to a degraded confinement of the energetic particles and thereby to particle loss and high heat loads on the first-wall components.^{3,4} As pointed out in Ref. 5, an energetic particle mode (EPM), determined by the properties of the energetic particle distribution function, may form.

In this paper, the resonant particle-wave interaction is studied analytically and numerically using a non-perturbative MHD-kinetic hybrid model, in which the background plasma is modelled using an ideal-MHD theory, whereas the fast particles are treated kinetically.

The aim is not to provide predictive results but to investigate general trends in the change of frequency, growth rate, and radial structure of the eigenfunction when energetic ions are present.

To assess the stability or instability of a given mode, various damping mechanisms such as Landau damping, radiative damping, and continuum damping are just as important as the kinetic drive of the energetic particle species.⁶ Therefore, a numerical tool, namely, a shooting code for toroidicity-induced Alfvén eigenmodes with kinetic extensions (STAE-K), has been developed, which is able to take into account all these different stabilizing and destabilizing contributions (but cannot completely describe collisional damping). The model used here is a consequent further development of analytical theory, which usually needs to assume highly localized modes and a perturbative ansatz (see, e.g., Refs. 2 and 7). Our numerical treatment, on the other hand, does not require such assumptions. Nevertheless, the equations are solved in the large-aspect-ratio and a low-beta approximation in either tokamak (circular flux surfaces) or stellarator geometry.

At the moment, other codes that can perform such calculations in three-dimensional stellarator geometry either work perturbatively (CAS3D-K,⁸ CKA-EUTERPE,⁹ or AE3D-K¹⁰) or employ a complex fully kinetic theory (EUTERPE), which requires a lot of computing power. STAE-K, with its non-perturbative but a simplified model, is speed-optimized and still captures key elements important for the modeling of especially stellarators. For

completeness, we note that a three-dimensional version of the MEGA code¹¹ is currently benchmarked.

The structure of the paper is as follows. First, the MHD-kinetic hybrid model will be introduced by discussing the MHD and the kinetic part separately. The numerical methods employed and the implementation of the model will be described in Sec. III. After the shooting code is benchmarked in Sec. IV, further results will be presented in Sec. V. Finally, conclusions are drawn in Sec. VI.

The three Appendixes elaborate on details of the theory outlined in Sec. II and summarize the various background-plasma and fast-particle parameters used in the numerical calculations, respectively.

II. THEORY

In this section, a simple MHD-kinetic hybrid model will be developed, which is well suited for fast and efficient numerical calculations. To this end, some simplifying assumptions are made. For both the tokamak and stellarator, large-aspect-ratio devices are considered. This simplifies the metric tensor, because only contributions due to toroidicity and helical shaping have to be taken into account. In addition, a low-beta plasma is assumed, and only shear Alfvén waves are included in this analysis by taking $\mathbf{A}^{(1)} = A_{\parallel}^{(1)} \mathbf{b}$, where \mathbf{A} is the vector potential and \mathbf{b} is the unit vector along the magnetic field \mathbf{B} . In the following, the superscripts ⁽⁰⁾ and ⁽¹⁾ will be used to label equilibrium and perturbed quantities, respectively. The symbols \parallel and \perp indicate vector components parallel or perpendicular to the direction of the equilibrium magnetic field. The perturbations, which are assumed to be much smaller than the equilibrium quantities, are supposed to vary in time as $\exp(-i\omega t)$ with the mode frequency $\omega \in \mathbb{C}$.

In order to improve the performance of the numerical implementation, as many calculations as possible are performed on an analytical level.

The eigenmode equation is derived from the quasi-neutrality condition $\nabla \cdot \mathbf{j}^{(1)} = 0$, which can be split into an MHD part and the kinetic contribution of the fast particles

$$\nabla \cdot \mathbf{j}_{\text{MHD}}^{(1)} + \nabla \cdot \mathbf{j}_{\text{fast}}^{(1)} = 0. \quad (1)$$

Here, the perturbed energetic-particle current density can be calculated using

$$\mathbf{j}_{\text{fast}}^{(1)} = Z_{\text{fast}} \mathbf{e} \int d^3 v f^{(1)} \mathbf{v}_{\text{D}} + \nabla \times \mathbf{m}_{\text{fast}}^{(1)}, \quad (2)$$

with $f^{(1)}$ being the perturbed distribution function of the kinetically treated fast-particle species and \mathbf{v}_{D} being their drift velocity ($Z_{\text{fast}} \mathbf{e}$ is the charge of the fast particles). The second term on the right-hand side of Eq. (2) is the magnetization current of the fast particles,¹² which is unimportant, because it is divergence-free. In the following, the two terms in Eq. (1) will be discussed separately.

A. MHD part

As the MHD-terms of the model have already been derived by others,^{13–15} those calculations need not be repeated in the present paper. Thus, just a brief overview is given here.

The linearized MHD momentum equation is used to solve for $\mathbf{j}_{\perp}^{(1)}$. Using Maxwell's equations gives

$$\begin{aligned} \nabla \cdot \mathbf{j}_{\text{MHD}}^{(1)} &= (\mathbf{B}^{(0)} \cdot \nabla) \left(\frac{\mathbf{B}^{(0)} \cdot \mathbf{j}^{(1)}}{B^2} \right) + (\mathbf{B}_{\perp}^{(1)} \cdot \nabla) \\ &\quad \times \left(\frac{\mathbf{B}^{(0)} \cdot \mathbf{j}^{(0)}}{B^2} \right) + \frac{i\omega}{\mu_0} \nabla \cdot \left(\frac{\nabla_{\perp} \Phi^{(1)}}{v_A} \right), \end{aligned} \quad (3)$$

if the perturbed plasma flow is approximated by the $\mathbf{E} \times \mathbf{B}$ -drift. Here, $v_A = B/\sqrt{\mu_0 n_i m_i}$ is the Alfvén velocity of the background-plasma ions with mass m_i and density n_i . μ_0 is the vacuum permeability, and the electric potential is denoted by Φ . Following Ref. 14, the term with the equilibrium current density is dropped for simplicity in the case of stellarators like Wendelstein 7-X (W7-X).

In the large-aspect-ratio and small-plasma-beta limit, several possible simplifications of Eq. (3) have been discussed extensively in Ref. 13. They involve expressing $\mathbf{B}^{(0)} \cdot \mathbf{j}^{(1)}$ and $\mathbf{B}_{\perp}^{(1)}$ in terms of the perturbed vector potential. The ideal-MHD condition $E_{\parallel} = 0$ leads to $i\omega A_{\parallel}^{(1)} = (\mathbf{b} \cdot \nabla) \Phi^{(1)}$ and provides the necessary connection to $\Phi^{(1)}$. After using these simplifications, a Fourier transform finally leads to

$$\begin{aligned} \mathcal{FT} \left(\frac{i\omega \mu_0 \sqrt{g}}{r R_0} \nabla \cdot \mathbf{j}_{\text{MHD}}^{(1)} \right) &= \left[\frac{1}{r} \frac{d}{dr} r \left(k_{m,n}^2 - \frac{\omega^2}{v_A^2} \right) \frac{d}{dr} - \frac{1}{r} \left(\frac{d}{dr} k_{m,n}^2 \right) - \frac{m^2}{r^2} \left(k_{m,n}^2 - \frac{\omega^2}{v_A^2} \right) \right] \Phi_m^{(1)} \\ &\quad + \left[-\frac{2}{r} \frac{d}{dr} r \frac{\omega^2}{v_A^2} \left(\Delta' + \frac{r}{R_0} \right) \frac{d}{dr} - \frac{2}{r^2} \frac{\omega^2}{v_A^2} \Delta' m(m+1) \right] \Phi_{m+1}^{(1)} \\ &\quad + \left[-\frac{2}{r} \frac{d}{dr} r \frac{\omega^2}{v_A^2} \left(\Delta' + \frac{r}{R_0} \right) \frac{d}{dr} - \frac{2}{r^2} \frac{\omega^2}{v_A^2} \Delta' m(m-1) \right] \Phi_{m-1}^{(1)}, \end{aligned} \quad (4)$$

where \sqrt{g} is the determinant of the metric tensor used in Ref. 13 and $k_{m,n} = (n - m/q)/R_0$ denotes the parallel wave vector with poloidal and toroidal mode numbers m and n , respectively. R_0 is the major radius of the toroidal

device and $q = 1/i$ is the safety factor (i being the rotational transform). The Shafranov shift is denoted by Δ , and primes label a derivative with respect to the radial variable r .

An equation very similar to Eq. (4) has been derived in Ref. 14 for stellarators

$$\begin{aligned} \mathcal{F}\mathcal{T}\left(\frac{i\omega\mu_0 r^2}{\alpha^2 \delta_0} \nabla \cdot \mathbf{j}_{\text{MHD}}^{(1)}\right) &= Q_{m,n} \Phi_{m,n}^{(1)} + \frac{1}{r^2} \frac{d}{dr} r^3 \left\{ \left(k_{m,n}^2 - \frac{\omega^2}{v_A^2} \right) \left(\frac{1}{r} \frac{d}{dr} - \frac{1}{r^2} \right) \Phi_{m,n}^{(1)} \right. \\ &+ \sum_{\mu,\nu} \left[k_{m,n} k_{m+\mu,n+\nu N_P} \frac{\epsilon_g^{(\mu,\nu)}}{2} - \frac{\omega^2}{v_A^2} \epsilon^{(\mu,\nu)} \right] \left(\frac{1}{r} \frac{d}{dr} - \frac{1}{r^2} \right) \Phi_{m+\mu,n+\nu N_P}^{(1)} \\ &\left. + \sum_{\mu,\nu} \left[k_{m,n} k_{m-\mu,n-\nu N_P} \frac{\epsilon_g^{(\mu,\nu)}}{2} - \frac{\omega^2}{v_A^2} \epsilon^{(\mu,\nu)} \right] \left(\frac{1}{r} \frac{d}{dr} - \frac{1}{r^2} \right) \Phi_{m-\mu,n-\nu N_P}^{(1)} \right\}. \end{aligned} \quad (5)$$

Here, $\epsilon^{(\mu,\nu)} = \epsilon_g^{(\mu,\nu)}/2 - 2\epsilon_B^{(\mu,\nu)}$ determines the strength of the mode coupling due to geometry. It is given in the following representations for the rr -component of the metric tensor:

$$g^{rr} = \delta_0 \left[1 + \sum_{\mu,\nu} \epsilon_g^{(\mu,\nu)} \cos(\mu\Theta - \nu N_P \varphi) \right] \quad (6)$$

(δ_0 is connected to the elongation of the plasma) and for the magnetic field strength¹⁴

$$B = B_0 \left[1 + \sum_{\mu,\nu} \epsilon_B^{(\mu,\nu)} \cos(\mu\Theta - \nu N_P \varphi) \right] = B_0 \alpha. \quad (7)$$

Here, μ and ν characterise the mode coupling in poloidal and toroidal directions, respectively. The corresponding angles are Θ and φ , and N_P denotes the number of field periods. Furthermore,

$$Q_{m,n} = \frac{1}{r^2} \left(k_{m,n}^2 - \frac{\omega^2}{v_A^2} \right) (1 - m^2) - \frac{1}{r} \frac{d}{dr} \left(\frac{\omega^2}{v_A^2} \right). \quad (8)$$

Taking into account only the toroidal coupling $\mu = 1$, $\nu = 0$ reduces Eq. (5) to its tokamak equivalent, Eq. (4).¹⁶

In any case, a coupled system of ordinary second-order differential equations in r has to be solved. The system becomes larger the more poloidal (and toroidal) modes of $\Phi^{(1)}$ are taken into account.

B. Fast-particle part

The contribution of the energetic particles to Eq. (1) is given by

$$\nabla \cdot \mathbf{j}_{\text{fast}}^{(1)} = Z_{\text{fast}} e \int d^3 v \nabla \cdot (f^{(1)} \mathbf{v}_D) \cong Z_{\text{fast}} e \int d^3 v \nabla \cdot (h^{(1)} \mathbf{v}_D). \quad (9)$$

Note that the perturbed fast-particle distribution function can be approximated by its non-adiabatic part $h^{(1)}$, because the particle-wave resonance condition is only contained in $h^{(1)}$.¹⁷ The adiabatic part of $f^{(1)}$, on the other hand, would only contribute to the fluid part. $h^{(1)}$ is given by

$$\begin{aligned} h_{m,n}^{(1)} &= \frac{Z_{\text{fast}} e v_{D,0}}{2} \frac{1}{\omega - v_{\parallel} k_{m,n}} \frac{\partial F}{\partial \varepsilon} \left(1 - m \frac{\omega_*}{\omega} \right) \\ &\times \left[\left\{ \frac{d}{dr} - \frac{m-1}{r} \right\} \Phi_{m-1}^{(1)} - \left\{ \frac{d}{dr} + \frac{m+1}{r} \right\} \Phi_{m+1}^{(1)} \right] \end{aligned} \quad (10)$$

for tokamaks.¹³ Here, $v_{D,0}$ is the magnitude of the toroidal drift at $r=0$, and F is the equilibrium distribution function of the fast particles, whose kinetic energy is denoted by ε . At present, F is taken to be an isotropic Maxwellian, which is a good assumption for, e.g., alpha particles being produced by fusion reactions. For plasmas heated by neutral beam injection, F could be a pitch-angle dependent slowing-down distribution function. ω_* is the energetic-ion diamagnetic drift frequency defined as

$$\omega_* = \frac{\partial F / \partial r}{\partial F / \partial \varepsilon} \frac{1}{M \Omega_0 r}, \quad (11)$$

with mass M and on-axis gyration frequency Ω_0 . Note that for stellarators Eq. (10) is generalized to

$$\begin{aligned} h_{m,n}^{(1)} &= \frac{R_0 Z_{\text{fast}} e v_{D,0}}{2r} \frac{1}{\omega - v_{\parallel} k_{m,n}} \frac{\partial F}{\partial \varepsilon} \left[\left(1 - m \frac{\omega_*}{\omega} \right) \right. \\ &\times \left\{ \sum_{\mu,\nu} \frac{d\epsilon_B^{(\mu,\nu)}}{dr} \left[(m - \mu) \Phi_{m-\mu,n-\nu N_P}^{(1)} \right. \right. \\ &+ \left. \left. (m + \mu) \Phi_{m+\mu,n+\nu N_P}^{(1)} \right] - \sum_{\mu \neq 0,\nu} \epsilon_B^{(\mu,\nu)} \right. \\ &\left. \left. \times \frac{d}{dr} \left[\Phi_{m-\mu,n-\nu N_P}^{(1)} - \Phi_{m+\mu,n+\nu N_P}^{(1)} \right] \right\} \right]. \end{aligned} \quad (12)$$

After some straightforward algebra, where it must be pointed out that the integration over velocity space in Eq. (9) has been performed analytically for the Maxwellian F , one arrives also for the fast particles at a coupled system of second-order differential equations in r . The resulting equation for $\nabla \cdot \mathbf{j}_{\text{fast}}^{(1)}$ is given in Appendix A for the stellarator case.

C. Radiative damping

Up to now, the model only contains second-order differential operators. Radiative damping by the background-plasma is described by a fourth-order operator.^{18,19} Here, a term derived in Ref. 18 that takes into account finite-Larmor-radius (FLR) effects as well as a parallel electric field that arises due to the kinetic modelling of the electron dynamics will be included. This term enables the coupling of TAEs to kinetic Alfvén waves (KAW) and opens up a new energy loss channel, i.e., damps the TAEs. Following Ref. 18, this term is added to Eq. (1) and reads as

$$D = \nabla \cdot \left[\nabla_{\perp} \left\{ d_{\text{rad}} \frac{1}{m_i n_i} \nabla \cdot (m_i n_i \nabla_{\perp} \Phi^{(1)}) \right\} \right] \quad (13)$$

with

$$d_{\text{rad}} = k_{m,n}^2 \left[\frac{3}{4} \rho_i^2 + \rho_s^2 \frac{1 + i\hat{\nu}Z(x)}{1 + xZ(x)} \right] \quad (14)$$

and

$$x = \frac{\omega + i\nu}{k_{m,n} v_{\text{th},e}}, \quad (15)$$

where $\rho_i = \sqrt{k_B T_i m_i} / (Z_i e B)$ is the ion gyroradius, $\rho_s = \sqrt{k_B T_e m_i} / (Z_i e B)$ is the sound gyroradius, and $\hat{\nu} = \nu / (k_{m,n} v_{\text{th},e})$ is a normalized collision frequency with ν being the electron-ion collision frequency. $v_{\text{th},e} = \sqrt{2k_B T_e / m_e}$ is the electron thermal velocity, and Z is the well-known plasma dispersion function.²⁰

Subsequently, the radiative damping term is treated under the assumption that the derivatives do not act on the equilibrium quantities, i.e.,

$$D \cong d_{\text{rad}} (\nabla \cdot \nabla_{\perp})^2 \Phi^{(1)}, \quad (16)$$

implying that the equilibrium does not change much over the radial extent of the mode. Then it only remains to perform a Fourier transform of the simplified term, taking into account the poloidal dependence of the metric tensor components in the large-aspect-ratio approximation. (A cylindrical approximation has been used for the stellarator.) This yields a coupled system of differential equations in r , but now every single equation is of fourth order.

III. NUMERICAL IMPLEMENTATION

A. General scheme

Depending on whether radiative damping is taken into account, a system of second-order or fourth-order ordinary differential equations in the radial variable r has to be solved. Considering, for simplicity, a tokamak with the fourth-order radiative damping term being present, results in the following system of equations (with the superscript ⁽¹⁾ omitted from this point on):

$$M_4 \Phi^{(iv)} + M_3 \Phi''' + M_2 \Phi'' + M_1 \Phi' + M_0 \Phi = \mathbf{0}, \quad (17)$$

which is obtained by combining Eq. (4) with the Fourier transformed versions of Eq. (9) (see Appendix A) and Eq. (16). The M_i , ($i=0, \dots, 4$) are complex $\Delta m \times \Delta m$ -matrices, and the vector $\Phi = (\phi_{m,n}, \dots, \phi_{m+\Delta m, n})^T$ contains the Δm poloidal modes of the perturbed electric potential that are taken into account. For a stellarator, there would be an additional variation in the toroidal mode number n , leading to a larger system.

One aim of the STAE-K code is to survey the effects of changing fast-particle parameters (e.g., fast-ion temperature or fast-ion density) on the properties (e.g., growth rate and mode structure) of a TAE. Therefore, a shooting code making use of the method of invariant imbedding (often called

the Riccati method, see Refs. 21 and 22) has been used for this purpose, as it is especially suited for such parameter scans.¹⁶ For instance, because of the matrix formulation, only the eigenvalue and not the slope of the vector Φ at a boundary has to be iterated. This is especially advantageous for larger systems.

Since the Riccati method can be used to solve any system of ordinary differential equations, consider for the moment a general linear system

$$\chi_1' = A\chi_1 + B\chi_2 \quad \chi_2' = C\chi_1 + D\chi_2, \quad (18)$$

where it is shown below how the matrices A , B , C , and D and the vectors χ_1 and χ_2 are related to the M_i and Φ of the original system given in Eq. (17).

In the Riccati method, the vectors χ_1 and χ_2 are linked by the so-called Riccati matrix R via

$$\chi_1 = R\chi_2. \quad (19)$$

From Eqs. (18) and (19), it is possible to infer a matrix differential equation (Riccati equation)

$$R' = AR + B - RCR - D \quad (20)$$

for R ,²¹ which is to be solved instead of the original system. The Riccati equation is integrated from both end points of the interval $[0, a]$ (a is the minor radius of the toroidal device) simultaneously towards an arbitrarily chosen fit point ξ at which R equals R_{left} and R_{right} , respectively.^{16,21} The eigenvalue is found by iterating ω until $\det(R_{\text{left}} - R_{\text{right}}) = 0$ holds at the fit point. The code uses a complex secant method to find the roots of the determinant and an accurate integration scheme with adaptive step size for the integration of Eq. (20).

The eigenfunctions are computed using Eq. (19) once ω and therefore also $R(\omega, r)$ have been found. The initial value for χ_2 at ξ comes from a singular value decomposition of $R_{\text{left}} - R_{\text{right}}$.¹⁶

B. Boundary conditions

By employing the Riccati scheme, the boundary conditions of the physical problem are transformed into initial conditions for R .²¹ The initial conditions are always chosen as $R(0) = R(a) = 0$, which can via Eq. (19) be translated to $\chi_1(0) = \chi_1(a) = 0$. It therefore depends on the definition of χ_1 and χ_2 which physical boundary conditions are realized.

For the fourth-order system, the physically correct boundary conditions are given as

$$\begin{aligned} \Phi(0) = 0, \quad \Phi(a) = \mathbf{0}, \\ \Phi''(0) = 0, \quad E_{\parallel}(a) = \mathbf{0}, \end{aligned} \quad (21)$$

if an ideally conducting wall surrounds the plasma. But since it is difficult to access the parallel electric field directly in the code, the condition $\Phi''(a) = \mathbf{0}$ is chosen instead of $E_{\parallel}(a) = \mathbf{0}$ (making the boundary conditions symmetric). According to Ref. 23, the parallel electric field can be approximated by

$$E_{\parallel} \cong -i\rho_s^2 (1 - i\delta) k_{m,n} (\nabla \cdot \nabla_{\perp}) \Phi, \quad (22)$$

092501-5 Slaby, Könies, and Kleiber

where $\delta \ll 1$ is related to the imaginary part of d_{rad} given in Eq. (14). Taking into account that

$$\nabla \cdot \nabla_{\perp} = \delta_0 \left[1 + \sum_{\mu, \nu} \epsilon_g^{(\mu, \nu)} \cos(\mu\Theta - \nu N_P \varphi) \right] \frac{\partial^2}{\partial r^2} + \frac{\delta_0}{r^2} \frac{\partial^2}{\partial \Theta^2} \quad (23)$$

for the stellarator, it can easily be verified that choosing $\Phi(a) = \Phi'(a) = 0$ indeed ensures $E_{\parallel}(a) = 0$ and that there is no conflict of boundary conditions. Generally, the conditions at $r = a$ are “real” boundary conditions determined by the nature of the plasma boundary, whereas the conditions at $r = 0$ are regularity conditions. They ensure a finite amplitude of the solution at the origin and are valid for $|m| > 0$.

Thus, it is feasible to define

$$\chi_1 = (\Phi, \Phi'')^T \quad \text{and} \quad \chi_2 = (\Phi', \Phi''')^T, \quad (24)$$

making it straightforward to find expressions for the matrices A , B , C , and D in terms of the M_i . These calculations yield

$$\begin{aligned} A &= \begin{pmatrix} \underline{0} & \underline{0} \\ \underline{0} & \underline{0} \end{pmatrix} & B &= \begin{pmatrix} \underline{1} & \underline{0} \\ \underline{0} & \underline{1} \end{pmatrix} \\ C &= \begin{pmatrix} \underline{0} & \underline{1} \\ -M_4^{-1}M_0 & -M_4^{-1}M_2 \end{pmatrix} \\ D &= \begin{pmatrix} \underline{0} & \underline{0} \\ -M_4^{-1}M_1 & -M_4^{-1}M_3 \end{pmatrix}, \end{aligned} \quad (25)$$

where $\underline{0}$ and $\underline{1}$ denote the zero and unity matrix of size $\Delta m \times \Delta m$, respectively.

IV. BENCHMARKS

STAE-K with its simplified physical model is primarily intended to be a numerically robust tool to quickly scan a certain region in parameter space for interesting fast-particle physics. The same region needs then to be investigated with more advanced gyrokinetic codes (such as GYGLES^{24–26} or EUTERPE, which require much more time for their simulations than STAE-K) to check whether the results from the simplified model hold. In order to check STAE-K within its range of validity, we present several benchmarks.

A. Benchmark with KIN-2DEM and others

This benchmark (referred to as benchmark-1 in Ref. 9 and introduced originally as a benchmark for KIN-2DEM²⁷) investigates the change of the real frequency of the mode and the development of the growth rate γ for different fast-particle temperatures. While repeatedly solving the eigenvalue problem, the fast-particle beta (using the usual symbols)

$$\beta_{\text{fast},0} = \frac{2\mu_0 k_B N_{\text{fast},0} T_{\text{fast},0}}{B_0^2} \quad (26)$$

on the magnetic axis will be held fixed by keeping $N_{\text{fast},0} T_{\text{fast},0} = 7.578 \times 10^{20} \text{ keV m}^{-3}$ constant. The two modes ($m_1 = 2$, $n_1 = 2$ and $m_2 = 3$, $n_2 = 2$) considered in this tokamak scenario

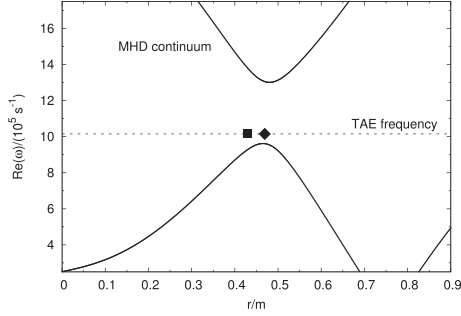
 Phys. Plasmas **23**, 092501 (2016)


FIG. 1. The Alfvén continuum without fast particles for the benchmark with KIN-2DEM and others as calculated by STAE-K. The TAE frequency (dashed line) lies in the continuum gap. The locations of the maxima of both eigenmode components Φ_m and Φ_{m+1} have been indicated by a square and a diamond, respectively.

form an MHD continuum that can be seen in Fig. 1. The background-plasma density profile and the fast-particle temperature profile are chosen to be flat, so that the drive of the mode only arises from the density gradient of the fast particles. All other bulk-plasma parameters are listed in Table I (see Appendix C). Note that the bulk plasma is treated within an ideal and reduced MHD framework with negligible plasma beta. This means that pressure terms and consequently any term including a finite bulk-plasma temperature have been left out. The remaining parameters of the energetic particles, which have a Maxwellian equilibrium distribution function, can be found in Table II.

The growth rate calculated by all the different codes is depicted in Fig. 2. As the fast-particle beta is kept constant here, the growth rate increases rather slowly, especially compared with the ITPA benchmark presented below. One can see that all MHD-kinetic hybrid codes (STAE-K, CAS3D-K, and NOVA-K) predict nearly the same result. In its general behaviour, STAE-K is closest to NOVA-K. Note that for this comparison, an older version of NOVA-K,^{28,29} which does not include finite-orbit-width (FOW)- and FLR

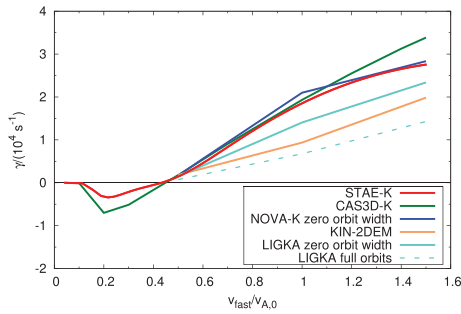


FIG. 2. Calculated growth rate of the TAE as a function of the fast-particle thermal velocity normalized to the on-axis Alfvén velocity. All the codes agree in their qualitative behaviour, and STAE-K especially matches the results of other hybrid codes (such as NOVA-K). The marginal point $\gamma = 0$ is the same for all codes. Curves other than STAE-K are taken from Refs. 27 and 30.

effects, was used, which makes the underlying physical model very similar to that of STAE-K. CAS3D-K is an eigenvalue code which relies on a model of ideal MHD for the background plasma and, similarly to STAE-K, treats the fast particles kinetically. However, CAS3D-K is a perturbative code, whereas STAE-K is non-perturbative. Just like STAE-K, LIGKA³⁰ is a non-perturbative eigenvalue code but with a much more complex model, and it is not surprising that these two codes show differences.

It can also be noted that for fast-ion velocities less than approximately $v_{A,0}/2$, the mode is still damped. All the codes agree very well in determining the location of the marginal point where the growth rate becomes zero. The existence of such a marginal point can be understood from Eq. (10). At the marginal point, the condition $m\omega_* = \omega$ is fulfilled, making $h_m^{(1)}$ exactly zero. Thus, there is no contribution of the energetic particles to the perturbed electric current density $\mathbf{j}^{(1)}$ in the plasma, and γ thus vanishes. In order to allow for a non-vanishing growth rate, the diamagnetic drift frequency of the energetic particles (multiplied by m) must exceed the mode frequency. As ω_* is given by

$$\omega_* = - \frac{k_B T_{\text{fast}} \left(\ln N_{\text{fast}} - \frac{3}{2} \ln T_{\text{fast}} \right)' + \varepsilon (\ln T_{\text{fast}})'}{M \Omega_0 r} \quad (27)$$

for a Maxwellian distribution function of the energetic particles, it is possible to increase ω_* by having steeper gradients in both the density and temperature profile, or by having a higher fast-particle energy ε if the temperature profile is not flat.

For the purpose of this benchmark, radiative damping and electron Landau damping have not been taken into account as they would modify the position of the marginal point and the total growth rate. The change of the real frequency, $\delta\omega = \text{Re}(\omega) - \omega_{\text{MHD}}$, is shown in Fig. 3. All codes show a good qualitative agreement. It can be observed that the mode frequency decreases rapidly in the beginning and that it increases again with rising fast-particle temperature. Due to the low aspect ratio of this case and the large radial extent of the MHD eigenmode, FOW effects are negligible for all the considered T_{fast} . This can be understood from a simple analytical estimate: The full width of a passing-particle orbit is given by $\delta = 2\rho_{\text{fast}}/l$, where ρ_{fast} is the energetic-particle Larmor radius. Neglecting FOW effects, and their respective averaging effect, is only possible while $\delta \ll \Delta_M$, with Δ_M being the width of the mode. Using $\delta = \Delta_M$ as a rough upper bound, we define a “critical” temperature

$$T_{\text{crit}} \cong \frac{(Z_{\text{fast}} e B_0 \Delta_M)^2}{4 M k_B q_a^2}. \quad (28)$$

In fact, Eq. (28) yields a very high $T_{\text{crit}} = 16$ MeV. Hence, there are no substantial differences between calculations with and without FOW effects.

With this first benchmark, the numerical feasibility of the Riccati shooting method used to solve the equations has been confirmed. STAE-K is able to calculate the curves in all the figures above in less than half an hour on a single 2.3 GHz core, making STAE-K one to two orders of magnitude faster than the other codes.

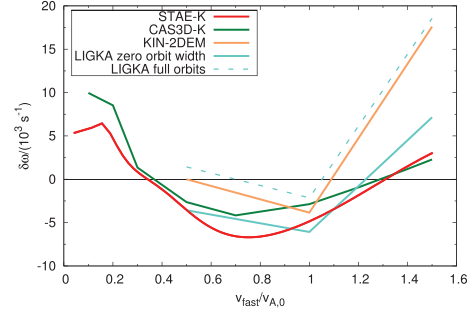


FIG. 3. Calculated real part of the TAE frequency as a function of the fast-particle thermal velocity normalized to the on-axis Alfvén velocity. Again STAE-K is close to other hybrid codes (especially CAS3D-K) in this case. The fully kinetic codes predict a much stronger frequency change for high temperatures. Curves other than STAE-K are taken from Refs. 27 and 30.

B. ITPA benchmark

The ITPA benchmark³¹ is one of the most rigorous benchmarks that have been performed of codes calculating fast-ion-driven instabilities. It consists of a rather idealized scenario, which involves only two modes with poloidal and toroidal mode numbers $m_1 = 10$, $n_1 = 6$ and $m_2 = 11$, $n_2 = 6$. They form a gap in the Alfvén continuum at exactly $r/a = 0.5$ as can be seen in Fig. 4. In this scenario, a large-aspect-ratio tokamak with circular flux surfaces is used. The background-plasma parameters are listed in Table III. For simplicity, the background-plasma density as well as the fast-particle temperature profile are again chosen to be flat. Hence, the only free energy source to drive the TAE unstable is the fast-particle density gradient. The fast-particle parameters can be found in Table IV. The energetic particles possess a Maxwellian equilibrium distribution function.

Starting with the real eigenfrequency of an ideal-MHD calculation, fast particles with increasing temperature are added. As the energetic-particle density profile has its maximum gradient in the region where the mode is localized,

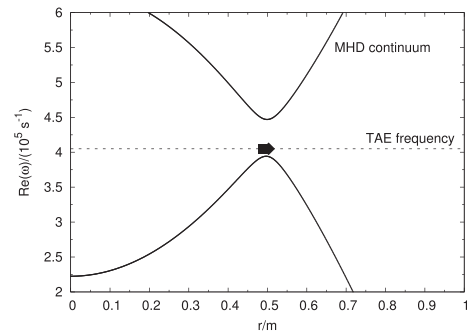


FIG. 4. The Alfvén continuum without fast particles for the ITPA benchmark as calculated by STAE-K. The TAE frequency (dashed line) lies in the continuum gap. The locations of the maxima of both eigenmode components Φ_m and Φ_{m+1} have been indicated by a square and a diamond, respectively.

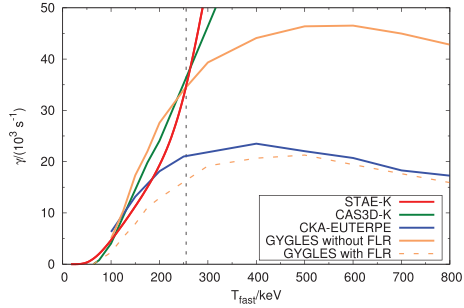


FIG. 5. Calculated growth rates of the TAE as a function of the fast-particle temperature within the ITPA framework. All the codes that exclude FOW- (and FLR-) effects show qualitatively the same strong increase in the growth rate. If those effects are taken into account, they substantially decrease the growth rate. The dashed vertical line shows the critical temperature from Eq. (28) over which FOW effects cannot be neglected. Curves other than STAE-K taken from Refs. 9 and 31.

energy transfer from the fast particles to the mode by means of inverse Landau damping is possible, driving the mode unstable. The results of this benchmark can be seen in Fig. 5, where STAE-K is compared with various other codes. CAS3D-K and STAE-K, although differing in detail, possess enough analogies that it is possible to expect a good agreement between the two codes, at least for low enough temperatures, where the perturbative approach of CAS3D-K is valid. CKA-EUTERPE and GYGLES are both particle-in-cell (PIC) codes, but while GYGLES is fully kinetic, CKA-EUTERPE employs an MHD-kinetic hybrid model.

In Fig. 5, one can see that, not taking into account FLR effects, all codes predict a strong increase in the growth rate γ for temperatures up to $T_{\text{fast}} \cong 250$ keV. For higher temperatures, finite-orbit-width (FOW) effects lead to a saturation of γ for CKA-EUTERPE and GYGLES. The reason is that FOW- and FLR effects introduce an averaging effect over the perturbed potential.^{9,28} This means that the effective particle-wave energy transfer is smaller, leading to a reduced growth rate. As expected, the quantitative agreement between CAS3D-K and STAE-K (both codes neglect FOW- and FLR effects) is good between zero and 250 keV, and they qualitatively agree in predicting a strong growth rate for higher fast-ion temperatures.

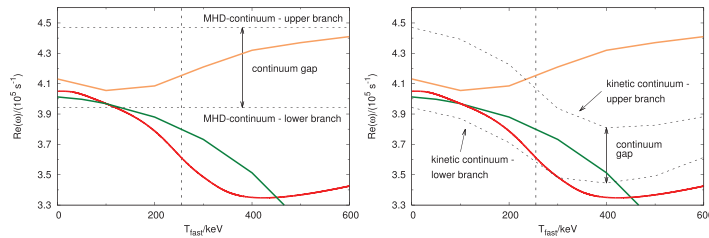


FIG. 6. Real part of the TAE frequency as a function of the fast-particle temperature within the ITPA framework. (The colours are the same as in Fig. 5.) The dashed vertical line shows the critical temperature from Eq. (28) over which FOW effects cannot be neglected. Left: Since the frequency is initially decreasing rapidly with increasing fast-ion temperature, the mode quickly leaves the MHD continuum gap. Right: Even though the frequency varies rapidly, the kinetic continuum mimics this behaviour so that the mode frequency remains longer inside the gap. For higher fast-particle temperatures, the mode sinks deeply into the continuum. GYGLES curve taken from Ref. 26.

For the ITPA benchmark, Eq. (28) predicts T_{crit} to be around 255 keV, indicated by a dashed vertical line in Fig. 5. For $T_{\text{fast}} < T_{\text{crit}}$, the models provide similar answers, while for $T_{\text{fast}} > T_{\text{crit}}$ the orbit-related discrepancies are obvious. Though being a rough upper estimate for the validity range of the model, Eq. (28) works quite well for the growth rate.

In this benchmark not only γ but also the change in the real frequency due to the presence of energetic particles has been calculated. The results are shown in Fig. 6, where the same codes (with the same colours) have been compared as in Fig. 5. (Again, the critical temperature is indicated by a dashed vertical line.) As before, STAE-K and CAS3D-K show the best agreement for low enough temperatures, which is to be expected due to the similarities in their mathematical models. The result from GYGLES shows a different behaviour because of its higher level of complexity: As mentioned before, GYGLES includes FOW effects that influence not only $\gamma(T_{\text{fast}})$ but the behaviour of the frequency as well. While deviations in the growth rate are small below T_{crit} , the frequencies computed by GYGLES and STAE-K only agree to about 100 keV. Comparing with the analytical estimate, which worked well for the growth rate, this means that the frequency reacts more sensitively to FOW effects than γ does, a fact deserving further investigation.

In summary, it can be stated that the crucial factors determining the low T_{crit} in this case are the high aspect ratio and thus the narrow mode width. Nevertheless, we will continue to track the development of this mode into the region of higher T_{fast} in order to show some generic features of the model, which we also observed for cases with different parameters, like the benchmark presented in Sec. IV A, where the model is valid up to much higher T_{fast} .

Please note that an initial-value approach like the PIC method converges to the fastest growing mode, which is not necessarily identical to the initial MHD eigenmode. STAE-K, on the other hand, is able to track the development of the same mode during a parameter scan.

On the left-hand side of Fig. 6, it is shown how the mode frequency decreases rapidly with increasing T_{fast} and thus quickly escapes from the MHD continuum gap. As soon as the mode frequency intersects the continuum, continuum damping sets in and the eigenfunctions develop singularities. Since these singularities in position space can be treated in

formal analogy to the singularities in velocity space present in conventional Landau damping, the path of integration was extended into the complex plane.¹⁶ The diagram on the left-hand side of Fig. 6 is inspired by the figures in Ref. 26, from where the results of GYGLES have been taken. As the mode frequency always stays inside the continuum gap for this curve, such a representation next to the MHD continuum is valid. The right-hand side of Fig. 6 shows the same results from the codes, but this time together with the kinetic continuum. (The reader is referred to Sec. VA and Fig. 8 for more details on the calculation of the continuum.) In contrast to the MHD continuum, the kinetic continuum changes with T_{fast} . For low T_{fast} , it moves together with the mode frequency. At larger temperatures, however, the gap gets narrower and the mode again leaves the continuum gap and becomes singular.

C. Landau damping in the ITPA benchmark

In this benchmark, only the contributions of Landau damping³² on the modes will be investigated. All gradients are therefore set to zero (corresponding to $\omega_* \equiv 0$) and thus only kinetic terms that act stabilizing are retained.

In Ref. 7, an analytic formula, capable of making a theoretical prediction about the Landau damping rate of gap modes, has been derived. A very similar equation

$$\delta\omega = -\frac{\beta_{\text{fast}}^*}{8k_{m,n}^* r_*^2} \omega \frac{r_*^2}{R_0^2} \sum_{j=\pm 1} G(x_j), \quad (29)$$

with

$$G(x_j) = 3x_j^2 + 2x_j^4 + x_j \text{Re}(Z(x_j)) [1 + 2x_j^2 + 2x_j^4] \quad (30)$$

and

$$x_j = \frac{|q^* R_0 k_{m,n}^*| v_A^*}{|q^* R_0 k_{m,n}^* + j| v_{\text{fast}}^*} \quad (31)$$

can also be found for the change of the real frequency. The superscript * indicates that the quantity in question should be evaluated in the centre of the TAE gap, i.e., where the continua would cross in the cylindrical limit. Hence, Eq. (29) is valid in the limit of very small inverse aspect ratio. Here, this is achieved by choosing a large major radius. The comparison of STAE-K with the analytic theory of Ref. 7 as well as with Eq. (29) is shown in Fig. 7 for the parameters of the ITPA benchmark. While the top diagram shows the normalized damping rate, the normalized deviation from the MHD frequency is depicted in the diagram on the bottom.

It can be observed that, even for small major radii, the qualitative behaviour of the damping rate calculated by STAE-K matches that from the analytic theory. If R_0 is increased further, the curves converge to the theoretical result.

In the top diagram of Fig. 7, it can be seen that the damping rate possesses two distinct minima. These correspond to resonances of the fast-particle thermal velocity with respect to the Alfvén velocity.^{7,8}

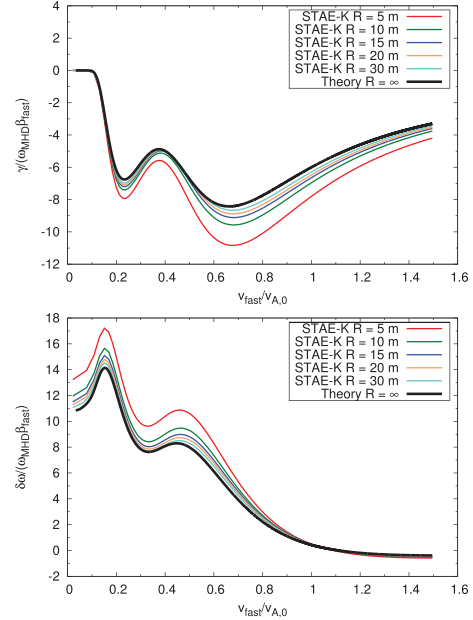


FIG. 7. Comparison of STAE-K to analytic theory in the limit of very small inverse aspect ratio for various fast-particle temperatures. Normalized Landau damping rate (top) and normalized change of the real frequency (bottom) as a function of the energetic-particle thermal velocity. STAE-K converges to the theoretical result (black curve) for increasing major radii.

V. RESULTS

A. Changes in the MHD continuum due to energetic-particle influences

STAE-K is not only able to calculate the growth rate, frequency, and the structure of the eigenfunction of the mode, but also the shear Alfvén wave continuum. This is done by computing the frequencies for which $\det M_2 = 0$, with M_2 from Eq. (17) in the absence of radiative damping, is satisfied. The continuum of M_2 , together with the MHD continuum, is resolved if the fourth-order term is taken into account, which leads to a discretization of the continuum as reported in Ref. 6.

Here, the influence of the fast particles on the MHD continuum without radiative damping is studied. The same magnetic geometry as in the ITPA benchmark has been used.

Fig. 8 shows that the continuum can be deformed substantially if the pressure of the energetic particles becomes comparable to the bulk-plasma pressure. (Kinetic continuum considering also bulk-plasma effects in tokamaks have recently been computed in Ref. 33.) This happens for $T_{\text{fast}} > T_{\text{crit}}$, where the results from STAE-K differ from those obtained by fully gyrokinetic codes, but are close to those of perturbative codes like CAS3D-K (see Sec. IV B). As indicated before, the investigation of the mode is nevertheless carried on in this parameter range to study cases that exhibit

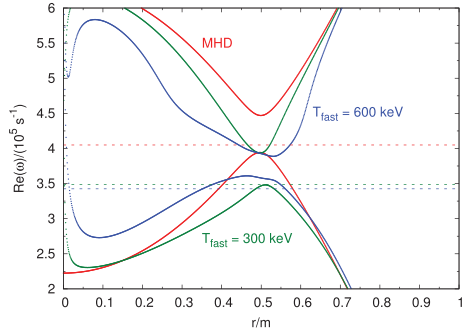


FIG. 8. Evolution of the shear Alfvén continuum with increasing temperature of the energetic particles for the parameters of the ITPA benchmark (see Tables III and IV). The TAE gap as well as the discrete eigenfrequency (dashed lines) are shifted to lower values. For $T_{\text{fast}} \approx 300$ keV, the mode frequency intersects the continuum, leading to continuum damping.

this mode-continuum interaction. This deformation of the continuum is useful to explain the results of the simplified models utilized in STAE-K and CAS3D-K. Since both the continuum as well as the discrete TAE frequency within the gap are shifted to lower frequencies, the mode can stay longer inside the gap and is not subject to continuum damping. This maximizes the kinetic drive of the mode. Note that eventually, for $T_{\text{fast}} \approx 300$ keV, the TAE intersects the continuum, so that the TAE transfers energy to singular continuum modes.

Strong deformations of the continua in the plasma center can be observed. This is a consequence of the fast-ion density profile chosen in the ITPA benchmark. This density profile has a small, but non-vanishing, gradient in the plasma center. If the profile was flat, just a beta-related up-shift would be observed. It is shown in Appendix B that the adiabatic part of the perturbed distribution function does not influence the kinetic continuum.

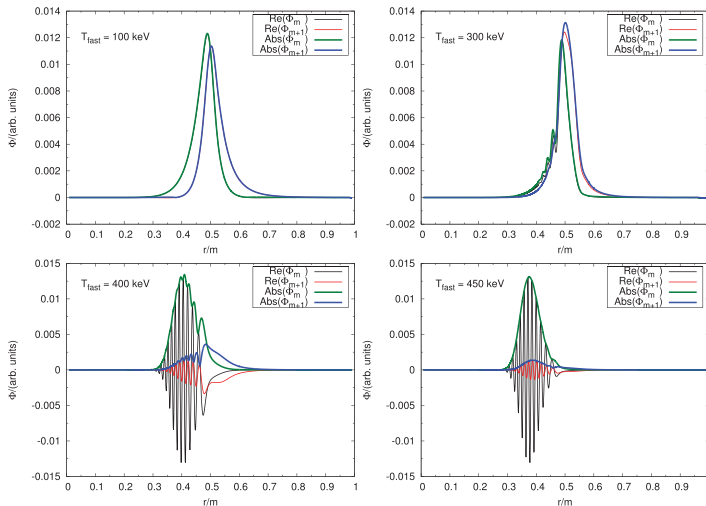


FIG. 9. Development of the eigenfunctions in the ITPA case including radiative damping. The mode transforms from a TAE into a KTAE and later into a KAW. Black and red curves show the real parts of both eigenmode components, whereas green and blue have been used for the absolute values.

B. Contribution of radiative- and background-plasma Landau damping

The singular eigenfunctions resulting from the continuum interaction indicate that the MHD-kinetic hybrid model is not well suited to explain the physics on very short spatial scales. The model can be improved by including kinetic effects of finite Larmor radii of the background-plasma ions, as well as a kinetically arising parallel electric field. They cause the so-called radiative damping, governed by the fourth-order operator given in Eq. (13).¹⁸

Since the addition of this term discretizes the MHD continuum (including also the fast-particle influences), it resolves any continuum interaction as can be seen in Fig. 9 for the parameters of the ITPA benchmark. A constant bulk-plasma temperature of 1 keV was chosen. The eigenfunctions show no singularities indicative of continuum damping. Instead, the figure shows the smooth transition of a TAE into a kinetically modified TAE (KTAE) and later into a kinetic Alfvén wave (KAW). Short-scale oscillations start to appear on the mode structure precisely when the fast-particle temperature is such that the mode would intersect the Alfvén continuum, if radiative damping were not present. The oscillations are only present in the real and imaginary part (not shown in the figure) of the eigenfunction. They are absent in the absolute value of the potential perturbation, which thus resembles the results of Ref. 26 very closely. Note that no short-scale oscillations in the eigenfunction are observed in Ref. 26. We conjecture that they are an effect of the much larger growth rate of this model due to the absence of FOW- and FLR effects. Additionally, the mode frequency in Ref. 26 never intersects the continuum, which is found to be an essential condition for the appearance of oscillations.

The final mode structure is broader, shifted towards the position of the maximal gradient in N_{fast} , and one poloidal harmonic dominates over the others. While these criteria have

been used to characterize EPMS in Ref. 26, they are also useful for the description of the presently computed KAWs.

The model includes the kinetic drive of the energetic particles as well as damping mechanisms such as Landau damping (of both the bulk ions and electrons), radiative damping, and, if the continuum gap is closed, continuum damping. In order to assess the overall stability of a mode, damping is just as important as the drive. For the ITPA case introduced above, calculations have also been performed without fast particles. The combined damping rate of radiative damping and Landau damping of the background-plasma electrons, whose damping dominates over that of bulk-ions for the present case, was $\gamma = -2.33 \times 10^3 \text{ s}^{-1}$, which is very close to results from more advanced codes like LIGKA and GYGLES giving $\gamma = -2.34 \times 10^3 \text{ s}^{-1}$ and $\gamma = -3.9 \times 10^3 \text{ s}^{-1}$, respectively.³¹

C. Stability diagrams

The properties of the damping terms are mainly determined by the background plasma, making it feasible to vary fast-particle parameters and background-plasma parameters independently. In doing so, it is possible to scan a whole region in parameter space and to answer the question whether the mode is stable or unstable in this region.

Such stability scans have been performed for the ITPA benchmark case and for a W7-X scenario (introduced below). The bulk and the energetic-particle temperature have been varied independently (N_{fast} and N_{bulk} were kept constant) to obtain the stability diagrams shown in Fig. 10 (ITPA benchmark on top and W7-X on the bottom). All calculations include the kinetic drive from the fast-particle species as well as Landau damping of the bulk ions/electrons and radiative damping. The W7-X calculation on the bottom left has been simplified to only include the toroidal coupling. Hence, it is very similar to the large-aspect-ratio tokamak directly above. For the W7-X calculation on the bottom right, also the helical coupling ($\mu = 1, \nu = 1$) and the helical side bands have been included.

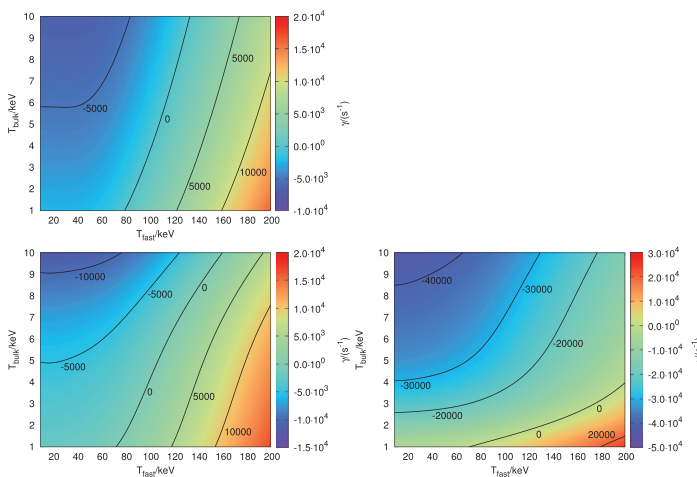


FIG. 10. Stability diagrams taking into account the kinetic drive of a fast-particle species, Landau damping by the background-plasma ions/electrons, and radiative damping. Black lines connect points of equal growth/damping rate. Top: ITPA benchmark. Bottom: W7-X case. For the W7-X case on the bottom right also the additional effects of the helical coupling were included.

Apart from the toroidal ($\mu = 1, \nu = 0$) resonances $v_{\text{res}}/v_A = 1/3$ and 1, additional ones according to

$$\frac{v_{\text{res}}}{v_A} = \left| 1 \pm \frac{\mu l^* + \nu N_P}{m l^* + n} \right|^{-1} \quad (32)$$

are possible.⁸ The helical resonances are well within the temperature range of the bulk ions and, because of the lack of any gradients, act stabilizing.

Thus, this second (more realistic) stability diagram for W7-X shows a much more stable mode. For the tokamak, the radiative damping term, which outweighs Landau damping, significantly increases the region of stability.

The stability scans are performed by repeatedly solving the eigenvalue problem in the plane spanned by T_{fast} and T_{bulk} . As such, computation of the scans parallelizes perfectly. Depending on whether radiative damping was included, these calculations typically take three to twelve hours on 128 processors for a resolution of about 256 points in each direction.

D. Application to W7-X

The code will be applied to the stellarator W7-X in more detail. The background-plasma and fast-particle parameters for the W7-X case are summarized in Tables V and VI, respectively, and they lead to an MHD continuum shown in Fig. 11.

As a first step, the influence of a rising energetic-particle temperature on the structure of the eigenfunction is studied. Only the fast particles have been treated kinetically. Note that the radiative damping term, with a background temperature of $T_{\text{bulk}} = 1 \text{ keV}$, has been present in all the calculations in this section. The results can be seen in Fig. 12, where the kinetic continuum and the eigenfunction for a high fast-particle temperature of 750 keV are shown. The kinetic continuum exhibits only minor differences compared with the ideal-MHD continuum. Furthermore, these changes are located at radial positions where the mode amplitude is almost vanishing. Consequently, the influence of the fast particles on the

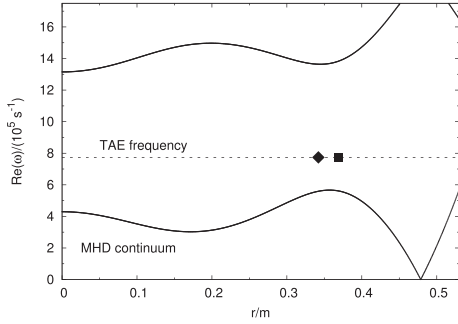


FIG. 11. The Alfvén continuum (showing the TAE gap) without fast particles for the W7-X case as calculated by STAE-K. The TAE frequency (dashed line) lies in the continuum gap. The locations of the maxima of eigenmode components $\Phi_{m,n}$ and $\Phi_{m+1,n}$ have been indicated by a square and a diamond, respectively.

structure of the eigenfunction is negligible. It must also be pointed out that while $T_{\text{fast}} = 750 \text{ keV} < 1.35 \text{ MeV} = T_{\text{crit}}$ (see Eq. (28)), such a temperature will most likely not be reached in W7-X. The specific case that has been chosen for this investigation is very insensitive to an increasing T_{fast} .

The fast-particle pressure can also be raised by increasing the fast-particle density. The eigenfunction depicted in Fig. 13 again shows no significant deviation from its ideal-MHD counterpart. As previously, this is due to the fact that the continuum only changes in the center and at the edge and that therefore the nature of the coupling between the poloidal harmonics remains unaffected.

In all the stellarator calculations, the helical side bands as well as the helical couplings have been included. It is important to distinguish both: The inclusion of helical side bands means that aside from the main Fourier harmonics that make up the TAE, $\phi_{m,n}$ and $\phi_{m+1,n}$ ($\phi_{m-1,n}$ has also been included), additionally $\phi_{m-1,n-N_p}$ and $\phi_{m+1,n+N_p}$ are considered in the calculations. In the present case, the helical side bands are negligible, as can be seen from Figs. 12 and 13. It then is a good approximation just to retain $\phi_{m,n}$ and $\phi_{m+1,n}$, while the operators (in case of the Riccati formulation the matrices M_i) still contain the helical couplings. Those come from the Fourier decomposition of the equilibrium magnetic field and provide the resonances. In summary, it may be stated that a combination of ϵ_{g} and ϵ_{B} determines the MHD mode structure, while ϵ_{B} alone gives the coupling to the kinetic term and is thus responsible for the instability.

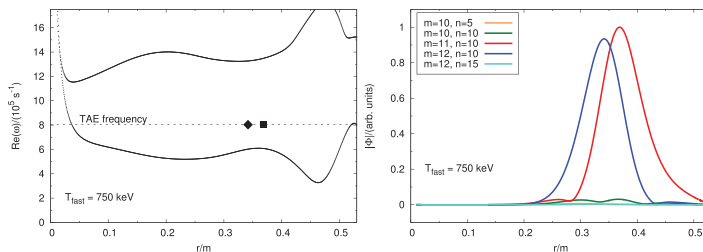


FIG. 12. Kinetic continuum with the TAE gap (left) and eigenfunction (right) for the W7-X case in the presence of energetic particles with high T_{fast} of 750 keV. The fast-particle density is $N_{\text{fast}} = 4.0 \times 10^{17} \text{ m}^{-3}$. The helical side bands $m=10$, $n=5$ and $m=12$, $n=15$ have been included in the calculation. The eigenfunction is nearly unchanged compared with the ideal-MHD case.

In the calculation of the stability diagrams, the helical resonances as well as the helical side bands were included to demonstrate the capability of the code to handle a larger system.

Generally, the transition of the TAE into a KTAE happens because the mode frequency gets close to the continuum and because the radiative damping term is present. For the two previous cases with increasing T_{fast} and N_{fast} , the mode frequency was nearly unaffected by the fast-particle population. Furthermore, the continuum only changed in regions where the mode was not localized. Thus, no transition into a KTAE could be observed. However, the influence of radiative damping on the structure of the eigenfunction can also be studied in the absence of fast particles by simply modifying the density profile of the background plasma in such a way that the TAE gap closes. Then a combined damping rate of continuum damping and radiative damping is calculated. Since the focus of this calculation is on the TAE gap and no fast particles are present, the helical coupling as well as the helical side bands will be neglected. The density profile is chosen as

$$n_{\text{bulk}}^{\text{profile}} = \frac{1}{2} \left[1 - \tanh \left(\frac{s_h - r}{0.1a} \right) \right] \quad (33)$$

with a shift parameter s_h . It represents the extreme case of a hollow density profile, where at $r = s_h$ the density has increased to half the value at the edge. Note that hollow density profiles are a topic for W7-X³⁴ as a result of localized on-axis ECRH in combination with the outwards directed thermo-diffusion. Here, the profile described in Eq. (33) is used as a proof of principle how radiative damping influences the case of extreme continuum damping. The results of this investigation, together with the different continua for various values of s_h are depicted in Fig. 14. Even though the continuum closes in a region where the mode has a finite amplitude, no singular eigenfunctions are observed. They are instead completely regularized by the presence of the fourth-order damping operator. Now, short-scale oscillations (less prominent than in Fig. 9) develop in the eigenfunctions, and the amplitude of one poloidal harmonic becomes much larger than that of the other one. This investigation without fast particles shows that such behaviour must not necessarily be interpreted as a sign of an EPM. It is merely a consequence of the TAE frequency leaving the continuum gap towards a region where mode coupling becomes less important. However, as can be concluded from the ITPA case, energetic particles may have a similar influence on the mode frequency and the continuum. These results are in qualitative

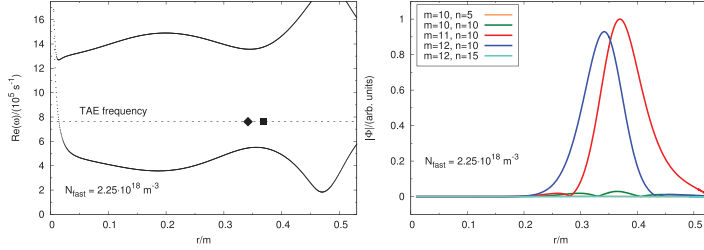


FIG. 13. Kinetic continuum with the TAE gap (left) and eigenfunction (right) for the W7-X case in the presence of energetic particles with a high ratio of $N_{\text{fast}}/N_{\text{bulk}} = 11.25\%$. The fast-particle temperature is $T_{\text{fast}} = 100\text{keV}$. The helical side bands $m = 10, n = 5$ and $m = 12, n = 15$ have been included in the calculation. The eigenfunction is nearly unchanged compared with the ideal-MHD case.

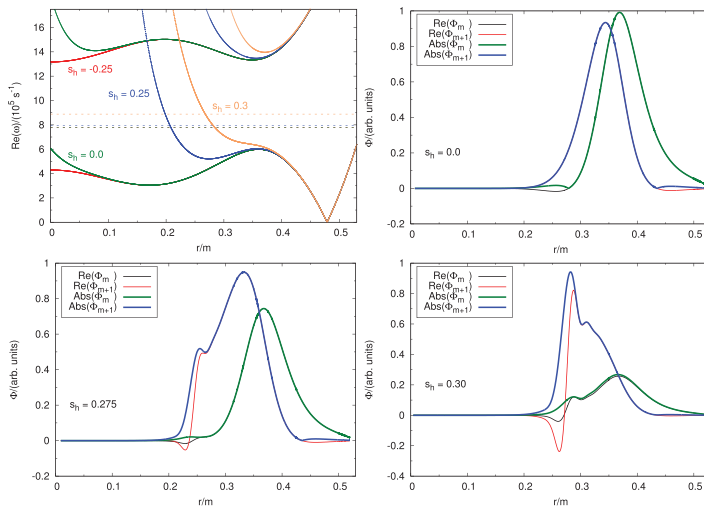


FIG. 14. Influence of the radiative damping term on the eigenfunctions for a closing TAE gap (see top left). The eigenfunctions for values of $s_h = 0.0$ (top right), $s_h = 0.275$ (bottom left), and $s_h = 0.3$ (bottom right) are shown. The fourth-order term prevents the development of singularities. No fast particles are present in this calculation.

agreement with Ref. 35. For the extreme case of $s_h = 0.3\text{ m}$, a damping rate of $(\gamma_{\text{continuum}} + \gamma_{\text{radiative}})/\omega_{\text{MHD}} = -2.32\%$ is measured, where the majority comes from continuum damping as can be observed in Fig. 15. Radiative damping alone accounts for approximately -0.12% .

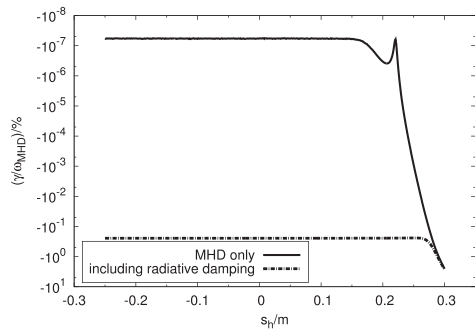


FIG. 15. Normalized continuum damping rate only taking into account the MHD terms (full curve) and a combination of radiative damping and continuum damping (dashed line). The shift parameter s_h used to control the density profile determines the strength of the damping.

The figure shows a strong increase of the damping rate $\gamma_{\text{continuum}}$ for $s_h \gtrsim 0.225\text{ m}$ when just the MHD terms are present. The path of integration has been extended into the complex plane to retain the contribution of the pole. Note that in this logarithmic plot the initial level of $\gamma_{\text{continuum}}$ for small values of s_h is not exactly zero only because of the numerically specified tolerance for convergence. In this initial phase, radiative damping outweighs continuum damping by many orders of magnitude. At some point, however, continuum damping also sets in when the fourth-order term is taken into account. In this case, it was not necessary to leave the real axis when integrating Eq. (20). As expected, there still are some slight differences in both curves of Fig. 15 for $s_h = 0.3\text{ m}$, but they seem to converge to the same damping rate in the limit of very strong damping.

VI. SUMMARY AND CONCLUSIONS

In this paper, the resonant interaction of fast particles with shear Alfvén waves, especially TAEs, leading to KTAEs and KAWs has been investigated in tokamaks and stellarators. The non-perturbative and non-local model used for this purpose treats the background plasma within the ideal MHD-theory and the fast particles kinetically. Furthermore, a higher-order differential operator, which describes radiative damping, has been added to the model. (To the best

knowledge of the authors, this is the first time that radiative damping has been addressed in stellarators.) Throughout this work, the large-aspect-ratio and low-plasma-beta approximations have been used.

The eigenvalue problem is solved by the novel code STAE-K, using a numerically robust and efficient shooting algorithm. Thanks to its high speed and its physically simplified model, the code is particularly well suited to perform parameter scans for varying fast-particle parameters.

After a scan has been conducted, specific regions in parameter space can be investigated by more advanced codes with physically more complex models. It can then be checked if the predictions from the simplified model utilized by STAE-K hold.

The behaviour of the shear Alfvén wave continuum in the presence of energetic particles was studied. It was found that the structure of the continuum may be influenced substantially. In particular, continuum resonances in regions where the mode has a finite amplitude become possible. In this case, continuum damping occurs and the TAE may smoothly be converted into a KAW, if radiative damping is accounted for.

Especially in the W7-X case, it could be observed that the structure of the MHD-eigenfunction is insensitive to changes of T_{fast} and N_{fast} . Thus, perturbative hybrid models like CAS3D-K and CKA-EUTERPE with a fixed mode structure might be applicable for a wide range of fast-

particle parameters in regimes where fast-ion FOW effects are negligible.

The ITPA benchmark showed that FOW effects play a critical role in determining the growth rate and frequency of the mode. While gap modes are treated well within the simplified model, the proper treatment of the orbits is important to study EPs, which is not possible with the present version of the code. However, the simple analytical expression Eq. (28) gives an estimate for the validity range of the simplified model. A topic left for future work will be to properly include FOW effects into STAE-K. Nevertheless, even in its present form STAE-K is one of the very few codes that can perform calculations for stellarators.

ACKNOWLEDGMENTS

This work has been carried out within the framework of the EUROfusion Consortium and has received funding from the Euratom research and training programme 2014–2018 under Grant Agreement No. 633053. The views and opinions expressed herein do not necessarily reflect those of the European Commission.

APPENDIX A: FAST-PARTICLE CONTRIBUTION IN DETAIL

Using Eqs. (9) and (12), the Fourier transformed fast-particle contribution to Eq. (1) is obtained as

$$\mathcal{F}\mathcal{T}\left(\frac{i\omega\mu_0 r^2}{z^2\delta_0}\nabla\cdot\mathbf{j}_{\text{fast}}^{(1)}\right)\cong\frac{\omega\mu_0 Z_{\text{fast}}eR_0^2\delta_0}{4}\left(A_{m,n}\Phi_{m,n}^{(1)}+B_{m+2\sigma,n+2\tau N_p}\Phi_{m+2\sigma,n+2\tau N_p}^{(1)}+C_{m-2\sigma,n-2\tau N_p}\Phi_{m-2\sigma,n-2\tau N_p}^{(1)}\right), \quad (\text{A1})$$

with

$$\begin{aligned} A_{m,n} = & \left\{ \eta_{\sigma,0}\sigma\left(\epsilon_{\text{B}}^{(\sigma,\tau)}\right)^2\left[-\mathcal{C}(z_+)-\mathcal{C}(z_-)\right] \right\} \frac{d^2}{dr^2} + \left\{ \eta_{\sigma,0}\epsilon_{\text{B}}^{(\sigma,\tau)'}\epsilon_{\text{B}}^{(\sigma,\tau)'}\left[-\mathcal{A}(z_+)+\mathcal{A}(z_-)\right] + \eta_{\sigma,0}\sigma\left(\epsilon_{\text{B}}^{(\sigma,\tau)}\right)^2\left[-\mathcal{B}(z_+)-\mathcal{B}(z_-)\right] \right. \\ & + \sigma\epsilon_{\text{B}}^{(\sigma,\tau)'}\epsilon_{\text{B}}^{(\sigma,\tau)'}\left[\left(m-\eta_{\sigma,0}\right)\mathcal{C}(z_+)-\left(m+\eta_{\sigma,0}\right)\mathcal{C}(z_-)\right] \left. \right\} \frac{d}{dr} + m\left(\epsilon_{\text{B}}^{(\sigma,\tau)'}\right)^2\left[\mathcal{A}(z_+)+\mathcal{A}(z_-)\right] \\ & + m\sigma\epsilon_{\text{B}}^{(\sigma,\tau)'}\epsilon_{\text{B}}^{(\sigma,\tau)'}\left[\mathcal{B}(z_+)-\mathcal{B}(z_-)\right] + m\sigma\epsilon_{\text{B}}^{(\sigma,\tau)'}\epsilon_{\text{B}}^{(\sigma,\tau)'}\left[\mathcal{C}(z_+)-\mathcal{C}(z_-)\right], \end{aligned} \quad (\text{A2})$$

$$\begin{aligned} B_{m+2\sigma,n+2\tau N_p} = & \left[\eta_{\sigma,0}\sigma\left(\epsilon_{\text{B}}^{(\sigma,\tau)}\right)^2\mathcal{C}(z_+) \right] \frac{d^2}{dr^2} + \left[\eta_{\sigma,0}\epsilon_{\text{B}}^{(\sigma,\tau)'}\epsilon_{\text{B}}^{(\sigma,\tau)'}\mathcal{A}(z_+) + \eta_{\sigma,0}\left(\epsilon_{\text{B}}^{(\sigma,\tau)}\right)^2\mathcal{B}(z_+) + \sigma\epsilon_{\text{B}}^{(\sigma,\tau)'}\epsilon_{\text{B}}^{(\sigma,\tau)'}\left(m+2\sigma+\eta_{\sigma,0}\right)\mathcal{C}(z_+) \right] \frac{d}{dr} \\ & + \left(m+2\sigma\right)\left[\left(\epsilon_{\text{B}}^{(\sigma,\tau)'}\right)^2\mathcal{A}(z_+) + \sigma\epsilon_{\text{B}}^{(\sigma,\tau)'}\epsilon_{\text{B}}^{(\sigma,\tau)'}\mathcal{B}(z_+) + \sigma\epsilon_{\text{B}}^{(\sigma,\tau)'}\epsilon_{\text{B}}^{(\sigma,\tau)'}\mathcal{C}(z_+)\right], \end{aligned} \quad (\text{A3})$$

and

$$\begin{aligned} C_{m-2\sigma,n-2\tau N_p} = & \left[\eta_{\sigma,0}\sigma\left(\epsilon_{\text{B}}^{(\sigma,\tau)}\right)^2\mathcal{C}(z_-) \right] \frac{d^2}{dr^2} + \left[-\eta_{\sigma,0}\epsilon_{\text{B}}^{(\sigma,\tau)'}\epsilon_{\text{B}}^{(\sigma,\tau)'}\mathcal{A}(z_-) + \eta_{\sigma,0}\left(\epsilon_{\text{B}}^{(\sigma,\tau)}\right)^2\mathcal{B}(z_-) - \sigma\epsilon_{\text{B}}^{(\sigma,\tau)'}\epsilon_{\text{B}}^{(\sigma,\tau)'}\left(m-2\sigma-\eta_{\sigma,0}\right)\mathcal{C}(z_-) \right] \frac{d}{dr} \\ & + \left(m-2\sigma\right)\left[\left(\epsilon_{\text{B}}^{(\sigma,\tau)'}\right)^2\mathcal{A}(z_-) - \sigma\epsilon_{\text{B}}^{(\sigma,\tau)'}\epsilon_{\text{B}}^{(\sigma,\tau)'}\mathcal{B}(z_-) - \sigma\epsilon_{\text{B}}^{(\sigma,\tau)'}\epsilon_{\text{B}}^{(\sigma,\tau)'}\mathcal{C}(z_-)\right]. \end{aligned} \quad (\text{A4})$$

Here, σ and τ represent the particular mode coupling, $z_{\pm} = (m \pm \sigma, n \pm \tau N_p)$ and $\eta_{\sigma,0}$ is a “reversed” Kronecker-delta: $\eta_{\sigma,0} = 1 - \delta_{\sigma,0}$.

The operators \mathcal{A} , \mathcal{B} , and \mathcal{C} are defined as

$$\mathcal{A}(\bar{m}, \bar{n}) = \bar{m}\left(1 + \frac{\bar{m}}{\omega}a\right)\mathcal{I}_1(\bar{m}, \bar{n}) + \frac{\bar{m}^2}{\omega}b\mathcal{I}_2(\bar{m}, \bar{n}), \quad (\text{A5})$$

$$\mathcal{B}(\bar{m}, \bar{n}) = \left[-\frac{1}{r} \left(1 + \frac{\bar{m}}{\omega} a \right) + c \left(1 + \frac{\bar{m}}{\omega} a \right) + \frac{\bar{m}}{\omega} \left(d - \frac{a}{r} \right) \right] \mathcal{I}_1(\bar{m}, \bar{n}) + \left[-\frac{1}{r} \frac{\bar{m}}{\omega} b + \frac{\bar{m}}{\omega} c b + e \left(1 + \frac{\bar{m}}{\omega} a \right) + \frac{\bar{m}}{\omega} \left(f - \frac{b}{r} \right) \right] \times \mathcal{I}_2(\bar{m}, \bar{n}) + \frac{\bar{m}}{R_0} \frac{q'}{q^2} \left(1 + \frac{\bar{m}}{\omega} a \right) \mathcal{I}_3(\bar{m}, \bar{n}) + \frac{\bar{m}}{R_0} \frac{q'}{q^2} \frac{\bar{m}}{\omega} b \mathcal{I}_4(\bar{m}, \bar{n}) + \frac{\bar{m}}{\omega} e b \mathcal{I}_5(\bar{m}, \bar{n}), \quad (\text{A6})$$

and

$$C(\bar{m}, \bar{n}) = \frac{A(\bar{m}, \bar{n})}{\bar{m}}. \quad (\text{A7})$$

While the quantities a, \dots, f contain the density and temperature gradients of the energetic particles

$$a = \frac{\delta_0^2 k_B}{M \Omega_0 r} \left[T(\ln N)' - \frac{3}{2} T' \right], \quad (\text{A8})$$

$$b = \frac{\delta_0^2}{M \Omega_0 r} (\ln T)', \quad (\text{A9})$$

$$c = (\ln N)' - \frac{5}{2} (\ln T)', \quad (\text{A10})$$

$$d = \frac{\delta_0^2 k_B}{M \Omega_0 r} \left[T'(\ln N)' + T(\ln N)'' - \frac{3}{2} T'' \right], \quad (\text{A11})$$

$$e = \frac{1}{k_B T} (\ln T)', \quad (\text{A12})$$

$$f = \frac{\delta_0^2}{M \Omega_0 r} (\ln T)'', \quad (\text{A13})$$

the different integrals over velocity space are denoted by

$$\mathcal{I}_1(\bar{m}, \bar{n}) = \int d^3 v \frac{v_{D,0}^2}{\omega - v_{\parallel} k_{\bar{m}, \bar{n}}} \frac{\partial F}{\partial \varepsilon}, \quad (\text{A14})$$

$$\mathcal{I}_2(\bar{m}, \bar{n}) = \int d^3 v \frac{v_{D,0}^2}{\omega - v_{\parallel} k_{\bar{m}, \bar{n}}} \frac{\partial F}{\partial \varepsilon} \varepsilon, \quad (\text{A15})$$

$$\mathcal{I}_3(\bar{m}, \bar{n}) = \int d^3 v \frac{v_{D,0}^2}{(\omega - v_{\parallel} k_{\bar{m}, \bar{n}})^2} v_{\parallel} \frac{\partial F}{\partial \varepsilon}, \quad (\text{A16})$$

$$\mathcal{I}_4(\bar{m}, \bar{n}) = \int d^3 v \frac{v_{D,0}^2}{(\omega - v_{\parallel} k_{\bar{m}, \bar{n}})^2} v_{\parallel} \frac{\partial F}{\partial \varepsilon} \varepsilon, \quad (\text{A17})$$

$$\mathcal{I}_5(\bar{m}, \bar{n}) = \int d^3 v \frac{v_{D,0}^2}{\omega - v_{\parallel} k_{\bar{m}, \bar{n}}} \frac{\partial F}{\partial \varepsilon} \varepsilon^2. \quad (\text{A18})$$

Note that the equations presented in this Appendix are valid for the stellarator. Their tokamak equivalents may be recovered by setting $\sigma = 1$, $\tau = 0$ (toroidal coupling), $\delta_0 = 1$ (circular flux surfaces), and $\epsilon_B^{(1,0)} = -r/R_0$.

APPENDIX B: HOW THE ADIABATIC PART OF $f^{(1)}$ INFLUENCES THE CONTINUUM

In Section II B, it was mentioned that only the non-adiabatic part of $f^{(1)}$ (denoted by $h^{(1)}$) was retained in the kinetic description of the energetic ions. In the more complete expression

$$f^{(1)} = \frac{\mathbf{b} \times \nabla_{\perp} \Phi^{(1)}}{i\omega B} \cdot \frac{\partial F}{\partial \mathbf{R}} \Big|_{\varepsilon, \mu} - \frac{B^{(1)}}{B} \frac{\partial F}{\partial \mu} \Big|_{\mathbf{R}, \varepsilon} + h^{(1)}, \quad (\text{B1})$$

the first two terms are the adiabatic part. Note that within the reduced ideal-MHD theory $B^{(1)} = 0$ holds, hence the second term vanishes. Thus, the adiabatic part of $f^{(1)}$ is only determined by one term proportional to the gradients of the equilibrium distribution function F and the $\mathbf{E} \times \mathbf{B}$ -drift. Working out the vector and the dot product in the large-aspect-ratio approximation, one finds

$$f^{(1)} = \frac{r B_0}{q g} \frac{1}{i\omega B^2} \frac{\partial F}{\partial r} \left(g_{\Theta\Theta} \frac{\partial \Phi^{(1)}}{\partial \varphi} - q g_{\varphi\varphi} \frac{\partial \Phi^{(1)}}{\partial \Theta} \right) + h^{(1)}. \quad (\text{B2})$$

Here, $g_{\Theta\Theta}$ and $g_{\varphi\varphi}$ are components of the covariant metric tensor.¹³ Note that the adiabatic part contains no radial derivative of $\Phi^{(1)}$. The reason is that F only depends on r and not on the angular variables.

If this adiabatic part were retained in the integral over velocity space described by Eq. (9), it would only lead to new terms proportional to zero and first-order radial derivatives of $\Phi^{(1)}$. (The term integrated over velocity space is $\mathbf{v}_D \cdot \nabla f^{(1)}$.) But since the continuum is determined by the prefactors of the second-order derivatives, the adiabatic part of $f^{(1)}$ does not change the kinetic continuum.

APPENDIX C: PARAMETERS OF THE NUMERICAL CALCULATIONS

Below, the parameters which have been used in the various benchmarks and in the W7-X calculation are listed.

TABLE I. Background-plasma parameters for the benchmark with KIN-2DEM and others.

Major radius R_0/m	4.0
Minor radius a/m	0.9
Mode numbers (m_1, n_1) and (m_2, n_2)	(2, 2) and (3, 2)
Magnetic field B_0/T on axis	5.0
Type of ions	Deuterium
Density $n_{i,0}/m^{-3}$ on axis	5.0×10^{19}
Density profile	Flat
q-profile	$q(r) = \sum_{j=0}^6 c_j r^j$
Coefficients	$c_0 = 1.048$, $c_1 = 0.101$, $c_2 = 0.077$ $c_3 = 3.334$, $c_4 = -6.748$, $c_5 = 5.965$ $c_6 = -2.024$

TABLE II. Fast-particle parameters for the benchmark with KIN-2DEM and others.

Type of ions	Hydrogen
Density $N_{\text{fast},0}$ on axis	Chosen to keep $T_{\text{fast},0} N_{\text{fast},0} \cong 7.6 \times 10^{20} \text{ keV} \cdot \text{m}^{-3}$ constant
Density profile	$N_{\text{fast}}(r) = \exp[-(c_0 + \sqrt{c_1 + c_2 r^2})/c_3]$
Coefficients	$c_0 = -1.75, c_1 = 3.063, c_2 = 5.556, c_3 = 0.09$
Temperature $T_{\text{fast},0}$ on axis	Chosen to keep $T_{\text{fast},0} N_{\text{fast},0} \cong 7.6 \times 10^{20} \text{ keV} \cdot \text{m}^{-3}$ constant
Temperature profile	Flat

TABLE III. Background-plasma parameters for the ITPA benchmark.

Major radius R_0/m	10.0
Minor radius a/m	1.0
Mode numbers (m_1, n_1) and (m_2, n_2)	(10, 6) and (11, 6)
Magnetic field B_0/T on axis	3.0
Type of ions	Hydrogen
Density $n_{i,0}/\text{m}^{-3}$ on axis	2.0×10^{19}
Density profile	Flat
q-profile	$q(r) = 1.71 + 0.16r^2$

TABLE IV. Fast-particle parameters for the ITPA benchmark.

Type of ions	Deuterium
Density $N_{\text{fast},0}/\text{m}^{-3}$ on axis	1.44×10^{17}
Density profile	$N_{\text{fast}}(r) = c_3 \exp[-c_2/c_1 \cdot \tanh\{(r - c_0)/c_2\}]$
Coefficients	$c_0 = 0.491, c_1 = 0.298, c_2 = 0.199, c_3 = 0.521$
Temperature $T_{\text{fast},0}/\text{keV}$ on axis	1...800
Temperature profile	Flat

TABLE V. Background-plasma parameters for the W7-X case.

Major radius R_0/m	5.5
Minor radius a/m	0.53
Mode numbers	(10, 5), (10, 10), (11, 10), (12, 10), (12, 15)
Magnetic field B_0/T on axis	2.31
Type of ions	Hydrogen
Density $n_{\text{bulk},0}/\text{m}^{-3}$ on axis	2.0×10^{19}
Density profile	Flat
q-profile	$q(r) = \sum_{i=0}^6 c_i r^{2i}$
Coefficients	$c_0 = 1.175, c_1 = 0.521, c_2 = -13.150$ $c_3 = 101.17, c_4 = -435.05, c_5 = 947.01$ $c_6 = -831.19$

TABLE VI. Fast-particle parameters for the W7-X case.

Type of ions	Hydrogen
Density $N_{\text{fast},0}/\text{m}^{-3}$ on axis	$4.0 \times 10^{17} \dots 3.0 \times 10^{18}$
Density profile	$N_{\text{fast}}(r) = \sum_{i=0}^9 c_i r^{2i}$
Coefficients	$c_0 = 0.99988, c_1 = -4.5984$ $c_2 = 42.474, c_3 = -473.91$ $c_4 = 606.59, c_5 = 66734$ $c_6 = -855490, c_7 = 4647400$ $c_8 = -11936000, c_9 = 11835000$
Temperature $T_{\text{fast},0}/\text{keV}$ on axis	10...1000
Temperature profile	Flat

¹M. N. Rosenbluth and P. H. Rutherford, *Phys. Rev. Lett.* **34**, 1428 (1975).

²G. Y. Fu and J. W. van Dam, *Phys. Fluids B* **1**, 1949 (1989).

³H. H. Duong, W. W. Heidbrink, E. J. Strait, T. W. Petrie, R. Lee, R. A. Moyer, and J. G. Watkins, *Nucl. Fusion* **33**, 749 (1993).

⁴R. B. White, E. Fredrickson, D. Darrow, M. Zarnstorff, R. Wilson, S. Zweben, K. Hill, Y. Chen, and G. Fu, *Phys. Plasmas* **2**, 2871 (1995).

⁵L. Chen, *Phys. Plasmas* **1**, 1519 (1994).

⁶P. Lauber and S. Günter, *Nucl. Fusion* **48**, 084002 (2008).

⁷Y. I. Kolesnichenko, V. V. Lutsenko, H. Wobig, and V. Yakovenko, *Phys. Plasmas* **9**, 517 (2002).

⁸A. Könies, A. Mishchenko, and R. Hatzky, in *Theory of Fusion Plasmas*, edited by X. Garbet, O. Sauter, and E. Sindoni (American Institute of Physics, New York, 2008), Vol. 1069, pp. 133–143.

⁹T. B. Fehér, Ph.D. thesis, Ernst-Moritz-Arndt-Universität Greifswald, 2013.

¹⁰D. A. Spong, B. N. Breizman, D. L. Brower, E. D'Azevedo, C. B. Deng, A. Könies, Y. Todo, and K. Toi, *Contrib. Plasma Phys.* **50**, 708 (2010).

¹¹Y. Todo and T. Sato, *Phys. Plasmas* **5**, 1321 (1998).

¹²A. H. Boozer, *Rev. Mod. Phys.* **76**, 1071 (2004).

¹³H. L. Berk, J. W. van Dam, Z. Guo, and D. M. Lindberg, *Phys. Fluids B* **4**, 1806 (1992).

¹⁴Y. I. Kolesnichenko, V. V. Lutsenko, H. Wobig, Y. V. Yakovenko, and O. P. Fesenyuk, *Phys. Plasmas* **8**, 491 (2001).

¹⁵Y. I. Kolesnichenko, V. V. Lutsenko, H. Wobig, and Y. V. Yakovenko, *Nucl. Fusion* **42**, 949 (2002).

¹⁶A. Könies and R. Kleiber, *Phys. Plasmas* **19**, 122111 (2012).

¹⁷A. Könies, *Phys. Plasmas* **7**, 1139 (2000).

¹⁸G. Y. Fu, H. L. Berk, and A. Pletzer, *Phys. Plasmas* **12**, 082505 (2005).

¹⁹P. Rodrigues, A. Figueiredo, J. Ferreira, R. Coelho, F. Nabais, D. Borba, N. F. Loureiro, H. J. C. Oliver, and S. E. Sharapov, *Nucl. Fusion* **55**, 083003 (2015).

²⁰T. H. Stix, *Waves in Plasmas* (American Institute of Physics, 1992).

²¹M. R. Scott, *J. Comput. Phys.* **12**, 334 (1973).

²²D. M. Sloan, *J. Comput. Phys.* **24**, 320 (1977).

²³J. Candy and M. N. Rosenbluth, *Plasma Phys. Controlled Fusion* **35**, 957 (1993).

²⁴M. Fivaz, S. Brunner, G. de Ridder, O. Sauter, T. M. Tran, J. Vaclavik, L. Villard, and K. Appert, *Comput. Phys. Commun.* **111**, 27 (1998).

²⁵A. Mishchenko, R. Hatzky, and A. Könies, *Phys. Plasmas* **11**, 5480 (2004).

²⁶A. Mishchenko, A. Könies, and R. Hatzky, *Phys. Plasmas* **16**, 082105 (2009).

²⁷H. Qin, W. M. Tang, and G. Rewoldt, *Phys. Plasmas* **6**, 2544 (1999).

²⁸N. N. Gorelenkov, C. Z. Cheng, and G. Y. Fu, *Phys. Plasmas* **6**, 2802 (1999).

²⁹G. Y. Fu, C. Z. Cheng, and K. L. Wong, *Phys. Fluids B* **5**, 4040 (1993).

³⁰P. Lauber, S. Günter, A. Könies, and S. D. Pinches, *J. Comput. Phys.* **226**, 447 (2007).

³¹A. Könies, S. Briguglio, N. Gorelenkov, T. Fehér, M. Isaev, P. Lauber, A. Mishchenko, D. A. Spong, Y. Todo, W. A. Cooper *et al.*, in 24th IAEA International Conference on Fusion Energy, San Diego, CA (2012).

³²W. Baumjohann and R. A. Treumann, *Basic Space Plasma Physics* (Imperial College Press, 1997).

³³P. Lauber, *Plasma Phys. Controlled Fusion* **57**, 054011 (2015).

³⁴H. Maaßberg, C. D. Beidler, and E. E. Simmet, *Plasma Phys. Controlled Fusion* **41**, 1135 (1999).

³⁵S. Briguglio, X. Wang, F. Zonca, G. Vlad, G. Fogaccia, C. D. Troia, and V. Fusco, *Phys. Plasmas* **21**, 112301 (2014).

Appendix A. Thesis articles

On-surface potential and radial electric field variations in electron root stellarator plasmas (A.7)

Full citation:

J. M. García-Regaña, T. Estrada, I. Calvo, J. L. Velasco, J. A. Alonso, D. Carralero, R. Kleiber, M. Landreman, A. Mollén, E. Sánchez, C. Slaby, TJ-II Team, and W7-X Team. On-surface potential and radial electric field variations in electron root stellarator plasmas. *Plasma Physics and Controlled Fusion*, **60** (10) 104002 (2018).






DOI:

10.1088/1361-6587/aad795 (<https://doi.org/10.1088/1361-6587/aad795>)

Reproduced with the permission of IOP Publishing, CIEMAT, and EUROfusion.

Appendix A. Thesis articles

On-surface potential and radial electric field variations in electron root stellarator plasmas

J M García-Regaña¹ , T Estrada¹, I Calvo¹, J L Velasco¹ , J A Alonso¹, D Carralero¹, R Kleiber², M Landreman³ , A Mollén² , E Sánchez¹ , C Slaby² and TJ-II Team and W7-X Team

¹Laboratorio Nacional de Fusión CIEMAT, Av. Complutense 40, E-28040 Madrid, Spain

²Max-Planck-Institut für Plasmaphysik, Wendelsteinstr. 1, D-17491 Greifswald, Germany

³Institute for Research in Electronics and Applied Physics, University of Maryland, College Park, MD 20742, United States of America

E-mail: jose.regana@ciemat.es

Received 24 April 2018, revised 18 July 2018

Accepted for publication 2 August 2018

Published 22 August 2018



Abstract

In the present work we report recent radial electric field measurements carried out with the Doppler reflectometry (DR) system in the TJ-II stellarator. The study focuses on the fact that, under some conditions, the radial electric field measured at different points over the same flux surface shows significantly different values. A numerical analysis is carried out considering the contribution arising from the radial dependence of Φ_1 as a possible correction term to the total radial electric field. Here Φ_1 is the neoclassical electrostatic potential variation over the surface. The comparison shows good agreement in some aspects, like the conditions under which this correction is large (electron-root conditions) or negligible (ion-root conditions). But it disagrees in others like the sign of the correction. The results are discussed together with the underlying reasons of this partial disagreement. In addition, motivated by the recent installation of the dual DR system in Wendelstein 7-X (W7-X), Φ_1 estimations for W7-X are revisited considering core electron-root confinement plasmas from its first experimental campaign. The simulations show larger values of Φ_1 under electron-root conditions than under ion root. The contribution from the kinetic electron response is shown to become important at some radii. All this results in a potential variation size in W7-X noticeably larger than estimated in our previous work (García-Regaña *et al* 2017 *Nucl. Fusion* **57** 056004), for other plasma parameters and another configuration.

Keywords: stellarators, neoclassical transport, tangential electric fields, impurity transport

(Some figures may appear in colour only in the online journal)

1. Introduction

The radial electric field is one of the physical quantities with significant prominence in stellarator transport physics problems. In particular, for the radial transport of impurities and their accumulation, its role becomes more important as the charge state of the impurity increases. In stellarators, the explanation for this is framed by the standard neoclassical formalism. There, one can express the flux-surface-averaged

fluxes as a linear combination of thermodynamic forces and the so-called thermal transport matrix coefficients L_{ij}^a :

$$\frac{\langle \Gamma_a \cdot \nabla r \rangle}{n_a} = -L_{11}^a \left(\frac{n_a'}{n_a} - \frac{Z_a e E_r}{T_a} + \frac{L_{12}^a T_a'}{L_{11}^a T_a} \right), \quad (1)$$

with a the species index, n_a the density, T_a the temperature, Z_a the charge state, e is the proton charge, Γ_a the particle flux density and $\langle \dots \rangle$ the flux surface average operator. In the present work r is a flux surface label with the character of an

effective radial coordinate such that the volume enclosed by a flux surface is $V = 2\pi^2 R_0^2 r^2$, and R_0 is the major radius of the stellarator. The prime ' denotes differentiation with respect to r . The radial electric field vector is $\mathbf{E}_r = E_r \nabla r$ with $E_r = -\Phi_0'$ and $\Phi_0 = \Phi_0(r)$ the part of the electrostatic potential constant on the flux surface. An important well-known difference between particle transport in stellarators respect to that in (axi-symmetric) tokamaks is that the particle transport of the different species does not obey ambipolarity at any E_r . In other words, the total radial flux-surface-averaged current does not vanish and quasi-neutrality is not preserved along the radial direction. Then, the radial electric field in stellarators is determined by imposing this ambipolarity condition, that reads, see e.g. [1]

$$\sum_a Z_a e (\Gamma_a \cdot \nabla r) = 0. \quad (2)$$

Despite the apparently explicit linear dependence of the fluxes on E_r , see equation (1), the role that the radial electric field plays on the confinement of the trapped particle orbits in the long-mean-free-path regimes, makes the matrix transport coefficients depend also on E_r . This leads the ambipolarity condition to become a non-linear equation with multiple roots [2, 3]. However, only two of them are usually identified in laboratory plasmas. For simplicity, assuming the presence of only bulk ions and electrons, when the collisionality of both species is such that the radial particle flux of the ions needs to be reduced in order to satisfy ambipolarity, the ambipolar electric field typically points radially inward and $E_r < 0$. If, on the contrary, the electron radial particle flux needs to be retarded to fulfill ambipolarity the radial electric field points radially outwards, $E_r > 0$. These two situations are referred to as ion and electron root regimes respectively. In general, standard neoclassical theory predicts ion root conditions for all collisionalities when the ion and electron temperatures are comparable, $T_i \sim T_e$, and fairly large and positive (electron root) E_r values at low collisionality with strongly localized electron heating that leads to $T_e \gg T_i$, see e.g. [4, 5]. The concern for the intrinsic character of the impurity accumulation in stellarators and ion root conditions has been traditionally tight together, since the inward convection related to E_r can, for sufficiently high Z_a , exceed in most situations the outward counterparts driven by the temperature and density gradients. This has also been observed in numerous stellarator experiments, see e.g. [6] and references therein.

However, this simple explanation concerning impurity accumulation has been broadened in recent years motivated by a few experiments that question it, like the hollow impurity density profiles observed in LHD [7] or the exceptionally low impurity confinement time of the HDH mode in W7-AS plasmas [8]. For decades it has been known that a variation of the electrostatic potential over the flux surface $\Phi_1 = \Phi_1(r, \theta, \phi)$ can be relatively large for low collisionality plasmas in non-omnigenous stellarators [2, 9, 10]. Here θ and ϕ are some angular poloidal and toroidal coordinates, respectively. This piece of the electrostatic potential is necessary in order to restore quasi-neutrality over the flux surfaces, which the cumulative effect of the non-vanishing bounce-averaged

radial displacement of the particle drift orbits violates. Although it can be in most situations negligible for main ion and electron transport, the importance of Φ_1 for impurities resides in the fact that the radial component of the $E \times B$ drift, $\mathbf{v}_{E1} = -\nabla \Phi_1 \times \mathbf{B}/B^2$, can become of the same order as the radial component of the magnetic drift \mathbf{v}_m , basically because the latter scales as Z_a^{-1} while the former does not. Consequently, its role as source of radial transport can become as important as the inhomogeneous confining magnetic field for sufficiently high charge state. Since the first numerical calculations of Φ_1 [11] performed with the code EUTERPE [12, 13] and the experimental measurement in a stellarator [14], other works have followed this line: the estimation of its effect on the radial flux of impurities for some selected ion-root plasmas for different stellarator configurations in [15]; the analytical development of the formalism [16] and the code (KNOSOS) [17] that integrates the drift kinetic equation and transport quantities of interest, including Φ_1 , for optimized stellarators; new LHD impurity plasmas analyzed under the effect of Φ_1 with the SFINCS code [18], including the self-consistent modification of E_r by Φ_1 and including non-trace impurities [19]. Apart from these works, others have looked into the screening of impurities in stellarators, like [20] where high T_i plasmas with negative but small $|E_r|$ are shown to coexist with outward impurity flow. Finally, [21] has analytically addressed the radial particle flux of highly collisional impurities in low collisional bulk plasmas, concluding that in the case without Φ_1 , the radial transport of impurities may only weakly depend on E_r and temperature screening can arise; and [22] where the previous derivation is generalized including Φ_1 , which makes the impurity radial particle flux to depend strongly on E_r .

The conclusions from the works dealing with Φ_1 [15, 17, 19] coincide on their prediction about its magnitude, that reaches for LHD values of up to $e\Delta\Phi_1/T_i \sim 0.1$, with $\Delta\Phi_1 = (\Phi_1^{\max} - \Phi_1^{\min})$ and Φ_1^{\max} and Φ_1^{\min} the maximum and minimum values, respectively, of the potential over a given flux surface. The direction and magnitude of the impact of Φ_1 on the impurity radial transport is not trivial. It depends on the charge state of the impurities, the collisional regime where the impurity is, how its distribution function couples to Φ_1 , etc. However, based on the available numerical simulations it can be stated without too much lack of generality that variations of that magnitude undeniably introduces a strong correction to the standard neoclassical prediction in LHD, even considering low- Z impurities like carbon. For TJ-II similar values of the normalized potential variation are also predicted [15], despite the higher collisionality of its plasmas. Moreover, the estimations in TJ-II qualitatively agree with the experimental measurements of the plasma floating potential difference at the plasma edge [14]. Regarding W7-X, the variations are typically shown one order of magnitude lower than those for LHD plasmas at comparable collisionality. However, as noted below only few simulations are available, in particular, for the magnetic configurations and plasma parameters from the experimental campaigns.

The present work aims at broadening the scanned parameter space with a comparative view between ion root and

electron root conditions in TJ-II and W7-X, with the focus mainly on the second of these regimes. There are several reasons for this: first, all the numerical effort has looked so far into ion root plasmas, with the underlying hope that Φ_1 could, at least, cancel the predicted E_r -driven inward pinch. A similar analysis for electron-root plasmas is missing despite the fact that Φ_1 can indeed be larger than in ion-root for the same absolute value of E_r , as pointed out in [14]; second, although its impact is predicted to be large for impurities, the value of Φ_1 is still small compared to the lower order part of the potential Φ_0 , and its direct detection is instrumentally difficult. In the present work, under the light of recent Doppler reflectometry (DR) measurements of the radial electric field in TJ-II, where strong differences over the same flux surfaces have been found under electron root conditions, we investigate whether the radial dependence of the calculated Φ_1 can explain those differences; and finally, since the configuration and parameter space of W7-X is rather large [23], the results obtained for the few configurations and parameters considered in [15, 19] should not be generalized. In the present work, we have based our calculations in typical parameters of OP1.1 [24] core-electron-root-confinement (CERC) plasmas considering a configuration with large effective ripple. We show numerically that Φ_1 can then be as large as in the reported LHD cases. This exercise has also been performed considering adiabatic and kinetic electrons, in order to provide explicitly a validity check for the adiabatic electron approximation, that for codes like EUTERPE can result in considerably less computation time.

After this section, a brief overview of the equations and tools employed are described in section 2. The TJ-II results, both numerical and experimental, are presented and discussed in section 3. The numerical analysis for W7-X CERC conditions is shown in section 4. Finally, the conclusions are summarized in section 5.

2. Equations and numerical methods

In this section we give an overview of the numerical method, the relevant equations of the problem and the numerical code used, EUTERPE [12, 13]. The content of this section concerns the neoclassical version of the code. For a more complete description of how the present problem is approached we refer the reader to section 2 of [15]. Other aspects dealing with the neoclassical version can be found in [11, 25, 26], and those closer to the numerical implementation in [27–29].

EUTERPE is a δf particle-in-cell (PIC) Monte Carlo code. For a given kinetic species, it considers a splitting of the distribution $f = f_0 + f_1$, with f_0 an analytically known expression with the role of a control variate, which does not have to be necessarily linked to any approximation. The code solves for each of the kinetic species of the problem the equation for the f_1 part: $df_1/dt = -df_0/dt + C(f)$, with $C(f)$ a collision operator. The choice of phase space coordinates is the following: in real space, in order to characterize the guiding center position \mathbf{R} of the Monte Carlo markers, the magnetic PEST [30]

poloidal and toroidal angles θ and ϕ , and a flux surface label r are employed. In velocity space the parallel component of the velocity v_{\parallel} and normalized magnetic moment $\mu = v_{\perp}^2/2B$ are considered. Here $f_0 = f_M \exp(-Ze\Phi_1/T)$, with $f_M = [n_0/(2\pi)^{3/2}v_{th}^3] \exp[-(v_{\parallel}^2 + v_{\perp}^2)/v_{th}^2]$ the Maxwellian distribution, v_{\perp} the perpendicular component of the velocity, $n_0 = n_0(r)$ the constant part of the density of the flux surface, T the temperature, $v_{th} = \sqrt{2T/m}$ the thermal speed, m the mass and B the magnetic field strength. With these definitions, the kinetic equation takes the form:

$$\begin{aligned} \frac{\partial f_1}{\partial t} + \dot{\mathbf{R}} \cdot \nabla f_1 + v_{\parallel} \frac{\partial f_1}{\partial v_{\parallel}} = & -f_0 (\mathbf{v}_m + \mathbf{v}_{E1}) \cdot \nabla r \\ & \times \left[\frac{n'}{n} + \frac{Ze}{T} \Phi_0' + \left(\frac{mv^2}{2T} - \frac{3}{2} + \frac{Ze}{T} \Phi_1 \right) \frac{T'}{T} \right] + C(f). \end{aligned} \quad (3)$$

The overdot $\dot{}$ denotes differentiation with respect to time t . Finally, the following equations of motion enter the left-hand side of equation (3):

$$\dot{\mathbf{R}} = v_{\parallel} \mathbf{b} + \frac{\mathbf{b} \times \nabla \Phi_0}{B}, \quad (4)$$

$$\dot{v}_{\parallel} = -\mu m \mathbf{b} \cdot \nabla B - \frac{v_{\parallel}}{B^2} (\mathbf{b} \times \nabla B) \cdot \nabla \Phi_0 - \frac{Ze}{m} \mathbf{b} \cdot \nabla \Phi_1, \quad (5)$$

$$\dot{\mu} = 0, \quad (6)$$

with $\mathbf{b} = \mathbf{B}/B$. In order to obtain Φ_1 , quasi-neutrality among all the species is imposed up to first order: $\sum_a Z_a e n_a = 0$, with $n_a = n_{0a}(r) \exp(-Z_a e \Phi_1/T_a) + n_{1a}$ the density of the different species. Considering singly charged bulk ions (i) and electrons (e) and assuming $e\Phi_1/T \ll 1$, quasi-neutrality yields:

$$\Phi_1 = \frac{T_e}{e} \left(n_{0e} + n_{0i} \frac{T_e}{T_i} \right)^{-1} (n_{1i} - n_{1e}). \quad (7)$$

Note that in [15] the assumption of adiabatic electrons, i.e. $n_e \approx n_{0e}(r) \exp(e\Phi_1/T_e)$, implies that on the right-hand side of expression (7) only n_{1i} appears. In the present work, in section 4, this approximation is relaxed and the results with adiabatic and kinetic electrons are compared with each other.

Another difference between [15] and the present work is the treatment of the collision operator $C(f)$. While in [15] pitch angle scattering collisions without momentum conservation were applied, in the present work, a momentum-restoring field particle term similar to that implemented in other codes [31, 32] is added to the self-collisions. The detailed description of the conservation scheme implemented in EUTERPE can be found in [33] but we reproduce it here for convenience. The collision operator that describes the self-collision of any species can be expressed as

$$C(f) = C_{\text{fp}}(f) + C_{\text{ip}}(f), \quad (8)$$

where $C_{\text{ip}}(f) = C(f_1, f_M)$ is the usually referred to as test-particle term, that describes the collisions of the perturbed part of the distribution function against the background part, and $C_{\text{fp}}(f) = C(f_M, f_1)$ is the field particle term, which captures the background reaction. In the simulations

presented in next sections, both for the bulk ion and electron self-collisions, the test-particle term used has been the pitch angle collision operator:

$$C_{\text{ip}}(f_i) = \frac{\nu}{2} \frac{\partial}{\partial \xi} (1 - \xi^2) \frac{\partial}{\partial \xi} f_i, \quad (9)$$

with $\xi = v_{\parallel}/v$ the pitch-angle variable, v the particle velocity and ν the deflection collision frequency of the colliding species

$$\nu = \nu_0 \frac{\text{erf}(x) - G(x)}{x^3}, \quad (10)$$

and $\nu_0 = ne^4 \ln \Lambda / 4\pi\epsilon_0^2 m^2 v_{\text{th}}^3$ for bulk ions with $Z = 1$ and electrons, $x = v/v_{\text{th}}$, $\ln \Lambda$ the Coulomb logarithm, erf the error function and G the Chandrasekhar function. On the other hand, the field particle term has the following form in order to fulfill self-adjointness of the collision operator [34]

$$C_{\text{fp}} = [N(\mathbf{v})\mathcal{N} + P(\mathbf{v})\mathcal{P} + E(\mathbf{v})\mathcal{E}]f_M, \quad (11)$$

with

$$N(\mathbf{v}) = \nu - 3\sqrt{\frac{\pi}{8}} \nu_E x^2, \quad (12)$$

$$P(\mathbf{v}) = \nu_s \frac{v_{\parallel}}{v_{\text{th}}^2}, \quad (13)$$

$$E(\mathbf{v}) = \nu_E x^2, \quad (14)$$

and $\nu_s = 4\nu_0 G(x)/x$ the slowing down frequency and $\nu_E = [-2\nu + (2 + 1/2x^2)\nu_s]$ the energy-diffusion collision frequency. Evaluating at each spatial bin of the simulation domain the non-conserved number density ΔN , parallel momentum ΔP and energy ΔE after performing the test-particle collisional step, the coefficients \mathcal{N} , \mathcal{P} and \mathcal{E} are obtained by imposing conservation of the respective moments of the collision operator (8), which results in

$$-\begin{pmatrix} \Delta N \\ \Delta P \\ \Delta E \end{pmatrix} = \int d^3v f_M \begin{pmatrix} N(\mathbf{v}) & P(\mathbf{v}) & E(\mathbf{v}) \\ v_{\parallel} N(\mathbf{v}) & v_{\parallel} P(\mathbf{v}) & v_{\parallel} E(\mathbf{v}) \\ v^2 N(\mathbf{v}) & v^2 P(\mathbf{v}) & v^2 E(\mathbf{v}) \end{pmatrix} \begin{pmatrix} \mathcal{N} \\ \mathcal{P} \\ \mathcal{E} \end{pmatrix}. \quad (15)$$

Finally, in section 4, where kinetic electrons have also been considered, the collision operator employed for the electrons colliding against the background ions, assumed to be at rest with respect to the former, has been

$$C_{ei}(f_{ie}) = \frac{\nu_{ei}}{2} \frac{\partial}{\partial \xi} (1 - \xi^2) \frac{\partial}{\partial \xi} f_{ie}, \quad (16)$$

with $\nu_{ei} = n_i e^4 \ln \Lambda / 4\pi\epsilon_0^2 m_e^2 v_e^3$, n_i the bulk ion density, v_e velocity of the electrons and m_e their mass.

3. Potential variations in TJ-II: comparison between ion- and electron-root plasmas

3.1. TJ-II DR system

TJ-II is a heliac-type stellarator where, for the standard configuration considered for this work, the average magnetic field is 0.95 T on axis, the rotational transform is $\iota \approx 1.5$ at the center of the plasma and 1.6 approximately at the edge and

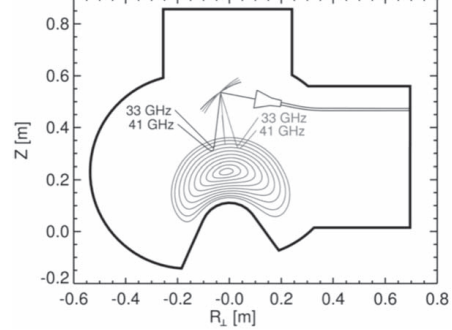


Figure 1. Schematic representation of the TJ-II vacuum vessel with DR antenna-mirror arrangement showing the two plasma regions that can be probed by the system. Here $R_{\perp} = R - R_0$, with R the cylindrical radial coordinate used below and R_0 the major radius of the device.

the effective minor radius and major radius are $a = 0.2$ m and $R_0 = 1.5$ m, respectively. The available heating power consists of two gyrotrons delivering 300 kW each (operated both in X-mode at the second harmonic of the electron cyclotron frequency) and two NBI heating systems, one co- and another counter-injecting each a port-through power of up to 700 kW. For the results presented below, only ECH on-axis was used. With this heating scheme the central electron density typically reaches values of $n_e \approx 0.5\text{--}1 \times 10^{19} \text{ m}^{-3}$, the electron temperature is $T_e \approx 1\text{--}2$ keV and the ion temperature $T_i \approx 80\text{--}100$ eV.

For the experimental results discussed in this section the technique used has been DR. It allows the measurement of density fluctuations and their perpendicular rotation velocity at different turbulence scales, with good spatial and temporal resolution. From the perpendicular rotation velocity the radial electric field, the central quantity in this section, can be obtained. The DR system in operation at TJ-II [35] works in a frequency hopping mode in the Q-band: 33–50 GHz, covering typically the radial region from $r/a = 0.6$ to $r/a = 0.9$. Its front-end consists of a compact corrugated antenna and an ellipsoidal mirror. The mirror can be tilted to probe different perpendicular wave-numbers of the turbulence in the range $k_{\perp} \approx 1\text{--}14 \text{ cm}^{-1}$, at different plasma regions poloidally separated, as both positive and negative probing beam angles with respect to normal incidence can be selected, see figure 1. Assuming that the electron density is constant on each flux surface, this characteristics makes it possible to access different points of measurement over the same flux surface. Apart from its interest for studying the spatial localization of instabilities predicted in stellarators by gyro-kinetic simulations [12, 36, 37], for the results presented in this work this feature has been exploited to characterize the radial electric field measured on the left and right regions with respect to the incidence angle where the launched beam is normal to the last closed flux surface. Throughout the present section these regions are referred to as ‘left’ and ‘right’ regions, see figure 1.

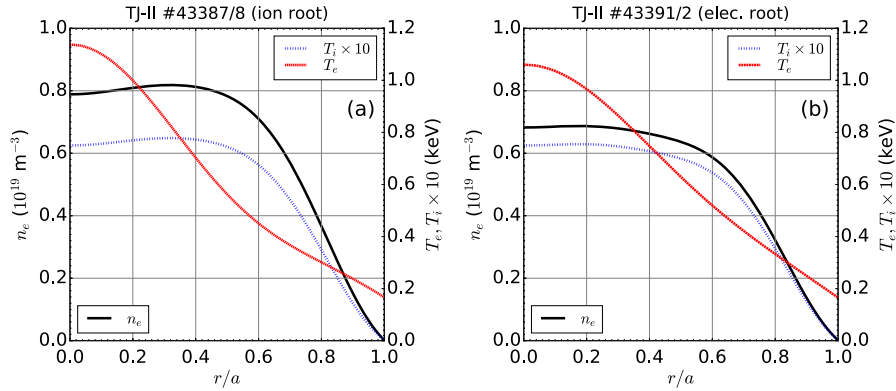


Figure 2. Left: radial profiles of electron density (n_e , solid black line), electron temperature (T_e , dashed red line) and ion temperature multiplied by 10 (T_i , dotted blue line) considered for the EUTERPE simulations based on the TJ-II discharges #43387 and #43388 and the data from the Thomson Scattering diagnostic (n_e and T_e) and the NPA (T_i) systems. Right: same quantities as on the left but considering the TJ-II discharges #43391 and #43392.

3.2. Experimental and numerical results

Two pairs of TJ-II discharges are considered. The main difference between them is the sign of the radial electric field. The first couple of discharges (#43387 and #43388) are representative for ion root regime while the second couple of discharges (#43391 and #43392) are for electron root. The plasma parameters for each of these pairs are represented in figure 2 (left) and (right) respectively. The difference in the density profiles determines what regime is accessed. TJ-II plasmas exhibit this ion-to-electron root change when the line-averaged density, obtained with a microwave interferometer [38], is close to the critical value of $\bar{n}_e^{cr} \sim 0.6 \times 10^{19} \text{ m}^{-3}$ (for the standard magnetic configuration and the used heating power), which standard neoclassical calculations capture without difficulty, see e.g. [39, 40]. The characteristic of the DR analysis that has motivated the numerical simulations is the difference that the radial electric field value for each set of profiles, shows when the measurement is taken on the left probing region and on the right. Or in other words, the different values of the radial electric field measured at different points over the same flux surface.

The radial electric field was obtained for the first discharge of each pair (this is for the shots #43387 and #43391) on the left side of the DR measurement plane. For the second of the discharges of each pair (this is for shots #43388 and #43392) the DR beam was launched to measure the radial electric field on the right side. It is worth recalling that the radial electric field provided by the Doppler reflectometer, E_r^{DR} , is obtained from the measured plasma background perpendicular flow u_{\perp} and relates to it as $E_r^{DR} = u_{\perp} B$ (B the modulus of the local magnetic field at the point where the beam is reflected). Assuming the phase velocity of density fluctuations much smaller than the $E \times B$ flow velocity, $\mathbf{v}_{E0} = E_r \nabla r \times \mathbf{B}/B^2$, u_{\perp} is assumed to be equal to the latter. Typically the value provided, E_r^{DR} , is that of the local radial electric field, which carries with the local dependence of the

flux expansion term ∇r . This term is comparable in the two plasma regions the system can access, and cannot lead to large differences in the local radial electric field. But, since the present work focuses on the different value of the radial electric field at points located over the same flux surface, the modulus of the flux expansion term has been divided out from the experimental E_r^{DR} in order to work with, strictly speaking, the supposedly flux function quantity E_r . This is indeed the quantity neoclassical codes require as input. The radial electric field is represented as a function of the normalized effective radius r/a in figure 3 (left) for the ion root discharges and 3 (right) for the electron root discharges. The points with errorbars show the experimental data, and the solid lines correspond to different fitted curves used in the EUTERPE simulations presented in next subsection. The values obtained at the left side of the plane of measurement are represented with red open squares while those taken at the right side are represented by blue open circles. Note that the DR system can measure over different flux surfaces by scanning the frequency of the launched microwaves. Due to their X-mode polarization and the dependence of the X-mode cutoff not only on the electron density but also on the magnetic field strength, the accessible radial range when the beam is oriented toward the left and right regions of the plane of measurement is not exactly the same. This fact is reflected in the measurements shown in figure 3 and when the numerical analysis is addressed considering the estimated measurement positions with ray tracing techniques. As it is observed in figure 3 (left), for the ion-root plasmas (shots #43387/8) the difference between the radial electric field measured at each side is small, in all the accessible radial domain. Only around $r/a = 0.6$ a slight separation between them can be appreciated. On the contrary, under electron root conditions (shots #43391/2), see figure 3 (right), the measured radial electric field is appreciably larger on the right side than on the left side on a wide portion of the accessed radial

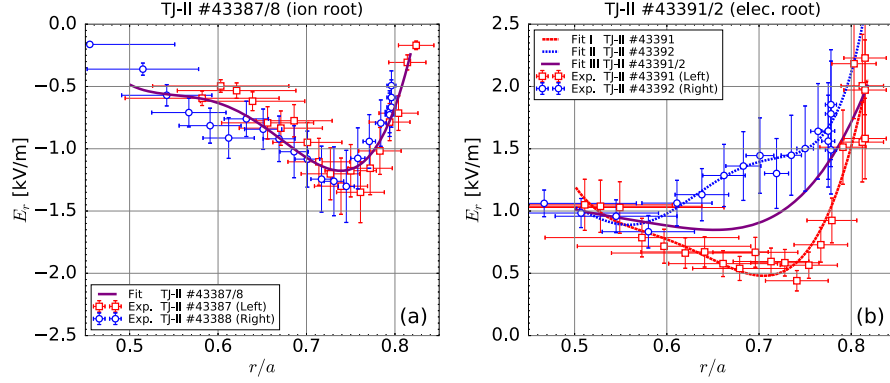


Figure 3. Left: radial electric field E_r as a function of the normalized effective radius for the TJ-II ion root plasmas, discharges #43387 and #43388. Right: the same but for the electron root plasmas from discharges #43391 and #43392. In both cases the measurements performed on the left and right sides of the DR measurement plane are represented with red squares and blue circles, respectively. The solid lines correspond to the input radial electric field profiles used for the Φ_1 EUTERPE simulations.

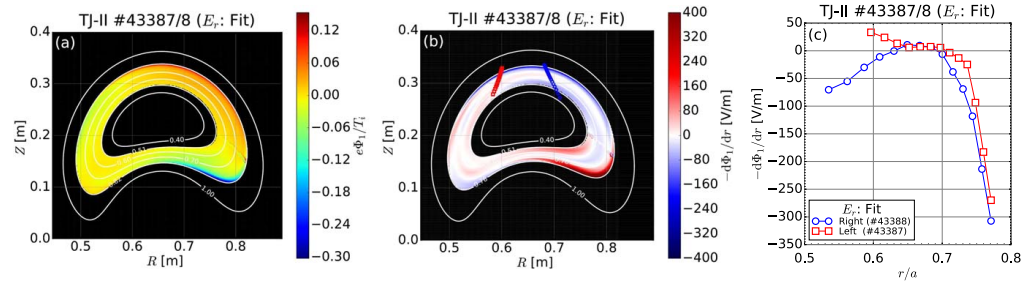


Figure 4. For the ion root conditions TJ-II plasmas: (a) potential variation normalized to the ion temperature $e\Phi_1/T_i$ at the Doppler reflectometry probing plane in the range of simulated radii; (b) over the same plane, radial electric field component $-d\Phi_1/dr$, together with the specific positions of measurement on the left and right DR probing regions, estimated with ray tracing; (c) value of $-d\Phi_1/dr$ at those positions where, as before, red squares and right blue circles correspond to the estimations along the left and right measurement positions respectively.

range. In the interval $r/a = 0.6-0.8$ discrepancies of up to 1 kV m^{-1} can be observed. In the numerical analysis that follows we try to quantify to what extent the radial dependency of the potential Φ_1 can introduce corrections in the total radial electric field through the term $-\Phi_1' = -d\Phi_1/dr$.

For the numerical simulations different fitting curves for the input ambipolar electric field have been considered. They are depicted with solid lines in figure 3. For the ion root scenario only one case has been used while for electron root three have been considered, due to the ambiguity in the choice of E_r given the disparate values measured at each measurement region. One of the curves considers the data measured on the left side of the probing plane ('fit 1'), another the data measured on the right side of the plane ('fit 2') and a third one the mean value of the previous two ('fit 3').

The numerical results for the ion root case are shown in figures 4(a)–(c), where the following quantities are represented: (a) the potential variation Φ_1 in a corona of the measurement plane that covers approximately the same radial

range as the experimental data; (b) the radial electric field term $-\Phi_1'$ resulting from the potential represented in the previous figure. The DR measurement positions on the right and left regions are indicated with red and blue points (these positions have been obtained with the ray tracing code TRUBA [41]); (c) $-\Phi_1'$ at the positions indicated in the previous plot. The results estimated on the left regions are indicated in red color, while those concerning the right side are indicated in blue. In figure 4(a) it is observed that the normalized potential $e\Phi_1/T_i$ takes at different poloidal positions near the outermost radii of the simulated region minimum and maximum values of around -0.3 to 0.15 , respectively. This leads the modulus of Φ_1' to reach up to 400 V m^{-1} approximately, comparable to the input E_r at that position, see figure 3(a). In such situation, neglecting the radial drift $\mathbf{b} \times \nabla\Phi_1/B$ at the time that the tangential drift $\mathbf{b} \times \nabla\Phi_0/B$ is retained in equation (4) is not justified. Then, apart from the fact that the radial region with $r/a \gtrsim 0.7$ has exceptionally large values of Φ_1' , further quantitative

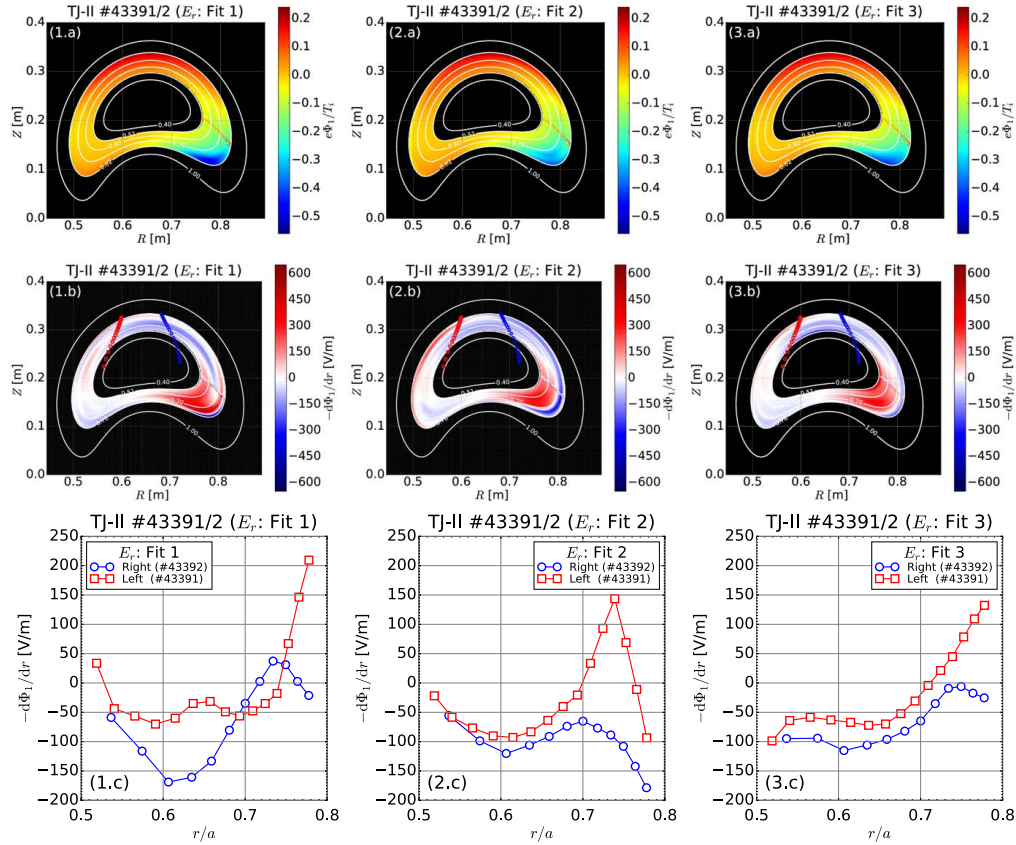


Figure 5. For the electron root conditions TJ-II plasmas: (1–3.a) potential variation normalized to the ion temperature $e\Phi_1/T_i$ at the Doppler reflectometry probing plane in the range of simulated radii, from left to right for the input E_r , denoted as fit 1–3 in figure 3(b); (1–3.b) over the same plane, radial electric field contribution $-\mathrm{d}\Phi_1/\mathrm{d}r$, together with the specific positions of measurement on the left and right DR probing regions, estimated with ray tracing techniques, for the three E_r fits considered; (1–3.c) value of $-\mathrm{d}\Phi_1/\mathrm{d}r$ at those positions where, as before, red squares and right blue circles correspond to the estimations along the left and right regions, respectively.

conclusions can difficultly be drawn from these results. On the other hand at more internal r/a regions, where Φ_1 and Φ_1' have more moderate values, one can observe in figure 4(c) that there is barely no difference between the value of $-\Phi_1'$ on the left measurement positions and those on the right region. Only at around $r/a = 0.6$ the curves in figure (c) separate from each other a few tens of $\mathrm{V}\,\mathrm{m}^{-1}$ —like in the experimental measurements, see figure 2(a)—which is well below the value of the ambipolar electric field at that position $E_r \approx -600\,\mathrm{V}\,\mathrm{m}^{-1}$. In that sense the numerical results agree relatively well with the experiment.

For the electron-root plasmas the same (a)–(c) plots are represented from top to bottom in the set of figures 5, for each of the input E_r , considered for EUTERPE in a different column. Looking at the figures (1–3.c), in contrast to the ion-root case, a more appreciable difference is observed between the results for the left and right regions. In the three cases the

correction term $-\Phi_1'$ would make the total radial electric field larger on the left side than on the right side, as the curve of $-\Phi_1'$ indicating the left side values is situated almost at all radii above the curve indicating the values on the right region. The difference between the results with different input E_r , are given only on the location where the maximum differences on $-\Phi_1'$ are found. Considering the fit 1, the difference reaches up to values of around $200\,\mathrm{V}\,\mathrm{m}^{-1}$, and these take place in the interval $r/a = 0.6$ – 0.7 and the outermost radial region. For the fit 2 differences of up to around $250\,\mathrm{V}\,\mathrm{m}^{-1}$, larger on the left than on the right side, are observed at around $r/a \sim 0.75$; and finally fit 3 leads to differences that only show up at the outermost represented radii, reaching values of around $200\,\mathrm{V}\,\mathrm{m}^{-1}$. The numerical difference for the three cases considered are neither as large as those found in the DR measurements shown in figure 3 (right) nor the sign coincides numerically and experimentally. In the simulations the radial

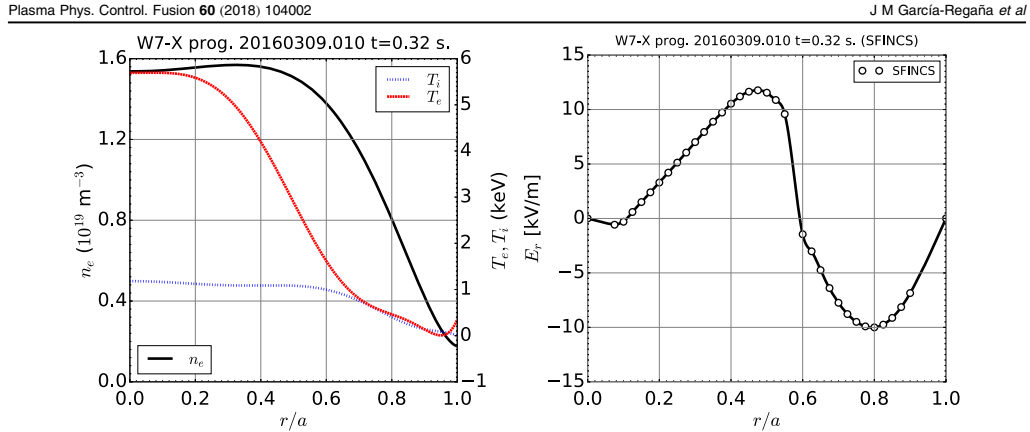


Figure 6. (a) Electron density (n_e , solid black line), electron temperature (T_e , dashed red line) and ion temperature (T_i , dotted blue line) considered for the EUTERPE simulations based on those of W7-X program 20160309.010 at $t = 0.32$ ms measured with the Thomson Scattering (n_e and T_e) and the XICS (T_i) systems. (b) ambipolar radial electric field obtained with the SFINCS code (dots) considering the profiles on the left, and the curve used as input for EUTERPE.

electric field becomes larger on the left than on the right probing regions, while in the experiments the opposite happens. However, out of the measurement positions, along any flux surface contour over the probing plane much larger values of $-\Phi_1'$ are achieved. See for instance the reddish areas at the bottom right part of the DR section and the top blue areas the contour $r/a = 0.5$ passes through in figures 5 (1–3.b) plots. As it has been already discussed regarding the outermost flux surfaces of the ion-root case, these large deviations cast strong doubts about the applicability of the trajectories, equations (4)–(6) assumed in our simulations, since all terms related to Φ_1' have been neglected. The correction to the total radial electric field arising from $-\Phi_1'$ represents in these electron root TJ-II plasmas a significant fraction compared to the input ambipolar electric field. In contrast to the ion-root case, where this happened near the outermost radial boundary only, in this electron-root example the problem shows up at almost any of the represented flux surfaces regardless of the considered profile of E_r . This limits our conclusion substantially, and reduces it to the statement that in TJ-II electron root plasmas the magnitude of Φ_1 and related contribution to the total radial electric field $-\Phi_1'$ can become locally a non-negligible fraction of Φ_0 and E_r , respectively.

4. Potential variations in W7-X: CERC plasmas and effect of kinetic electrons

Variations of the electrostatic potential on the flux surfaces have so far been estimated small in W7-X plasmas and its impact on impurity transport negligible. However, these conclusions, drawn from the results presented in [15, 19], cover still a very narrow parameter and configuration window of W7-X. In particular all plasmas studied in those references are ion root plasmas foreseen during the future W7-X

operation phase OP2. The calculations in [15] were performed for one of the W7-X configurations with lowest neoclassical transport, whose low effective ripple, the target figure of merit for the neoclassical optimization and design of W7-X, is lower than in the configurations for which most of the experiments have been performed so far. The case studied in this work widens the parameter window considering CERC plasma parameters from the operation phase OP1.1 [42], in particular the physics program 20160309.010 at the time $t = 0.320$. The radial profiles based on that program and instant, used for the simulations discussed below are represented in figure 6 (left). The represented profiles are fitted to the Thomson Scattering system [43] data for the electron density n_e and temperature T_e , while the bulk ion density T_i considers the XICS [44] experimental data. The radial profile of E_r used as EUTERPE input has been provided by the SFINCS code and is represented in figure 6 (right).

The reasons for choosing this plasma are the following. On the one hand, it is an example of CERC plasma [45] where a root transition takes place. E_r is positive (electron root) at the inner core and negative (ion root) at the outer part of the core and edge. This feature is interesting since, as pointed out in [14], under ion root conditions the thermodynamic force related to the ambipolar radial electric field opposes to the density and temperature gradients, while in electron root all thermodynamic forces have in general for the ions (except deeply hollow profiles, which is not the case here) the same sign. This leads to a larger source term in the drift kinetic equation that forces the perturbed part of the distribution function f_{i1} to be larger. Since the lack of quasi-neutrality among the charge density related to this piece of the distribution function is what gives rise to the potential Φ_1 , this reasoning should lead to expect larger Φ_1 too. In addition, the change in the direction of the $E \times B$ precession from electron to ion root should introduce appreciable changes on the phase of the potential. These two statements can be checked by

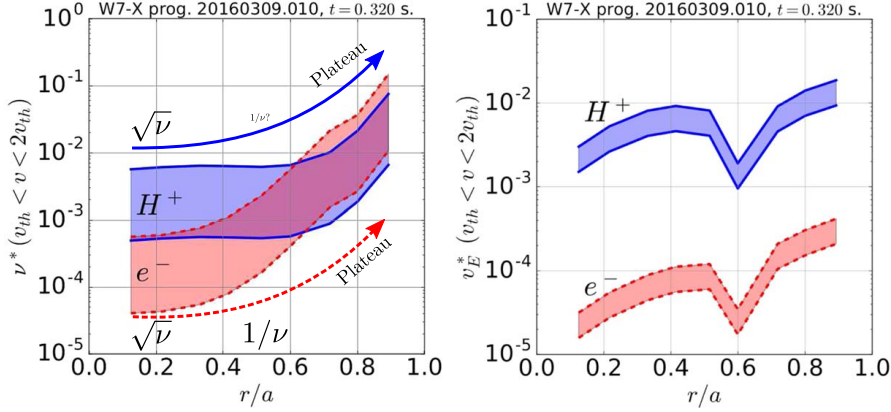


Figure 7. Left: normalized collision frequency as a function of the normalized effective radius for the electrons (red shadowed area) and main ions (blue shadowed area) with velocities in the range of one and two thermal velocities considering the profiles of figure 6(a). Right: normalized $E_r \times B$ velocity for electrons (red shadowed area) and main ions (blue shadowed area) with velocities in the range of one and two thermal velocities considering the profiles of figures 6(a) and (b).

comparing how Φ_1 looks on each side of the radial electric field root transition.

Furthermore the fact that the temperature of the electrons is significantly higher than that of the ions leads to a situation where the electron contribution ECH to Φ_1 eventually may become important. Note that in [15] the electrons are considered adiabatic, based on the condition $T_i \sim T_e$ and the higher density of the plasmas there, and thus the electron contribution to Φ_1 is neglected. In order to know whether the electrons may contribute to Φ_1 , let us recall first that for a given magnetic configuration and for one single kinetic energy or velocity v , the parameters to find in which collisional regime each species is, are the normalized $E_r \times B$ drift velocity $v_E^* = E_r/vB_0$ and the normalized collision frequency $\nu^* = R_0\nu/(v)$. See for instance [46], where several configurations are considered and the main thermal transport matrix coefficients are represented as a function of ν^* for different values of v_E^* . In particular, in the scalings depicted for the normalized transport matrix coefficient D_{i1}^* , helpful visual references of the collisionality interval at which the $1/\nu$ scaling begins and when transits to the $\sqrt{\nu}$ regime are found. This so-called mono-energetic view is somewhat limited since the Maxwellian velocity distribution function covers a range of velocities and not just one. In figure 7 the range of ν^* and v_E^* values as a function of r/a are represented for electrons and ions (H^+) with velocity between $v = v_{th}$ and $v = 2v_{th}$, considering the plasma parameters of figure 6. Looking at the values of ν^* and v_E^* for the ion parameters and comparing with the scanned ranges in [46] for W7-X, one can conclude that the ions should mostly be in the $\sqrt{\nu}$ regime at the innermost radial positions and in the plateau regime at the edge, passing through a practically inexistent $1/\nu$ regime. Regarding the electrons, their much lower normalized collisionality compared to that of the ions at the core make them mainly reside in the $\sqrt{\nu}$ regime in that region as well. They

also exhibit ν^* values at the edge characteristic of the plateau regime but, contrarily to the ions, the much lower v_E^* places them on a more robust and wider (in collisionality) $1/\nu$ regime in between. This consequently should make the electrons to be deep in the $1/\nu$ regime on a radially wide region of the core. Finally, since the perturbed part of the distribution function (and consequently the perturbed part of the density entering in the equation for the potential variation) scales in the $1/\nu$ regime with ρ^*/ν^* while in the $\sqrt{\nu}$ regime is independent of ρ^* and ν^* (with ρ^* the normalized Larmor radius to the stellarator size) [16, 47], the core of these plasmas are particularly favorable to show differences between considering kinetic or adiabatic electrons in the calculations of Φ_1 . This is the numerical comparison presented and discussed in the following paragraph.

The calculations of Φ_1 have been performed for nine radial positions, approximately separated between each other $\Delta r/a = 0.1$. These radii are $r/a = \{0.12, 0.22, 0.33, 0.41, 0.51, 0.60, 0.72, 0.80, 0.90\}$. As in section 3.2, the simulations are local and each considers a different value of the ambipolar radial electric field. In particular the following values are given for each of the flux surfaces just mentioned: $E_r = \{0.59, 3.89, 8.16, 10.95, 11.14, 9.98, -1.38, -8.52, -10.0\}$ kV m $^{-1}$. As it is well known any local code that keeps the tangential $E_r \times B$ drift but neglects the tangential component of magnetic drift, as it is our case, has problems when approaching the value of $E_r = 0$, where an unphysically large magnitude of f_1 is obtained [16, 17]. For this reason we have avoided the exact root transition flux surface where $E_r = 0$. However, the figures of the potential on the toroidal planes have been obtained by interpolation using the value over the simulated flux surfaces, which passes through the entire transition region. For this reason the results represented in the vicinity of that radius must be taken indicatively. In figure 8 the potential variation is represented, from top to

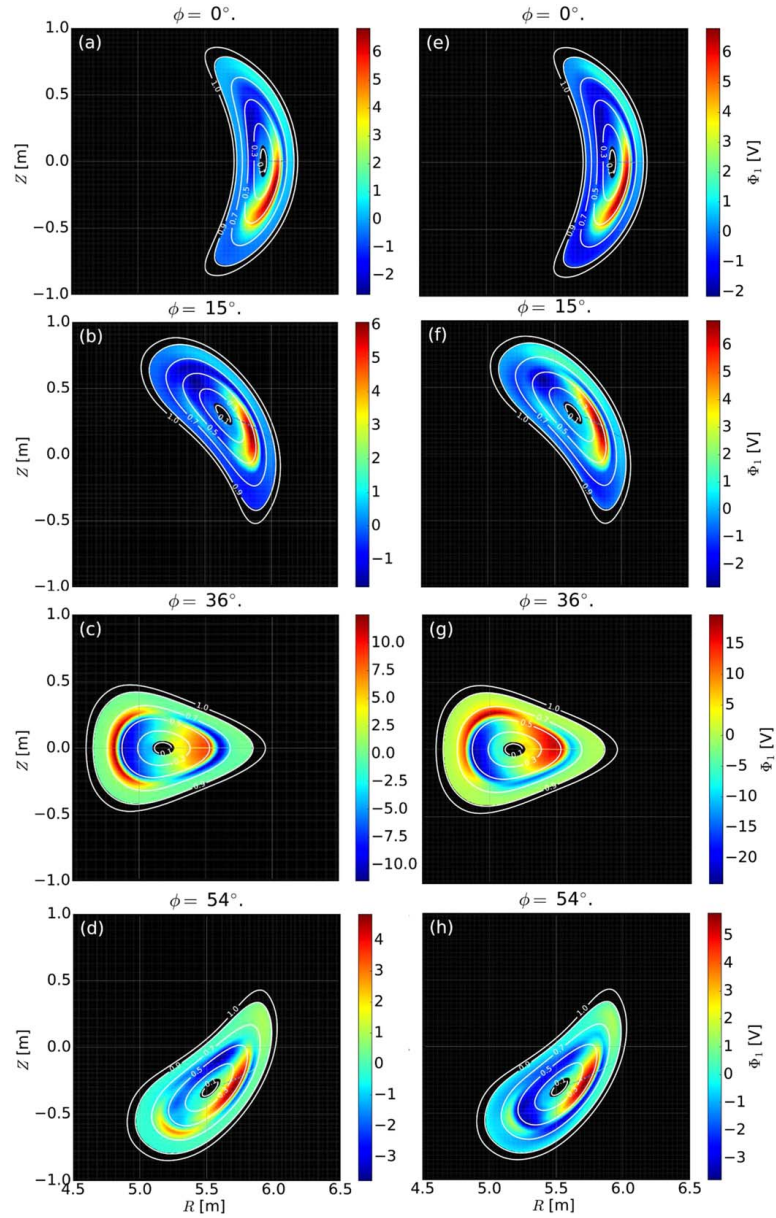


Figure 8. For the simulations with adiabatic electrons (left column) and kinetic electrons (right column), from top to bottom: calculated potential for the W7-X (KJM configuration) at the toroidal planes $\zeta = 0^\circ, 15^\circ, 36^\circ$ and 54° . Note the different color scales on the left and right plots, employed to appreciate the changes in the shape of Φ_1 when considering adiabatic instead of kinetic electrons.

bottom, for the toroidal planes $\phi = 0^\circ, 15^\circ, 36^\circ$ and 54° . The first of these toroidal planes has the practical interest that a Doppler and a correlation reflectometer probe that plane in order to characterize the experimental radial electric field. At $\phi = 15^\circ$ a second Doppler reflectometer is also installed. The other two planes have been considered since the distance between them in ϕ is one fourth of a the machine period. The first of them corresponds to the frequently represented triangular plane where other essential diagnostics for impurity transport are installed, like the soft-x rays multi-camera tomography system [48] or the bolometry cameras [49]. The difference between the figures on the left, with labels (a)–(d), and on the right, with labels (e)–(h), is that while the former show the results assuming adiabatic electrons, the latter do it for the cases considering kinetic electrons. First of all, note that the range in the color scale changes from plot to plot, in order to make appreciable the changes in the shape of the potential, that keeping the same scale for all cross sections would not allow to appreciate. Looking at those color scales and their ranges, it can be seen that the largest Φ_1 values are very localized on the triangular plane, where they become much larger than on the other planes. Second, the size of the potential for the case with kinetic electrons is roughly up to twice as large as the results with adiabatic electrons. This is evident on the triangular plane while on the other the difference is not remarkable. Looking at the potential at the triangular plane, it is also observed that the shape experiences appreciable changes when the electrons are considered as a kinetic species compared to the case with adiabatic electrons. In particular, the negative values of Φ_1 , that in the case with adiabatic electrons 8(c) are located on the low field side and below the equatorial plane, are displaced towards the high field side when electrons are kinetic 8(g). This is also compatible with what is known about the symmetry properties of Φ_1 [50]. When only the contribution from the ions is considered, since they must be mostly in the $\sqrt{\nu}$ regime, Φ_1 must necessarily have cosine components dominating its spectrum, leading to the clear in-out asymmetry as figure 8(c) illustrates. When kinetic electrons are considered, since they must, as we have hypothesized, add their contribution from the $1/\nu$ regime, the consequent introduction of sine component leads that in-out asymmetry to blur as 8(g) shows. Other changes in the shape are observed in other planes, although not as clear as on the triangular plane.

Other features can more clearly be observed in figure 9, where the maximum normalized potential difference ($\Delta\Phi_1 = (\Phi_1^{\max} - \Phi_1^{\min})/2T_i$) is represented. The results are shown for both calculations, with adiabatic electrons and with kinetic electrons. Roughly speaking the potential variation size is shown to be considerably larger in the portion of the plasma in electron root than in that under ion root. In addition, a much larger contribution of the kinetic electron response is observed in the first of these regions than in the second. However, the point located in ion root immediately after the root transition at $r/a = 0.6$ exhibits a large value as well. A vertical line represents the exact position where the root changes. At that point the ambipolar electric field is rather low

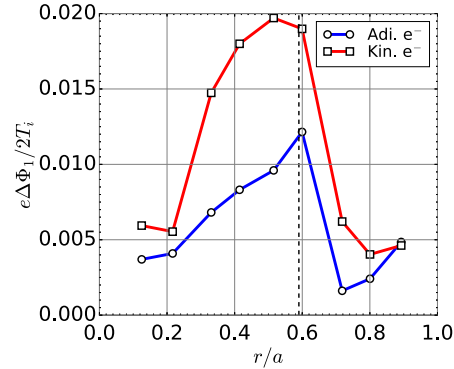


Figure 9. Maximum difference of the potential $\Delta\Phi_1 = \Phi_1^{\max} - \Phi_1^{\min}$ on each of the simulated flux surfaces normalized to the ion temperature T_i as a function of the normalized effective radius r/a for the calculations with adiabatic electrons (circles connected with blue segments) and kinetic electrons (squares connected with red segments). The dashed vertical line indicates the radial position where $E_r = 0$. On the left and right of this line the input radial electric field is positive and negative, respectively.

$E_r = -1.38 \text{ kV m}^{-1}$, compared to the value at the other positions in ion root where $|E_r| > 7 \text{ kV m}^{-1}$. This low value of E_r can be the cause of adding a large contribution to Φ_1 from ions in the $1/\nu$ regime. Another interesting feature results from the large variations at each side of the root transition together with the abrupt change of its phase. To appreciate this one can look at the triangular plane represented in figure 8(g) for the calculation including kinetic electrons. This change is present at almost any poloidal position in the vicinity of that radius and is given in a relatively narrow region (the two radii simulated immediately before and after the root change are separated by $\Delta r/a = 0.09$). It is then natural to ask whether this can introduce some important contribution to the radial electric field. This correction, $-\Phi_1'$, is represented at the triangular plane, considering kinetic electrons, in figure 10. Moderate values of a few hundreds of V m^{-1} are present on that cross section but near to the root change the value is considerably larger, reaching around 1 kV m^{-1} , both positive and negative. In our characteristic trajectories, see equations (4)–(6), the $E \times B$ drift related to this component of the radial electric field is not kept to lowest order. This is applicable since, as it happens at almost all positions, E_r is substantially larger than the represented $-\Phi_1'$. However, it becomes of the same order at the innermost simulated radius under ion root conditions (where as above-mentioned E_r was -1.38 kV m^{-1}). Then, to this respect the calculations on that specific position should be taken, as well as the conclusions drawn from it, cautiously.

5. Conclusions

The present work has addressed the calculation of the neo-classical potential variation, with the emphasis on electron-root

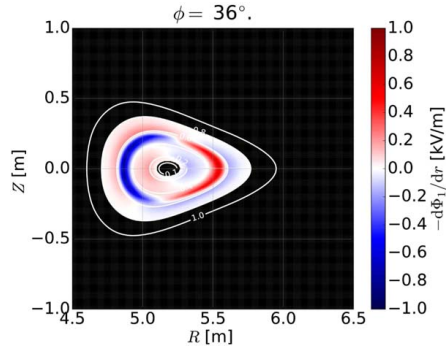


Figure 10. Radial electric field term $\Phi'_1 = -d\Phi_1/dr$ obtained at the toroidal plane $\phi = 36^\circ$, considering the corresponding potential Φ_1 for the case with kinetic electrons represented in figure 8(g).

plasmas. The standard configuration for TJ-II and a high mirror configuration of W7-X have been used, considering plasma parameters of discharges from their recent experimental campaigns.

In TJ-II, the DR radial electric field measurements and, in particular, the strong difference of its value at different points over the same flux surface, has motivated looking into the radial dependence of Φ_1 and investigating to what extent the term $-\Phi'_1$ can contribute to the total radial electric field. What has been found by numerical simulations agrees qualitatively with the experimental results. The difference in the total electric field that the potential variations can make is large in the electron root cases, although still a non-negligible factor smaller than the experimental one. On the other hand this correction is practically not present in the ion root plasmas, both numerically and experimentally. These conclusions are drawn from the comparison made at the specific measurement positions of the DR system over the same flux surface. Out of these locations $-\Phi'_1$ is found large both under ion and electron root conditions. This fact questions the applicability of the characteristic trajectories of the simulated particles, since terms containing $-\Phi'_1$ are neglected based on its size compared to $-\Phi'_0$, although *a posteriori* the former is not found that small compared to the latter. This and the possibility that the kinetic electrons could introduce a non-negligible contribution to the potential, as proven in the section by the numerical simulations results for W7-X, are possible reasons that may have frustrated a better agreement.

Regarding W7-X we have considered a configuration with significantly larger effective ripple than the standard configuration analyzed in past works [15]. The plasma parameters correspond to a standard CERC plasma from OP1.1. The analysis has demonstrated that W7-X can access regimes with potential variations significantly larger than what has already been reported. In this occasion the simulations have been performed with adiabatic and kinetic electrons. The comparison between them have shown that the contribution from the kinetic electron response, when the parameters are such that in the $1/\nu$ regime, can be significant in the size and

shape of the potential. This occurred mostly in a broad portion of the plasma in electron root, where in addition, the resulting size of Φ_1 was considerably larger than in ion root. Other features have been found, like the localization of these large variations on the triangular plane of W7-X, and the smaller values near the boundaries of the machine period. Interestingly, on that triangular plane, at each side of the root transition and at the closest radii the potential reaches its maximum values. This, together with the fact that the phase is the opposite on one side and the other of the root change, gives rise to a large radial electric field term $-\Phi'_1$.

Acknowledgments

This work has been carried out within the framework of the EUROfusion Consortium and has received funding from the Euratom research and training programme 2014–2018 under grant agreement No 633053. The views and opinions expressed herein do not necessarily reflect those of the European Commission.

This research was supported in part by grants ENE2015-70142-P and FIS2017-88892-P, Ministerio de Economía y Competitividad, Spain.

ORCID iDs

J M García-Regaña <https://orcid.org/0000-0001-7632-3357>
 J L Velasco <https://orcid.org/0000-0001-8510-1422>
 M Landreman <https://orcid.org/0000-0002-7233-577X>
 A Mollén <https://orcid.org/0000-0002-9257-7864>
 E Sánchez <https://orcid.org/0000-0003-1062-7870>

References

- [1] Calvo I, Parra F I, Velasco J L and Alonso J A 2013 Stellarators close to quasisymmetry *Plasma Phys. Control. Fusion* **55** 125014
- [2] Mynick H E and Hitchon W N G 1983 Effect of the ambipolar potential on stellarator confinement *Nucl. Fusion* **23** 1053
- [3] Hastings D E, Houlberg W A and Shaing K C 1985 The ambipolar electric field in stellarators *Nucl. Fusion* **25** 445
- [4] Maaßberg H, Burhenn R, Gasparino U, Kühner G and Ringle H 1993 Experimental and neoclassical electron heat transport in the Imfp regime for the stellarators W7-A, L-2, and W7-AS *Phys. Plasmas* **5** 3627
- [5] Maaßberg H, Beidler C D and Simmet E E 1999 Density control problems in large stellarators with neoclassical transport *Plasma Phys. Control. Fusion* **41** 1135
- [6] Burhenn R *et al* 2009 On impurity handling in high performance stellarator/heliotron plasmas *Nucl. Fusion* **49** 065005
- [7] Ida K *et al* (LHD Experimental Group) 2009 Observation of an impurity hole in a plasma with an ion internal transport barrier in the large helical device *Phys. Plasmas* **16** 056111
- [8] McCormick K *et al* 2002 New advanced operational regime on the W7-AS stellarator *Phys. Rev. Lett.* **89** 015001

- [9] Ho D D-M and Kulsrud R M 1987 Neoclassical transport in stellarators *Phys. Fluids* **30** 442–61
- [10] Beidler C D and Maaßberg H 2005 Implications of the quasi-neutrality condition for neoclassical transport in stellarators *15th Int. Stellarator Workshop (Madrid)*
- [11] García-Regaña J M, Kleiber R, Beidler C D, Turkin Y, Maaßberg H and Helander P 2013 On neoclassical impurity transport in stellarator geometry *Plasma Phys. Control. Fusion* **55** 074008
- [12] Kornilov V, Kleiber R, Hatzky R, Villard L and Jost G 2004 Gyrokinetic global three-dimensional simulations of linear ion-temperature-gradient modes in Wendelstein 7-X *Phys. Plasmas* **11** 3196
- [13] Kornilov V, Kleiber R and Hatzky R 2005 Gyrokinetic global electrostatic ion-temperature-gradient modes in finite β equilibria of Wendelstein 7-X *Nucl. Fusion* **45** 238
- [14] Pedrosa M A, Alonso J A, García-Regaña J M, Hidalgo C, Velasco J L, Calvo I, Silva C, Helander P and Kleiber R 2015 Electrostatic potential variations along flux surfaces in stellarators *Nucl. Fusion* **55** 052001
- [15] García-Regaña J M *et al* 2017 Electrostatic potential variation on the flux surface and its impact on impurity transport *Nucl. Fusion* **57** 056004
- [16] Calvo I, Parra F I, Velasco J L and Alonso J A 2017 The effect of tangential drifts on neoclassical transport in stellarators close to omnigenicity *Plasma Phys. Control. Fusion* **59** 055014
- [17] Velasco J L, Calvo I, García-Regaña J M, Parra F I, Satake S, Alonso J A and LHD Team 2018 Large tangential electric fields in plasmas close to temperature screening *Plasma Phys. Control. Fusion* **60** 074004
- [18] Landreman M, Smith H M, Mollén A and Helander P 2014 Comparison of particle trajectories and collision operators for collisional transport in nonaxisymmetric plasmas *Phys. Plasmas* **21** 042503
- [19] Mollén A, Landreman M, Smith H M, García-Regaña J M and Nunami M 2018 Flux-surface variations of the electrostatic potential in stellarators: impact on the radial electric field and neoclassical impurity transport *Plasma Phys. Control. Fusion* **60** 084001
- [20] Velasco J L *et al* (The LHD Experimental Team, and The TJ-II Team) 2017 Moderation of neoclassical impurity accumulation in high temperature plasmas of helical devices *Nucl. Fusion* **57** 016016
- [21] Helander P, Newton S L, Mollén A and Smith H M 2017 Impurity transport in a mixed-collisionality stellarator plasma *Phys. Rev. Lett.* **118** 155002
- [22] Calvo I, Parra F I, Velasco J L, Alonso J A and García-Regaña J M 2018 Stellarator impurity flux driven by electric fields tangent to magnetic surfaces arXiv:1803.05691
- [23] Geiger J, Beidler C D, Feng Y, Maaßberg H, Marushchenko N B and Turkin Y 2015 Physics in the magnetic configuration space of W7-X *Plasma Phys. Control. Fusion* **57** 014004
- [24] Klinger T *et al* (The Wendelstein 7-X Team) 2017 Performance and properties of the first plasmas of Wendelstein 7-X *Plasma Phys. Control. Fusion* **59** 014018
- [25] Kauffmann K, Kleiber R, Hatzky R and Borchardt M 2010 Global linear gyrokinetic simulations for LHD including collisions *J. Phys.: Conf. Ser.* **260** 012014
- [26] Kauffmann K 2012 Including collisions in gyrokinetic tokamak and stellarator simulations *PhD Thesis* Ernst-Moritz-Arndt-Universität Greifswald
- [27] Borchardt M, Kleiber R and Hackbusch W 2012 A fast solver for the gyrokinetic field equation with adiabatic electrons *J. Comput. Phys.* **231** 6207–62
- [28] Kleiber R and Hatzky R 2012 A partly matrix-free solver for the gyrokinetic field equation in three-dimensional geometry *Comput. Phys. Commun.* **183** 305–8
- [29] Kleiber R, Hatzky R, Könies A, Kauffmann K and Helander P 2011 An improved control-variate scheme for particle-in-cell simulations with collisions *J. Comput. Phys.* **182** 1005–12
- [30] Grimm R C, Dewar R L and Manickam J 1983 Ideal MHD stability calculations in axisymmetric toroidal coordinate systems *J. Comput. Phys.* **49** 94
- [31] Satake S, Kanno R and Sugama H 2008 Development of non-local neoclassical transport code for helical configurations *Plasma Fusion Res.* **3** S1062
- [32] Vernay T, Brunner S, Villard L, McMillan B F, Jolliet S, Tran T M, Bottino A and Graves J P 2010 Neoclassical equilibria as starting point for global gyrokinetic simulations *Phys. Plasmas* **17** 122301
- [33] Slaby C, Könies A, Kleiber R and García-Regaña J M 2018 Effects of collisions on the saturation dynamics of TAES in tokamaks and stellarators *Nucl. Fusion* **58** 082018
- [34] Abel I G, Barnes M, Cowley S C, Dorland W and Schekochihin A A 2008 Linearized model fokker-planck collision operators for gyrokinetic simulations: I. Theory *Phys. Plasmas* **15** 122509
- [35] Happel T, Estrada T, Blanco E, Tribaldos V, Cappa A and Bustos A 2009 Doppler reflectometer system in the stellarator TJ-II *Rev. Sci. Instrum.* **80** 073502
- [36] Xanthopoulos P, Plunk G G, Zooco A and Helander P 2016 Intrinsic turbulence stabilization in a stellarator *Phys. Rev. X* **6** 021033
- [37] Riemann J, Kleiber R and Borchardt M 2016 Effects of radial electric fields on linear ITG instabilities in W7-X and LHD *Plasma Phys. Control. Fusion* **58** 074001
- [38] Sáchez M, Sánchez J, Estrada T, Sánchez E, Acedo P and Lamela H 2004 High resolution CO₂ interferometry on the TJ-II stellarator by using an ADC-based phase meter *Rev. Sci. Instrum.* **75** 3414–6
- [39] Velasco J L, Alonso J A, Calvo I and Arévalo J 2012 Vanishing neoclassical viscosity and physics of the shear layer in stellarators *Phys. Rev. Lett.* **109** 135003
- [40] Velasco J L, Alonso J A, Calvo I, Arévalo J, Sánchez E, Eliseev L, Perfilov S, Estrada T, López-Fraguas A, Hidalgo C and the TJ-II Team 2013 Damping of radial electric field fluctuations in the TJ-II stellarator *Plasma Phys. Control. Fusion* **55** 124044
- [41] Tereshchenko M A, Castejon F and Cappa Á 2008 Truba user manual *Informes Técnicos del Ciemat* No. 1134 (www-fusion.ciemat.es/InternalReport/IR1134.pdf)
- [42] Wolf R C *et al* 2017 Major results from the first plasma campaign of the Wendelstein 7-X stellarator *Nucl. Fusion* **57** 102020
- [43] Pasch E, Beurskens M N A, Bozhenkov S A, Fuchert G, Knauer J, Wolf R C and W7-X Team 2016 The Thomson scattering system at Wendelstein 7-X *Rev. Sci. Instrum.* **87** 11E729
- [44] Langenberg A *et al* (The W7-X Team) 2017 Argon impurity transport studies at Wendelstein 7-X using x-ray imaging spectrometer measurements *Nucl. Fusion* **57** 086013
- [45] Yokoyama M *et al* 2007 Core electron-root confinement (CERC) in helical plasmas *Nucl. Fusion* **47** 1213
- [46] Beidler C D *et al* 2011 Benchmarking of the mono-energetic transport coefficients-results from the international collaboration on neoclassical transport in stellarators (icnts) *Nucl. Fusion* **51** 076001
- [47] Calvo I, Velasco J L, Parra F I, Alonso J A and García-Regaña J M 2018 Electrostatic potential variations on stellarator magnetic surfaces in low collisionality regimes *J. Plasma Phys.* **84** 905840407

- [48] Brandt C, Broszat T, Thomsen H, Laube R, Marquardt M, Franz P, Schülke M, Sieber T and Weißflog S 2017 Installation of the soft x-ray multi-camera tomography system (XMCTS) in the Wendelstein 7-X stellarator *Proc. 29th Symp. on Fusion Technology (SOFT-29) (Prague, Czech Republic, 5–9 September 2016)*; *Fusion Eng. Des.* **123** 891
- [49] Zhang D *et al* 2010 Design criteria of the bolometer diagnostic for steady-state operation of the W7-X stellarator *Rev. Sci. Instrum.* **81** 10E134
- [50] Alonso J A, Calvo I, García-Regaña J M and Velasco J L 2017 Can we use the variations of the electrostatic potential along flux surfaces to control impurity transport in stellarators? *1st JPP Frontiers in Plasma Physics Conf.*

Appendix B

Additional unpublished material

B.1 An analytical dispersion relation including Krook collisions

In cylindrical geometry with constant magnetic field and constant background-plasma profiles an analytical dispersion relation for kinetic Alfvén waves (KAWs) can easily be calculated. Even when a Krook-type collision operator [68], which does not add any derivatives, is present an analytical solution can still be found. It is a very good approximation to only treat the electron dynamics while the ions just provide a static background to satisfy quasi-neutrality, i.e. $n_i = n_e$. The kinetic equation for this problem is given by

$$\frac{\partial f_e}{\partial t} + \dot{\mathbf{R}} \cdot \nabla f_e + \dot{v}_{\parallel} \frac{\partial f_e}{\partial v_{\parallel}} = -\nu (f_e - F_e), \quad (\text{B.1})$$

where the index e is used to denote electrons. As usual, this equation is linearized by splitting the distribution function into $f_e = f_e^{(1)} + F_e$ and keeping only the terms linear in the perturbation. (F_e denotes the constant background.) Furthermore, using conventional notation, a plane-wave ansatz for the perturbation

$$f_e^{(1)} \sim \exp [i (\mathbf{k}_{\perp} \cdot \mathbf{r}_{\perp} + k_{\parallel} z - \omega t)] \quad (\text{B.2})$$

is applied. The magnetic field is taken to point in the z -direction. This leads to

$$-i\omega f_e^{(1)} + v_{\parallel} i k_{\parallel} f_e^{(1)} = \frac{q_e}{m_e} \left(i k_{\parallel} \phi^{(1)} - i\omega A_{\parallel}^{(1)} \right) \frac{\partial F_e}{\partial v_{\parallel}} - \nu f_e^{(1)}, \quad (\text{B.3})$$

where the equations of motion

$$\dot{\mathbf{R}} = v_{\parallel} \mathbf{b} + \frac{1}{B} \mathbf{b} \times \nabla \left[\phi^{(1)} - v_{\parallel} A_{\parallel}^{(1)} \right] \quad (\text{B.4})$$

$$\dot{v}_{\parallel} = -\frac{q_e}{m_e} \left[\mathbf{b} \cdot \nabla \phi^{(1)} + \frac{\partial A_{\parallel}^{(1)}}{\partial t} \right] \quad (\text{B.5})$$

have been used. Note that many terms do not contribute in a straight and constant magnetic field or because they would be non-linear in the perturbations. The equations of motion are those of the v_{\parallel} -formulation, which has been used for the derivation presented in this section. The calculation could however be repeated in p_{\parallel} -formulation with exactly the same dispersion

Appendix B. Additional unpublished material

relation being found in the end. An overview of the different formulations of gyro-kinetic theory is presented in App. B.2.

Defining a shifted frequency $\tilde{\omega} = \omega + i\nu$, the kinetic equation may be recast into an expression for the perturbation

$$f_e^{(1)} = \frac{q_e}{m_e} \left(k_{\parallel} \phi^{(1)} - \omega A_{\parallel}^{(1)} \right) \frac{1}{v_{\parallel} k_{\parallel} - \tilde{\omega}} \frac{\partial F_e}{\partial v_{\parallel}}. \quad (\text{B.6})$$

Neglecting the ion dynamics, this expression can now be inserted into the equation for the electrostatic potential (including a Padé approximation)

$$\frac{m_i n_i}{B^2} k_{\perp}^2 \phi^{(1)} = (1 + \rho_i^2 k_{\perp}^2) q_e \int dv_{\parallel} f_e^{(1)} \quad (\text{B.7})$$

and Ampère's law

$$k_{\perp}^2 A_{\parallel}^{(1)} = \mu_0 q_e \int dv_{\parallel} v_{\parallel} f_e^{(1)} \quad (\text{B.8})$$

in order to obtain a coupled system of equations for both potentials. The ion gyro-radius is denoted by $\rho_i = \sqrt{k_B T_i m_i} / (q_i B)$. Two integrals over velocity space need to be calculated. If F_e is chosen as a Maxwellian, one finds

$$I_1 = \int d^3v \frac{1}{v_{\parallel} k_{\parallel} - \tilde{\omega}} \frac{\partial F_e}{\partial v_{\parallel}} = -\frac{n_e}{v_{\text{th},e}^2} \frac{1}{k_{\parallel}} \left[1 + \tilde{\zeta} Z(\tilde{\zeta}) \right] \quad (\text{B.9})$$

$$I_2 = \int d^3v \frac{v_{\parallel}}{v_{\parallel} k_{\parallel} - \tilde{\omega}} \frac{\partial F_e}{\partial v_{\parallel}} = \sqrt{2} v_{\text{th},e} \tilde{\zeta} I_1 \quad (\text{B.10})$$

with $v_{\text{th},e} = \sqrt{k_B T_e / m_e}$, $\tilde{\zeta} = \tilde{\omega} / (\sqrt{2} v_{\text{th},e} k_{\parallel})$ and Z the plasma dispersion function. After substituting the integrals over velocity space into the field equations, the whole system may be written in matrix form (eigenvalue problem) as

$$\begin{pmatrix} \frac{m_i n_i}{B^2} \frac{k_{\perp}^2}{1 + \rho_i^2 k_{\perp}^2} - \frac{q_e^2}{m_e} k_{\parallel} I_1 & \frac{q_e^2}{m_e} \omega I_1 \\ -\mu_0 \frac{q_e^2}{m_e} \sqrt{2} v_{\text{th},e} \tilde{\zeta} k_{\parallel} I_1 & k_{\perp}^2 + \mu_0 \frac{q_e^2}{m_e} \sqrt{2} v_{\text{th},e} \tilde{\zeta} \omega I_1 \end{pmatrix} \begin{pmatrix} \phi^{(1)} \\ A_{\parallel}^{(1)} \end{pmatrix} = \mathbf{0}. \quad (\text{B.11})$$

As usual, the dispersion relation is obtained by setting the determinant of the coefficient matrix to zero. After some straightforward algebra the final dispersion relation is found to be

$$1 - \beta_e \frac{T_i}{T_e} \frac{m_i}{m_e} \frac{1}{\rho_i^2 k_{\perp}^2} \left\{ \tilde{\zeta} \zeta - \frac{m_e}{m_i} \frac{1}{\beta_e} (1 + \rho_i^2 k_{\perp}^2) \right\} \left[1 + \tilde{\zeta} Z(\tilde{\zeta}) \right] = 0. \quad (\text{B.12})$$

This dispersion relation has been used in article A.1 and App. B.2 in order to compare both the Legendre approach as well as EUTERPE to analytical theory.

Note that for setting $\tilde{\zeta} = \zeta$ (corresponding to $\nu = 0$) the collisionless limit of the dispersion relation given by Eq. (B.12) is recovered.

This complex dispersion relation for kinetic Alfvén waves also includes the much simpler dispersion relation of shear Alfvén waves, which can also be obtained using, for example, MHD theory. Here, we derive it by taking the collisionless limit ($\tilde{\zeta} \rightarrow \zeta$) of Eq. (B.12) and expanding the plasma dispersion function for $\zeta \rightarrow 0$, which is valid for low-frequency waves. One thus arrives at a simpler form

$$\omega^2 = v_A^2 k_{\parallel}^2 \left[1 + \rho_i^2 k_{\perp}^2 \left(1 + \frac{T_e}{T_i} \right) \right] \quad (\text{B.13})$$

of the KAW dispersion relation. If one finally considers the limit $\rho_i k_\perp \rightarrow 0$, the result is the familiar equation [37]

$$\omega^2 = v_A^2 k_\parallel^2. \quad (\text{B.14})$$

B.2 The different formulations of gyro-kinetic theory

Depending on the choice of independent variables to describe the reduced velocity space, there are several different formulations of gyro-kinetic theory (see e.g. Ref. [61] for an overview). All of them have their benefits and shortcomings. This section aims to give a short overview of some possible formulations and tries to emphasize why certain approaches were chosen for the various articles in this thesis.

B.2.1 The v_\parallel -formulation

The most intuitive way to describe the reduced velocity space is to use the parallel velocity v_\parallel and the magnetic moment μ as coordinates. The kinetic equation for species s then becomes

$$\frac{\partial f_s}{\partial t} + \dot{\mathbf{R}} \cdot \nabla f_s + \dot{v}_\parallel \frac{\partial f_s}{\partial v_\parallel} + \dot{\mu} \frac{\partial f_s}{\partial \mu} = 0 \quad (\text{B.15})$$

neglecting the collision operator. The equations of motion for the numerical marker particles are the characteristics of the kinetic equation [60]. They can be written as

$$\begin{aligned} \dot{\mathbf{R}} = & v_\parallel \mathbf{b} + \frac{m_s}{q_s} \left[\frac{\mu B + v_\parallel^2}{BB_\parallel^*} \mathbf{b} \times \nabla B + \frac{v_\parallel^2}{BB_\parallel^*} (\nabla \times \mathbf{B})_\perp \right] \\ & + \frac{v_\parallel}{BB_\parallel^*} [\mathbf{b} \times \nabla B + (\nabla \times \mathbf{B})_\perp] \langle A_\parallel \rangle + \frac{1}{B_\parallel^*} \mathbf{b} \times \nabla \langle \psi \rangle \end{aligned} \quad (\text{B.16})$$

$$\begin{aligned} \dot{v}_\parallel = & -\mu \nabla B \cdot \left[\mathbf{b} + \frac{m_s}{q_s} \frac{v_\parallel}{BB_\parallel^*} (\nabla \times \mathbf{B})_\perp \right] - \frac{q_s}{m_s} \frac{\partial \langle A_\parallel \rangle}{\partial t} \\ & - \frac{q_s}{m_s} \left\{ \mathbf{b} + \frac{m_s}{q_s} \frac{v_\parallel}{BB_\parallel^*} [\mathbf{b} \times \nabla B + (\nabla \times \mathbf{B})_\perp] \right\} \cdot \nabla \langle \phi \rangle \end{aligned} \quad (\text{B.17})$$

$$\begin{aligned} & - \frac{\mu}{B_\parallel^*} \left[\mathbf{b} \times \nabla B \cdot \nabla \langle A_\parallel \rangle + \frac{1}{B} \nabla B \cdot (\nabla \times \mathbf{B})_\perp \langle A_\parallel \rangle \right] \\ \dot{\mu} = & 0 \end{aligned} \quad (\text{B.18})$$

with

$$\psi = \phi - v_\parallel A_\parallel \quad (\text{B.19})$$

$$B_\parallel^* = B + \left[\frac{m_s}{q_s} v_\parallel + \langle A_\parallel \rangle \right] \mathbf{b} \cdot \nabla \times \mathbf{b}. \quad (\text{B.20})$$

m and q denote the particle mass and charge, respectively. In this formulation the field equations for the electromagnetic potential (i.e. Poisson's equation and Ampère's law) are

$$-\nabla \cdot \left(\frac{m_i n_0}{B^2} \nabla_\perp \phi \right) = (1 - \nabla \cdot \rho_i^2 \nabla_\perp) \sum_s q_s \langle n_s \rangle \quad (\text{B.21})$$

$$-\nabla \cdot \nabla_\perp A_\parallel = \mu_0 \sum_s \langle j_{\parallel,s} \rangle, \quad (\text{B.22})$$

using a Padé approximation in Poisson's equation. The field equations are easily implemented into numerical codes as the so-called cancellation problem (see App. B.2.2) is absent, which is the main benefit of this approach. Furthermore, v_{\parallel} is the actual physical parallel velocity which simplifies the interpretation of any numerical results. It also facilitates the straightforward inclusion of collisions. The main disadvantage (from a numerical point of view) of this formulation is the partial time derivative of A_{\parallel} in the equations of motion (see Eq. (B.17)), which prevents the use of any straightforward explicit numerical integration scheme [89, 90], for instance a Runge-Kutta algorithm (see e.g. Ref. [91]) which is usually used in EUTERPE.

The v_{\parallel} -formulation is nevertheless used in the CKA-EUTERPE model [1]. The reason is that an ideal-MHD approximation is employed. (See articles A.2, A.4, and A.5 for details.) In ideal-MHD theory the parallel electric field vanishes

$$E_{\parallel} = -\mathbf{b} \cdot \nabla \phi - \frac{\partial A_{\parallel}}{\partial t} = 0, \quad (\text{B.23})$$

which gives a condition that can be used to eliminate the partial time derivative of the vector potential from the equations of motion, which thus become easily usable. The simplified equation for \dot{v}_{\parallel} can be found in article A.2 (see page 57).

B.2.2 The p_{\parallel} -formulation

Another possibility of expressing the equations is to use the so-called p_{\parallel} -formulation, in which the parallel canonical momentum (divided by the mass)

$$u_{\parallel} = \frac{p_{\parallel}}{m_s} = v_{\parallel} + \frac{q_s}{m_s} A_{\parallel} \quad (\text{B.24})$$

is used as coordinate in velocity space. The kinetic equation

$$\frac{\partial f_s}{\partial t} + \dot{\mathbf{R}} \cdot \nabla f_s + u_{\parallel} \frac{\partial f_s}{\partial u_{\parallel}} + \dot{\mu} \frac{\partial f_s}{\partial \mu} = 0 \quad (\text{B.25})$$

still has the same form (albeit living in a different space), but the equations of motion

$$\begin{aligned} \dot{\mathbf{R}} = & u_{\parallel} \mathbf{b} + \frac{m_s}{q_s} \left[\frac{\mu B + u_{\parallel}^2}{BB_{\parallel}^*} \mathbf{b} \times \nabla B + \frac{u_{\parallel}^2}{BB_{\parallel}^*} (\nabla \times \mathbf{B})_{\perp} \right] \\ & - \frac{q_s}{m_s} \left\{ \mathbf{b} + \frac{m_s}{q_s} \frac{u_{\parallel}}{BB_{\parallel}^*} [\mathbf{b} \times \nabla B + (\nabla \times \mathbf{B})_{\perp}] \right\} \langle A_{\parallel} \rangle + \frac{1}{B_{\parallel}^*} \mathbf{b} \times \nabla \langle \psi \rangle \end{aligned} \quad (\text{B.26})$$

$$\begin{aligned} \dot{u}_{\parallel} = & -\mu \nabla B \cdot \left[\mathbf{b} + \frac{m_s}{q_s} \frac{u_{\parallel}}{BB_{\parallel}^*} (\nabla \times \mathbf{B})_{\perp} \right] \\ & - \frac{q_s}{m_s} \left\{ \mathbf{b} + \frac{m_s}{q_s} \frac{u_{\parallel}}{BB_{\parallel}^*} [\mathbf{b} \times \nabla B + (\nabla \times \mathbf{B})_{\perp}] \right\} \cdot \nabla \langle \psi \rangle \end{aligned} \quad (\text{B.27})$$

$$\dot{\mu} = 0 \quad (\text{B.28})$$

change. Here, the abbreviations

$$\psi = \phi - u_{\parallel} A_{\parallel} \quad (\text{B.29})$$

$$B_{\parallel}^* = B + \frac{m_s}{q_s} u_{\parallel} \mathbf{b} \cdot (\nabla \times \mathbf{b}) \quad (\text{B.30})$$

have been used. Since the transformation from v_{\parallel} to p_{\parallel} also affects the current density,¹ Ampère's law changes to

$$-\nabla \cdot \nabla_{\perp} A_{\parallel} + \sum_s \frac{\mu_0 n_0 q_s^2}{m_s} A_{\parallel} = \mu_0 \sum_s \langle j_{\parallel,s} \rangle. \quad (\text{B.31})$$

Comparing the p_{\parallel} -formulation with the v_{\parallel} -approach, it can be confirmed that the equations of motion are simpler in the p_{\parallel} -formulation. Especially the partial time derivative of the vector potential has disappeared. In this regard, those equations are more suitable for the numerical treatment. The drawback of the variable transformation is that Ampère's law has gained an additional term, the so-called skin term. The problem is that the skin term can be much larger than the actual physical current and thus threatens to overpower the relevant dynamics. It should, however, be cancelled exactly by the adiabatic part of j_{\parallel} [2], which is numerically not necessarily the case. This is the origin of the so-called cancellation problem, which plagues the p_{\parallel} -approach in practice [69, 92, 93].

The p_{\parallel} -formulation is not used in any of the EUTERPE simulations performed in this thesis. This is partly due to the numerical issues mentioned above, but mainly because the collision operators are formulated with the physical parallel velocity. Hence, as article A.1 showed, they would need to be transformed to fit the p_{\parallel} -formulation.

B.2.3 The mixed formulation

The so-called mixed formulation of the gyro-kinetic equations (see e.g. Refs. [69, 70, 94]) aims to combine the best properties of the v_{\parallel} - and p_{\parallel} -formulation without adopting their respective disadvantages. The idea was first developed in Ref. [93]. The particle Lagrangian and second-order equations of motion for the particles were derived in a subsequent publication [70]. The basic idea is to split the parallel vector potential into a Hamiltonian and a 'symplectic' part, $A_{\parallel} = A_{\parallel}^h + A_{\parallel}^s$. The transformation to a new coordinate in velocity space is carried out using only the Hamiltonian part

$$\tilde{u}_{\parallel} = v_{\parallel} + \frac{q_s}{m_s} A_{\parallel}^h. \quad (\text{B.32})$$

Defining the kinetic equation

$$\frac{\partial f_s}{\partial t} + \dot{\mathbf{R}} \cdot \nabla f_s + \tilde{u}_{\parallel} \frac{\partial f_s}{\partial \tilde{u}_{\parallel}} + \dot{\mu} \frac{\partial f_s}{\partial \mu} = 0 \quad (\text{B.33})$$

with this variable again leads to modified equations of motion [70]:

$$\begin{aligned} \dot{\mathbf{R}} = & \left[\tilde{u}_{\parallel} - \frac{q_s}{m_s} \langle A_{\parallel}^h \rangle \right] \mathbf{b} + \frac{m_s}{q_s} \left[\frac{\mu B + \tilde{u}_{\parallel}^2}{BB_{\parallel}^*} \mathbf{b} \times \nabla B + \frac{\tilde{u}_{\parallel}^2}{BB_{\parallel}^*} (\nabla \times \mathbf{B})_{\perp} \right] \\ & + \mathbf{b} \times \kappa \frac{\tilde{u}_{\parallel}}{B_{\parallel}^*} \left(\langle A_{\parallel}^s \rangle - \langle A_{\parallel}^h \rangle \right) + \frac{1}{B_{\parallel}^*} \mathbf{b} \times \nabla \left[\langle \phi \rangle - \tilde{u}_{\parallel} \left(\langle A_{\parallel}^h \rangle + \langle A_{\parallel}^s \rangle \right) \right] \end{aligned} \quad (\text{B.34})$$

¹The current density is defined as $\langle j_{\parallel,s} \rangle = q_s \int d^3v \, d^3R \, u_{\parallel} f_s \delta(\mathbf{R} + \boldsymbol{\rho} - \mathbf{r})$ in the p_{\parallel} -formulation. u_{\parallel} would need to be exchanged with v_{\parallel} and \tilde{u}_{\parallel} in the v_{\parallel} - and mixed formulation, respectively.

$$\begin{aligned} \dot{u}_{\parallel} = & -\mu \nabla B \cdot \left[\mathbf{b} + \frac{m_s}{q_s} \frac{\tilde{u}_{\parallel}}{B B_{\parallel}^*} (\nabla \times \mathbf{B})_{\perp} \right] - \frac{q_s}{m_s} \frac{\partial \langle A_{\parallel}^s \rangle}{\partial t} \\ & - \frac{q_s}{m_s} \mathbf{b} \cdot \nabla \left[\langle \phi \rangle - \tilde{u}_{\parallel} \langle A_{\parallel}^h \rangle \right] - \frac{\tilde{u}_{\parallel}}{B_{\parallel}^*} \mathbf{b} \times \boldsymbol{\kappa} \cdot \nabla \left(\langle \phi \rangle - \tilde{u}_{\parallel} \langle A_{\parallel}^h \rangle \right) \end{aligned} \quad (\text{B.35})$$

$$\begin{aligned} & - \frac{\mu}{B_{\parallel}^*} \left[\mathbf{b} \times \nabla B \cdot \nabla \langle A_{\parallel}^s \rangle + \frac{1}{B} \nabla B \cdot (\nabla \times \mathbf{B})_{\perp} \langle A_{\parallel}^s \rangle \right] \\ \dot{\mu} = & 0. \end{aligned} \quad (\text{B.36})$$

The magnetic curvature is denoted by $\boldsymbol{\kappa}$. Ampère's law in this formulation is [70]

$$-\nabla \cdot \nabla_{\perp} A_{\parallel}^h + \sum_s \frac{\mu_0 n_0 q_s^2}{m_s} A_{\parallel}^h = \mu_0 \sum_s \langle j_{\parallel, s} \rangle + \nabla \cdot \nabla_{\perp} A_{\parallel}^s \quad (\text{B.37})$$

and potentially still includes the cancellation problem. Similarly, the partial time derivative of A_{\parallel}^s is still present in the equations of motion. Both can be remedied by using the freedom that the arbitrary splitting of A_{\parallel} provides to postulate another equation. Such an equation is needed to close the system. Here, we choose ‘ideal Ohm’s law’

$$\frac{\partial A_{\parallel}^s}{\partial t} + \mathbf{b} \cdot \nabla \phi = 0, \quad (\text{B.38})$$

but only defined with the symplectic part of A_{\parallel} . This is a good approximation for shear Alfvén waves [69, 93] and thus minimizes the skin term in Ampère’s law, which is proportional to A_{\parallel}^h . It further removes the partial time derivative of A_{\parallel}^s in Eq. (B.35).

In order to permanently prevent the cancellation problem from re-appearing, the Hamiltonian part of A_{\parallel} needs to remain small. Algorithmically this is achieved by resetting A_{\parallel}^h after every time step, by adding its value to A_{\parallel}^s and then setting $A_{\parallel}^h = 0$. The distribution function is transformed back into v_{\parallel} -space, which makes this approach well suited to incorporate collision operators, which are naturally formulated using the physically meaningful v_{\parallel} -coordinate. In EUTERPE the collision step is performed after the distribution function is transformed back to v_{\parallel} -space, which happens after the particles have been advected along the characteristics of the kinetic equation.

This formulation of the gyro-kinetic equations is used in article A.1, in which the implementation of pitch-angle collisions into the electromagnetic version of EUTERPE is benchmarked. Simultaneously, the compatibility of the mixed formulation with collisions is validated. Such a test is important, since the mixed formulation is the one used in fully gyro-kinetic EUTERPE simulations. While in this thesis mainly the simplified CKA-EUTERPE model has been used, we aim to perform non-linear simulations including collisions with the fully gyro-kinetic version of EUTERPE in the future.

B.2.4 Comparison

Fig. B.1 shows a comparison of the v_{\parallel} -, p_{\parallel} -, and mixed formulation (used by EUTERPE in this figure) of the gyro-kinetic equations. The analytical dispersion relation has been derived in App. B.1. The example chosen for illustrative purposes is the kinetic Alfvén wave investigated in article A.1. The simulations include a Krook operator [68], which necessitates the inclusion of

B.3. Effect of collisions in velocity space (EUTERPE)

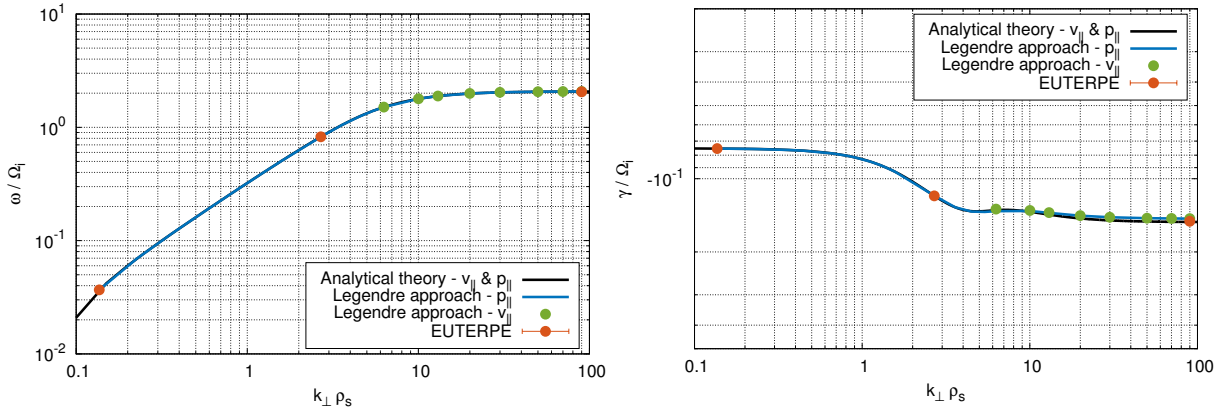


Figure B.1: Comparison of the v_{\parallel} -, p_{\parallel} -, and mixed formulation (EUTERPE) of gyro-kinetics for the case of a kinetic Alfvén wave in slab geometry presented in article A.1. The left-hand side shows the frequency of the mode. The damping rate is shown on the right-hand side. The simulations include a Krook operator. As expected, all approaches agree very well.

a correction term [95] in the p_{\parallel} -formulation. The reason is that also in p_{\parallel} the Krook operator needs to relax the distribution function to a Maxwellian defined with the physically meaningful velocity (see also article A.1). On the left-hand side of the figure, which shows the frequency dependence on $k_{\perp} \rho_s$, all approaches agree perfectly. On the right-hand side, the damping rate is shown. The agreement of all approaches is, again, very good. This confirms the correct implementation of the Legendre approach for a problem that is analytically solvable. Note that for very high values of $k_{\perp} \rho_s > 20$ there is a slight discrepancy between the theoretical results and the Legendre approach. This is most likely caused by insufficient numerical resolution (i.e. the number of Legendre polynomials used to expand the distribution function).

B.3 Effect of collisions in velocity space (EUTERPE)

Article A.1 showed the direct influence of pitch-angle scattering on the structure of the perturbed distribution function in velocity space (see Fig. 4 on page 48). However, the distribution function was only calculated with the Legendre approach. (Since it did not fit the narrative of article A.1, a comparison to EUTERPE was omitted.) Therefore, we present the comparison with the EUTERPE results here.

Fig. B.2 shows the absolute value of the perturbed distribution function $f_e^{(1)}$, calculated by EUTERPE, in velocity space. The left-hand-side column shows a collisionless simulation, while the results including pitch-angle scattering are visible on the right-hand side. The resonance condition is indicated as a black line in all plots. The mode numbers and the collision frequency are the same as in Fig. 4 of article A.1.

Comparing these results with the ones shown here, it can be seen that both EUTERPE and the Legendre approach agree very nicely for $t\Omega_i = 35$ and $t\Omega_i = 70$. Also in the EUTERPE simulations (those without collisions) the perturbed distribution function becomes more and more localized in the vicinity of the resonances.

The last row of Fig. B.2 shows the long-time behaviour, which was not investigated in article A.1. On the right-hand side it can be seen that pitch-angle collisions have completely isotropized the velocity space in the ξ' -variable, which is expected from analytical theory.

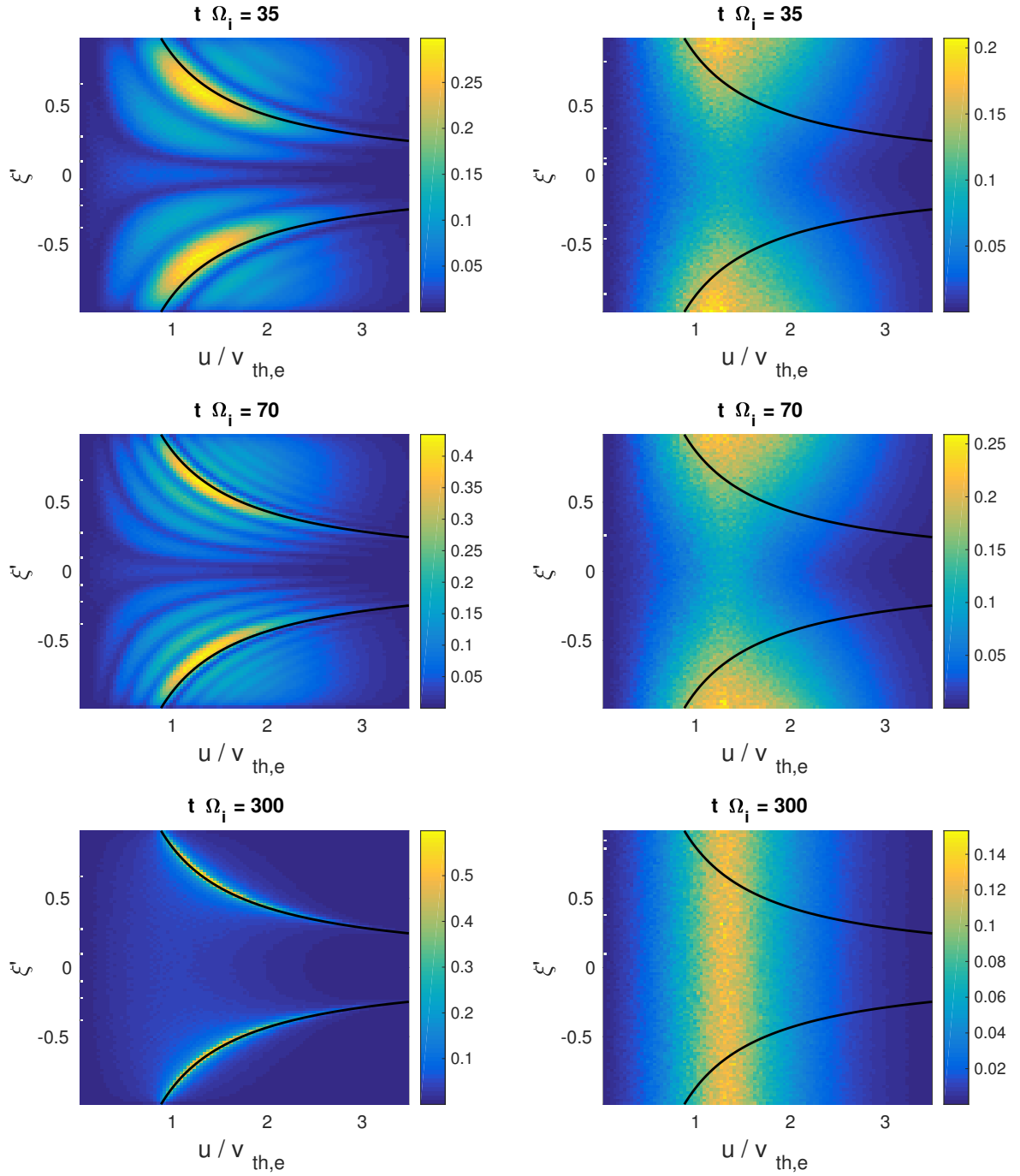


Figure B.2: Perturbed electron distribution function in velocity space as calculated by EUTERPE for the same case as shown in article A.1 (see Fig. 4 on page 48). Only the right-hand side includes pitch-angle scattering. The distribution function calculated by EUTERPE shows the same behaviour as the one calculated with the Legendre approach [94].

B.4 The conservation scheme

All the collision operators introduced in Sec. 1.5 are not entirely complete. Following Ref. [66], it must be taken into account that the linearized collision operator (F is a Maxwellian and $f^{(1)}$ is the perturbation)

$$\mathcal{C}(f) = \mathcal{C}(f^{(1)}, F) + \mathcal{C}(F, f^{(1)}) \quad (\text{B.39})$$

is composed of two parts. The first term describes the collisions of particles in the perturbation with the background Maxwellian. The second term is the back-reaction on the Maxwellian. Following standard convention these two parts will be referred to as the test-particle operator $\mathcal{C}_{\text{tp}}(f^{(1)})$, and the field-particle operator $\mathcal{C}_{\text{fp}}(f^{(1)})$, respectively.

It is important to note that only the full operator conserves particle number, linear momentum, and energy

$$\int d^3v \left[\mathcal{C}_{\text{tp}}(f^{(1)}) + \mathcal{C}_{\text{fp}}(f^{(1)}) \right] \{1, v_{\parallel}, v^2\} = 0. \quad (\text{B.40})$$

If, however, only the test-particle operator is taken into account, conservation of these moments may be violated

$$\int d^3v \mathcal{C}_{\text{tp}}(f^{(1)}) \{1, v_{\parallel}, v^2\} = \{\Delta N, \Delta P, \Delta E\}. \quad (\text{B.41})$$

It is for this reason crucial that the field-particle operator is taken into account in numerical simulations. To calculate it directly would however require the knowledge about the Rosenbluth potentials [96] of the a-priori unknown $f^{(1)}$. Numerically, it would be possible to calculate $f^{(1)}$ in each time step via binning procedures. But this operation is expensive and would introduce particle noise [97, 98] into the Rosenbluth potentials and thus ultimately also into the field-particle collision operator. For these reasons it is numerically more advantageous to introduce an ansatz for $\mathcal{C}_{\text{fp}}(f^{(1)})$ that ensures that the full operator is self-adjointed, has an H-theorem (increases entropy), and obeys Eq. (B.40). As is reported in articles A.2 and A.7, EUTERPE uses the scheme described in Refs. [99–101].

Thus we make the following ansatz for the field-particle operator

$$\mathcal{C}_{\text{fp}}(f^{(1)}) = [N(\mathbf{v})\mathcal{N} + P(\mathbf{v})\mathcal{P} + E(\mathbf{v})\mathcal{E}]F, \quad (\text{B.42})$$

where

$$N(\mathbf{v}) = \nu_{\text{D}} - 3\sqrt{\frac{\pi}{8}}\nu_{\text{E}}x^2 \quad (\text{B.43})$$

$$P(\mathbf{v}) = \nu_{\text{s}}\frac{v_{\parallel}}{v_{\text{th}}^2} \quad (\text{B.44})$$

$$E(\mathbf{v}) = \nu_{\text{E}}x^2. \quad (\text{B.45})$$

We have defined $x = v/(\sqrt{2}v_{\text{th}})$ with $v_{\text{th}} = \sqrt{k_{\text{B}}T/m}$. The collision frequencies appearing in the above equations are the deflection frequency, the slowing-down frequency, and the energy-diffusion

frequency, respectively [66]. They are defined as

$$\nu_{\text{D}} = \nu_0 \frac{\Phi(x) - G(x)}{x^3} \quad (\text{B.46})$$

$$\nu_{\text{s}} = 4\nu_0 \frac{G(x)}{x} \quad (\text{B.47})$$

$$\nu_{\text{E}} = -2\nu_{\text{D}} + \left(2 - \frac{1}{2x^2}\right) \nu_{\text{s}} \quad (\text{B.48})$$

$$(\text{B.49})$$

for self-collisions. (Work is currently in progress to extend the conservation scheme to be applicable to inter-species collisions.) Furthermore,

$$\nu_0 = \frac{nZ^4 e^4 \ln \Lambda}{4\pi \epsilon_0^2 m^2 2^{3/2} v_{\text{th}}^3} \quad (\text{B.50})$$

and Φ and G denote the error function and the Chandrasekhar function, respectively [66]. $\ln \Lambda$ is the Coulomb logarithm.

The quantities \mathcal{N} , \mathcal{P} , and \mathcal{E} have to be determined such that Eq. (B.40) is fulfilled in each spatial bin of the simulation domain. This leads to a linear system

$$-\begin{pmatrix} \Delta N \\ \Delta P \\ \Delta E \end{pmatrix} = \int d^3v \left[F \begin{pmatrix} N(\mathbf{v}) & P(\mathbf{v}) & E(\mathbf{v}) \\ v_{\parallel} N(\mathbf{v}) & v_{\parallel} P(\mathbf{v}) & v_{\parallel} E(\mathbf{v}) \\ v^2 N(\mathbf{v}) & v^2 P(\mathbf{v}) & v^2 E(\mathbf{v}) \end{pmatrix} \right] \begin{pmatrix} \mathcal{N} \\ \mathcal{P} \\ \mathcal{E} \end{pmatrix} \quad (\text{B.51})$$

of three coupled equations for the three coefficients which is solved by directly inverting the 3×3 -matrix. (This is done only when there is more than one particle in the spatial bin. Otherwise the matrix is singular. This sets a lower limit for the number of markers to be used in the simulation. In practice, this limit is much lower than what is required to minimize particle noise and thus not important.) The amount of ‘non-conservation’ (the Δ ’s on the left-hand side of Eq. (B.51)) are determined in each bin as differences after and before the test-particle collision step. For the parallel momentum, this is done according to

$$\Delta P = \sum_{p \in \text{bin}} w_p \left(v_{\parallel, p}^{\text{after}} - v_{\parallel, p}^{\text{before}} \right), \quad (\text{B.52})$$

where p is the particle index and w_p is the individual particle weight. ΔN and ΔE are treated equivalently.

Note that some model test-particle collision operators conserve certain moments exactly. The pitch-angle-scattering operator, for instance, conserves particle number and energy, but violates the conservation of linear momentum. Still, all the terms in Eq. (B.42) will be kept to ensure the conservation of all the moments also on the numerical level.

B.4.1 Benchmarking the conservation scheme

Before the conservation scheme can be used for realistic cases, it needs to be benchmarked in a well-understood environment.

Besides its main purpose (testing the compatibility of pitch-angle collisions with the pullback scheme [69, 70]), the slab benchmark case reported on in article A.1 can also be used to verify the

numerical implementation of the conservation scheme in the limit where only pitch-angle collisions are included. For this purpose the Legendre approach (see article A.1) has been extended in the sense that a momentum-conserving collision operator is now used on the right-hand side of the kinetic equation. Formally, this corresponds to the substitution

$$\mathcal{L} \longrightarrow \mathcal{C} = \mathcal{L} + P(\mathbf{v}) \mathcal{P} \left(f_e^{(1)} \right) F_e, \quad (\text{B.53})$$

where \mathcal{L} is the pitch-angle-scattering operator used before. Note that for this analytical consideration the fact that \mathcal{L} conserves particle number and energy has been used. Only a momentum-correction needs to be applied. In this case it is not necessary to solve a linear system of equations numerically, since the analytical solution

$$\bar{\mathcal{P}} = \int d^3v v_{\parallel} \nu_D f_e^{(1)} / \left(\frac{1}{3} \int d^3v \frac{v^2}{v_{\text{th},e}^2} \nu_s F_e \right) \quad (\text{B.54})$$

can be found. Furthermore, using the same decomposition of the perturbed distribution function into Legendre polynomials as in article A.1, one finds for the integrals

$$\int d^3v v_{\parallel} \nu_D f_e^{(1)} = \frac{4\pi}{3} \int dv v^3 \nu_D f_1 F_e \quad (\text{B.55})$$

$$\frac{1}{3} \int d^3v \frac{v^2}{v_{\text{th},e}^2} \nu_s F_e = \frac{4\pi}{3} \frac{1}{v_{\text{th},e}^2} \int dv v^4 \nu_s F_e, \quad (\text{B.56})$$

which leads to

$$\mathcal{P}_l = v_{\text{th},e}^2 \frac{\int dv v^3 \nu_D f_l F_e}{\int dv v^4 \nu_s F_e}. \quad (\text{B.57})$$

Hence, the kinetic equation in the v_{\parallel} -formulation including the momentum-conserving collision operator (first and second term on the right-hand side of the equation) is

$$\begin{aligned} \frac{\partial}{\partial t} \left(f_l + \frac{q_e}{m_e} \frac{v}{v_{\text{th},e}^2} A_{\parallel} \delta_{l,1} \right) + ik_{\parallel} v \left(\frac{l+1}{2l+3} f_{l+1} + \frac{l}{2l-1} f_{l-1} \right) \\ = -\frac{\nu_D}{2} l(l+1) f_l + \frac{\nu_s v}{v_{\text{th},e}^2} \mathcal{P}_l \delta_{l,1} - \frac{q_e}{m_e} ik_{\parallel} \frac{v}{v_{\text{th},e}^2} \phi \delta_{l,1} \end{aligned} \quad (\text{B.58})$$

and can be compared to Eq. (40) from article A.1 (see page 49).

We are now in a position to compare the conservation scheme of EUTERPE with the (more analytical) Legendre approach presented above. Note that EUTERPE also implements particle number and energy conservation, which the Legendre approach does not. It has been found, however, that these quantities are conserved to high accuracy (almost machine precision) for electron-electron pitch-angle collisions.

The results of this benchmark are summarized in Fig. B.3. Next to the data already shown in article A.1 without the momentum-conserving collision operator (black circles) the results using momentum conservation can be seen as triangles. Note the good agreement between EUTERPE (red) and the Legendre approach (blue). Employing the conservation scheme generally leads to a less stable mode, i.e. it reduces the damping rate. The damping rates get closer to the collisionless results, which are shown as a black dashed line in Fig. B.3. It can be concluded that, for this case, neglecting momentum conservation leads to an over-estimation of the damping rate.

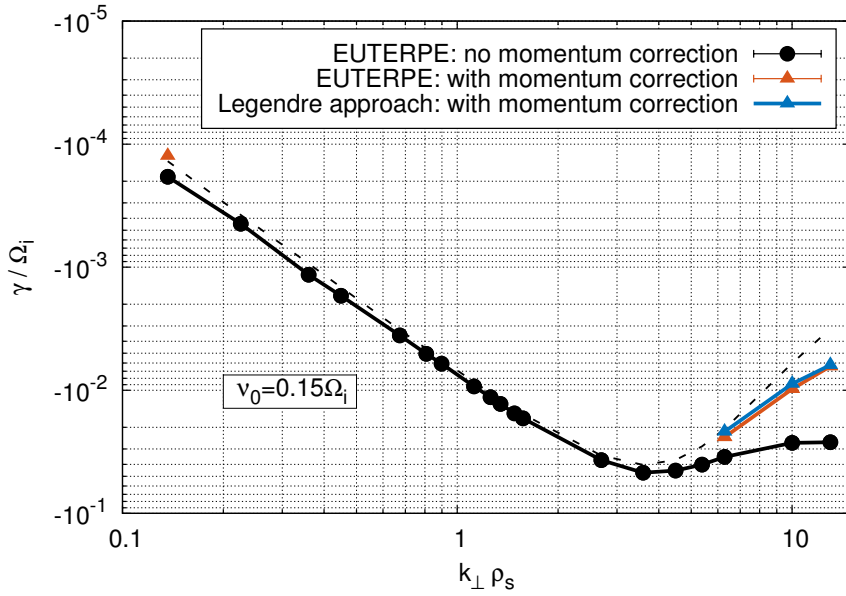


Figure B.3: Benchmarking the momentum-conserving pitch-angle collision operator for a kinetic Alfvén wave in slab geometry as presented in article A.1 (compare with Fig. 2 on page 47). The black line shows the EUTERPE results without accounting for the conservation of linear momentum in the collision step. The coloured curves show the effect of a momentum-conserving collision operator. EUTERPE and the Legendre approach agree. The black dashed line is the damping rate without any collisions.

The same has been found in article A.2 for a more relevant tokamak case. This comparison of the Legendre approach with EUTERPE has only been done for the three highest mode numbers (largest $k_{\perp}\rho_s$), since under these conditions the Legendre approach is stable in the v_{\parallel} -formulation. This is the formulation used for the implementation of the conservation scheme into the Legendre approach. Also note that a higher particle number than in article A.1 ($4.0 \cdot 10^6$ vs. 10^7 markers) was used for EUTERPE in the case with the momentum-conserving collision operator. This is done in order to ensure that enough particles reside in each spatial bin, which is important for the conservation scheme to work properly.

Fig. B.4 shows a measure of the total momentum non-conservation (red circles) before the correction step is performed in EUTERPE. The amount by which the momentum is corrected is shown in blue. Especially when looking at the small insert, which shows a zoomed-in view, it can easily be confirmed that the red and blue circles lie on top of each other. This is additional confirmation that the conservation scheme is working correctly. The average value of the momentum violation (and therefore also the correction) oscillates in time. This corresponds to oscillations of the perturbed distribution function (and the electrostatic potential) with the same frequency.

B.5 Implementation of the fast-ion collision operator

If one considers a plasma with a fast-ion population that is much faster than the Maxwellian background-plasma ions it is possible to simplify the Fokker-Planck collision operator introduced

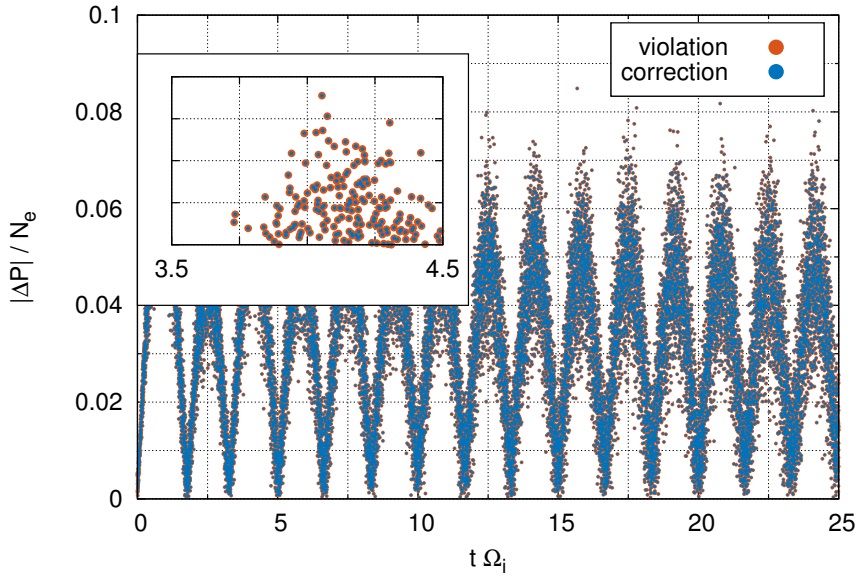


Figure B.4: Diagnostic output of EUTERPE showing a measure of the total non-conservation of linear momentum (red) and the subsequent correction (blue) for the largest- $k_{\perp}\rho_s$ case shown in Fig. B.3. The violation is corrected exactly (see insert).

in Sec. 1.5 and to obtain the so-called fast-ion collision operator² [66]

$$\mathcal{C}(f_f) = \underbrace{\frac{1}{v^2\tau_s} \frac{\partial}{\partial v} [(v^3 + v_c^3) f_f]}_{\text{slowing-down}} + \underbrace{\frac{m_i}{m_f} \frac{v_c^3}{v^3\tau_s} \mathcal{L}(f_f)}_{\text{pitch-angle}}. \quad (\text{B.59})$$

Here, τ_s is the slowing-down time and v_c denotes the critical velocity. The collision operator is composed of two terms which relate to different physical processes: The first term describes the drag that the fast ions feel because of their interaction with the electrons and ions of the background plasma. It is responsible for slowing down the fast ions. (Note that, because of the first-order derivative with respect to velocity, this term can be understood as a force acting on the fast ions.) The second term in Eq. (B.59) characterizes pitch-angle collisions of the fast ions with the bulk ions, which are comparable in mass. The operator \mathcal{L} is given as

$$\mathcal{L} = \frac{1}{2} \frac{\partial}{\partial \xi} (1 - \xi^2) \frac{\partial}{\partial \xi} \quad (\text{B.60})$$

and denotes the pitch-angle collision operator introduced in Sec. 1.5. This part of the whole operator is more important at low fast-ion velocities and includes effects such as the isotropization in velocity space. Pitch-angle collisions between fast ions and electrons are neglected because of their mass difference.

Before this operator is included in EUTERPE, an operator splitting is performed. Since the slowing-down part of Eq. (B.59) only includes a first-order derivative with respect to the velocity v , it can be integrated into the existing advection step of EUTERPE in which the numerical particles are pushed along the characteristics of the kinetic equation. Combining the

²For the reasons given in article A.5 a more complete version of the fast-ion collision operator is used in the standard EUTERPE simulations.

slowing-down part with the existing advection step is beneficial, since a more accurate numerical integrator can be used (usually a fourth-order Runge-Kutta method). Ref. [67] and article A.1 describe how a first-order stochastic scheme is used for the remaining pitch-angle part.

However, one subtlety remains: Eq. (B.59) is defined in a (v, ξ) velocity space, while EUTERPE operates in (v_{\parallel}, μ) space. Hence, the equations of motion, which for the slowing-down part of Eq. (B.59) are given as

$$\dot{v} = -\frac{v^3 + v_c^3}{v^2 \tau_s}, \quad \dot{\xi} = 0, \quad (\text{B.61})$$

have to be transformed according to

$$v = \sqrt{v_{\parallel}^2 + 2\mu B}, \quad \xi = \frac{v_{\parallel}}{v}. \quad (\text{B.62})$$

Inverting this system yields

$$v_{\parallel} = v\xi, \quad \mu = \frac{v^2(1 - \xi^2)}{2B} \quad (\text{B.63})$$

making it possible to transform the equations of motion from (v, ξ) to (v_{\parallel}, μ)

$$\dot{v}_{\parallel} = \dot{v}\xi + v\dot{\xi} = -\frac{v^3 + v_c^3}{v^2 \tau_s} \frac{v_{\parallel}}{v} = -\frac{v_{\parallel}(v^3 + v_c^3)}{v^3 \tau_s} \quad (\text{B.64})$$

$$\dot{\mu} = \frac{2v\dot{v}(1 - \xi^2) - 2v^2\xi\dot{\xi}}{2B} \quad (\text{B.65})$$

$$= \frac{v\dot{v}(1 - \xi^2)}{B} = -\frac{v^3 + v_c^3}{v^2 \tau_s} \frac{v}{B} (1 - \xi^2) = -\frac{v^3 + v_c^3}{vB\tau_s} (1 - \xi^2). \quad (\text{B.66})$$

Note that this simplified fast-ion collision operator was derived under the assumption that the fast ions are much faster than the background-plasma ions, but slower than the electrons [66]. In a particle simulation, the fast ions are loaded with a velocity distribution, which means that there exist ‘slow’ fast ions which are slower than the bulk ions. While for the initial benchmark presented below Eqs. (B.64) and (B.66) have been implemented, physically more meaningful cases have been investigated in articles A.3, A.4, and A.5 using a less simplified collision operator, which behaves asymptotically correctly for small velocities. Its derivation is presented in article A.5.

B.5.1 Testing the implementation

The implementation of the slowing-down part of the fast-ion collision operator (recall that the pitch-angle part has already been tested in article A.1) is now verified for a simplified case. The kinetic equation

$$\frac{\partial f_{\text{f}}}{\partial t} - \frac{1}{v^2 \tau_s} \frac{\partial}{\partial v} [(v^3 + v_c^3) f_{\text{f}}] = S\delta(v - v_{\text{birth}}) \quad (\text{B.67})$$

is solved only for the fast-ion species. Bulk ions and electrons are not considered in this simulation. The parameters of this case are chosen as (in normalized EUTERPE units)

$$\tau_s = 1, \quad v_c = 1, \quad B = 1, \quad v_{\text{birth}} = 2 \quad (\text{B.68})$$

for simplicity.

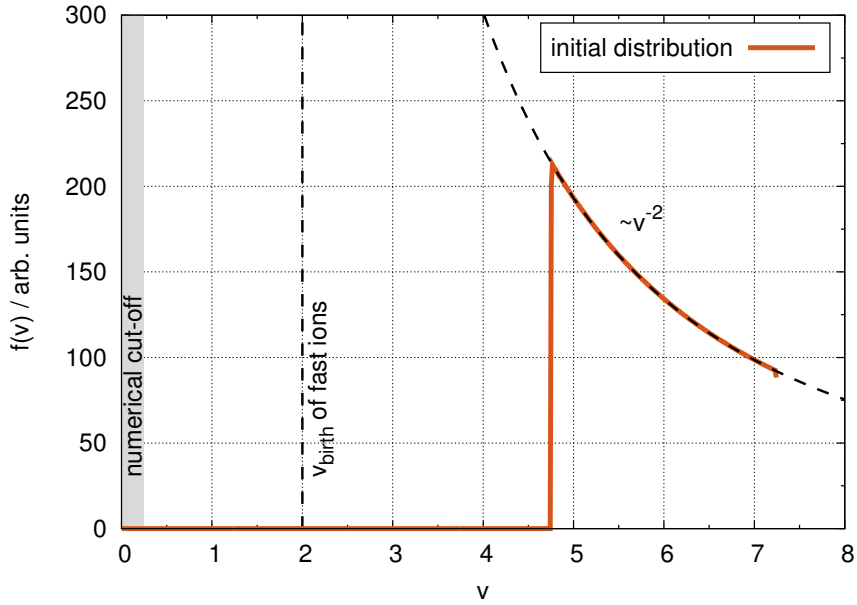


Figure B.5: Initial distribution of particles in velocity space. The particles are uniformly distributed in a spherical velocity space.

We start with an initial distribution of particles in velocity space as shown in Fig. B.5. This distribution is chosen to be proportional to v^{-2} since this corresponds to uniformly distributed particles in a spherical velocity space. More precisely, $f(v)J = \text{const.}$, with J being the Jacobian, is enforced. When the simulation begins, the 10^6 numerical particles that make up the initial distribution are pushed towards $v = v_{\text{birth}}$. However, at this stage, the particles do not follow their ‘real’ equations of motion. Instead, $\dot{v} = -1$ is used. This corresponds to

$$\dot{v}_{\parallel} = -\frac{v_{\parallel}}{v\tau_s} \quad (\text{B.69})$$

$$\dot{\mu} = -\frac{v(1-\xi^2)}{B\tau_s} \quad (\text{B.70})$$

in the EUTERPE implementation. The reason why these ‘artificial’ equations of motions are used in the initial phase of the simulation is to account for the fact that the flow of particles should be incompressible until they reach $v = v_{\text{birth}}$. Together with the choice of the initial shape of the distribution, this provides a particle source that is constant in time.

Once a particle fulfils the condition $v \leq v_{\text{birth}}$ for the first time, its velocity is reset to $v = v_{\text{birth}}$ and it is assigned a random pitch angle $\xi = \cos[\pi\mathcal{U}(0,1)]$, where \mathcal{U} is a uniform distribution of random numbers. From this the initial values for v_{\parallel} and μ can be calculated. Furthermore, from now on the ‘real’ equations of motion are solved for that particle and its weight is allowed to evolve. The weight equation is given as

$$\dot{w} = S\delta(v - v_{\text{birth}}) \quad (\text{B.71})$$

where, for numerical reasons, the delta distribution is extended to a narrow rectangle centred around v_{birth} . Thus, in practice the right-hand side of the weight equation is

$$S\delta(v - v_{\text{birth}}) = \begin{cases} 1 & \text{for } |v - v_{\text{birth}}| \leq 0.025 \\ 0 & \text{otherwise} \end{cases} \quad (\text{B.72})$$

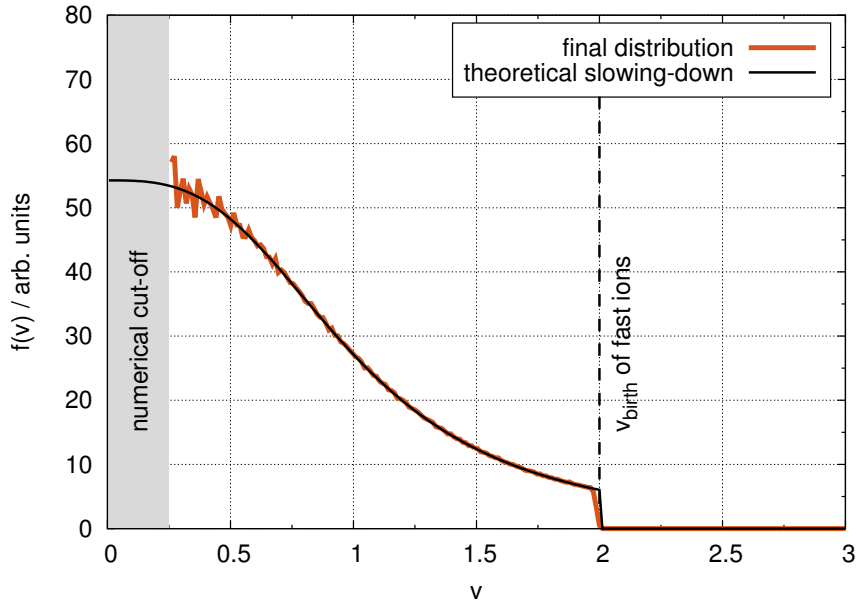


Figure B.6: Final distribution of particles in velocity space. The simulation result (red) matches the theoretically expected shape for the slowing-down distribution function (black), which is the analytical solution of Eq. (B.67) in steady state [66].

After 10^4 time steps with $\Delta t = 5.0 \cdot 10^{-4}$ a final particle distribution as depicted in Fig. B.6 is formed. This distribution is obtained by generating a histogram of the final particle velocities taking into account the numerical weight of each particle. Furthermore, the result is divided by v^2 , proportional to the Jacobian in spherical coordinates. Note how the red curve obtained by EUTERPE and the theoretical curve (black) agree very well. The theoretical curve corresponds to the steady-state solution of Eq. (B.67)

$$f_f(v) = \frac{\text{const.}}{v^3 + v_c^3} H(v_{\text{birth}} - v) \quad (\text{B.73})$$

with H denoting the Heaviside step function. The constant in Eq. (B.73) is calculated from a fit to the EUTERPE result. The reason why the EUTERPE result becomes more noisy for lower velocities is that, in the original curve, where the division by v^2 was not yet performed, only few particles are present at low velocities. Therefore the particle noise, inherent to any PIC simulation (see, for instance, Refs. [97,98]), is stronger. Obviously, the noise level could be decreased by using more particles.

For $v \leq 0.25$ no data are available from EUTERPE, since a numerical cut-off for low velocities has been implemented, the reason being that the equation of motion for v is highly non-linear and $|\dot{v}|$ increases rapidly for $v \rightarrow 0$. After a particle has crossed into the region of the numerical cut-off its equations of motion are no longer integrated in time. Avoiding the need of a cut-off is part of the reason why the operator was modified in article A.5. Furthermore, if μ is very small it can become negative due to small numerical errors. As this is not physical, the sign of μ is then changed artificially.

B.6 Evolving multiple modes in a single simulation

Here, we show first results of the newly implemented multi-mode version of CKA-EUTERPE, in which multiple modes are evolved together in a single simulation. This is a significant improvement of the previous model as it allows for the transfer of energy between the modes. Furthermore, the modes can influence each other via their combined interaction with the fast-ion distribution function in a non-linear simulation. We thus expect the non-linear results (like frequency chirping and the initial and long-term saturation levels) to change in a multi-mode simulation. Note that in realistic experimental conditions a variety of modes can ‘be active’ at the same time (see e.g. Refs. [4, 88]), a fact that is accounted for in the multi-mode model.

We have shown in previous simulations (see articles A.2 and A.3) that a single Alfvén eigenmode saturates non-linearly by wave particle trapping [8, 73] accompanied by a local flattening of the fast-ion density profile. The present case, including multiple modes, could be a scenario in which the combination of multiple modes leads to a flattening of the fast-ion density profile throughout the entire radial domain.

In CKA-EUTERPE, the multi-mode model is implemented as follows [102]: As before, the CKA code [71] is used to determine the frequency and eigenmode structure of the Alfvén waves. But now, more than one mode is considered and transferred to EUTERPE. The power transfer remains mode-specific, meaning that it is calculated for each mode k individually

$$P_k = - \int d\Gamma B_{\parallel}^* \left[\frac{m}{ZeB} \mathbf{b} \times \left(v_{\parallel}^2 \boldsymbol{\kappa} + \mu \nabla B \right) \cdot \left(Ze \nabla_{\perp} \phi_k^* (\mathbf{r}, t) f^{(1)} \right) \right]. \quad (\text{B.74})$$

Accordingly, the amplitude equations are modified to

$$\frac{\partial \hat{\phi}_k}{\partial t} = i\omega_k \left(\hat{A}_{\parallel,k} - \hat{\phi}_k \right) + 2 \left(\gamma_k(t) - \gamma_{d,k} \right) \hat{\phi}_k \quad \text{and} \quad \frac{\partial \hat{A}_{\parallel,k}}{\partial t} = i\omega_k \left(\hat{\phi}_k - \hat{A}_{\parallel,k} \right), \quad (\text{B.75})$$

where

$$\gamma_k(t) = \sum_l T_{kl}^{-1} P_l \quad (\text{B.76})$$

and $\gamma_{d,k}$ are the mode-specific growth rates and an array of externally specified damping rates, respectively. As is shown below, we can use STAE-K (see article A.6) to calculate the damping rates. The quantity

$$T_{kl} = \exp [i(\omega_k - \omega_l) t] \hat{\phi}_k \hat{\phi}_l^* \int d^3r \frac{m_i n_i}{2B^2} (\nabla_{\perp} \phi_{0,k}) \cdot (\nabla_{\perp} \phi_{0,l})^* \quad (\text{B.77})$$

is the so-called mode coupling matrix. This hermitian matrix ultimately governs the exchange of energy of the modes and thus couples their temporal evolution. In a non-linear simulation, it is important that the particles react to the combined perturbed field, which is calculated according to

$$\phi(\mathbf{r}, t) = \sum_k \hat{\phi}_k(t) \phi_{0,k}(\mathbf{r}) \exp(i\omega_k t) \quad (\text{B.78})$$

as a linear superposition of all modes. A_{\parallel} is treated equivalently. Considering only one mode, the whole system of equations (Eq. (B.74) – Eq. (B.78)) reduces to the previous single-mode case. (See Eq. (12) – Eq. (15) on pages 57 and 58.)

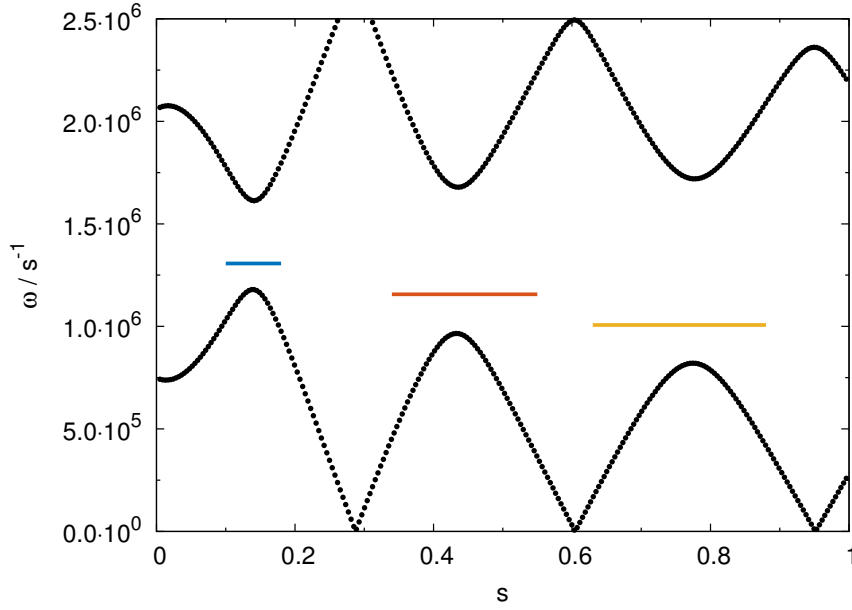


Figure B.7: Shear Alfvén wave continuum for the multi-mode benchmark case. The black circles indicate the continuum modes. The three horizontal lines illustrate the frequencies of the eigenmodes in the TAE gap. The length of the lines is equal to the full width at half maximum of the respective radial eigenfunctions.

B.6.1 Case description

As a first test case for the multi-mode version, we use a variant of the ITPA tokamak benchmark case [43, 44]. A notable difference is that we reduce the major radius to $R_0 = 3$ m, resulting in an aspect ratio of $R_0/a = 3$. The q -profile is chosen as

$$q(s) = 1.71 + 0.48s [1 - \operatorname{erfc}(4s)] \quad (\text{B.79})$$

in an effort to yield broad modes with sufficient radial overlap. s denotes the normalized toroidal flux. For simplicity, the equilibrium used for the VMEC [103] calculations has zero pressure, i.e. $\beta = 0$. The fast-ion density profile is chosen as

$$n_f(s) = n_{f,0} (1 - 0.95s) \quad (\text{B.80})$$

with $n_{f,0} = 2.0 \cdot 10^{17} \text{ m}^{-3}$. The temperature profiles of the fast ions and the bulk plasma are flat with $T_{f,0} = 400 \text{ keV}$ and $T_{b,0} = 1 \text{ keV}$, respectively. All other parameters are as defined in Refs. [43, 44]. For simplicity, collisions have been neglected throughout this section.

The shear Alfvén wave continuum for this case, calculated by the CONTI code [104], is depicted in Fig. B.7. We limit the view to the TAE gap, which due to the choice of parameters, is open throughout the entire minor radius. Within this gap, three discrete eigenmodes are found by CKA. Their radial structure is shown in Fig. B.8. Due to their radial localization the modes are labelled ‘core’, ‘middle’, and ‘edge’, respectively. As can be seen in the figure, the middle and edge mode overlap strongly. The core mode, on the other hand, is less coupled to the other two. The real frequencies of the modes are: $\omega^{\text{core}} = 1.31 \cdot 10^6 \text{ s}^{-1}$, $\omega^{\text{middle}} = 1.16 \cdot 10^6 \text{ s}^{-1}$, and $\omega^{\text{edge}} = 1.01 \cdot 10^6 \text{ s}^{-1}$. For this benchmark, we choose modes with the same toroidal mode number ($n = -6$), but different poloidal mode numbers. Thus, the modes couple linearly via the mode coupling matrix. Non-linearly the modes couple via the fast-ion density profile.

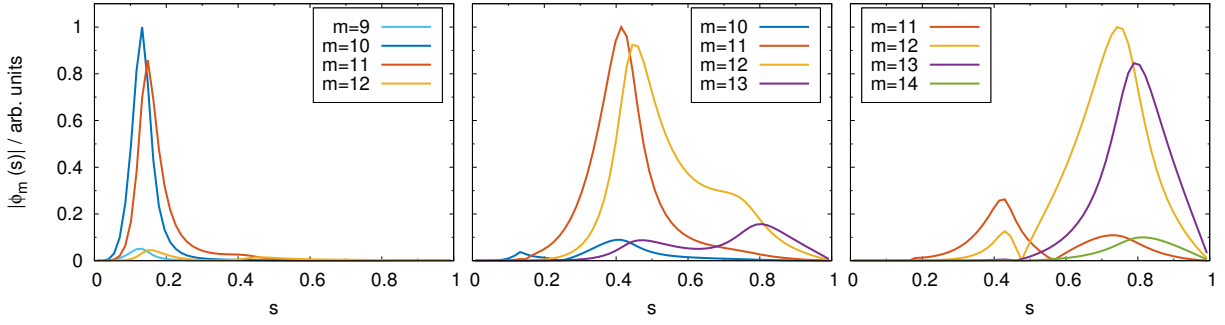


Figure B.8: Radial structure of the global eigenmodes (all TAEs) considered in this scenario. Due to their radial localization the modes are labelled ‘core’, ‘middle’, and ‘edge’ (from left to right), respectively. There is significant radial overlap between the middle and edge mode.

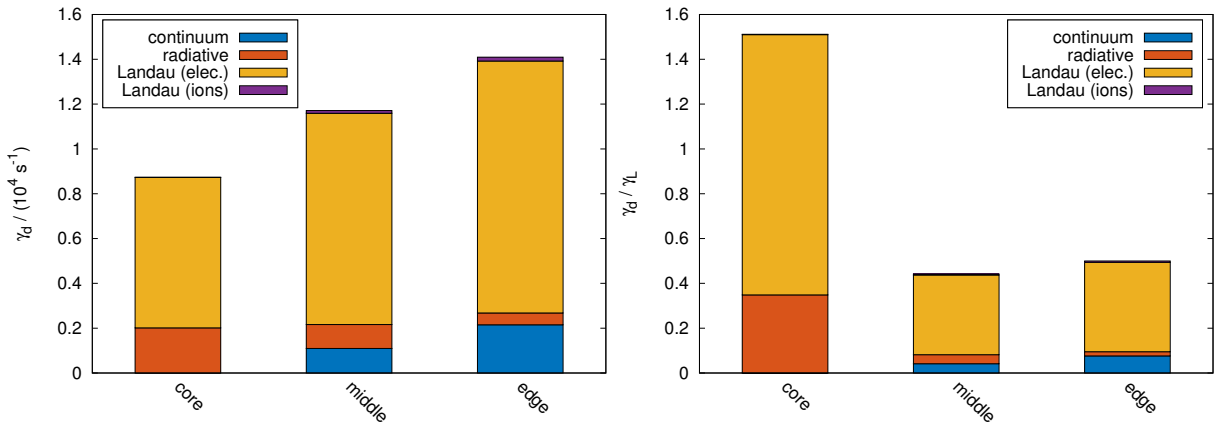


Figure B.9: Contributions of various physical mechanisms to the overall damping rates of the modes. The calculations are carried out using STAE-K (see article A.6). The left-hand side shows the damping rates in SI-units, the right-hand side normalized to the mode-specific linear growth rates. For all modes electron Landau damping is the largest contributor. On the other hand, ion Landau damping can be neglected.

Note that Ref. [105] reported that the number of particles required to achieve converged results increases with the number of modes considered in the simulation. In the EUTERPE simulations, we use $N_p = 10^6$ numerical marker particles to get converged results. The time step is $\Delta t = 20 \Omega_i^{-1}$.

B.6.2 Damping rates

Recall that in the CKA-EUTERPE model the damping rate γ_d is an external parameter. It has to be calculated by another code. Since CKA-EUTERPE is intended to be used for stellarators, we need a tool which can compute the damping rates of the eigenmodes in stellarator geometry. Here, we use STAE-K (introduced in article A.6) for this purpose. It can compute the total mode damping which is a combination of continuum [41, 45], radiative [47], and background-plasma Landau damping [46]. All these contributions to γ_d are shown in Fig. B.9. Note that in the new multi-mode version, each mode is generally damped differently. The left-hand side of the figure shows the damping rates in SI-units. On the right-hand side the damping rates are normalized to the individual growth rates of the modes (using linear growth rates measured in a non-linear calculation without damping which is not shown here). For all modes, electron Landau damping

Table B.1: Initial growth rates (including damping) of the Alfvén eigenmodes in the linear phases of the simulations for both the single-mode and multi-mode model.

mode	γ/s^{-1} (single-mode)	γ/s^{-1} (multi-mode)
core	$-2.90 \cdot 10^3$	$-2.95 \cdot 10^3$
middle	$1.57 \cdot 10^4$	$1.51 \cdot 10^4$
edge	$1.36 \cdot 10^4$	$1.43 \cdot 10^4$

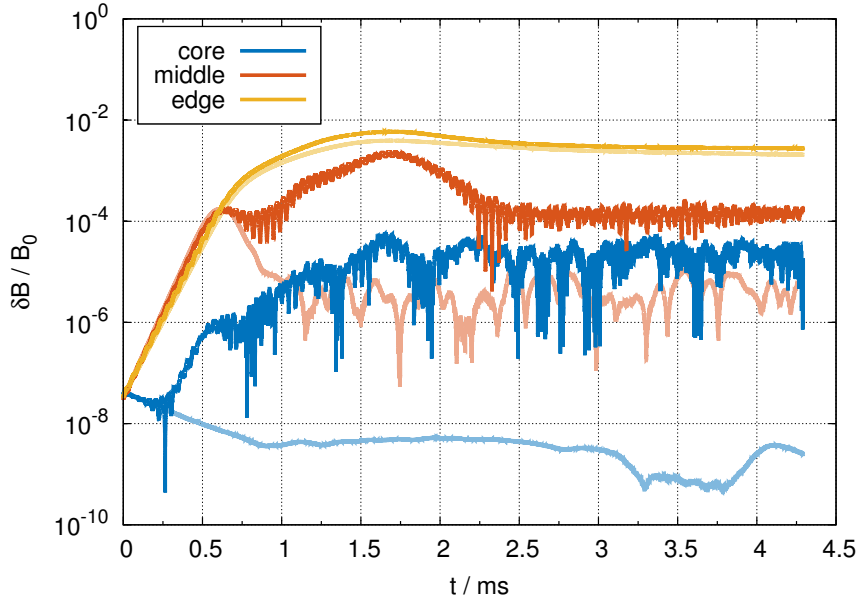


Figure B.10: Comparing the temporal development of the mode amplitudes in single-mode (light colours) and a multi-mode simulation (dark colours). The damping rates have been calculated by STAE-K. Considering the modes as independent or evolving them together leads to significant differences. This is most apparent for the core and middle modes and less so for the edge mode.

is the largest contributor. The strengths of radiative and continuum damping depend very much on the mode itself. The core mode has negligible continuum damping, since it is highest in frequency and therefore lies entirely in the TAE gap. As expected, background-ion Landau damping could have been neglected.

The ratio γ_d/γ_L equals 1.51, 0.44, and 0.49 for the core, middle, and edge mode, respectively. Hence, the damping outweighs the drive for the core mode. It is expected to be stable in a single-mode simulation.

B.6.3 Multi-mode results

Knowing now the damping rates of all modes, we can perform a non-linear multi-mode simulation including both damping and fast-ion drive. The effective linear growth rates, $\gamma = \gamma_L - \gamma_d$, are listed in Tab. B.1, where we compare the single-mode results with the ones obtained in the multi-mode simulation. As expected, the growth rates are similar, but some measurable differences are visible. The largest change is seen for the edge mode, for which γ changes by 5%. In Fig. B.10 we directly compare the time evolution of the mode amplitudes in the single-mode simulations (light colours) to the multi-mode results (dark colours). Very clearly, differences

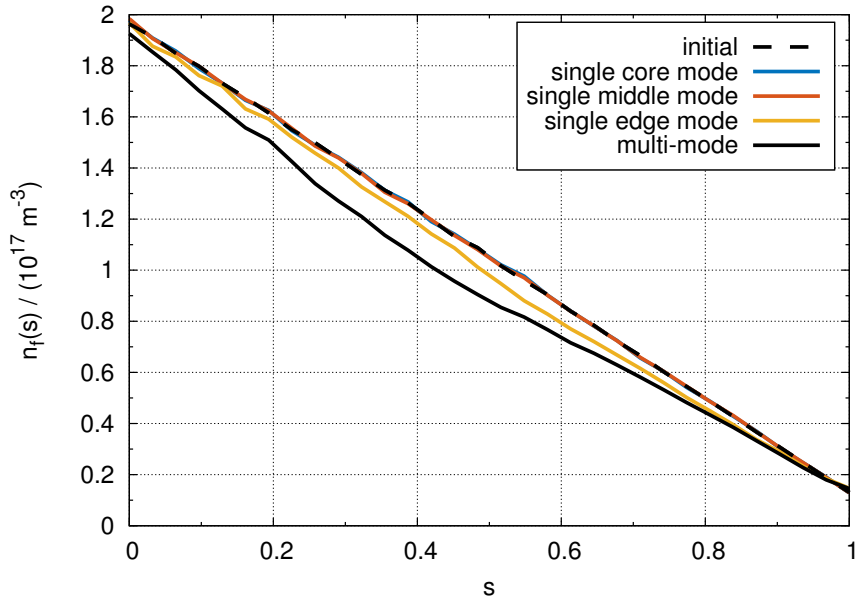


Figure B.11: Fast-ion density profile at the beginning (dashed black line) and end of the single-mode (coloured lines) and multi-mode (black line) simulations. Considering the single-mode simulations, only the edge mode can flatten the fast-ion density profile. In a multi-mode simulation, however, the flattening is much stronger.

are visible: While the core mode, due to its low growth rate in the absence of damping, is stable – once damping is taken into account – and saturates at a very low level in a single-mode simulation, the same mode is destabilized in the multi-mode simulation. It then grows with a rate similar to that of the other two modes. The saturation level is enhanced by four orders of magnitude, which clearly shows that estimates linking the linear growth rate and the saturation level (like the ones in Refs. [9, 10, 73, 106]) should be taken with care. Overall, the behaviour of the core mode is strongly linked to the dynamics of the other two.

A similar observation, albeit not quite as extreme, can be made for the middle mode. In the single-mode simulation this mode decays after its initial saturation (first maximum of the mode amplitude after the linear phase) at $t \approx 0.6$ ms. In the multi-mode simulation, on the other hand, the mode continues to grow, which results in a significantly enhanced saturation level. The difference is between one and two orders of magnitude. In the multi-mode simulation the middle mode shows short-period oscillations that could be linked to frequency chirping. The edge mode, despite having a higher γ_d/γ_L -ratio exhibits no oscillations. Moreover, the edge mode shows only small differences as far as comparing the single and multi-mode simulation is concerned.

Note that Fig. B.10 is very reminiscent of Fig. 13 in Ref. [105], which shows features like significantly enhanced saturation levels and originally stable modes becoming destabilized by the multi-mode interactions that we also observe. This can be expected due to the closeness of the models (here: STAE-K and CKA-EUTERPE vs. the LIGKA / HAGIS model [107] in Ref. [105]) even though different cases have been considered.

The effects that the modes have on the fast-ion density profile individually and combined, respectively, is shown in Fig. B.11. The initial profile is shown as a dashed black line. The final profiles at the end of the non-linear simulations are shown as full lines. Colour indicates the single-mode results, while the black line corresponds to the multi-mode simulation including the combined effect of all modes. It can be observed that the core and middle mode alone do

not lead to any measurable change in the density profile. This is expected due to their very low saturation levels in the single-mode simulations. The edge mode, with its practically unchanged saturation level on the other hand, can flatten the density profile non-linearly.

In the multi-mode simulation, however, a much stronger flattening is observed. This can be attributed to two leading causes: Firstly, the saturation levels of all modes (though mainly core and middle mode) are enhanced in the multi-mode simulation. Secondly, the radial overlap of multiple modes present in a single simulation can lead to higher transport since the particles ‘see’ a much broader fluctuation. This assessment is supported by the fact that the profile is most strongly flattened around $s \approx 0.4$, which coincides with the location of the middle mode that saturates on a lower level than the edge mode.

The plan for the future is to verify this multi-mode version of CKA-EUTERPE against the LIGKA / HAGIS model [105,107] and then to perform simulations for W7-X.

Nomenclature

Abbreviations

AE	Alfvén eigenmode
ASDEX-U	Axisymmetric Divertor Experiment Upgrade, a tokamak in Germany
BAE	Beta-induced Alfvén eigenmode
EAE	Ellipticity-induced Alfvén eigenmode
EPM	Energetic-particle mode
FLR	Finite Larmor radius
FOW	Finite orbit width
GAE	Global Alfvén eigenmode
HAE	Helicity-induced Alfvén eigenmode
ICRH	Ion-cyclotron-resonance heating
ITPA	International Tokamak Physics Activity
JT-60U	Japan Torus-60 Upgrade, a tokamak in Japan
KAW	Kinetic Alfvén wave
KTAE	Kinetically modified TAE
LHD	Large Helical Device, a stellarator in Japan
MAE	Mirror-induced Alfvén eigenmode
MHD	Magnetohydrodynamics
NBI	Neutral beam injection
NSTX	National Spherical Torus Experiment, a tokamak in the United States of America
PIC	Particle in cell
TAE	Toroidicity-induced Alfvén eigenmode

Nomenclature

TFTR	Tokamak Fusion Test Reactor, a tokamak previously operated in the United States of America
TJ-II	Tokamak de la Junta de Energía Nuclear II, a stellarator in Spain
W7-AS	Wendelstein 7-AS, a stellarator previously operated in Germany (predecessor of W7-X)
W7-X	Wendelstein 7-X, a stellarator in Germany

Codes

ASCOT	A particle-following code able to calculate the distribution function of fast ions in tokamaks and stellarators [6, 7, 108]
CKA	An eigenvalue code able to calculate Alfvén eigenmode frequencies and mode structures in tokamaks and stellarators [71]
DKES	A local drift-kinetic neoclassical transport code [109]
EUTERPE	A three-dimensional non-linear particle-in-cell code that can be used to calculate frequencies, growth rates, and mode structures of electrostatic micro-turbulence and electromagnetic Alfvén eigenmodes (used for the majority of the work presented in this thesis)
NTSS	A neoclassical transport code especially designed for stellarators [75]
SFINCS	A drift-kinetic neoclassical transport code for non-axisymmetric configurations, includes full linearized Fokker-Planck collision operator [110]
STAE-K	A shooting code, including kinetic effects non-perturbatively, able to calculate frequencies, growth and damping rates, as well as mode structures of Alfvén eigenmodes in tokamaks and stellarators [57]

General

$a^{(0)}$	Unperturbed part of a general quantity a
$a^{(1)}$	Perturbed part of a general quantity a
\mathbf{a}_\perp	Part of a general vector \mathbf{a} that is perpendicular to the magnetic field
a_\parallel	Part of a general vector \mathbf{a} that is parallel to the magnetic field
i, e, f	Labels ions, electrons, and fast ions, respectively

Symbols

\mathbf{A}	Vector potential
a	Minor radius of the toroidal device
A_\parallel^h	Hamiltonian part of A_\parallel
A_\parallel^s	Symplectic part of A_\parallel

β	Kinetic pressure of the plasma normalized to magnetic pressure (plasma beta), $\beta = 2\mu_0 k_B T n / B^2$
\mathbf{B}	Vector of the magnetic flux density (called ‘magnetic field’ throughout the thesis)
\mathbf{b}	Unit vector along the background magnetic field
B	Magnitude of the magnetic field
B_{\parallel}^*	The Jacobian of gyro-centre coordinates
\mathcal{C}	Collision operator
\mathcal{C}_{fp}	Field-particle collision operator
\mathcal{C}_{tp}	Test-particle collision operator
δB	Perturbed magnetic field (usually denotes the poloidal component)
δB^{sat}	The value of δB at saturation (first maximum after the linear phase)
δf	Deviation of the distribution function from the chosen control variate (usually the background)
δn	Density change induced by the presence of a mode
$\Delta N, \Delta P, \Delta E$	Errors made in the conservation of particle number, linear momentum, and energy by just including the test-particle collision operator
Δt	Time step in the simulation
Δ	Usually denotes the Shafranov shift
$\delta\omega$	A frequency change
$\delta_{l,\nu}$	Kronecker delta
$d\Gamma$	Infinitesimal phase-space element
ϵ_0	Vacuum permittivity, $\epsilon_0 = 8.854 \cdot 10^{12} \text{ Fm}^{-1}$
\mathbf{E}	Electric field
e	Elementary charge, $e = 1.602 \cdot 10^{-19} \text{ C}$
E_{max}	Maximum injection energy of the NBI system
E_r	Radial electric field
F	(also $f^{(0)}$ and f_0) Equilibrium (background) distribution function, f^{M} specifically denotes a Maxwellian background
f	Distribution function (also denotes the mode frequency in Hz)
$f^{(1)}$	(also f_1) Perturbed part of the distribution function

Nomenclature

f_l	Coefficients for the expansion into Legendre polynomials
γ	Imaginary part of the complex frequency: growth or damping rate
γ_d	Damping rate (external parameter in CKA-EUTERPE)
γ_L	Linear growth rate
H	Heaviside step function
ι	Rotational transform
i	Imaginary unit
\mathbf{j}	Vector of the current density
κ	Curvature of the magnetic field lines
\mathbf{k}	Wave vector of the mode, with perpendicular and parallel components \mathbf{k}_\perp and k_\parallel (also $k_{m,n}$), respectively
k_B	Boltzmann constant, $k_B = 1.381 \cdot 10^{-23} \text{ JK}^{-1}$
$\ln \Lambda$	Coulomb logarithm
\mathcal{L}	Pitch-angle collision operator
μ	Magnetic moment per mass, $\mu = v_\perp^2 / (2B)$ (also denotes mode coupling in poloidal direction)
μ_0	Vacuum permeability, $\mu_0 = 4\pi \cdot 10^{-7} \text{ Hm}^{-1}$
m	Poloidal mode number (also denotes particle mass, which is sometimes denoted by M)
$\mathcal{N}, \mathcal{P}, \mathcal{E}$	Coefficients in the field-particle collision operator
ν	Collision frequency (also denotes mode coupling in toroidal direction)
ν_D	Pitch-angle scattering frequency
ν_E	Energy diffusion frequency
ν_{Krook}	Rate at which the distribution function is rebuilt using a Krook operator
ν_s	Slowing-down frequency
ν_\parallel	Parallel velocity diffusion frequency
n	Toroidal mode number (also denotes particle density, which is sometimes denoted by N)
N, P, E	Functions used as a linear combination in the field-particle collision operator
N_p	Number of numerical marker particles used in simulations (also denotes number of field periods, which is sometimes denoted by N)

Ω	Gyration frequency, $\Omega = qB/m$
ω	Mode frequency in rad/s^{-1}
ω_b	Bounce frequency of a particle trapped in the wave
$\hat{\phi}, \hat{A}_{\parallel}$	Complex amplitudes of ϕ and A_{\parallel} in the CKA-EUTERPE framework
ϕ	(also Φ) Electrostatic potential
ϕ_1	Neoclassical electrostatic potential variation on a flux surface
φ	(also ϕ) Toroidal angle
p	Pressure
p_{\parallel}	Parallel canonical momentum, $p_{\parallel} = mv_{\parallel} + qA_{\parallel}$
P_l	The l^{th} Legendre polynomial
q	Safety factor (also denotes particle charge)
\mathbf{R}	Gyro-centre position of the particle
\mathbf{r}	Spatial position
ρ	(thermal) gyro-radius of a particle, $\rho = v_{\text{th}}/\Omega$ (also denotes the mass density of the plasma)
ρ_s	Sound gyro-radius, $\rho_s = \sqrt{k_B T_e m_i}/(q_i B)$
R_0	Major radius of the toroidal device
s	Normalized toroidal flux, $s = r^2/a^2$ (radial coordinate usually used in stellarators)
τ_s	Slowing-down time
θ	(also Θ) Poloidal angle
T	Temperature
t	Time
\tilde{u}_{\parallel}	Parallel velocity coordinate in the mixed formulation, $\tilde{u}_{\parallel} = v_{\parallel} + q/mA_{\parallel}^h$
u	Magnitude of the velocity in the p_{\parallel} -formulation
u_{\parallel}	Parallel velocity coordinate in the p_{\parallel} -formulation, $u_{\parallel} = v_{\parallel} + q/mA_{\parallel}$
v	Magnitude of the particle velocity in the v_{\parallel} -formulation
v_A	Alfvén velocity, $v_A = B/\sqrt{\mu_0 m_i n_i}$
v_c	Critical velocity
v_{th}	Thermal velocity, $v_{\text{th}} = \sqrt{k_B T/m}$

Nomenclature

v_{\parallel}	Parallel velocity in the v_{\parallel} -formulation
ξ	Pitch-angle variable, $\xi = v_{\parallel}/v$
ξ'	Pitch-angle variable in the p_{\parallel} -formalism, $\xi' = u_{\parallel}/u$
Z	Charge number of the particle (also denotes the plasma dispersion function)
z	Direction parallel to the magnetic field

Eigenständigkeitserklärung

Hiermit erkläre ich, dass diese Arbeit bisher von mir weder an der Mathematisch-Naturwissenschaftlichen Fakultät der Universität Greifswald noch einer anderen wissenschaftlichen Einrichtung zum Zwecke der Promotion eingereicht wurde.

Ferner erkläre ich, dass ich diese Arbeit selbstständig verfasst und keine anderen als die darin angegebenen Hilfsmittel und Hilfen benutzt und keine Textabschnitte eines Dritten ohne Kennzeichnung übernommen habe.

Christoph Slaby

Eigenständigkeitserklärung

Scientific contributions

Refereed publications in scientific journals

1. C. Slaby, A. Könies, and R. Kleiber. Numerical investigation of non-perturbative kinetic effects of energetic particles on toroidicity-induced Alfvén eigenmodes in tokamaks and stellarators. *Physics of Plasmas*, **23** (9) 092501 (2016).
2. C. Slaby, R. Kleiber, and A. Könies. Combining electromagnetic gyro-kinetic particle-in-cell simulations with collisions. *Computer Physics Communications*, **218** 1–9 (2017).
3. C. Slaby, A. Könies, R. Kleiber, and J. M. García-Regaña. Effects of collisions on the saturation dynamics of TAEs in tokamaks and stellarators. *Nuclear Fusion*, **58** (8) 082018 (2018).
4. J. M. García-Regaña, T. Estrada, I. Calvo, J. L. Velasco, J. A. Alonso, D. Carralero, R. Kleiber, M. Landreman, A. Mollén, E. Sánchez, C. Slaby, and TJ-II Team, and W7-X Team. On-surface potential and radial electric field variations in electron root stellarator plasmas. *Plasma Physics and Controlled Fusion*, **60** (10) 104002 (2018).
5. C. Slaby, A. Könies, R. Kleiber, S. Äkäslompolo, and J. Kontula. Parametric study of fast-ion-driven modes in Wendelstein 7-X. *Journal of Physics: Conference Series*, **1125** 012019 (2018).
6. C. Slaby, A. Könies, R. Kleiber, and H. Leyh. On non-linear frequency chirping in connection with collisions. *submitted to Nuclear Fusion* (2018).

Non-refereed publications

1. C. Slaby, A. Könies, R. Kleiber, S. Äkäslompolo, and J. Kontula. Numerical investigation of fast-ion-driven modes in Wendelstein 7-X. *Europhysics Conference Abstracts*, **42A** P4.1098 (2018).

Conference and workshop contributions

1. C. Slaby, A. Könies, and R. Kleiber. Energetic Particle Modes in Tokamaks and Stellarators (talk). *Garching-Greifswald Theory Meeting*. 23 – 27 November 2015, Plau am See, Germany.
2. C. Slaby, A. Könies, and R. Kleiber. Non-perturbative kinetic influences due to energetic particles on toroidicity-induced Alfvén eigenmodes (poster). *DPG Spring Meeting*. 28 February – 4 March 2016, Hannover, Germany.

3. C. Slaby, R. Kleiber, and A. Könies. Combining electromagnetic gyro-kinetic particle-in-cell simulations with collisions (talk). *Garching-Greifswald Theory Meeting*. 7 – 11 November 2016, Ringberg Castle, Germany.
4. C. Slaby, R. Kleiber, and A. Könies. Combining electromagnetic particle-in-cell simulations with collisions (poster). *DPG Spring Meeting*. 13 – 17 March 2017, Bremen, Germany.
5. C. Slaby, A. Könies, and R. Kleiber. Effects of collisions on the saturation dynamics of TAEs in tokamaks and stellarators (poster). *15th IAEA Technical Meeting on Energetic Particles in Magnetic Confinement Systems*. 5 – 8 September 2017, Princeton, USA.
6. C. Slaby, A. Könies, and R. Kleiber. Effects of collisions on the non-linear dynamics of TAEs in tokamaks and stellarators (poster). *21st International Stellarator-Heliotron Workshop*. 2 – 6 October 2017, Kyoto, Japan.
7. C. Slaby, A. Könies, and R. Kleiber. Effects of collisions on the saturation dynamics of TAEs in tokamaks and stellarators (talk). *Garching-Greifswald Theory Meeting*. 20 – 24 November 2017, Berlin, Germany.
8. C. Slaby, A. Könies, R. Kleiber, A. Mishchenko, M. Borchardt, and H. Leyh. Simulation of fast-ion-driven instabilities in W7-X (talk). *Workshop on Fast-Ion Physics in W7-X*. 22 – 23 January 2018, Greifswald, Germany.
9. C. Slaby, A. Könies, and R. Kleiber. Gyro-kinetic simulations of tokamaks and stellarators including collisions (talk). *DPG Spring Meeting*. 5 – 9 March 2018, Erlangen, Germany.
10. C. Slaby, A. Könies, R. Kleiber, S. Äkäslompolo, and J. Kontula. Numerical investigation of fast-ion-driven modes in Wendelstein 7-X (poster). *45th EPS Conference on Plasma Physics*. 2 – 6 July 2018, Prague, Czech Republic.
11. C. Slaby, A. Könies, R. Kleiber, S. Äkäslompolo, and J. Kontula. Parametric study of fast-ion-driven modes in Wendelstein 7-X (poster). *Joint Varenna – Lausanne International Workshop on Theory of Fusion Plasmas*. 27 – 31 August 2018, Varenna, Italy.

Summer schools

1. Summer University for Plasma Physics and Fusion Research, 14 – 18 September 2015, Max Planck Institute for Plasma Physics, Garching (near Munich), Germany.
2. International HPC Summer School on HPC Challenges in Computational Sciences, 26 June – 1 July 2016, Ljubljana, Slovenia.

Christoph Slaby

Acknowledgement

I wish to thank Per Helander for giving me the opportunity to study this subset of the fascinating topics that are magnetic confinement fusion and stellarator theory in particular. I appreciate that he gave me the freedom to pursue every angle I saw fit. At the same time the door to his office was always open when discussions were needed.

Great thanks goes to my daily supervisors Axel Könies and Ralf Kleiber. We had many interesting discussions about plasma physics, numerical methods, the best strategies for finding a bug in the code, and sometimes also about the recent political developments of the day. Their openness contributed to a great working atmosphere.

Thanks goes out to my office mates Michael Cole, Ksenia Aleynikova, and Daniel Kennedy for providing a friendly atmosphere in the office. I note that having first Michael and later Daniel around was very convenient for asking questions about the intricacies of the English language.

I thank Matthias Borchardt and Henry Leyh for helping me with many computer issues on the workstation, the local cluster, and various remote supercomputers.

Jutta Gauger has always been helpful with planning conference trips and organizing other things related to the tedious issue of administration.

I also wish to thank the core-members of our daily coffee round, Håkan Smith, Ksenia Aleynikova, Daniel Kennedy, Jonathan Faustin, Axel Hallenbert, Sophia Henneberg, Brendan Shanahan, and Pavel Aleynikov, for loosening up the daily work routine and the possibility to have (often quite funny) conversations about issues not related to physics. I will also fondly remember the barbecue parties we had in Gutsweg 8.

Last but not least, I want to thank my family for always supporting me during the time of the writing of this thesis.